

AB INITIO MODELLING OF MATERIALS PROPERTIES FOR CATALYTIC
AND DEVICE APPLICATIONS

A THESIS SUBMITTED TO
THE GRADUATE SCHOOL OF NATURAL AND APPLIED SCIENCES
OF
MIDDLE EAST TECHNICAL UNIVERSITY

BY

MEHMET GÖKHAN ŞENSOY

IN PARTIAL FULFILLMENT OF THE REQUIREMENTS
FOR
THE DEGREE OF DOCTOR OF PHILOSOPHY
IN
PHYSICS

SEPTEMBER 2017

Approval of the thesis:

**AB INITIO MODELLING OF MATERIALS PROPERTIES FOR CATALYTIC
AND DEVICE APPLICATIONS**

submitted by **MEHMET GÖKHAN ŞENSOY** in partial fulfillment of the requirements for the degree of **Doctor of Philosophy in Physics Department, Middle East Technical University** by,

Prof. Dr. Gülbin Dural Ünver
Dean, Graduate School of **Natural and Applied Sciences** _____

Prof. Dr. Altuğ Özpineci
Head of Department, **Physics** _____

Assoc. Prof. Dr. Hande Toffoli
Supervisor, **Physics Department, METU** _____

Assoc. Prof. Dr. Daniele Toffoli
Co-supervisor, **Department of Chemical and Pharmaceutical
Sciences, University of Trieste** _____

Examining Committee Members:

Prof. Dr. Mehmet Çakmak
Physics Department, Gazi University _____

Assoc. Prof. Dr. Hande Toffoli
Physics Department, METU _____

Assoc. Prof. Dr. Emrah Özensoy
Department of Chemistry, Bilkent University _____

Prof. Dr. Hatice Kökten
Physics Department, METU _____

Prof. Dr. Şenay Katırcıoğlu
Physics Department, METU _____

Date: _____

I hereby declare that all information in this document has been obtained and presented in accordance with academic rules and ethical conduct. I also declare that, as required by these rules and conduct, I have fully cited and referenced all material and results that are not original to this work.

Name, Last Name: MEHMET GÖKHAN ŞENSOY

Signature :

ABSTRACT

AB INITIO MODELLING OF MATERIALS PROPERTIES FOR CATALYTIC AND DEVICE APPLICATIONS

Şensoy, Mehmet Gökhan

Ph.D., Department of Physics

Supervisor : Assoc. Prof. Dr. Hande Toffoli

Co-Supervisor : Assoc. Prof. Dr. Daniele Toffoli

September 2017, 163 pages

The first-principles computations based on density functional theory is used to study the adsorption properties and the activation of CO, CO₂ and H₂O on γ -Al₂O₃(100) surface. A systematic study has been conducted to identify the most stable adsorption sites for both mono- and di-atomic Pt clusters. Several stable adsorption geometries have been identified for the species as well as introduces their interaction with Pt clusters and the support. In this context, analysis of the adsorption properties allows us to establish the most stable configuration in a reaction mechanism.

Another important factor in the reactivity of catalyst is the support material which has a great influence on the efficiency and activity of a catalytic reaction. Transition metal carbides (TMCs) are a good alternative as a support material in a catalytic reaction. Therefore, studying on the surfaces of platinum carbide (PtC) as a support material is being important. While the bulk structure of zincblende (ZB) PtC has

been investigated several times, a detailed understanding of the electronic and structural properties of its low-index surfaces is lacking. Within this study, we present an ab-initio investigation of the properties of five crystallographic ZB PtC surfaces, Pt/C-terminated PtC(100), PtC(110) and Pt/C-terminated PtC(111). Adsorption geometries have been identified for the atomic oxygen, and its interaction with surface atoms is characterized in terms of adsorption energies and the nature of bonding between the adsorbed and surface atoms. Calculated vacancy formation energies indicate facile C removal (exothermic) on the ZB PtC(111) surface, and Pt-vacancy formation is endothermic with respect to the vacancy formation energy. An ab-initio thermodynamical analysis shows that the most stable surfaces are the Pt-terminated PtC(100) and PtC(111) surfaces, and the higher oxygen coverages of PtC(100) surface are stable even at temperature as high as 3000 K.

In addition to the catalytic properties of an oxide surface and TMCs, we have also studied the interaction of chlorine (Cl) atom with graphene sheet and H-terminated graphene nanoribbons (GNRs) based on density functional theory (DFT). We have discussed the electronic and structural properties of adsorbed Cl atom on pristine and defective graphene under applied electric field. We have found that the most stable adsorption configurations are the on-site geometry and hollow site aligned parallel to the graphene plane for single and molecular Cl atom (Cl_2), respectively. The energy band structures are also performed to understand the nature of size effect including the effects on the magnetization, adsorption behavior of single Cl atom and charge transfer in graphene nanoribbons with zig-zag and armchair edges.

Keywords: Water-gas shift reaction, Transition Metal Carbides (TMCs), platinum carbide (PtC), Graphene, Graphene Nanoribbon

ÖZ

KATALİTİK VE AYGIT UYGULAMALARI İÇİN MALZEME ÖZELLİKLERİNİN İLK PRENSİP MODELLENMESİ

Şensoy, Mehmet Gökhan

Doktora, Fizik Bölümü

Tez Yöneticisi : Assoc. Prof. Dr. Hande Toffoli

Ortak Tez Yöneticisi : Assoc. Prof. Dr. Daniele Toffoli

Eylül 2017, 163 sayfa

γ -Al₂O₃ (100) yüzeyine takviye edilen Pt kümeleri üzerinde CO, CO₂ ve H₂O moleküllerinin yüzeye tutunma (adsorpsiyon) özelliklerini ve aktivasyonunu incelemek için yoğunluk fonksiyoneli teorisini esas alan ilk prensip bilgisayar hesaplamaları metodu kullanıldı. Tekli- ve ikili-atomik Pt kümelerinin her ikisi için en kararlı yüzeye tutunma bölgelerini tanımlamak için sistematik bir çalışma gerçekleştirildi. Türler için bir çok kararlı yüzeye tutunma geometrisinin tanımlanmasının yanı sıra bunları Pt kümeleri ve alttaş ile etkileşimleri de gösterildi. Bu kapsamda, yüzeye tutunma özelliklerini analiz etmek önemlidir çünkü bu analizler bir reaksiyon mekanizmasındaki en kararlı konfigürasyonu belirlememize olanak sağlar.

Katalizörlerin reaktivitesindeki bir diğer önemli faktör ise katalitik bir reaksiyonun verimliliği ve aktivitesi üzerinde büyük bir etkisi olan alttaş malzemedir. Geçiş metali karbürler (TMCs) katalitik bir reaksiyonda alttaş bir malzeme olarak iyi bir alternatiftir. Dolayısıyla, alttaş bir malzeme olarak platinyum karbür (PtC)'ün yüzeylerini

incelemek önemlidir. Zinblendede kristal yapıdaki PtC'nin özellikleri bir çok kez çalışılmışken, düşük indeksli yüzeylerin elektronik ve yapısal özelliklerinin ayrıntılı olarak anlaşılması eksik kalmıştır. Bu çalışma kapsamında, beş farklı kristalografik ZB yapıdaki PtC yüzeyinin (Pt/C ile biten PtC(100), PtC(110) ve Pt/C ile biten PtC(111)) özelliklerinin temel prensipler incelenmesi verilmiştir. Atomik oksijen için bağlanma geometrileri tespit edilmiş ve bunların yüzey atomları ile olan etkileşimleri, yüzeye tutunma enerjileri, ve yüzeye tutunan atomlarla yüzey atomları arasındaki ilişki bağlanma doğası cinsinden karakterize edilmiştir. Oluşan yapının boşluk oluşma enerjisine göre ZB PtC(111) yüzeyi üzerinde C'nin yok edilmesi kolay olup dışarı ısı verenken, Pt'nin yok edilmesi dışarıdan ısı alandır. Temel-prensip termodinamiksel analizler göstermektedir ki Pt- ile biten PtC(100) ve PtC(111) yüzeyleri en kararlı yüzeylerdir ve yüksek oksijen katkılı PtC(100) yüzeyi 3000 K gibi sıcaklıklarda bile kararlıdır.

Okside ve geçiş metal karbür yüzeylerinin katalitik özelliklerine ek olarak, klor (Cl) atomunun grafen yüzeyi ve hidrojen ile doyurulmuş grafen nanoşeritleri ile olan etkileşimleri de yoğunluk fonksiyoneli yöntemleri ile çalışılmıştır. Elektrik alan altındaki temiz ve kusurlu grafen yüzeyi üzerine bağlanmış Cl atomunun elektronik ve yapısal özellikleri tartışılmıştır. En kararlı yapıların sırasıyla Cl atomu için grafen üzerinde C atomu üzerinde olduğu, Cl molekülü (Cl₂) içinse grafen yüzeyine paralel altıgen karbon zincirinin merkezinde (hollow) olduğu bulunmuştur. Zig-zag ve armchair grafen nanoşeritlerinin boyutlarının, mıknatıslanma, Cl atomunun bağlanma özellikleri ve yük geçişlerine olan etkileri de dahil olmak üzere enerji bant yapıları elde edilmiştir.

Anahtar Kelimeler: Su-gaz değişimi reaksiyonu, Geçiş Metal Karbür, Platinyum Karbür (PtC), Grafen, Grafen Nanoşerit

To My Family

ACKNOWLEDGEMENTS

My academic life has undergone a rapid increase when I started my graduate studies in the Physics Department at Middle East Technical University. I could see that I will have plenty of time to reflect on the effects of possible research topics with the guidance of researcher in the department. It would be impossible without the mentorship of my advisors Assoc.Prof.Dr. Hande Toffoli and Assoc.Prof.Dr. Daniele Toffoli. I am very grateful to them for giving a chance to be a member of their research group and providing many opportunities while working on our research projects. I would like to thank to Assoc.Prof. Hande Toffoli for all advices in my academic life and having given me the opportunity to continue my thesis research in Kaxiras Research Group in John A. Paulson School of Engineering and Applied Sciences at Harvard University.

It was my great pleasure to Prof.Dr. Efthimios Kaxiras for his guidance and advices for my thinking skills while working exiting projects, and his personal supports for me when I have been in Cambridge, Massachusetts.

I have been very lucky to being a member of Kaxiras group, and work together with researchers, in particular; Dr. Dmitry Vinichenko and Robert Hoyt. Dr. Dmitry Vinichenko was a great colleague and a very knowledgeable resource for chemistry of materials.

I would like to acknowledge the Physics Department at Middle East Technical University, and my doctoral committee, Prof.Dr. Mehmet akmak, Assoc.Prof.Dr. Emrah zensoy, Prof.Dr. Hatice Kkten and Prof.Dr. Őenay Katırcıođlu, for their valuable suggestions and criticisms.

The completion of this thesis would not be possible without help and her support from my lovely friend, Dr. Elif Cinciođlu. I am delighted that you have always been with me.

I would like to thank my family, Recep Şensoy, Nurten Şensoy and Göksel Tolga Şensoy, for their love and supports throughout all these years. You are really great and the best thing in my life.

In my PhD. Education, I have been awarded by The Scientific and Technological Research Council of Turkey (TUBITAK) in the program of 2214-A for one year research scholarship during my thesis studies at Harvard University.

TABLE OF CONTENTS

ABSTRACT	v
ÖZ	vii
ACKNOWLEDGEMENTS	x
TABLE OF CONTENTS	xii
LIST OF TABLES	xvi
LIST OF FIGURES	xix
LIST OF ABBREVIATIONS	xxvii
CHAPTERS	
1 INTRODUCTION	1
1.1 Catalysis	2
1.1.1 Water Gas Shift Reaction	3
1.1.2 Structure of Alumina (Al ₂ O ₃)	6
1.2 Transition Metal Carbides and Nitrides	7
1.3 Graphene and Graphene Nanoribbons	9
1.3.1 Fabrication Methods	11
1.3.2 Structural Properties of Graphene and Graphene Nanoribbons	12

1.4	Overview of the Thesis	14
2	THEORETICAL BACKGROUND	17
2.1	Electronic Structural Methods	17
2.1.1	Density Functional Theory (DFT)	19
2.1.1.1	Pseudopotential Method	25
2.2	Transition State Method	28
2.2.1	Nudged Elastic Band Method (NEB)	29
2.3	Atomistic Thermodynamic DFT	30
2.3.1	Basics of Thermodynamics	30
2.3.2	Ab Initio Atomistic Thermodynamics	34
2.4	Adsorption and Desorption of Molecules on Surfaces	36
2.4.1	Physisorption and Chemisorption of Molecules	37
2.4.2	Desorption of Molecules	38
2.5	Vibrational Motions of an Adsorbate on Surface	38
2.6	Charges on Atoms	41
3	CO, CO ₂ AND H ₂ O ADSORPTION ON γ -Al ₂ O ₃ (100) SUPPORTED PLATINUM CLUSTERS	43
3.1	Introduction	43
3.2	Computational Details	46
3.3	Results and Discussion	48
3.3.1	Mono- and Di-atomic Pt Clusters on γ -Al ₂ O ₃ (100)	48

3.3.2	Molecular Adsorption of CO, CO ₂ and H ₂ O on Bare γ -Al ₂ O ₃ (100)	49
3.3.3	CO, CO ₂ and H ₂ O Adsorption on γ -Al ₂ O ₃ (100) Supported Pt and Pt ₂ Clusters	55
3.3.3.1	Adsorption of CO	55
3.3.3.2	Adsorption of CO ₂	59
3.3.3.3	Adsorption of H ₂ O	60
4	STRUCTURAL AND ELECTRONIC PROPERTIES OF BULK AND LOW-INDEX SURFACES OF ZINCBLLENDE PLATINUM-CARBIDE	65
4.1	Introduction	65
4.2	Computational Details	67
4.3	Results and Discussion	70
4.3.1	Bulk Properties of RS and ZB PtC	70
4.3.2	Surface Properties of ZB PtC	73
4.3.2.1	ZB PtC(100) Surface	73
4.3.2.2	ZB PtC(110) Surface	74
4.3.2.3	ZB PtC(111) Surface	77
4.3.3	Vacancies on C- and Pt-terminated ZB PtC(111) Surfaces	81
4.3.4	Adsorption Properties on ZB PtC(100), PtC(110) and PtC(111) Surfaces	82
4.3.4.1	Oxidation Behavior of ZB PtC(100), PtC(110) and PtC(111) Surfaces	83

	4.3.4.2	Atomic Adsorption on ZB PtC(100), PtC(110) and PtC(111) Surfaces . . .	89
5		CHLORINATED GRAPHENE AND GRAPHENE NANORIBBONS	97
	5.1	Introduction	97
	5.2	Computational Details	99
	5.3	Results and Discussion	100
	5.3.1	Adsorption of Chlorine on Pristine Graphene . . .	100
	5.3.1.1	Adsorption of Single Cl Atom	100
	5.3.1.2	Adsorption of Di-atomic Cl ₂ Molecule	104
	5.3.2	Adsorption of Chlorine on Defective Graphene . .	106
	5.3.3	Chlorinated Graphene Under Electric Field	109
	5.3.4	Chlorinated Zig-zag and Armchair Graphene Nanorib- bons	113
6		CONCLUSION	121
		REFERENCES	125
		CURRICULUM VITAE	161

LIST OF TABLES

TABLES

<p>Table 3.1 C-O and C-Al bond distances (d), partial Bader charge (ρ) of CO and shift of the vibrational mode frequencies of adsorbed CO molecule on bare γ-Al₂O₃. Distances are in Å and partial Bader charges in e. Vibrational frequencies are given in cm^{-1}. Vibrational frequencies are shifted by the value of 2142.4 cm^{-1} for the CO in gas phase.</p>	51
<p>Table 3.2 Bond angle, C-O and C-Al bond distances, partial Bader charge of CO₂ and shift of vibrational mode frequencies of adsorbed CO₂ molecule on bare γ-Al₂O₃(100) surface. Distances are in Å and partial Bader charges in e. Vibrational frequencies are given in cm^{-1}. Vibrational frequencies are shifted by the value of $\nu_b=634.0 \text{ cm}^{-1}$, $\nu_s=1312.9 \text{ cm}^{-1}$ and $\nu_a=2367.4 \text{ cm}^{-1}$ for the CO₂ in gas phase. $\Delta\nu_b^{[ip]}$ and $\Delta\nu_b^{[oop]}$ are shift of in-plane and out of-plane bending mode frequencies. ν_s: symmetric stretching, ν_a: asymmetric stretching and ν_b: bending modes.</p>	53
<p>Table 3.3 Bond angle, O-H and O-Al bond distances, partial Bader charge of H₂O and shift of vibrational mode frequencies of adsorbed H₂O molecule on bare γ-Al₂O₃(100) surface. Distances are in Å and partial Bader charges in e. Vibrational frequencies are given in cm^{-1}. Vibrational frequencies are shifted by the value of $\nu_s=3768.7 \text{ cm}^{-1}$, $\nu_a=3892.4 \text{ cm}^{-1}$ and $\nu_b=1566.8 \text{ cm}^{-1}$ for the H₂O in gas phase.</p>	54
<p>Table 3.4 Al-O bond distances (in Å) in the intermediate neighborhood of the surface H₂O adsorption sites.</p>	55

Table 3.5 C-O bond distance, partial Bader charges of CO and Pt and shift of vibrational mode frequencies of adsorbed CO molecule on γ -Al ₂ O ₃ (100) supported mono- and di-atomic Pt clusters. Distances are in Å and partial Bader charges in e . Vibrational frequencies are given in cm ⁻¹ . Vibrational frequencies are shifted by the value of $\nu=2142.4$ cm ⁻¹ for the CO in gas phase.	58
Table 3.6 C-O bond distance, bond angle, partial Bader charges of CO ₂ and Pt and shift of vibrational mode frequencies of adsorbed CO ₂ molecule on γ -Al ₂ O ₃ (100) supported mono- and di-atomic Pt clusters. Distances are in Å and partial Bader charges in e . Vibrational frequencies are given in cm ⁻¹ . Vibrational mode frequencies are shifted by the value of $\nu_s=1312.9$, $\nu_a=2376.4$ and $\nu_b=634.0$ cm ⁻¹ for the CO ₂ in gas phase.	61
Table 3.7 O-H bond distance, bond angle, partial Bader charges of H ₂ O and Pt and shift of vibrational mode frequencies of adsorbed H ₂ O molecule on γ -Al ₂ O ₃ supported mono- and di-atomic Pt clusters. Distances are in Å and partial Bader charges in e . Vibrational frequencies are given in cm ⁻¹ . Vibrational mode frequencies are shifted by the value of $\nu_s=3768.7$, $\nu_a=1566.8$ and $\nu_b=3892.4$ cm ⁻¹ for the H ₂ O in gas phase.	63
Table 4.1 Lattice constants, bulk modulus, pressure derivatives of the bulk modulus, and cohesive energies of the RS and ZB phase of PtC.	72
Table 4.2 Bader charges of Pt and C atoms on the top layer for the ZB PtC(110) surface and the top two layers for the ZB PtC(100) and ZB PtC(111) surfaces. The work function, Φ , is also reported.	81
Table 4.3 Adsorption energies (E_{ads}), oxygen partial charges (ρ_O) and descriptions of the initial and optimized geometries of the adsorption configurations presented in Figures 4.16, 4.17 and 4.18. The numerical codes in the initial configurations column correspond to the locations shown in the corresponding figures.	86

Table 4.4 Adsorption energies of Al, B, F, H, N and S atoms on the C-terminated ZB PtC(100) surface.	92
Table 4.5 Adsorption energies of Al, B, F, H, N and S atoms on the ZB PtC(110) surface.	93
Table 4.6 Adsorption energies of Al, B, F, H, N and S atoms on the C-terminated ZB PtC(111) surface.	93
Table 5.1 Adsorption energies, total and absolute magnetization and partial Bader charge (ρ_{Cl}) of Cl atom on graphane sheet.	103
Table 5.2 Adsorption energies, Cl-C bond distance and partial Bader charges of di-atomic Cl ₂ molecule on graphane sheet.	106
Table 5.3 Relative energy (E_R), Fermi level shift (ΔE_F), total and absolute magnetization and partial Bader charge of Cl atom for the defective graphene under electric field ($ \mathbf{E} =0.54$ V/nm)	113

LIST OF FIGURES

FIGURES

- Figure 1.1 Bulk structure of nonspinel, tetragonal and fully dehydrated γ - Al_2O_3 . White and red small balls stand for Al and O, respectively. 7
- Figure 1.2 Typical crystal structures of TMNs and TMCs. Adapted from "Microscopic theory of hardness and design of novel superhard crystals" by Tian *et al.* [55]. 8
- Figure 1.3 (a) Hexagonal lattice structure of graphene. The lattice vectors \mathbf{a}_1 and \mathbf{a}_2 , and the nearest neighbor vectors δ_1 , δ_2 and δ_3 . (b) The first Brillouin zone of the hexagonal lattice and the Dirac point \mathbf{K} and \mathbf{K}' . (c) Energy band structure for 1×1 unit-cell of graphene. A and B stands for the carbon atoms. 13
- Figure 1.4 Graphene nanoribbon structures with (a) armchair and (b) zig-zag edges. m and n are positive integers and define the width and length of GNRs, respectively. Red and black dashed-line rectangles represent the unit-cell of GNRs. 14
- Figure 2.1 A two dimensional potential energy surface. Example of PES with two equivalent minima with two saddle points. The points M_1/M_2 and SP_1/SP_2 represent the local minima and saddle points, respectively. 28

Figure 3.1 Mono- and di-atomic Pt clusters on γ -Al₂O₃. Mono-atomic Pt clusters are in (a)-(c) embedded geometry, (d)-(e) Pt-on-top and -bridge geometry. (f)-(l) Di-atomic Pt clusters are in Pt₂-on-top geometry. The relative adsorption energies and partial Bader charges of Pt and Pt₂ clusters are given for each configuration. White, red, and dark green balls stand for Al, O, and Pt atoms, respectively. 49

Figure 3.2 Adsorption of CO on bare γ -Al₂O₃(100) surface. (a) The top view of bare γ -Al₂O₃(100) surface with the most stable adsorption sites for the CO molecule. (b) The side view of the most stable adsorption geometries with the adsorption energies. The adsorption energies in parenthesis refer to the previous works [229]. (c) Projected density of states (PDOS) of CO molecule on the surface. White, red, and cyan balls stand for Al, O, and C atoms, respectively. 50

Figure 3.3 Adsorption of CO₂ on bare γ -Al₂O₃(100) surface. (a)-(b) The top and side views of the most stable adsorption geometries with the adsorption energies. The adsorption energies in parenthesis refer to the previous works [238]. (c) PDOS of CO₂ molecule on the surface. White, red, and cyan balls stand for Al, O, and C atoms, respectively. 52

Figure 3.4 Adsorption of H₂O on bare γ -Al₂O₃(100) surface. (a)-(b) The top and side views of the most stable adsorption geometries with the adsorption energies. The adsorption energies in parenthesis refer to the previous works [238]. (c) PDOS of H₂O molecule on the surface. White, red, and blue balls stand for Al, O, and H atoms, respectively. 54

Figure 3.5 (a)-(c) The side view of the most stable adsorption geometries with the adsorption energies and (b)-(d) PDOS of CO molecule on γ -Al₂O₃(100) surface supported mono-atomic Pt cluster. Bond distances are in Å. White, red, cyan and dark green balls stand for Al, O, C and Pt atoms, respectively. 56

Figure 3.6 (a)-(c) The side view of the most stable adsorption geometries with the adsorption energies and (b)-(d) PDOS of CO molecule on γ -Al ₂ O ₃ (100) surface supported di-atomic Pt ₂ cluster. Bond distances are in Å. White, red, cyan and dark green balls stand for Al, O, C and Pt atoms, respectively.	57
Figure 3.7 The side view of the most stable adsorption geometries with the adsorption energies and PDOS of CO ₂ on γ -Al ₂ O ₃ (100) supported mono-atomic Pt (a)-(b) and di-atomic Pt ₂ (c)-(d) clusters. Bond distances are in Å. White, red, cyan and dark green balls stand for Al, O, C and Pt atoms, respectively.	60
Figure 3.8 (a) The side view of the most stable adsorption geometries with the adsorption energies and (b) PDOS of H ₂ O molecule on γ -Al ₂ O ₃ (100) surface supported mono-atomic Pt cluster. Bond distances are in Å. White, red, blue and dark green balls stand for Al, O, H and Pt atoms, respectively.	62
Figure 3.9 (a)-(c) The side view of the most stable adsorption geometries with the adsorption energies and (b)-(d) PDOS of CO molecule on γ -Al ₂ O ₃ (100) surface supported di-atomic Pt ₂ cluster. Bond distances are in Å. White, red, blue and dark green balls stand for Al, O, H and Pt atoms, respectively.	62
Figure 4.1 The unit cell of (a) RS and (b) ZB phase of PtC structures. (c) Calculated bulk energies as a function of primitive unit cell volume (d) Enthalpy as a function of pressure at zero temperature for RS and ZB phase of PtC. Gray and black balls stand for Pt and C atoms, respectively. .	70
Figure 4.2 Band structures with PDOS profiles of bulk (a) RS and (b) ZB PtC.	71
Figure 4.3 The phonon dispersion relation and phonon density of states (PH-DOS) for bulk ZB PtC. Energies are shifted to the Fermi energy level. . . .	73

Figure 4.4	The side views and the relaxation patterns of (a) C-terminated and (b) Pt-terminated ZB PtC(100) surfaces. Small black and larger gray balls represent C and Pt atoms, respectively. For each surface, the per cent difference of interlayer separation from the bulk value (Δd) along the direction of interest is displayed as a function of increasing layer number in the slab model.	74
Figure 4.5	PDOS and surface charge density contour plots for (a) C- and (b) Pt-terminated ZB PtC(100) surfaces	75
Figure 4.6	Bader charge analysis of each interlayer for C- (a) and Pt-terminated (b) ZB PtC(100) surfaces.	75
Figure 4.7	(a) The side view and (b) the relaxation patterns of the ZB PtC(110) surface. Small black and larger gray balls represent C and Pt atoms, respectively.	76
Figure 4.8	(a) PDOS and (b) surface charge density contour plots for ZB PtC(110) surface	76
Figure 4.9	Bader charge analysis of each interlayer for ZB PtC(110) surface.	77
Figure 4.10	The side views and the relaxation patterns of the C- (a) and Pt-terminated (b) ZB PtC(111) surfaces. Small black and larger gray balls represent C and Pt atoms, respectively.	78
Figure 4.11	PDOS (left panel) and surface charge density contour (right panel) plots for (a) C- and (b) Pt-terminated ZB PtC(111) surfaces	79
Figure 4.12	Bader charge analysis of each interlayer for (a) C- and (b) Pt-terminated PtC(111) surfaces.	79
Figure 4.13	Surface free energies (γ) as a function of the chemical potential of C atom (μ_C) for ZB PtC(100), PtC(110) and PtC(111) surfaces.	80
Figure 4.14	Charge density profiles and PDOS plots of (a)-(c) the C vacancy on C-terminated ZB PtC(111) surface and (b)-(d) the Pt vacancy on the Pt-terminated ZB PtC(111) surface.	82

Figure 4.15 A schematic representation of the stable adsorption configurations which are identified as <i>on-top</i> , <i>bridge</i> and <i>hollow</i> on PtC(100), PtC(110) and PtC(111) surfaces.	83
Figure 4.16 Atomic O adsorption on the (a) C- and (b) Pt-terminated ZB PtC(100) surfaces. For each termination, initial adsorption configurations (red circles) are indicated in the leftmost scheme with numbers. Red, black and gray spheres represent O, C and Pt atoms, respectively.	84
Figure 4.17 Atomic O adsorption on the ZB PtC(110) surface. For each termination, initial adsorption configurations (red circles) are indicated in the leftmost scheme with numbers. Red, black and gray spheres represent O, C and Pt atoms, respectively.	85
Figure 4.18 Atomic O adsorption on (a) C- and (b) Pt-terminated ZB PtC(111) surfaces. For each termination, initial adsorption configurations (red circles) are indicated in the leftmost scheme with numbers. Red, black and gray spheres represent O, C and Pt atoms, respectively.	85
Figure 4.19 (a) The locations of the adsorption sites. The surface Gibbs free energy of adsorption per area of the C-terminated ZB PtC(100) surface at (b) T = 300 K and (c) T = 3000 K	87
Figure 4.20 (a) Top and side view, (b) Charge density profiles and (c) PDOS plots of the adsorbed single O atom on the Pt vacancy defect on Pt-terminated ZB PtC(111) surface.	88
Figure 4.21 (a) Top and side view, (b) Charge density profiles and (c) PDOS plots of the adsorbed single O atom on the C vacancy defect on C-terminated ZB PtC(111) surface.	89
Figure 4.22 Top and side views of adsorption configurations with adsorption energies (eV) of atomic Al, B and F on the C-terminated ZB PtC(100). Gold, pink, green, black and gray spheres represent Al, B, F, C and Pt atoms, respectively.	90

Figure 4.23 Top and side views of adsorption configurations with adsorption energies (eV) of atomic H, N and S on the C-terminated ZB PtC(100). Light blue, dark blue, yellow, black and gray spheres represent H, N, S, C and Pt atoms, respectively.	91
Figure 4.24 Top and side views of adsorption configurations with adsorption energies (eV) of atomic Al, B and F on the ZB PtC(110). Gold, pink, green, black and gray spheres represent Al, B, F, C and Pt atoms, respectively.	94
Figure 4.25 Top and side view of adsorption configurations with adsorption energies (eV) of atomic H, N and S on the ZB PtC(110). Light blue, dark blue, yellow, black and gray spheres represent H, N, S, C and Pt atoms, respectively.	95
Figure 4.26 Top and side views of adsorption configurations with adsorption energies (eV) of atomic Al, B, F, H, N and S on the C-terminated ZB PtC(111). Gold, pink, green, light blue, dark blue, yellow, black and gray spheres represent Al, B, F, H, N, S, C and Pt atoms, respectively.	96
Figure 5.1 Adsorption sites and majority (red) and minority (blue) spin band structures with PDOS of chlorine atom at the adsorption sites on graphene. (a) Top view of adsorption sites of Cl atom with adsorption energies. (b) Energy band structures and (c) PDOS for three different adsorption geometries. Gray and brown balls represent C and Cl atoms, respectively. H: <i>hollow</i> , B: <i>bridge</i> and T: <i>on top</i> sites.	102
Figure 5.2 PDOS of neighboring C atom at around adsorbed Cl atom on top-site. Maj. and Min. means the majority and minority states, respectively. Green dashed circles show the C-Cl hybridization.	103
Figure 5.3 Diffusion path for atomic Cl atom along the symmetry direction of graphene structure. Gray and brown balls stand for C and Cl atoms, respectively.	104

Figure 5.4 Adsorption geometries (upper panel) and charge density difference plots (lower panel) of di-atomic Cl ₂ molecule on graphene sheet with the calculated adsorption energies. Cl ₂ molecules are parallel to the graphene sheet. Gray and brown balls stand for C and Cl atoms, respectively.	105
Figure 5.5 Adsorption geometries (upper panel) and charge density difference plots (lower panel) of di-atomic Cl ₂ molecule on graphene sheet with the calculated adsorption energies. Cl ₂ molecules are on opposite sides of the graphene sheet. Gray and brown balls stand for C and Cl atoms, respectively.	105
Figure 5.6 Optimized geometries of (a)-(c) bare and (b)-(d) chlorinated defective graphene sheet. Bond distances are in unit Å. Red arrows show the C-Cl bond distances. Gray and brown balls stand for C and Cl atoms, respectively.	108
Figure 5.7 Energy band structures with PDOS plots of the Cl atom on defected graphene sheet with (a)-(b) SV and (c)-(d) DV. The Fermi energy is shifted to zero.	109
Figure 5.8 Isosurfaces of defect states $ \varphi_x(\vec{r}) ^2$ and $ \varphi_y(\vec{r}) ^2$ on bare and chlorinated defective graphene sheet; the nodal planes are shown as dashed lines in each cases. Gray and brown balls stand for C and Cl atoms, respectively.	110
Figure 5.9 (a) Adsorption energies of Cl atom and (b) Fermi level shifts relative to the graphene without applied electric field as a function of applied electric field.	111
Figure 5.10 (a) The C-Cl bond distance, (b) the total and absolute magnetization values and (c) partial Bader charge of Cl atom for chlorinated graphene under electric field.	111
Figure 5.11 Relative energies induced by the external electric field for the pristine and chlorinated graphene.	113

Figure 5.12 The adsorption energies of Cl atom on (a) ZGNR and (b) AGNR. The adsorption sites (red dashed circles) are given as inset figures. Gray and blue balls stand for the C and H atoms, respectively.	115
Figure 5.13 (a) Total and absolute magnetization as a function of length and (b) width of ZGNRs. (c) Transferred Bader charges to the single Cl atom on ZGNRs as a function of length.	116
Figure 5.14 Energy band structure of (a) bare and (b) chlorinated ZGNRs as a function of length. Sizes of ZGNRs are given at the top of the figure for each. Blue and yellow lines represent the majority and minority spin states, respectively.	116
Figure 5.15 Energy band structure of bare (a) and chlorinated (b) ZGNRs as a function of width. Sizes of ZGNRs are given at the top of the figure for each. Blue and yellow lines represent the majority and minority spin states, respectively.	117
Figure 5.16 (a) Calculated adsorption energy of single Cl atom as a function of length of AGNRs. (b) Transferred Bader charges to the adsorbed Cl atom as a function of length of AGNRs. (c) and (d) C-Cl bond distance of adsorbed Cl atom as a function of length and width of AGNRs.	118
Figure 5.17 Energy band structure as a function of length of bare (a) and chlorinated (b) AGNRs. Sizes of AGNRs are given at the top of the figure for each. Blue and yellow lines represent the majority and minority spin states, respectively.	119
Figure 5.18 Energy band structure as a function of width of (a) bare and (b) chlorinated AGNRs. Sizes of AGNRs are given at the top of the figure for each. Blue and yellow lines represent the majority and minority spin states, respectively.	120

LIST OF ABBREVIATIONS

0D	zero-dimensional
1D	one-dimensional
2D	two-dimensional
3D	three-dimensional
AGNRs	Armchair Graphene Nanoribbons
bcc	body-centered cubic
BJ	Becke and Johnson
CI	Climbing-Image
DFT	Density Functional Theory
DIIS	Direct Inversion of the Iterative Subspace
fcc	face-centered cubic
FETs	Field-Effect Transistors
GGA	General Gradient Approximation
GNRs	Graphene Nanoribbons
hcp	hexagonal close packed
HF	Hartree-Fock
HOMO	Highest Occupied Molecular Orbital
HTS	High Temperature Shift
KS	Khon-Sham
LDA	Local Density Approximation
LTS	Low Temperature Shift
LUMO	Lowest Unoccupied Molecular Orbital
MEP	Minimum Energy Path
ML	Monolayer
NEB	Nudged Elastic Band
PBE	Perdew-Burke-Ernzerhof
PEM	Proton Exchange Membrane
PES	Potential Energy Surface
QMC	Quantum Monte Carlo

RMM	Residual Minimization
SCF	Self Consistent Field
STM	Scanning Tunneling Microscope
TMCs	Transition Metal Carbides
TMNs	Transition Metal Nitrides
TS	Tkatchenko and Scheffler
vdW	van der Waals
WGS	Water-Gas Shift
ZB	Zinc-blende
ZGNRs	Zigzag Graphene Nanoribbons
ZPE	Zero Point Energy

CHAPTER 1

INTRODUCTION

Nanoscience is a phenomena related with a system in scale of nanometer dimensions. Many unique properties of nanosystems arise from the size of the systems. Nano is used as on a scale of nanometers in the world of physics, chemistry and material science. In the talk of Richard Feynman to American Physical Society with the name of “There’s a Plenty of Room at the Bottom”, he laid out the possibility of measuring and manipulating materials with developing of the technology. He also asked his audience:

“I don’t know how to do this on a small scale in a practical way, but I do know that computing machines are very large; they fill rooms. Why can’t we make them very small, make them of little wires, little elements, and by little, I mean little?”

His lecture can be seen as a seminal in the world of nanoscience, and the most of people in nanoscience are impressed with his talk. Nanoscience is based on atomic physics which is a combination of physics and chemistry of complex systems, and quantum mechanical properties dominates in the world of atoms in a nanosystems which contain atoms in the range of hundreds to thousands. The discovery of a new materials in nano-world bring some of the most excited and breakthrough scientific discoveries with many technological research. Theoretical and experimental studies give rise to understand and control the materials at the atomic scales. Moreover, the unprecedented developments and increase of available computing power in computational science leads to rapid progress in research area and allows to explore new research topics and helps to tackle scientific problems. In this work, we mainly focus on structural and electronic properties of considering systems which are mostly used structures in catalytic and technological applications. In order to understand of mate-

rials performance, a first-principles computations based on density functional theory was performed to get a microscopic insight of the systems. In the concept of the thesis, we have investigated three different systems. The first example is aluminum oxide (Al_2O_3) which is a well-known support material in catalysis, the second one is platinum carbide (PtC) which is first proposed for the catalytic applications as used a support material in this thesis, and the last one is graphene which is a two-dimensional material can be used and/or combined with other materials, and it has the potential to create future technologies.

This part of thesis will examine a relevant background information including previous experimental and theoretical studies on the heterogeneous catalyst systems, transitional metal carbides and also nitrides and as well as an introduction to the graphene and graphene nanoribbons.

1.1 Catalysis

The “catalysis” means the acceleration of a chemical reaction by a catalyst. A definition of “catalyst” is a substance that increases the rate of a reaction without any change the overall Gibbs free energy of the reaction [1]. This means that the catalyst chemically interacts with the reactants and lowers the energy barrier for the formation of the product. Catalysts can be classified as “homogeneous” and “heterogeneous” catalysis. In homogeneous catalysis, the reactants and the catalyst are in the same phase. The interaction of the reactants and the catalyst can be easier due to the same phase of the reactants and catalyst. This gives rise to the high selectivity and allowing the catalyst to make a specific reaction pathways. However, in the heterogeneous catalysis the reactants and catalyst are in different phases. The catalyst is generally the surface and its active sites exhibits many different structures, and this can reduce the selectivity. The advantage of the heterogeneous catalysis is separation of the reactants and the catalyst, and the catalysts can be used again in the system. Moreover, the surface of the catalyst is accessible to the reactants and becomes engaged in a chemical reaction. Hence, the surface area-volume ratio becomes important to increase the activity of catalysts.

1.1.1 Water Gas Shift Reaction

The water-gas shift reaction (WGS) is one of the most important chemical methods in the production of clean H₂ gas to be used as energy carrier in fuel cells. The WGS reaction is a fuel processing reactions which is studied in conjunction with fuel cells. Many studies [2, 3] focus on the reaction ranges from catalyst synthesis to mechanistic studies. Recent technologies such as nuclear, coal-burning, etc. interest in fuel cells as an alternative way to provide energy for efficient energy production. Comparing conventional industrial plants, the sizes of catalytic reactor is mandatory to compete with the traditional ways of electricity generation in automobile applications for hydrogen production due to the larger scale of industrial catalysts. The need to design new catalytic systems has recently boosted large-scale research on the WGS reaction and new catalytic systems. These needs require to overcome many problems such as lack of detailed knowledge of the reaction mechanisms.

The WGS reaction was studied first by Felice Fontana [4] in 1780, and it was applied to industry for ammonia production [5]. Basically, a fuel cell produces electricity from the chemical energy of fuels. As an example to produce electricity in an environmentally friendly way is the proton exchange membrane (PEM) fuel cell. In the case of PEM fuel cell, hydrogen dissociation happen on a platinum catalyst at the anode into protons and electrons. The hydrogen as the fuel is not totally pure, and the performance of the fuel cell depends heavily on the quality of the reformat stream that feeds the fuel cell. In a typical plant, hydrocarbons or alcohols are used to feed a reformer which converts the fuel into CO₂, CO, H₂O and H₂ in a catalytic process which is called as steam reforming. Then, oxygen is also injected to provide the heat needed for the endothermic steam reforming [6]. In the next step, the reformer's reformat stream undergoes WGS in two stages as high temperature shift (HTS) and low temperature shift (LTS), and the WGS reaction is given as



The WGS reaction is a reversible and exothermic reaction ($\Delta H = -41.2 \text{ kJ/mol}$), and it is thermodynamically unfavorable at elevated temperatures due to the being an exothermic reaction. These HTS and LTS stages work to convert the energy trapped

in the unwanted carbon monoxide in addition to the usable hydrogen for the fuel cell. The preferential oxidation is the last step and it provides CO oxidation to CO₂ before it is sent to the fuel cell. This step generally operated at lower temperatures, and it occurs over a highly selective precious-metal catalyst on which oxygen reacts with the unwanted CO without wasting substantial hydrogen. If the fuel is a kind of hydrocarbon fuel, it contains sulfur and is required a desulphurization step to reduce the sulfur level in the fuel processing [6]. Moreover, there is no substantial effect on the fuel cell performance in the presence of the CO₂ in the reformat, and it passes through the anode to the exhaust.

Depending on the type of catalysts, two different stages, HTS and LTS, can be used. For example, while iron-based catalyst is used for HTS operations, copper-based catalyst is used industrially for the LTS operations [7]. In these catalysts different supports such as zinc-oxide (ZnO) / Alumina (Al₂O₃) / ceria (CeO₂) can be used depending on the their specific applications.

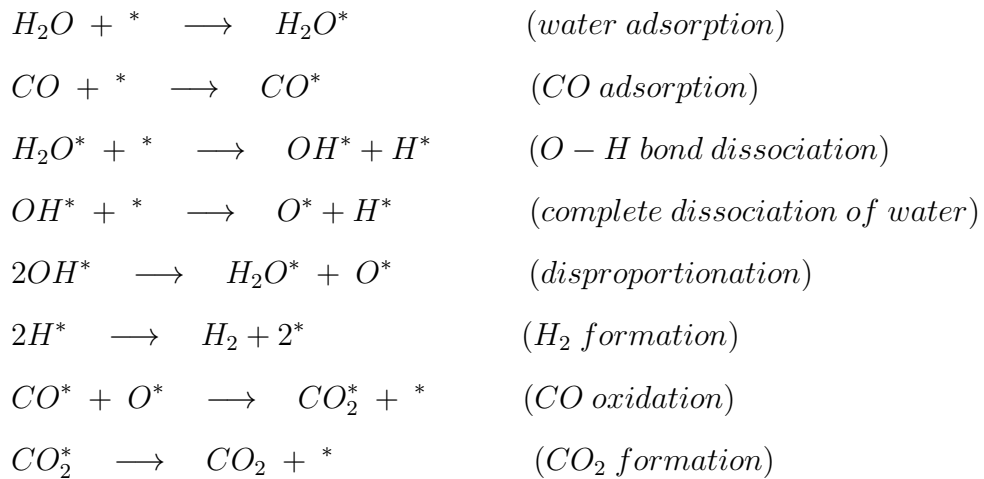
For HTS operation the catalyst is typically prepared as a combination of iron (Fe₃O₄) and chromia (Cr₂O₃) [8]. The active magnetite form of Fe₃O₄ is obtained upon reduction of Fe₂O₃. After exposure to air, the catalyst must be re-reduced and stabilized by surface oxidation at low surface oxygen concentration before it is used again.

The commercial LTS catalyst is composed of the copper, ZnO and Al₂O₃, and the copper- and zinc oxide-based catalysts are stable under reaction conditions. The ZnO provides some protection of the copper from sulfur poisoning by reaction with adsorbed sulfur compounds. The LTS catalyst can be more sensitive to deactivation caused by sintering than the HTS catalyst due to the low melting point of copper under reaction conditions. Therefore, the operating temperature can only be around 250°C.

Recently, the noble metal based WGS catalyts are under development for efficient fuel-cell applications. Several systems based on noble metals such as Pt and Au are using in the most promising systems in literature. The studies generally focused on the synthesis methods, support modification, structural effects and oxidation of noble metal [9–15]. For Pt-based WGS catalysis, several supports which are classified as *reducible* and *non-reducible* oxides are used to get efficient WGS reactions.

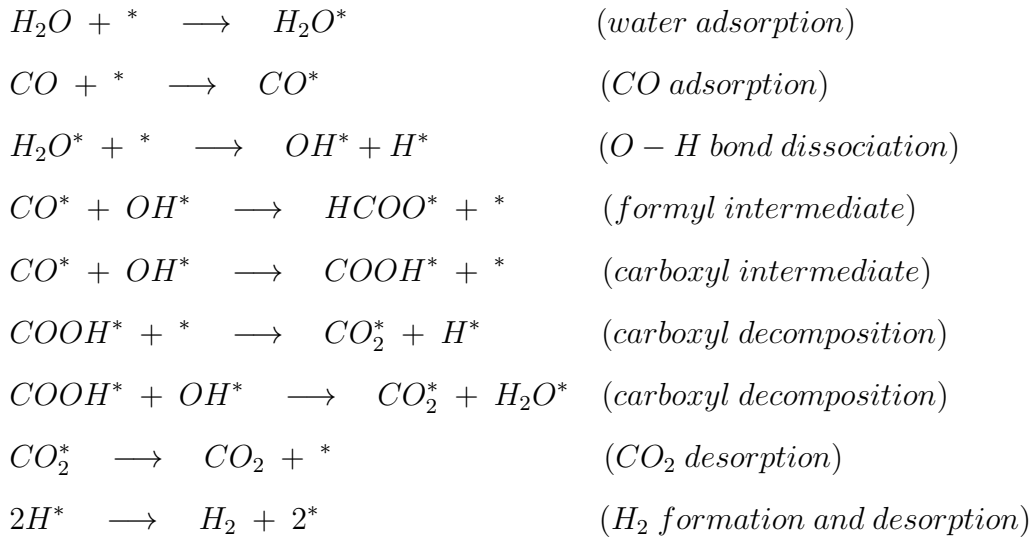
In the previous study by Olympiou *et al.* [16] it was predicted that the activity of Pt is better than Rh and Pd on Al₂O₃. It was shown that the water dissociation occurs on the support, and the activated species migrates from the support to the noble metal in the work of Grenoble *et al.* [17]. The reducible supports such as titania (TiO₂) [18–24], CeO₂ [14, 25–31] and Al₂O₃ are the most studied, and they exhibit an important enhancement of the catalytic activity. The importance of the strong metal-support interaction to describe the contributions of the site information on the support material was reported in the study by Tauster *et al.* [32]. It was found that the hydrogenation activity of the noble metal is described by the structural effects such as partial coverage or decoration of the active metal sites.

In general, the catalytic activity of the supported metal particles is effected by particle size, shape, metal oxidation state and metal-oxide interaction. Recent studies give more attention to the importance of the noble metal-support interactions and the role for the catalytic activity. In literature, two main reaction pathways have been generally proposed as *redox* and *associative* mechanisms. The proposed redox mechanism [33–36] is given as



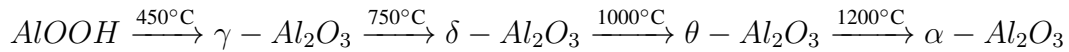
where CO adsorbs on surface and diffuse to the metal-support interface and reacts with surface oxygen to form CO₂. H₂O adsorbs and dissociates on the support, and H₂ is produced. Here, the star sign (*) represents the surface site.

The associative mechanism [25, 26, 37] involves adsorbed species of formyl or carboxyl, and the reaction pathways is given as



1.1.2 Structure of Alumina (Al₂O₃)

Al₂O₃ has thermodynamically stable α -Al₂O₃ and many meta-stable forms which are called as γ -, δ -, κ -, η - and θ - Al₂O₃. The transformation sequence that leads bohemite (AlOOH) to be converted into of meta-stable phases;



The γ -Al₂O₃ is a catalyst in heterogeneous catalysis due to the mechanical strength and thermal stability under oxidizing conditions, and its higher surface area-volume ratio [38, 39]. The surface OH groups act as weak Brønsted acids, the unsaturated Al⁺³ atoms act as Lewis acid sites and O⁻² atoms act as Lewis base sites [40].

The γ -Al₂O₃ has two kinds of structure as *spinel* with vacancies introduced in order to match the stoichiometry [41], and *non-spinel* derived from bohemite [42, 43]. The spinel structure named after mineral spinel MgAl₂O₄. The cations occupy 1/8 of tetrahedral sites and 1/2 of the octahedral sites [44]. In the spinel-like structure, the magnesium atoms in MgAl₂O₄ are replaced by Al atoms, and some of the lattice positions remain empty (vacancies) to satisfy the γ -Al₂O₃ stoichiometry.

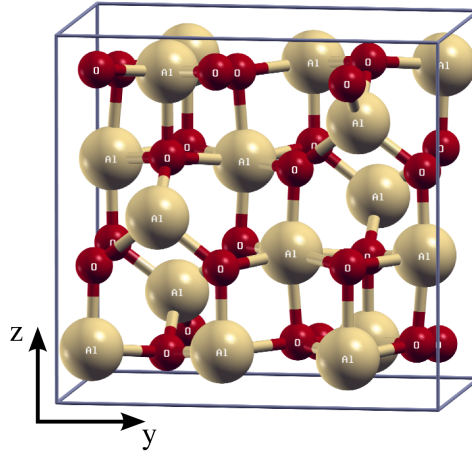


Figure 1.1: Bulk structure of nonspinel, tetragonal and fully dehydrated γ - Al_2O_3 . White and red small balls stand for Al and O, respectively.

The non-spinel structure of γ - Al_2O_3 proposed by Krokidis and Digne [42, 43] contains 16 Al and 24 O atoms, and the Al^{+3} cations occupy 3/4 of penta-coordinated lattice sites and the remaining 1/4 are tetra-coordinated. The unit-cell of bulk γ - Al_2O_3 structure is presented in Figure 1.1.

1.2 Transition Metal Carbides and Nitrides

In recent decades, transition metal carbides (TMCs) and nitrides (TMNs) of the fourth and sixth group of the periodic table have been attracting much attention due to their remarkable physical and chemical properties. Most of carbides and nitrides have high melting points and exhibit resistance against corrosion. However, their main commercial importance stems from their extreme hardness properties, and they are used as cutting tools in many industrial applications. The nitrides of this group have also hardness properties, but they are used in mainly integrated circuitry due to their electrical properties. Beside these, TMCs and TMNs have potential to be used in various applications in material science and heterogeneous catalysis [3, 45, 46]. For example, while TiN and CrN are used as hard coatings, VN is used as an electrode for supercapacitor [47]. NbC shows high conductivity which makes it suitable for many applications in mechanical, chemical, and microelectronic industries [48]. TiC is used as cutting tools and wear-resistant materials [49, 50]. WC and Mo_2C have

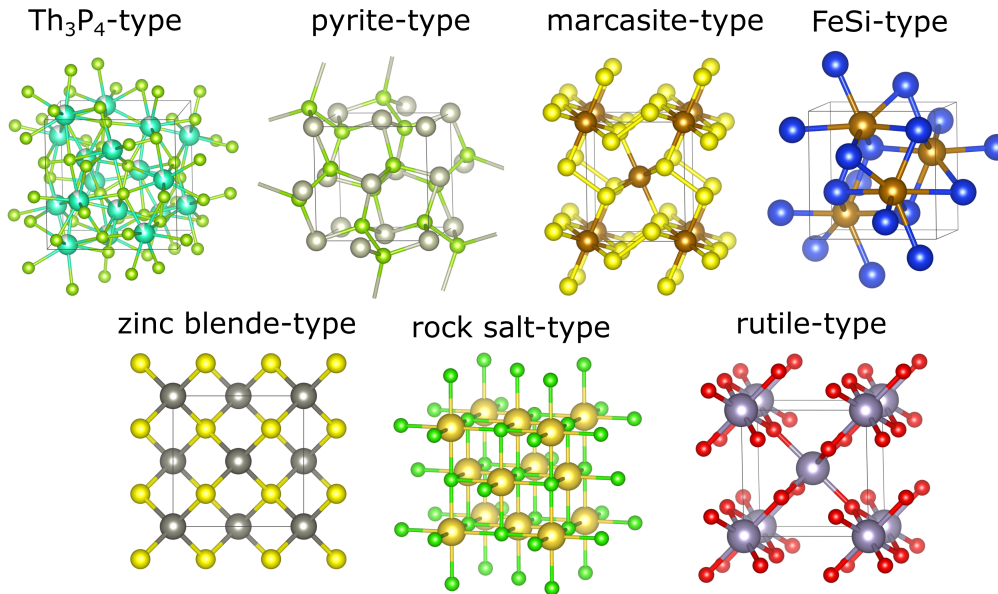


Figure 1.2: Typical crystal structures of TMNs and TMCs. Adapted from "Microscopic theory of hardness and design of novel superhard crystals" by Tian *et al.* [55].

excellent catalytic properties with and without noble metals as a catalyst [51–54].

Transition metal carbides and nitrides have similar structure types (see Figure 1.2), bond characters and electrical and magnetic properties. These similarities are closely related to electronic structure, size and electronegativity of C and N atoms, and they can not extend to the other light elements such as boron or oxygen [56]. The geometric and electronic factors are useful to formulate the carbide and nitride structures. For the geometric factor the ratio between the radius of non-metal atom and the metal atom is smaller than 0.59 [57, 58]. In the case of electronic factor, the resultant structure depends on the number of *sp* electrons. For example, while the Mo_2C is in hexagonal close packed (hcp) structure, the Mo_2N is in face-centered cubic (fcc) structure. The Mo is also in bcc structure, and the resultant structures, Mo_2C and Mo_2N , change from body-centered cubic (bcc) to hcp and bcc to fcc with increasing amounts of *sp* electrons. Therefore, the high proportion of *sp* electrons with the un-filled *d-band* produce a fcc structure of Mo_2N . Increasing the proportion of filled *d-band* can identify the hcp structure [59, 60]. The theory for the electronic factor of TMCs and TMNs is known as Engel-Brewer theory [61].

The extreme properties of TMCs and TMNs such as high thermal and electrical con-

ductivity [57, 62] arise from the combination of metallic, covalent and ionic bonding character of the materials [57]. The complex combination of metal-metal and metal-non-metal interaction leads to the covalent and metallic bonding, and a small amount of ionic bonding especially in nitrides. Covalent bonding arises from directional bonds formed by the overlap of the C 2p electrons and the metal d electrons [63]. The combination of metallic, covalent and ionic bonds also determines their reactivity and stability, and it makes suitable for the catalytic applications [64, 65]. Especially, the p-d hybridization causes an expansion of metal lattice with the effect of a contraction of the metal d-band. This gives rise to a higher density of states (DOS) near the Fermi level approaching the d-band of Pt [59, 66, 67]. The catalytic behaviour of transition metal carbides and nitrides [68–74] is comparable to the noble metal catalysts in some reactions such as hydrogenation, dehydrogenation [75], ammonia synthesis [76] and electrochemical reactions [66, 67, 77]. Another important property of the TMCs and TMNs is their defective structures. The presence of ordered or disordered vacancies significantly affects of physical and chemical properties. Different processes cause to the different defect structures with different properties. As an example, during a catalytic process, active participation of surface vacancies in heterogeneous catalysis is a commonly observed phenomenon [78–80]. Therefore, the defective TMCs and TMNs are important in assessing the potential of a surface as a catalyst.

Many of compounds of TMCs and TMNs are chemically stable at room temperature and interact slowly with very concentrated acid solutions. For example the VC slowly interacts with acid solution, and they can be oxidised in form of oxides at high temperatures. Additionally, the TMCs are extremely strong materials at high temperatures, and their Young's modulus are higher than many transition metals. However, at room temperatures many of them can be brittle [56].

1.3 Graphene and Graphene Nanoribbons

Carbon has four valence electrons which have similar energies, and the wavefunctions of valence electrons can easily mix facilitating hybridization. The two inner shell electrons of 2s, 2p_x, 2p_y, and 2p_z orbitals are spherically symmetric, while 1s orbital is tightly bound, and its energy is far from the Fermi energy of carbon. There-

fore, the 2s and 2p orbitals can contribute to the solid state properties of graphite. This unique property of the carbon atom allows carbon to form in 0D, 1D, 2D and 3D systems [81]. The three dimensional form of carbon, diamond, is sp^3 bonded forming four covalent bonds with the neighboring carbon atoms into a fcc atomic structure. Due to nature of the covalent bonding, diamond has high Young's modulus and thermal conductivity. This form of carbon is an insulator with a huge band gap around 5.5 eV [82–84]. A low dimensional form of carbon is known as fullerenes which consist of the C_{60} molecule, and one dimensional form of it is called carbon nanotubes. A single walled carbon nanotube is known as a single layer of graphite, referred to as graphene, rolled into a cylindrical tube with a ~ 1 nm diameter. Carbon nanotubes can be found in metallic or semiconducting character, and their mechanical properties are similar to diamond. Their remarkable properties were studied in the research community during the early 2000. This interest in nanotubes brought a big attention to the graphene as a potentially important material with interesting mechanical and electrical properties.

The two dimensional sp^2 hybridized forms of the carbon are known as graphene and graphite. Graphite is a layered material formed of stacks of graphene sheets held together by weak van der Waals (vdW) forces between the graphene sheets [85]. Graphene is a zero band gap semiconductor with two linearly dispersing bands that touch at the corners of the first Brillouin zone [86]. The spectrum at the K points is similar with the Dirac cones of massless relativistic particles. This gives an opportunity to test the relativistic quantum effects in solid state materials. This picture can change with spin-orbit coupling which gives an amount of mass to the particles, introducing a gap in the spectrum.

Graphene is one of the potential materials for electronic applications due to its electronic properties. One of the goals of the electronic industry is to reduce the dimension of the electronic devices to improve their performance. The unique properties of graphene give rise to an alternative material in microelectronic industry such as graphene transistors. Moreover, it can be used for many other applications including single molecule gas detectors [87], supercapacitors [88], transparent conducting electrodes [89] and field-effect transistors (FETs) [90, 91]. The exceptional mobility of graphene allows to observe the quantum hall effect at low temperature and high

magnetic field [92–94]. Unfortunately, graphene has no band gap and correspondingly resistivity changes are small. This limitation gives rise to low on/off ratio in a graphene transistor, but it can be overcome by cutting the graphene sheets as narrow ribbons. This operation changes the momentum of the charge carriers becoming quantized, and opens a band gap which is proportional to the width of graphene ribbon [95, 96].

1.3.1 Fabrication Methods

Graphene was first investigated using a tight binding (TB) method by P. R. Wallace [86] in 1947, and he showed a linear dispersion relation between \mathbf{K} and \mathbf{K}' points and semi-metallic behaviour of graphene material. Then, it was long believed that graphene could not exist in nature due to the thermodynamic instability of two-dimensional crystals [97–99]. Surprisingly, the study by Novoselov and collaborators [92, 100] showed the possibility of producing a single atomic layer of graphite (graphene) by mechanical exfoliation (repeated peeling or micromechanical cleavage) starting from bulk graphite. The growth of graphene multilayers on top of silicon carbide (SiC) by thermal decomposition was reported by Berger *et al.* [101]. Since its discovery allows the study of graphene as a system in many applications [90, 91, 93, 94, 102–111].

P. Kim's group proposed a technique which makes possible to graphene can be patterned into strips with different widths by using e-beam lithography and an etching mask [112]. This technique allows to perform transport experiments on sample with a variety of widths (20-500 nm) and lengths ($\sim 1 \mu\text{m}$). Another method was proposed by Jia *et al.* to use Joule heating and electron beam irradiation [113]. This method is useful to create structures with smooth edges. Also, Cai *et al.* [114] proposed a method of creating ribbons with width less than 1 nm.

The electronic properties of graphene nanoribbons are related with the chirality of the graphene nanoribbon, and the variety of different chiralities and widths gives rise to different electronic properties. Mainly, the graphene nanoribbon is chemically synthesized by unzipping a carbon nanotube [115, 116]. The presence of 1D GNR edge states was confirmed by using scanning tunneling microscope (STM), and can

be predicted general rules for the existence of edge states [117].

The first theoretical works on graphene nanoribbons and electronic structures had appeared several years before graphene was discovered. A tight binding study by Tanaka *et al.* [118] showed a decrease in the band gap for molecules with a wider graphene structure added to the polymer backbone. A decrease in the HOMO-LUMO (Highest Occupied Molecular Orbital and Lowest Unoccupied Molecular Orbital) gap was found with increasing molecule size on hexagonally symmetric aromatic molecules, which are good examples for the small pieces of graphene, in the work of Stein *et al.* [119]. Many studies in the middle of 90s focused on the edge chirality and size of GNRs [95, 96, 120].

1.3.2 Structural Properties of Graphene and Graphene Nanoribbons

Graphene is a single layer of graphite, and its electronic properties are not much more different from graphite because of weak interaction between the atomic layers in graphite [85]. The distance between the layers is around 3.35 Å and it is more than twice the C-C distance in single layer. Carbon atoms make sp^2 hybridization in graphene. C s-orbital combines with two p-orbitals which leads a trigonal planar structure. A single sheet of graphene is a hexagonal structure with σ bonds forming from 3 valence electrons with each of its nearest neighbours. These covalent bonds give diamond like electrical and mechanical properties to graphene. The fourth valence electron is not part of the covalent bonding. This $2p_z$ state is oriented perpendicular to the sheet forming a conducting π band.

Carbon has four valence electrons, and three of them make tightly bound to the neighbouring atoms in the plane. The unit-cell of the hexagonal layer contains two carbon atom as labeled A and B in Figure 1.3 (a). The distance between the two A and B carbon atoms is $a = 1.42 \text{ \AA}$ and the fundamental lattice constant $\mathbf{a}_1 = \mathbf{a}_2 = \sqrt{3} \times 1.42 \text{ \AA} = 2.46 \text{ \AA}$. The first Brillouin zone is a hexagon of which the sides are at a distance $4\pi/3a$ from its center, see Figure 1.3 (b). The density of electron states in k space is $2S$ where S is the area of the crystal, and the zone has one electron per atom. Therefore, the first Brillouin zone has $2N$ electron states and second Brillouin zone is empty of graphene.

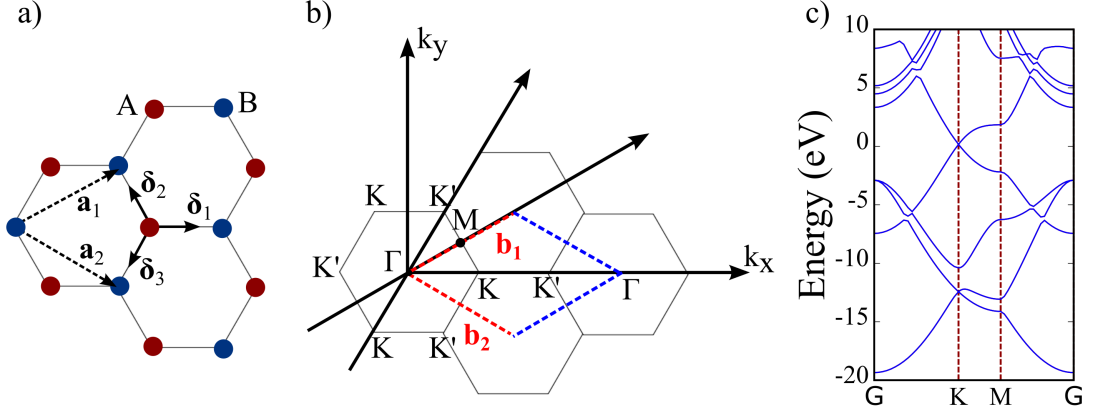


Figure 1.3: (a) Hexagonal lattice structure of graphene. The lattice vectors \mathbf{a}_1 and \mathbf{a}_2 , and the nearest neighbor vectors δ_1 , δ_2 and δ_3 . (b) The first Brillouin zone of the hexagonal lattice and the Dirac point \mathbf{K} and \mathbf{K}' . (c) Energy band structure for 1×1 unit-cell of graphene. A and B stands for the carbon atoms.

The lattice vectors \mathbf{a}_1 and \mathbf{a}_2 can be written as

$$\mathbf{a}_1 = \frac{3a}{2}(\hat{i} + \frac{1}{\sqrt{3}}\hat{j}), \quad \mathbf{a}_2 = \frac{3a}{2}(\hat{i} - \frac{1}{\sqrt{3}}\hat{j}) \quad (1.2)$$

where a is the C-C distance (1.42 Å). The reciprocal lattice vectors \mathbf{b}_1 and \mathbf{b}_2 is given as

$$\mathbf{b}_1 = \frac{2\pi}{3a}(\hat{i} + \sqrt{3}\hat{j}), \quad \mathbf{b}_2 = \frac{2\pi}{3a}(\hat{i} - \sqrt{3}\hat{j}) \quad (1.3)$$

The position of Dirac points $\mathbf{K} = \frac{2\pi}{3a}(\hat{i} + \frac{1}{\sqrt{3}}\hat{j})$ and $\mathbf{K}' = \frac{2\pi}{3a}(\hat{i} - \frac{1}{\sqrt{3}}\hat{j})$ are located at the corners of the Brillouin zone. The three nearest neighbour vectors are given as $\delta_1 = a/2(\hat{i} + \sqrt{3}\hat{j})$, $\delta_2 = a/2(\hat{i} - \sqrt{3}\hat{j})$ and $\delta_3 = -a\hat{i}$, see Figure 1.3(a) [121].

Graphene nanoribbons are graphene sheets with finite size and can be described the ribbons of 1D which is infinitely long in one of the dimensions while the width is finite along the other direction. A 2D graphene sheet should be cut to obtain a 1D ribbon such that length is infinitely long side and width is finite which is cut in nano-scale. In the honeycomb structure of graphene sheet, there are two high symmetry directions which are called as “armchair” and “zigzag”, see Figure 1.4.

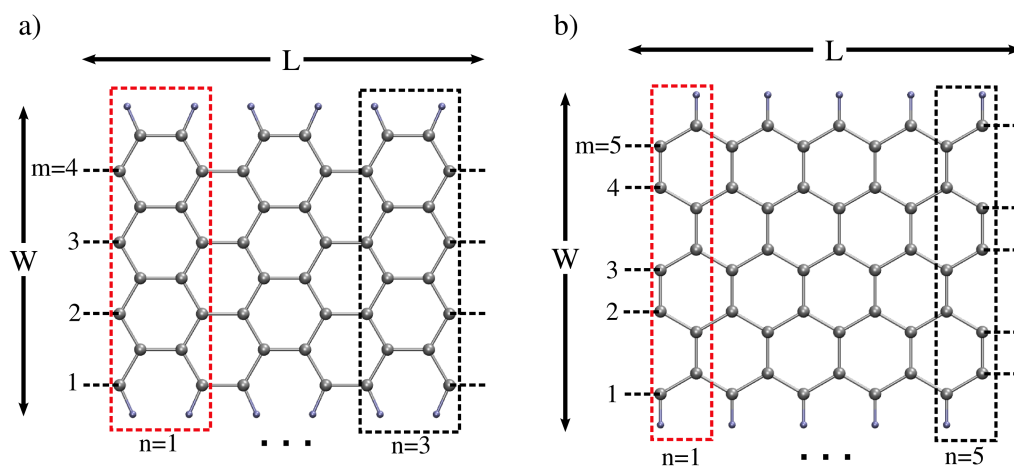


Figure 1.4: Graphene nanoribbon structures with (a) armchair and (b) zig-zag edges. m and n are positive integers and define the width and length of GNRs, respectively. Red and black dashed-line rectangles represent the unit-cell of GNRs.

For the zigzag chirality of GNRs the length and width sides have zigzag and armchair shape, respectively. On the contrary, the length and width sides have armchair and zigzag shapes, respectively for AGNRs. In general, the AGNRs and ZGNRs are labeled as " mW - n AGNR/ZGNR". AGNRs are classified by considering the number of dimer lines across the ribbon width, while ZGNRs are classified by the number of zigzag chains across the ribbon width, namely m . According to this notation, the AGNR in Figure 1.4 (a) is denoted as $4W$ - 3 AGNR, and the ZGNR in Figure 1.4 (b) is called as $5W$ - 5 ZGNR. In this part of study, the hydrogenated zigzag and armchair edges GNRs where the hydrogen atoms are added to the first and n^{th} row carbon atoms are used as seen in Figure 1.4.

1.4 Overview of the Thesis

Chapter 2 introduces the basics of DFT including atomistic thermodynamic DFT method and vibrational frequencies in DFT as well as an introduction to the basics of adsorption and desorption of a species. In *Chapter 3*, we present the adsorption properties of some species, CO, CO₂ and CO₂, which are relevant in water gas shift reactions, on bare γ -Al₂O₃ and supported Pt clusters. *Chapter 4* contains a more de-

tailed approach to the structural and electronic properties of zinc-blend phase of PtC. While the bulk structure of PtC have been studied in literature, the surfaces of PtC are first investigated including defective structure of PtC, as well as oxidation properties of PtC(100), PtC(110) and PtC(111) surfaces in this part of thesis. Moreover, the adsorption properties of IA and some of IIIA-VIIA group of elements are also studied. In the following *Chapter 5*, the adsorption characteristic of chlorinated graphene sheet in different geometries are given, including the defective bare and chlorinated graphene sheets. This chapter contains a more detailed information of the electronic properties of chlorinated graphene and graphene nanoribbons. Moreover, the adsorption properties are investigated under applied electric field including the nature of the band structure of the structures. A brief of summary of the results in the context of the thesis with a brief discussion of each part of study are given in *Chapter 6*.

CHAPTER 2

THEORETICAL BACKGROUND

2.1 Electronic Structural Methods

Schrödinger equation is the basic equation of quantum mechanics, that yields a wavefunction Ψ , from which all physical properties of a complex system can be determined. The complexity of the solution which defines any system increases with the increasing number of particles in the system. The time-dependent Schrödinger equation for a particle moving in some potential \hat{V} described by the wavefunction Ψ . This kind of equation is a second order differential equation and expressed as

$$\left(-\frac{\hbar^2}{2m}\nabla^2 + \hat{V} \right) \Psi(\vec{r}, t) = i\hbar \frac{\partial \Psi(\vec{r}, t)}{\partial t} \quad (2.1)$$

where \vec{r} is position vector of the particle, t is time, ∇^2 is Laplace operator, \hat{V} is potential energy operator, and \hbar is Planck constant divided by 2π .

In the above equation, the Hamiltonian can be defined as a sum of kinetic and potential energy operators:

$$\hat{H} = \left[-\frac{\hbar^2}{2m}\nabla^2 + \hat{V} \right] \quad (2.2)$$

After decoupling of the time evolution of nuclei and electrons by assuming that the electrons react instantaneously to any change in the position of nuclei, the electronic part of the problem may be expressed in terms of time-independent Schrodinger equation. Consider a system of N-particles interacting with each other via Coulomb potential and subjected to an external potential \hat{v}_{ext} .

The Schrodinger equation can be written as

$$\hat{H}(\vec{r}_i, \vec{R}_I)\Psi(\vec{r}_1, \vec{r}_2, \dots, \vec{r}_N) = E\Psi(\vec{r}_1, \vec{r}_2, \dots, \vec{r}_N) \quad (2.3)$$

where $\Psi(\vec{r}_1, \vec{r}_2, \dots, \vec{r}_N)$ is the many-body wavefunction, \vec{r}_i are electron coordinates, $i=1, \dots, n$, and \vec{R}_I are ion positions, $I=1, \dots, N$. The many-body Hamiltonian $\hat{H}(\vec{r}_i, \vec{R}_I)$ includes terms corresponding to kinetic energy of electrons, electron-electron interaction, electron-nuclei interaction, and the nuclear repulsion¹;

$$\hat{H}(\vec{r}_i, \vec{R}_I) = -\frac{1}{2} \sum_i \nabla_i^2 + \frac{1}{2} \sum_{i < j} \frac{1}{|\vec{r}_i - \vec{r}_j|} - \sum_{i, I} \frac{Z_I}{|\vec{r}_i - \vec{R}_I|} + \frac{1}{2} \sum_{I < J} \frac{Z_I Z_J}{|\vec{R}_J - \vec{R}_I|} \quad (2.4)$$

where Z_I is the corresponding charge, $\frac{1}{2} \nabla_i^2$ is the second derivative of the wavefunction with respect to the electron i positions, proportional to the operator of kinetic energy of electron i . The last two terms, $\sum_{i, I} \frac{Z_I}{|\vec{r}_i - \vec{R}_I|}$ and $\sum_{I < J} \frac{Z_I Z_J}{|\vec{R}_J - \vec{R}_I|}$ correspond to external potential, \hat{v}_{ext} .

The main difficulty of solving the Equation 2.4 arises from the interaction between the electrons makes impossible to find any exact solution for the system. Therefore, many theories starting from Hartree [122], Hartree-Fock (HF) [123], Thomas-Fermi-Dirac [124–127] to modern density functional theory (DFT) have been developed to get approximate solutions of the Schrodinger equation. Some approaches exist to get over the difficulties on the solution of the many-body Schrödinger equation. The first group of those methods, which is so-called mean-field methods, assumes that the many-body wavefunction can be factorized into one-body contributions from orbitals. This assumption implies that $e^- - e^-$ interaction term is replaced by an effective potential described the electrostatic potential in a mean-field. Each electron interacts with an average electrostatic potential which is created by all other electrons inside the mean-field. The main drawback of these mean-field theories is unfavorable scaling with the number of electrons in the system.

Another method is based on the wavefunction which is only necessary for computation of observable quantities, and by itself is only an auxiliary tool. Therefore, one

¹ The order of the magnitude of the nuclei-nuclei interaction is negligible in ab-initio calculation

can attempt to infer the properties of the system, such as density of electrons. This group of methods is known as DFT. The details of DFT method will be given in the following section.

2.1.1 Density Functional Theory (DFT)

The idea of DFT is to describe an interacting system of fermions in terms of electron density of the system. First of all, this approach is based on the work of Thomas and Fermi [124, 128], but the relation was not proven until the work of Hohenberg and Kohn [129]. It was shown that there is a unique correspondence between the electron density of the system and the external potential which includes coulomb potential of the nuclei and electric field. The true ground state of electron density minimizes the total energy of the system, but the exact expression of the total energy was not proven as a function of electron density.

One of the components of the total energy, the kinetic energy term was especially challenging to express in terms of the density that leads to the failure to predict chemical bonding in the system. To overcome this problem, Kohn and Sham [130] proposed a reference system of non-interacting negatively charged fermions. The behavior of such reference was governed by single-particle equations due to absence of direct many-body interactions in the system, and it can be written in terms of single particle orbitals $\phi_i(\vec{r})$:

$$-\frac{1}{2}\nabla^2\phi_i(\vec{r}) + \left[\hat{v}_{ext}(\vec{r}) + \int d\vec{r}' \frac{n(\vec{r}')}{|\vec{r} - \vec{r}'|} + \hat{v}_{xc} \right] \phi_i(\vec{r}) = \varepsilon_i \phi_i(\vec{r}) \quad (2.5)$$

where the exchange-correlation potential, $\frac{\delta E_{xc}}{\delta n(\vec{r})} = \hat{v}_{xc}$, is given by

$$\hat{v}_{xc} = \left[E_{xc}[n] + n(\vec{r}) \frac{\delta E_{xc}[n]}{\delta n(\vec{r})} \right] \phi_i(\vec{r}) \quad (2.6)$$

In the above expression, $E_{xc}[n(\vec{r})]$ is the exchange correlation energy density, and it will be discussed below. The sum of the Kohn-Sham eigenvalues, ε_i , can be obtained

from Equation 2.5, and the total energy, $E[n(\vec{r})]$, can be calculated directly in terms of the electron density $n(\vec{r})$:

$$E[n(\vec{r})] = T[n(\vec{r})] + \int n(\vec{r})\hat{v}_{ext}(\vec{r})d\vec{r} + \frac{1}{2} \int \int d\vec{r} d\vec{r}' \frac{n(\vec{r})n(\vec{r}')}{|\vec{r} - \vec{r}'|} + E_{xc}[n(\vec{r})] \quad (2.7)$$

where $T[n(\vec{r})]$ is the kinetic energy of non-interacting fermions, $\hat{v}_{ext}(\vec{r})$ is the external potential and $E_{xc}[n(\vec{r})]$ is the exchange-correlation energy. The $T[n(\vec{r})]$ term is determined by the single body wavefunction, $\phi_i(\vec{r})$, and it can be expressed as

$$T[n(\vec{r})] = \frac{1}{2} \sum_i \int \phi_i(\vec{r}) \nabla^2 \phi_i(\vec{r}) d\vec{r} \quad (2.8)$$

The exchange-correlation energy, $E_{xc}[n(\vec{r})]$, contains three components: The first one is the difference between the kinetic energies of the reference system of non-interacting fermions (Equation 2.8) and the actual kinetic energy of electrons. Second is the correction for dynamic correlation of motion of electrons and associated lowering of the energy since electrons tend to avoid each other due to Coulomb repulsion. The last component is the so-called “exchange” energy. The exchange energy is supposed to eliminate or mitigate two effects: First, electrons are fermions and it implies that the probability of finding two electrons with the same spin state at same point in space is exactly zero. Hence, the associated many-body wavefunction becomes antisymmetric. Second is so-called “self-interaction” energy which is the contribution from any given particle is counted twice in the expression of the Coulomb interaction of two fermions.

As suggested by Kohn-Sham, for a system that conserves the number of particles, the kinetic energy term can be split up into two terms which are exchange-correlation part and non-interacting part. Thus one can arrive at a set of effective single particle equations known as Kohn-sham equations. For the single body wavefunction $\phi_i(\vec{r})$ can be written as

$$\begin{aligned}
\hat{H}_{KS} &= \left(-\frac{1}{2}\nabla^2 + \hat{v}_{ext}(\vec{r}) + \int d\vec{r}' \frac{n(\vec{r}')}{|\vec{r} - \vec{r}'|} + \hat{v}_{xc}(\vec{r}) \right) \phi_i(\vec{r}) \\
&= \varepsilon_i \phi_i(\vec{r})
\end{aligned} \tag{2.9}$$

The difference between this equation and the single particle Schrödinger equation is external potential and effective potential displacement. The effective potential is given by

$$\hat{v}_{eff}(\vec{r}) = \hat{v}_{ext}(\vec{r}) + \int d\vec{r}' \frac{n(\vec{r}')}{|\vec{r} - \vec{r}'|} + \hat{v}_{xc}(\vec{r}) \tag{2.10}$$

where the exchange correlation potential v_{xc} is defined as the functional derivative of exchange correlation energy with respect to the $n(\vec{r})$: $v_{xc} = \partial E_{xc} / \partial n(\vec{r})$. The external potential $\hat{v}_{ext}(\vec{r})$ is typically expressed in terms of the pseudopotentials.

The Kohn-Sham effective Hamiltonian depends on the density of fermions in the system, and this equation needs to be solved iteratively as follows:

1. Initial approximation for the density of electrons in the system is created by taking a superposition of atomic densities.
2. The Hamiltonian is formed.
3. The eigenvalue problem is solved for a new set of orbitals, ϕ_i .
4. The corresponding density is formed according to $n(\vec{r}) = \sum_i |\phi_i(\vec{r})|^2$.
5. The new Hamiltonian is formed.

This process is continued until the density of electrons which is used to create the Hamiltonian matches the density corresponding to the orbitals induced by that Hamiltonian. This condition is called “self-consistency”. Additionally, the creation of the new density involves creating a linear combination of densities from the previous steps. For this reason, some algorithms can be used as the direct inversion of the iterative subspace (DIIS) algorithm [131, 132] or Davidson algorithm [133, 134] or residual minimization (RMM-DIIS) [135].

Since Hohenberg-Kohn theorems only specify that the functionals exist and don't provide any guidance for obtaining the actual expressions, many approximations are used. Mainly, the functional is split into two components as exchange and correlation:

$$E_{xc}[n(\vec{r})] = E_x[n(\vec{r})] + E_c[n(\vec{r})] \quad (2.11)$$

The correlation energy is defined as the difference between the total exact energy and the sum of kinetic and exchange energies. Correlations are a result of the collective behaviour of electrons to screen and decrease the Coulombic interactions. Unlike the exchange term, the correlations become more pronounced for opposite spins since they are more likely to occupy nearby locations. However, the exact solution of the correlation contribution can not be analytically possible. Hence, several approaches such as Wigner [136], Gellman and Breuckner [137] and quantum Monte Carlo (QMC) [138, 139] calculations have been proposed for the correlation energy terms. For partially spin-polarized systems, the total exchange energy per electron may be written in terms of the density in a given spin channel as

$$E_x[n(\vec{r})] = -\frac{3}{4} \left(\frac{6}{\pi} n(\vec{r}) \right)^{1/3} \quad (2.12)$$

The spin-polarized exchange and correlation energies depend on the total density and difference between densities of the two spin channels defined by

$$\xi = \frac{n^\uparrow - n^\downarrow}{n^\uparrow + n^\downarrow} \quad (2.13)$$

The oldest and the most popular of the exchange-correlation functional, the local density approximation (LDA), is based on the assumption of a linear functional of the density. The exchange-correlation energy density at every position in space for the molecule is the same as it would be for the uniform electron gas having the same density as found at that position. Here, the exchange and correlation energies are a function of slowly changing electron density. The exchange term [127] can be written as

$$E_x[n(\vec{r})] = -2^{1/3} \frac{3}{4} \left(\frac{3}{\pi}\right)^{1/3} n(\vec{r})^{1/3} \left[(1 + \xi)^{4/3} + (1 - \xi)^{1/3} \right] \quad (2.14)$$

where ξ is the spin polarize density. The correlation energy is determined by an interpolation formula [139]. The exchange-correlation energy can be written as

$$E_{xc}^{LDA} = \int d\vec{r} n(\vec{r}) \epsilon_{xc}^{hom}(n(\vec{r})) \quad (2.15)$$

where $\epsilon_{xc}^{hom}(n(\vec{r}))$ is the exchange correlation energy density of an interacting homogeneous electron gas at the density $n(\vec{r})$.

LDA treats all systems as homogeneous. However, real systems are clearly inhomogeneous with spatially varying electric fields due to nuclei and screening. In order to take this into account, a step may be taken beyond the LDA by including the derivative information of the density into the exchange-correlation functionals. This is so-called the “general gradient approximation (GGA)”. The most used version of this approximation currently is Perdew-Burke-Ernzerhof (PBE) functional [140–142]. In general, the GGA exchange-correlation functional can be written as

$$E_{xc}^{GGA} = \int d\vec{r} \epsilon_{xc} \left(n(\vec{r}), |\nabla n(\vec{r})|, n(\vec{r}) \right), \quad (2.16)$$

where the energy density ϵ_{xc} is a semi-local function of electron density. *Semi-local* means that the locality of ϵ_{xc} in LDA is complemented by the information on the behavior of the electron density in the vicinity of a point \vec{r} , since the electron density is smooth almost everywhere, and the density gradient allows to predict variations of the density near \vec{r} . GGA exchange-correlation functionals lead to many improvements in a description of chemical bonds with an additional computational effort compared to LDA. As an example, the covalent bonds are well described with GGA functional. However, intermolecular interactions have many difficulties with both approaches.

The recent approximations are called “hybrid” methods for which the exchange energy is computed analogously to Fock exchange term in the Hartree-Fock method [143, 144]. The Hartree-Fock method does not include the self-interaction of electrons

which is the main problem of the DFT. Therefore, the “exact” exchange energy will be involved in the exchange-correlation energy term. The functionals are typically parameterized using data from available experimental compounds. The *hybrid* methods suggests that a combination of Hartree-Fock exchange and DFT calculations might be useful, and the exchange correlation functional for the mentioned methods can be defined as

$$E_{xc}^{hybrid} = \alpha E_{xc}^{HF} + E_c \quad (2.17)$$

where α can be chosen to satisfy particular criteria, and E_{xc}^{HF} is Hartree-Fock exchange correlation functional and E_c is the correlation functional (which comes from DFT part). A formal justification for such hybrid schemes was given by Gorling and Levy [145]. As an example to the hybrid functional, the B3LYP functional, [144] which is widely used in the chemical community. Additionally, the other modification is the splitting of exchange component into short-and long-range terms [146–148]. This splitting allows recovering the correct asymptotical behavior of the electron-electron interaction. These modifications are especially useful for computing excited states in the system.

LDA and GGA approaches completely lack a mechanism for a description of the van der Waals (vdW) interaction, but there are some possibilities to add into the functional term. Basically, the vdW interaction between two small molecules (closed-shell atoms) is represented in an asymptotic form [149]

$$E \sim -\frac{C_6}{R^6} \quad (2.18)$$

where the R is the inter-atomic distance and C_6 is the material dependent coefficient. The vdW interaction energy can be found with the sum of inter-atomic pairwise potentials in the form of Equation 2.18. However, this equation is not generally applicable because of divergence at $R = 0$. It is possible to resolve this problem by multiplying Equation 2.18 by a damping function. So, the asymptotic form of the equation at $R \rightarrow \infty$ still remains and the new form of the potential is well-behaved at small R . This modification to the Equation 2.18 has been proposed in several forms,

but the well-known ones have been introduced in the work of Grimme [149–151], Tkatchenko and Scheffler (TS) [152] and Becke and Johnson (BJ) [153, 154]. In the method by Grimme, known as *DFT-D* [149] and *DFT-D2* [150], the energy corrections are taken into account for all pairs of atoms. The dispersion correction can be written in the form

$$E_{disp} = -S_6 \sum_{i=1}^{N-1} \sum_{j=i+1}^N \frac{C_6^{ij}}{R_{ij}^6} f_{damp}(R_{ij}), \quad (2.19)$$

where N is the number of atoms in the system, S_6 is the global scaling factor which is independent of material but it depends on the different GGA functionals. The damping function f_{damp} is given by

$$f_{damp} = \frac{1}{1 + e^{-d(R/R_0-1)}} \quad (2.20)$$

where R_0 is the sum of atomic van der Waals radii and the d is the steepness of the damping function. For the *DFT-D* and *DFT-D2* methods, the coefficients C_6^{ij} are defined as $\frac{C_6^i C_6^j}{C_6^i + C_6^j}$ and $\sqrt{C_6^i C_6^j}$, respectively. However, these two methods have some drawbacks such as lack of flexibility and dependency on the electron distribution. Moreover, the polarisabilities of molecules depends on electronic states, but the coefficients C_6^{ij} for each atom are taken as rigid. For this reason, it is impossible to distinguish between di- and trivalent atoms. To overcome this problem, the *DFT-D3*, TS and BJ methods have been proposed. For example, the *DFT-D3* method takes into account the the chemical environment of each atom by assigning a coordination number. The C_6 coefficients are re-scaled based on the charge distribution in TS method, while, in BJ, they are calculated on the basis of the exchange-hole model. It is important to note that, there are more than one method to determine these empirical coefficients.

2.1.1.1 Pseudopotential Method

The pseudopotential is based on the idea that the effects of the core electrons are replaced with an effective potential. The electrons in the system under considera-

tion can be partitioned into the valence electrons, actively participating in the formation of chemical bonds, and core electrons, which undergo only slight rearrangements [148, 155]. The pseudopotential generation procedure starts with the solution of the atomic problem using the Kohn-Sham (KS) approach to obtain KS orbitals, and make an arbitrary distinction between valence and core states. The core states are assumed to change very little due to changes in the environment, so their effect is replaced by a model potential derived in the atomic configuration. The valence states are seen to oscillate rapidly close to the core regions. Therefore, the valence states are made smoother due to the interaction of the new transferable model potential. More specifically, if we denote the valence orbitals as $|\psi_v\rangle$ and core orbitals as $|\psi_c\rangle$, then the valence orbitals can be expressed as a sum of a smooth “*pseudo-orbital*” $|\varphi_c\rangle$, and the valence orbitals from the orthogonality can be written as

$$|\psi_v\rangle = |\varphi_v\rangle - \sum_c |\psi_c\rangle \langle \psi_c | \varphi_v \rangle \quad (2.21)$$

Applying the Hamiltonian onto the expression in Equation 2.21 for the smooth $|\varphi_v\rangle$, we get

$$\hat{H}_{KS}|\varphi_v\rangle = E_v|\varphi_v\rangle + \sum_c (E_c - E_v) \langle \psi_c | \varphi_v \rangle |\psi_c\rangle \quad (2.22)$$

from where it follows that the smooth function satisfies Shrodinger equation with energy-dependent “pseudo-Hamiltonian” [156] $\hat{H}_{PP} = \hat{H}_{KS} - \sum_c (E_c - E) |\psi_c\rangle \langle \psi_c|$. Analogously, the pseudopotential can be written as

$$\hat{V}_{PP}(E) = \hat{v}_{nl} - \sum_c (E_c - E) |\psi_c\rangle \langle \psi_c| \quad (2.23)$$

where \hat{v}_{nl} is the coulomb potential of the nucleus. In the case of isolated atoms, the indices n and l corresponds to the principal quantum number and the angular momentum quantum numbers, respectively. Actually, the potential does not include any terms that lift the m_l degeneracy, the coulomb potential of nucleus \hat{v}_{nl} is written only depends on the n and l .

In order to ensure the optimum smoothness and transferability, the typical approach to the creation of the pseudopotentials goes as following: First of all, the atomic Schrodinger equation is solved with explicit consideration of all electrons. Then, the pseudo-wavefunction has to match the full electron solution outside a sphere of a pre-specified radius r_c , and it has to preserve the norm of the all-electron solution within that sphere [148]. These four criteria are given as follows:

1. Hamiltonian of the all-electron (AE) system and pseudo eigenvalues (PP) should give same eigenvalues.

$$\hat{H}|\psi_{nl}^{AE}\rangle = \epsilon_{nl}|\psi_{nl}^{AE}\rangle \quad (2.24)$$

$$(\hat{H} + \hat{v}_{nl})|\psi_{nl}^{PP}\rangle = \epsilon_{nl}|\psi_{nl}^{PP}\rangle \quad (2.25)$$

2. AE and PP wavefunctions agree beyond a certain cutoff, $r \geq r_c$.

$$\psi_{nl}^{AE}(r) = \psi_{nl}^{PP}(r) \quad (2.26)$$

3. The norm of the all-electron solution for the real and pseudo orbitals within the sphere (radius R) should be equal for all $R < r_c$.

$$\int_0^R r^2 |\varphi_{nl}^{AE}|^2 dr = \int_0^R r^2 |\varphi_{nl}^{PP}|^2 dr \quad (2.27)$$

4. The derivatives of AE and PP orbitals agree for all $R < r_c$.

$$\left[(r\varphi^{AE}(r))^2 \frac{d}{dE} \frac{d}{dr} \ln(\varphi^{AE}(r)) \right]_R = \left[(r\varphi^{PP}(r))^2 \frac{d}{dE} \frac{d}{dr} \ln(\varphi^{PP}(r)) \right]_R \quad (2.28)$$

According to the study by Vanderbilt [157], the norm conservation condition is not mandatory, since the “missing” charge can be added back to the valence electron density. The generated pseudopotentials with this way can produce much smoother pseudo-wavefunctions and smaller planewave cutoff. Therefore, the computational efforts can be reduced, and the transferability of the generated pseudopotentials can

be improved. Because of the mentioned feature, these generated pseudopotentials are called *ultra-soft* pseudopotentials.

2.2 Transition State Method

The transition state (TS) of a chemical reaction is a particular structure along the reaction coordinate, which is defined as the state corresponding to the highest potential energy along the minimum energy path (MEP), and it dominates the reaction rate. The MEP exists on the potential energy surface (PES), and it presents in Figure 2.1.

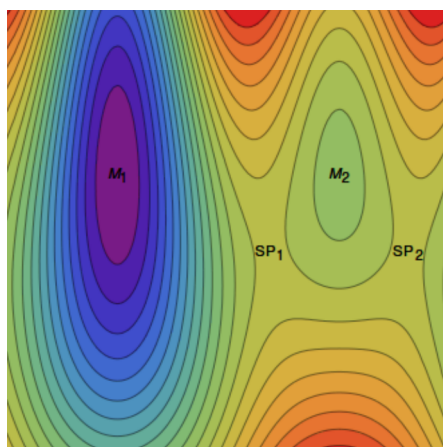


Figure 2.1: A two dimensional potential energy surface. Example of PES with two equivalent minima with two saddle points. The points M_1/M_2 and SP_1/SP_2 represent the local minima and saddle points, respectively.

The PES is a potential energy surface of the system and it is a high dimensional surface. For this reason, the visualization of the PES is hard but it can be considered two dimensional surface-like to understand the behavior of the potential energy surface, see Figure 2.1. For example, by considering the starting point M_1 (local minima), the system can move to another point with any given initial energy. If the initial energy is not enough, the system will oscillate at point M_1 . However, the TS theory does not describe constant energy systems, and it can predict the rate at which the system moves from one point to another. If the energy is enough to move the system to the another local minima (i.e. point M_2) at a constant temperature, the reaction rate of the system can be calculated. It is important to note that the movement of the system

from a local minima to another should be slowly but not so much.

To find the saddle-point (SP_1 and SP_2 in Figure 2.1), several methods [158] have been proposed, and the most popular one in DFT calculation methods for the surface catalysis are Nudged Elastic Band (NEB) Method [159–161] and Dimer method [162] as implemented in many DFT based codes such as QUANTUM ESPRESSO and Vienna Ab initio Simulation Package (VASP) [163–165]. Here a brief description of NEB method will be given in following.

2.2.1 Nudged Elastic Band Method (NEB)

This method was developed to find the activation energy of a considering system [166]. The foundation on which NEB is based, namely the harmonic transition state theory [167], applies particularly well to reactions taking place on solid surfaces due to the close-packed nature of crystal atoms [160]. In the NEB method the MEP is found by constructing an adequate number of images between the initial and final states [160]. It is proposed for finding saddle points and MEP between two energy minima which are known as reactant and product. In the traditional method [167], it makes a linear interpolation with fictitious springs of a set of images between the two local minima and minimizes the energy of each image. However, this method has two main disadvantages which are the sliding-down problem and the corner-cutting problem [159]. First problem comes from the using smaller spring constant in the calculation that gives rise to sliding the images away from the barrier region. Contrary to the first problem, the latter is due to the high spring constant. It caused to miss the the saddle point region. For these two main problem, the *nudging* method has been developed which introduces a force projection scheme to project out the perpendicular component of the spring force and the parallel component of the true potential force. With these corrections the competitive relation between the spring force and the true potential force is eliminated.

Furthermore, the traditional NEB method with a small modification called as *climbing image* NEB (CI-NEB) in which the image with the highest energy is identified as climbing image (i_{max}) and located at the saddle point. This image does not feel the spring force and the true potential force along the path is inverted.

The force acting on i_{max} is given as [160]

$$\vec{F}_{i_{max}} = -\vec{\nabla} E(\vec{R}_{i_{max}}) + 2\vec{\nabla} E(\vec{R}_{i_{max}})|_{\parallel} \quad (2.29)$$

where E is the energy of system, \vec{R} is the position of the intermediate image and $\vec{\nabla} E(\vec{R}_{i_{max}})|_{\parallel}$ is the opposite of the true potential force parallel to the elastic band. The reversed force can make the climbing image to an energy minimum in all directions perpendicular to the path and an energy maximum along the path. Therefore, the climbing image converges under this condition, and it would be the exact saddle point.

2.3 Atomistic Thermodynamic DFT

2.3.1 Basics of Thermodynamics

DFT provides information about the structural and electronic properties of a considering system at zero temperature and pressure. Actually, DFT can allow to have knowledge all about information on the potential energy surface due to the electronic density is a function of the atomic configuration. So, it contains the relevant information needed to describe the effect of temperature on the atomic positions. In order to be able to discuss finite temperature and pressure in a system, it needs to achieve a matching with thermodynamic data. This is so-called *ab initio atomistic thermodynamics* which employs the information of the first-principles potential energy surface to calculate enthalpy, entropy or the Gibbs free energy of the system [168–170]. Then, it is possible to evaluate macroscopic system properties using the standard thermodynamics methods.

Especially in the discussion of the oxidation behaviour of the surfaces, the Gibbs free energy at a finite temperature and pressure conditions is important. As a first step, the Gibbs free energy of a reference system needs to be calculated to get information on the chemical potential of the atom. For this reason, the partition function of the system needs to be calculated to obtain all thermodynamic quantities.

A thermodynamically large system (volume of the system and the number of particles are fixed) is in thermal contact with the environment at temperature T is considered.

This system is called a canonical ensemble, and the all possible states can be described as

$$Q = \sum_i e^{-\frac{E_i}{k_B T}} \quad (2.30)$$

where k_B is the Boltzmann constant, T is temperature and E_i is the energy of particles in the system. This expression is so-called *partition function* (Q). The factor of $\frac{1}{k_B T}$ is known as *Boltzman factor*. Here, Q is obtained as a result of summing over all macroscopic states and is not a function of an individual state. The probability of finding the canonical ensemble system in a given energy state E_i is written as

$$P_i = \frac{e^{-\frac{E_i}{k_B T}}}{Q} \quad (2.31)$$

The average energy U by using Equation 2.31 can be written as

$$U = \sum_i \frac{E_i e^{-\frac{E_i}{k_B T}}}{Q} \quad (2.32)$$

Using the second law of thermodynamic in terms of entropy, S , volume, V , temperature, T and pressure, P , the change in internal energy, $dU = TdS - PdV$, and the Helmholtz free energy $F = U - TS$, one of the fundamental equations of thermodynamic can be written as

$$F = k_B T \ln Q \quad (2.33)$$

In general, the energy of a diatomic molecule is the sum of the transitional energy and its energy in the centre of inertia reference frame. The energy of the molecule within the ideal gas approximation includes five different terms [171]

$$\mathcal{E} = \mathcal{E}_0 + \mathcal{E}_{trans} + \mathcal{E}_{rot} + \mathcal{E}_{vib} + \mathcal{E}_{elect} \quad (2.34)$$

where \mathcal{E}_0 is the energy in the lowest energetical state. The last four contributions can

be considered independently from each other, and the total partition function can be defined as a sum of the partition function of each contribution:

$$Q = Q_{trans} + Q_{rot} + Q_{vib} + Q_{elect} \quad (2.35)$$

It is important to note that here the nuclear energy is omitted since there is only the lowest nuclear energy is populated and the nuclear partition function reduces to a constant which is equal to the degeneracy of that level [172].

For the transitional contribution (\mathcal{E}_{trans}), the transitional contribution to the partition function, Q_{trans} and the transitional part of the Gibbs free energy, G_{trans} can be defined as follows

$$Q_{trans} = \frac{(2\pi k_B T m)^{3/2} k_B T}{h^3 p} \quad (2.36)$$

$$G_{trans} = -RT \ln \left(\frac{(2\pi k_B T m)^{3/2} k_B T}{h^3 p} \right) \quad (2.37)$$

where R is the thermodynamic gas constant, m is mass of atom, and h is Planck constant. The thermodynamic quantities, the partition function and the Gibbs free energy, for the rotational contribution, \mathcal{E}_{rot} are usually computed within the rigid rotor approximation. For symmetrical molecules, the partition function can be expressed as

$$Q_{rot} = \sum_{J=0}^{\infty} (2J+1) \exp \left(\frac{-J(J+1)\hbar^2}{2Ik_B T} \right) \quad (2.38)$$

where J is the rotational quantum number, and I is the moment of inertia. The Gibbs free energy can be calculated from $Q_{rot} = -RT \ln(Q_{rot})$. For the calculation of the rotational constant, the product of the moments of inertia, $I_A I_B I_C$, needs to be calculated as

$$I_1 I_2 I_3 = I_{xx} I_{yy} I_{zz} - 2I_{xy} I_{xz} I_{yz} - I_{xx}^2 I_{yy} - I_{xy}^2 I_{zz} - I_{yz}^2 I_{zz} \quad (2.39)$$

with the individual products, $I_{xx} = \sum_i m_i(y_i^2 + z_i^2)$, $I_{yy} = \sum_i m_i(x_i^2 + z_i^2)$, $I_{zz} = \sum_i m_i(x_i^2 + y_i^2)$, $I_{xy} = \sum_i m_i x_i y_i$, $I_{xz} = \sum_i m_i x_i z_i$ and $I_{yz} = \sum_i m_i y_i z_i$ in terms of the atomic masses, m_i , and x_i , y_i and z_i are atomic coordinates. Then the rotational partition function is given as

$$Q_{rot} = \frac{8\pi^2}{\sigma} \left(\frac{(2\pi k_B T m)^{3/2}}{h^2} \right) (I_1 I_2 I_3)^{1/2} \quad (2.40)$$

where σ is a classical symmetry number, indicating the number of indistinguishable orientations that the molecule can have. The symmetry number reduces the volume of phase space occupied by the molecule in the concept of the classical statistical thermodynamics. The rotational part of Gibbs free energy is

$$G_{rot} = -RT \ln \left(\frac{(2\pi k_B T m)^{3/2}}{h^2} \frac{8\pi^2}{\sigma} (I_1 I_2 I_3)^{1/2} \right) \quad (2.41)$$

The vibrational contribution (\mathcal{E}_{vib}) to the partition function is obtained within the harmonic approximation by writing the partition function as a sum over the harmonic oscillators of all N fundamental modes ω_i of the particle:

$$Q_{vib} = \sum_i^N \left[1 - \exp \left(\frac{-h\omega_i}{k_B T} \right) \right]^{-1} \quad (2.42)$$

$$G_{vib} = \sum_i^N \left[E^{ZPE} + RT \left(1 - \exp \left(\frac{-h\omega_i}{k_B T} \right) \right) \right]^{-1} \quad (2.43)$$

where the zero point energy E^{ZPE} is defined as $\sum_i N_A (\hbar\omega_i/2)$ and N_A is the Avogadro's number. The E^{ZPE} is the energy difference between the vibrational ground state and the lowest point on the Born-Oppenheimer [173] potential energy surface.

The electronic contribution, \mathcal{E}_{elect} , can also be computed as the total energy of the structure by using the DFT method. As a result, the total Gibbs free energy of the system can be calculated by summing of all contributions. By using standard thermodynamics approaches, the relative stability of different systems can be evaluated for a given system.

2.3.2 Ab Initio Atomistic Thermodynamics

DFT is a tool for the electronic calculation of a considered system. However, we would like to understand and describe a system such as heterogeneous catalysis in a macroscopic time and length scale. The aim is to find an appropriate linking between the microscopic and macroscopic regime. All information obtained in the microscopic regime can be transferred into the macroscopic regime. Therefore, the information obtained from the ab initio modeling of a system can be combined with concepts from thermodynamics and statistical mechanics to reach the macroscopic regime. The temperature and pressure information of a system are not included in the results from electronic structure calculation, and all physical quantities are only valid at zero temperature and pressure. The effect of the temperature on the atomic positions can be obtained by evaluating the total energy as a function of the nuclear positions, and it can be used to extract further information such as vibrational mode frequencies. The obtained results for the finite temperature and pressure can be used as an input to thermodynamic considerations. To study with the temperature and pressure depended ensemble, the key quantity is the Gibbs free energy, G :

$$G(T, p) = E^{tot} + E^{vib} - TS^{conf} + pV \quad (2.44)$$

where E^{tot} is the DFT total energy of system, E^{vib} is the vibrational contributions to the system, S^{conf} is the configurational entropy, p is pressure and V is the volume of the system. The vibrational energy contribution to the system, E^{vib} , can be written as

$$E^{vib} = E^{ZPE} - TS^{vib} \quad (2.45)$$

where E^{ZPE} is the zero-point energy (ZPE) of the system and S^{vib} is the entropy of vibrated system. Here, the vibrational motions are composed of a sum of the contributions from each vibrational mode of the system where only real modes are included. The ZPE is obtained from the vibrational motion of molecular systems at 0 K, and it is calculated as a sum of contributions of all vibrational modes (i) in a harmonic oscillator model of the system.

$$E^{ZPE} = \frac{1}{2} \sum_i \frac{hc}{\lambda_i} \quad (2.46)$$

The zero point corrected total energy, E^{corr} , of a system can be calculated adding the ZPE energy to the total energy of the system, E^{total} , and the E^{corr} is given as

$$E^{corr} = E^{total} + E^{ZPE} \quad (2.47)$$

It is important to note that the system is taken as in equilibrium in thermal conditions. This implies that the system in thermodynamic equilibrium can be divided into smaller sub-systems which are also in thermodynamic equilibrium. This is useful in an infinite homogeneous sub-systems such as a gas phase acting on a surface. The general concept of the atomistic thermodynamics is based on the calculation of free surface energy by using Gibbs free energy of the system.

The internal energy of a system in thermal equilibrium can be describe with the pressure p , the entropy S , the volume V and the number of particle N with the chemical potential μ as follows

$$E^{bulk} = TS - pV + N\mu \quad (2.48)$$

When the homogeneous bulk system is cleaved to two surfaces with surface area, A , the internal energy of the system has to increase by an amount of proportional to the surface area. The constant of proportionality is defined as the surface energy, γ , and the new internal energy of the system can be written as

$$E^{bulk} = TS - pV + N\mu + \gamma A \quad (2.49)$$

Introducing the Gibbs energy, $G = E - TS + pV$, to the above equation, the surface free energy can be written as

$$\gamma = \frac{1}{A} \left[G^{surf} - N\mu \right] \quad (2.50)$$

This equation can be written more general for a multi-component system as

$$\gamma(T, p_i) = \frac{1}{A} \left[G^{surf} - \sum_i N_i \mu_i(T, p_i) \right] \quad (2.51)$$

For example, we consider a metal-oxides system (M_mO_n) with a surrounding oxygen gas phase in thermal equilibrium. The free surface energy for the system can be calculated as

$$\gamma(T, p) = \frac{1}{A} \left[G^{surf}(T, p, N_M N_O) - N_M \mu_M(T, p) - N_O \mu_O(T, p) \right] \quad (2.52)$$

where N_M and N_O are the number of metal and oxygen atoms in the surface material, the μ_M and μ_O are the chemical potentials of metal and oxygen atoms. Here, the μ_M can be calculated from the total energy of bulk structure of metal atom per atom. Moreover, the chemical potentials of metal and oxygen of the system in equilibrium can not be varied independently. So, the Gibbs free energy of the bulk oxide can be defined as

$$G_{M_mO_n}^{bulk} = m\mu_M + n\mu_O \quad (2.53)$$

By using the above equation, the surface free energy can be re-written as

$$\begin{aligned} \gamma(T, p) = \frac{1}{A} \left[G^{surf}(T, p, N_M N_O) - \frac{N_M}{m} G_{M_mO_n}^{bulk}(T, p) \right. \\ \left. - \left(N_O - \frac{n}{m} \right) \mu_O(T, p) \right] \quad (2.54) \end{aligned}$$

2.4 Adsorption and Desorption of Molecules on Surfaces

In this part, the different adsorption mechanisms of molecules on surfaces and their relationship to the chemical activity will be discussed briefly.

2.4.1 Physisorption and Chemisorption of Molecules

In the study of surface chemical reactions, the related molecules should be adsorbed on a surface. This is possible in two ways: “physisorption” and “chemisorption”.

Physisorption of a molecule or a single atom could happen the result of van der Waals forces between the adsorbate and the surface. The adsorption energy of this kind of systems is mainly smaller than 0.50 eV. This weaker interaction does not give rise to significant changes in the structural properties of the adsorbate. The adsorbate retains its gas phase electronic structure without any chemical bonds. Basically, the van der Waals forces originate in the ground state fluctuation of the electronic charge of an atom, which generate a dipole moment \mathbf{p}_{fluct} . The induced electric field by this dipole moment at the position of another atom at distance r is given as $-\mathbf{p}_{fluct}/r^3$. The field also induces a dipole moment (\mathbf{p}_{ind}) onto the other atom in the strength of $\mathbf{p}_{ind} = \mathbf{p}_{fluct}/r^3$. The energy of induced dipole of the atom will be negative as a result of the attractive interaction, and this energy will be proportional to r^{-6} . Therefore, two atoms attract each other even in absence of any chemical bonds. At smaller distance, the Pauli repulsion can balance the attractive van der Waals interaction between two atoms. The Pauli repulsion increases exponentially with decreasing the distance and proportional to the overlap of wave functions. The exponential dependence in analytic calculations can be replaced by a factor of r^{-12} . This gives us the potential as form which is so-called *Lennard-Jones* potential [174, 175], Equation 2.55. Here, $-V_0$ is the potential at equilibrium distance r_0^9 .

$$V(r) = V_0 \left\{ \left(\frac{r_0}{r} \right)^{12} - 2 \left(\frac{r_0}{r} \right)^6 \right\} \quad (2.55)$$

In chemisorption of an adsorbate, the electronic orbitals of the adsorbate and the surface atoms should be overlap which can induce a weakening of the internal bindings of the adsorbate, and it may end up a dissociation of the adsorbate from the surface. Normally, the typical adsorption energy in chemisorption of an adsorbate is greater than 0.5 eV. In a chemical reaction, the chemisorption is an activated process, and the the activation energies can vary in wide range which is greater than 0.5 eV.

In the case of physisorption, the potential $V(r)$ represents only the interaction between the adsorbate and the atoms of the solid phase, and the vdW interaction with all the atoms of the solid. The potential $V(r)$ should be calculated as the summation over all two body potentials. The potential given in Equation 2.55 is meaningful only in the limit of large distances from the surface.

2.4.2 Desorption of Molecules

The desorption of an adsorbate from a surface can be determined by breaking of the interaction between the adsorbate and surface. This breaking process can occur by adding an extra energy into the system which has to be higher than the adsorption energy of the adsorbate. The source of the extra energy can be thermal, electronic or vibrational effects. The easiest way for a desorption process is the thermal driven desorption process, since the controlling of the temperature in a system is easier than the other processes.

2.5 Vibrational Motions of an Adsorbate on Surface

In three-dimensional space, three degrees of freedom are associated with the movement of a particle. A molecule in gas phase, $3N$ degrees of freedom exist for N atom species. For a non-linear species, there are three translations, three rotations and the rest ($3N-6$) are vibrational modes. However, for a linear species there are two rotation, three translations and $3N-5$ vibrational modes. The vibrational degeneracies are not possible for a species of such low symmetry, and has a normal mode corresponding to each of the vibrational degrees of freedom. If the system has degeneracies due to higher symmetries, some normal modes will be different in the direction of their overall vibrational displacements. Therefore, the number of normal modes reduce from $3N-6$ or $3N-5$ degrees of freedom. When an adsorbate is adsorbed on a surface, it contributes an extra three degrees of freedom. The classification and description of the degrees of freedom depend on the type of the species and the strength of the adsorption. The vibrational motion of a species on a surface should be converted to a vibration of the adsorbate against the surface. For example, in a physisorption pro-

cess the frequency of translation motion of the adsorbate parallel to the surface may be low due to weak interaction between the adsorbate and the surface. Therefore, the $3N-6$ internal vibrational modes of the species directly related to the modes of the species in gas phase. On the other hand, in the case of the chemisorption, the vibrational frequencies can change due to change of the bonding pattern in the system. In the analysis of the adsorbed species on a surface, the mixing of the vibrations of the adsorbate with the phonon modes of the surface must be ignored to understand the adsorbate and surface bonding [176].

Vibrations in a solid can be considered at local and global levels. At macroscopic level, the periodic atoms are found to participate in collective vibrational motions which is called as *phonons*, and are often treated as quasiparticles. This collective vibrations related to atomic motions in the direction parallel and perpendicular to the wavevector are called longitudinal (L) and transverse (T) modes, respectively. Basically, for one dimensional system the phonon frequency is expressed as follows [177].

$$\omega = \sqrt{\frac{4C}{m}} \left| \sin\left(\frac{\vec{k} \cdot \vec{a}}{2}\right) \right| \quad (2.56)$$

In the above equation, C is the force constant between the neighboring atoms, m is the atomic mass, \vec{a} is atomic distance and \vec{k} is the wavevector. The energy of phonon mode is quantized and the energy of each quantized state, E_n , is defined as $(n + 1/2)\hbar\omega$, where the half of the $\hbar\omega$ is the zero point energy of the system. For a crystal, the dispersion relation has two solutions which are two different types of modes as optical (positive sign) and acoustic (negative sign) vibrational modes. Generally, there are three acoustic (1L and 2T) and the rest are optical modes. In a solid with two atoms, the dispersion relation is given as

$$\omega^2 = C\left(\frac{m_1 + m_2}{m_1 m_2}\right) \pm C\sqrt{\left(\frac{m_1 + m_2}{m_1 m_2}\right)^2 - \frac{4\sin^2(ka)}{m_1 m_2}} \quad (2.57)$$

In DFT, the most intuitive way to calculate the phonon modes is to let all atoms in a large supercell vibrate and then evaluate the frequencies associated with the overall motion of the atoms in the supercell. This is called as *small displacement method*.

In this method, the force constants on each atom are calculated by taking double derivative of potential energy with respect to the atomic position, then these force constants are used to set-up the dynamical matrix. The eigenvalues and eigenvectors of the dynamical matrix give us the vibrational frequencies of the system. For a considering system, the vibrational Hamiltonian can be written as

$$H = \frac{1}{2} \left(\Delta \dot{\mathbf{x}}^T \mathbf{M} \Delta \dot{\mathbf{x}} + \Delta \mathbf{x}^T \mathbf{H} \Delta \mathbf{x} \right) \quad (2.58)$$

where $\Delta \mathbf{x}$ is the atomic displacement, \mathbf{M} is the diagonal matrix of atomic masses expressed as $\delta_{ij} m_i$ and \mathbf{H} is Hessian matrix. Introducing mass-weighted coordinates \mathbf{q} as $\mathbf{M}^{1/2} \Delta \mathbf{x}$, the Hamiltonian can transform into

$$H = \frac{1}{2} (\dot{\mathbf{q}}^T \dot{\mathbf{q}} + \mathbf{q}^T \mathbf{f} \mathbf{q}) \quad (2.59)$$

where \mathbf{f} is the mass-weighted Hessian matrix. The normal modes coordinates \mathbf{Q} are defined as a linear combination of mass-weighted coordinates, $\mathbf{Q} = \mathcal{L}^T \mathbf{q}$. \mathcal{L}^T is a transformation matrix from mass-weighted Cartesian to normal coordinates. From the orthogonality of the \mathcal{L} matrix, $\mathcal{L}^T \mathcal{L} = 1$, the transformation of Hessian matrix \mathbf{f} can be defined as $\mathcal{L}^T \mathbf{f} \mathcal{L} = \mathbf{F}$, where \mathbf{F} is $F_{ij} = \delta_{ij} \omega_i^2$ [178, 179]. The Hamiltonian given in Equation 2.58 can be written in terms of normal mode coordinates as

$$H = \sum_{i=1}^3 N \frac{1}{2} (\dot{Q}_i^2 + \omega_i^2 Q_i) \quad (2.60)$$

where the atomic displacement, $\Delta \mathbf{x}$, can transform to the normal mode coordinates as

$$\begin{aligned} \Delta \mathbf{x} &= \mathbf{M}^{-\frac{1}{2}} \mathbf{q} \\ &= \mathbf{M}^{-1/2} \mathcal{L} \mathbf{Q} \end{aligned} \quad (2.61)$$

After getting the Hamiltonian in terms of normal mode coordinates, mass-weighted Hessian matrix should be diagonalized to get the harmonic frequencies ω_i . When the analytic expression of potential energy is available, the calculation of Hessian

matrix is straightforward without using any approximation. The iterative solution of Kohn-Sham or Hartree-Fock equations yield an expression of the potential energy depends on the molecular orbitals. If local atomic basis function is used, the second derivative of the energy can be calculated iteratively from the self-consistent field (SCF) equation [180–182]. However, the basis set such as plane-waves does not allow the calculation without any approximation due to large dimension and nature of delocalization of the plane-waves.

2.6 Charges on Atoms

In many theoretical studies based on DFT, how charges change on atoms is useful for analyzing the chemical bonds as a result of adsorption a species. However, the definition of charge on atoms is not clear if the bonds are not purely ionic or covalent. For this reason, several methods exist defining the charge on an atom in a different way. The oldest one is the Mulliken population analysis to define the atomic charge [183–186]. This method uses the basis functions written in terms of molecular wave function. The Mulliken population Q_μ is given as

$$Q_\mu = D_{\mu,\mu}S_{\nu,\nu} + \sum_{(\nu \neq \mu)} \frac{1}{2}(D_{\mu,\nu}S_{\mu,\nu} + D_{\nu,\mu}S_{\nu,\mu}) \quad (2.62)$$

where $D_{\mu,\nu}$ is the density matrix and $S_{\mu,\nu}$ is the overlap matrix in terms of orbital occupations. The Mullikan charge on an atom can be obtained by summing up the population Q_μ for all basis functions $\chi_\mu(\vec{r})$ and subtracting them from the nuclear charge (Z), as expressed

$$Q^{Mulliken} = Z - \sum_{\mu} Q_\mu \quad (2.63)$$

This method gives rise to unrealistic atomic charges due to nature of basis set functions. To overcome this problem, some approaches [187–191] based on the atom-centered basis functions have been proposed. Instead of using basis sets to define the atomic charges, a different method 'Hirshfeld [192]' based on the electron density

as a function of space has been proposed. In this method, the atomic charge is defined in terms of electronic density of a fictitious promolecule (ρ_{promol}) and the charge population as follows

$$Q^{Hirshfeld} = Z - \int \frac{\rho(\vec{r})}{\rho_{promol}(\vec{r})} \rho_{promol}(\vec{r}) d\vec{r} \quad (2.64)$$

where $\rho(\vec{r})$ is the electron density and $\rho_{promol} = \sum \rho(\vec{r})$ is given as a sum of ground state atomic electron density.

Another and well-known method, *Bader* [193], is based on the spatial function, $\rho(\vec{r})$, which uses the topology of the electron density. The topology represents an atomic region starting from the minimum charge density points in a taken bond to the maximum electron density in the normal direction to the bond. This gives us the subvolumes in the simulation volume for each atom finding the surface of minimum charge density surrounding each atom. Then it makes bonds appear to have more ionic character [194]. The atomic charge in this method is expressed as follows

$$Q^{Bader} = Z - \int \rho(\vec{r}) d\vec{r}. \quad (2.65)$$

CHAPTER 3

CO, CO₂ AND H₂O ADSORPTION ON γ -Al₂O₃(100) SUPPORTED PLATINUM CLUSTERS

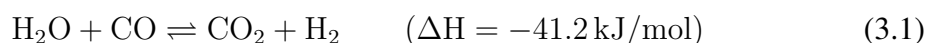
In this chapter we discuss the adsorption properties of CO, CO₂ and H₂O molecules on bare γ -Al₂O₃(100) and γ -Al₂O₃(100) supported mono- and di-atomic Pt clusters. The electronic and structural properties are investigated and, the most stable adsorption configurations are presented on γ -Al₂O₃ surface with/without Pt clusters. Vibrational frequencies of the adsorbed species are presented as a means of aiding in the atomistic level identification of the adsorption geometries. Therefore, we calculated vibrational frequencies related to adsorbed species on bare γ -Al₂O₃ and supported Pt clusters.

3.1 Introduction

One of the most immediate concerns related to human activity is the pursuit of efficient energy production techniques with a low environmental impact. As the global demand for energy increases rapidly, its cost on the environment increases in proportion. The design of efficient and affordable green catalysts is therefore pivotal in all branches of the energy harvesting industry to bring down the cost and strain of industrial activity in the environment. Generally, there are three categories of catalyst, namely are heterogeneous, homogeneous and enzyme catalyst [195]. In this chapter, we concentrate on heterogeneous catalysis, which are employed in diverse energy applications such as oil refining [196], bio-fuel production [197], solar cells [198] and fuel cells [199], and NO_x storage/reduction. Recent research efforts aim at the design of stable and durable new catalysts that can enable commercial application of fuel-cell technology [2].

The water-gas shift (WGS) reaction is one of the oldest key catalytic reactions in industrial applications carrying out two important functions, namely clean H₂ production and conversion of CO to CO₂, which has a smaller environmental impact [3, 200]. Especially, in the carbon based hydrogen production, WGS reaction is the intermediate step used for hydrogen enrichment and CO reduction in the synthesis gas. Considering the fact that the rate of the reaction is dependent on various parameters including the composition of the catalyst, the active surface and structure of catalyst, its operating temperature and pressure, the composition of the gases in the environment and the size of the catalyst.

The WGS reaction,



is an exothermic reaction. It is often equilibrium limited in industrial applications where a two-stage reaction with a high-temperature stage followed by a low-temperature stage is possible. However, the temperatures required for the high-temperature stage are not applicable in small scale applications such as fuel cells. Much effort has been placed into the development small-scale WGS catalysts in recent decades[201, 202].

A conventional WGS catalyst is composed of a support and a precious metal component. While precious metals such as Pt, Rh, Au, Cu, catalyses all the steps of the reaction, the support material such as CeO₂, SiO₂, TiO₂, Al₂O₃, TiC provides support, modifies the reactivity and selectivity of the metal component. In chemical engineering the catalyst for optimal performance involves the adjustment of a large number of parameters simultaneously. The elucidation of the reaction/deactivation mechanism, the role of promoters, and the unambiguous characterization of the catalytically active sites are crucial to rationalize the activity of these catalysts.

As a result of numerous studies, the oxide-supported Cu, Pt and Au metals have been shown to display better performance in WGS reactions. Especially oxide surfaces play an important role in water dissociation [203] and formation of surface carbonate [204]. WGS reaction on pure metal surfaces of Pt [35, 205, 206], Au [207], Cu [208] and Rh [209], and metal-oxide surfaces such as CeO₂ [210, 211], TiO₂ [201, 212], and Al₂O₃ [213–217] have been widely studied by first principle calculations to understand the effect of support and metals, and reaction pathways in WGS reac-

tions. In spite of the large body of research, consensus is difficult to reach regarding the particular reaction pathways and intermediates observed during the course of the reaction [14, 210, 211, 218]. While this intermediate plays a significant role in WGS reaction activity in Pt/CeO₂ systems [210, 211, 219], it could not be seen in Pt/TiO₂, Cu/Al₂O₃ and Pt/Al₂O₃ catalysts.

Although, Al₂O₃ surfaces are widely studied in WGS reaction experiments [43, 220, 221], a coherent account of the interface with the metal component in the context of the interaction of reactants, products and intermediates is missing. Previous studies on the Pt/Al₂O₃ interface provide promising results and a good basis for further studies [213–216, 222, 222, 223].

Catalytic systems of precious metal nano particles supported on partially reducible oxides represent a promising new class of very active catalysts. One of the most widely used oxides in heterogeneous catalysis is transition aluminas (Al₂O₃) known as activated aluminas. Different types of aluminas are generated by thermal treatment of alumina precursors at increasing temperature. Alumina has numerous polymorphs, denoted α , γ -, δ -, κ -, χ -, or η -Al₂O₃ depending on the synthesis process [224]. α -Al₂O₃ is the thermodynamically most stable one, but not much preferred in industrial applications due to the low surface area. They are widely used in heterogeneous catalysis because of catalytic activity and stability. The coexistence of Lewis acidic and basic sites on the Al₂O₃ surfaces makes them desirable support materials that can also enhance the desired properties of a wide range of adsorbates. γ -Al₂O₃ is used as a support material for Pd, Cu and Pt catalysts [222, 225, 226] which show good activity and has significant effects on adsorption mechanism. Wang *et al.* studied H₂ dissociation on Cu-Pd/ γ -Al₂O₃ and shows that supported Cu and Pd atoms are more active for H₂ dissociation than the clean γ -Al₂O₃ and Pd is more active than Cu [226]. Zhang *et al.* studied the effect of surface hydroxyls on CO₂ hydrogenation on Pd/ γ -Al₂O₃ catalyst and found that surface hydroxyls on the clean γ -Al₂O₃ decrease the activity of surface for the Pd and hydroxylation process plays an important role in the selectivity of CO₂ hydrogenation on Pd/ γ -Al₂O₃ surface [225]. CO₂ adsorption on γ -Al₂O₃ supported transition metal dimers was studied by Pan *et al.* [227] and they found that the presence of the metal dimer on surface enhances the adsorption of CO₂ on both bare and hydroxylated γ -Al₂O₃. Clean γ -Al₂O₃ can also play an important

role in catalyst, for instance in CO₂ reforming of CH₄ and adsorption of promoters such as CO, CO₂ and H₂O on clean γ -Al₂O₃ surface [228, 229]. The reactivity of surface atoms is generally related to coordination number, the lowest coordination number being associated to the highest acidity.

The new catalytic systems would prove considerably more advantageous than the industrial catalyst, requiring the use of cheaper support materials, (Al₂O₃ or SiO₂) and a lower loading of Pt. Many experimental and theoretical studies suggest that a small amount of precious metal clusters increases the activity of the surface by donating their charges to the surface molecules. Pan *et al.* [227] showed that transition metal dimers increase the activity of CO₂ molecule on γ -Al₂O₃ support.

In the present study, we choose the nonspinel, tetragonal and fully dehydrated bulk structure model of (100) γ -Al₂O₃ surface. Herein, the catalytically active sites for CO, CO₂ and H₂O are first investigated on bare surface. We then concentrate on the effects of supported Pt₁ and Pt₂ clusters on the electronic, structural and vibrational properties of CO, CO₂ and H₂O.

3.2 Computational Details

The calculations were performed using density functional theory (DFT) as implemented in QUANTUM ESPRESSO [163], using the generalized gradient-corrected exchange correlation functional of Perdew, Burke and Ernzerhof (PBE) [141, 230]. XcrysDen [231, 232], which is an open source program, was used to visualize the structures. The kinetic energy and density cutoffs for all calculations are 35 and 350 Ry, which ensures a good convergence of the energy. Electronic configurations of valence electrons for the adsorbates are 5d⁹ 6s¹ for Pt, 2s² 2p² for C and 2s² 2p⁴ for O.

Sampling of the Brillouin zone was performed using the Monkhorst-Pack scheme [233] with a 2×3×1 grid of k-points. Marzari-Vanderbilt smearing [234] has been used with a width of 0.02 Ry. All calculations are spin polarized. In slab calculations, the vacuum thickness of 10-12 Å is set between two periodically repeated slabs.

In this study, a (100) surface of $\gamma\text{-Al}_2\text{O}_3$ which is a non-spinel, tetragonal and fully dehydrated bulk structure model of $\gamma\text{-Al}_2\text{O}_3$ with no vacancies is studied for the DFT calculations. This structure was derived from a model created by Digne et. al [43] which is one of the most popular models for the $\gamma\text{-Al}_2\text{O}_3$ in the literature. The unit cell of the model consists of 16 Al atoms and 24 O atoms and a 2×1 unit cell was used for all calculations. A systematic study has been conducted to identify the most stable adsorption sites for both mono-atomic and di-atomic Pt clusters. Before adsorption, structural relaxation was carried out for the clean $\gamma\text{-Al}_2\text{O}_3(100)$ surface. Several stable adsorption geometries have been identified for CO, CO₂ and H₂O, and their interaction with both the precious metal and the support is characterized in terms of adsorption energies and the nature of the bond between the adsorbed molecules and the precious metal. The adsorption energy per atom is calculated using the formula

$$E_{ads} = \frac{1}{n}(E_{total} - E_{surf} - nE_{atom/mol}) \quad (3.2)$$

where E_{total} is the total energy of the whole structure, E_{surf} is the energy of the bare surface (without atom or molecule), $E_{atom/mol}$ is the energy of the atom or molecule in the gas phase and n is the number of atom or molecule in the system.

The charge difference density is defined as

$$\Delta\rho = \rho_{total} - \rho_{surf} - \rho_{atom/mol} \quad (3.3)$$

where ρ_{total} is the total charge density of the system, ρ_{surf} is the charge density of bare surface and $\rho_{atom/mol}$ is the charge density of the single atom or molecule. The blue and red colors in the charge density difference analysis correspond to $\Delta\rho > 0$ (excess electron) and $\Delta\rho < 0$ (electron deficiency), respectively. The charge density difference analysis is used in all configurations and can provide schemes for charge partition of the systems. This analysis gives charge distributions for CO, CO₂ and H₂O molecules on (100) surface of $\gamma\text{-Al}_2\text{O}_3$ supported Pt clusters. Bader charge analysis was performed by using the charge decomposition algorithm implemented in the program distributed by the Hankelman group [235, 236].

The shift of vibrational frequencies is calculated as

$$\Delta\nu = \nu_{ads} - \nu_{gas} \quad (3.4)$$

where ν_{ads} is DFT-calculated vibrational frequency of the adsorbed molecule and ν_{gas} is the DFT-calculated vibrational frequency of the molecule in gas phase on bare γ - $\text{Al}_2\text{O}_3(100)$ surface and γ - $\text{Al}_2\text{O}_3(100)$ supported Pt clusters. In the calculation of the vibrational frequencies of the molecules on the bare surface and the surface supported Pt clusters, the all system is fixed except the molecules to reduce the computational effort.

3.3 Results and Discussion

3.3.1 Mono- and Di-atomic Pt Clusters on γ - $\text{Al}_2\text{O}_3(100)$

In this part of the study, we studied the interactions of a single Pt and diatomic Pt_2 clusters on γ - $\text{Al}_2\text{O}_3(100)$ surface. The adsorption of a single Pt atom on the surface was studied by Deskins *et al.* [237] and they found that Pt atoms preferentially adsorb between the O and neighboring Al atoms on the surface as a part of the surface. In the present study, we have investigated several adsorption geometries, Pt-on-top, -bridge, -embedded and Pt_2 -on-top, on the surface for the mono- and diatomic-Pt clusters. In general, the most favorable adsorption configurations are embedded geometries (config. (a)-(b) in Figure 3.1) where the Pt atom is embedded into the surface, with slightly different adsorption energies from each other. Upon adsorption, the Pt atoms gained charge in the range of 0.24-0.46 $|e|$ from the surface. For Pt and Pt_2 , all stable adsorption configurations are presented in Figure 3.1 with the relative adsorption energies and partial Bader charges. The relative adsorption energies of mono- and diatomic Pt clusters are referenced to the adsorption geometry with minimum energy. All DFT calculations was performed spin unrestricted, and the small magnetization was observed for Pt adsorbed surfaces. The relative adsorption energies of embedded configurations are nearly same (in the range of 0.0-0.22 eV) and the other two bridge configurations are not favorable as embedded ones. For the diatomic Pt clusters, the adsorption configurations with the adsorption energies and Bader charges are presented in Figure 3.1 (f)-(l). The most favorable configuration is a combination of

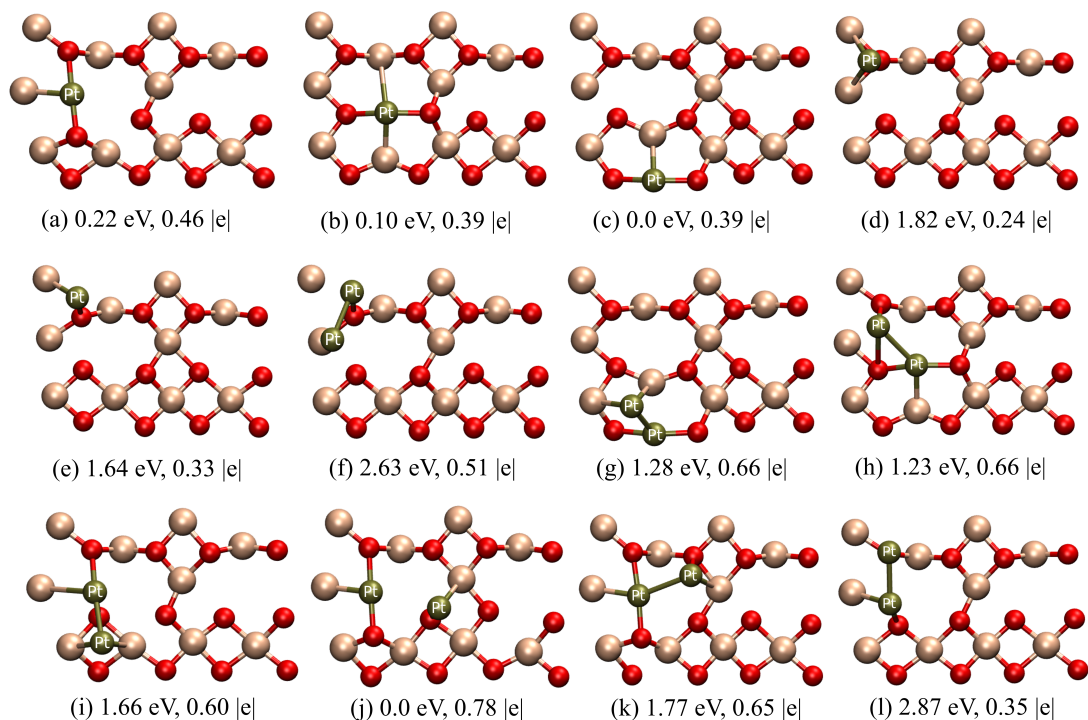


Figure 3.1: Mono- and di-atomic Pt clusters on γ -Al₂O₃. Mono-atomic Pt clusters are in (a)-(c) embedded geometry, (d)-(e) Pt-on-top and -bridge geometry. (f)-(l) Di-atomic Pt clusters are in Pt₂-on-top geometry. The relative adsorption energies and partial Bader charges of Pt and Pt₂ clusters are given for each configuration. White, red, and dark green balls stand for Al, O, and Pt atoms, respectively.

an embedded Pt and Pt atom in bridge geometry, see Figure 3.1 (j). The others adsorbed as Pt₂ clusters and the energies are in the range of 1.23-1.77 eV for the most stable ones as may be expected from the Pt-Pt dimer distances and Bader charges. Furthermore, we observed that a small amount of charge transfer in the range of 0.35 - 0.78 |e| from the surface to the cluster after adsorption of the Pt₂ dimers comparing the atomic Pt atoms (0.24-0.46 |e|) on the surface.

3.3.2 Molecular Adsorption of CO, CO₂ and H₂O on Bare γ -Al₂O₃(100)

Stable adsorption geometries with adsorption energies of CO, CO₂ and H₂O on the bare γ -Al₂O₃(100) surface are represented in Figure 3.2, 3.3 and 3.4, respectively. Stable configurations given in the present work can be directly compared with the data reported by Wischert *et al.* [229] for CO and by Cao *et al.* [238] for CO₂ and

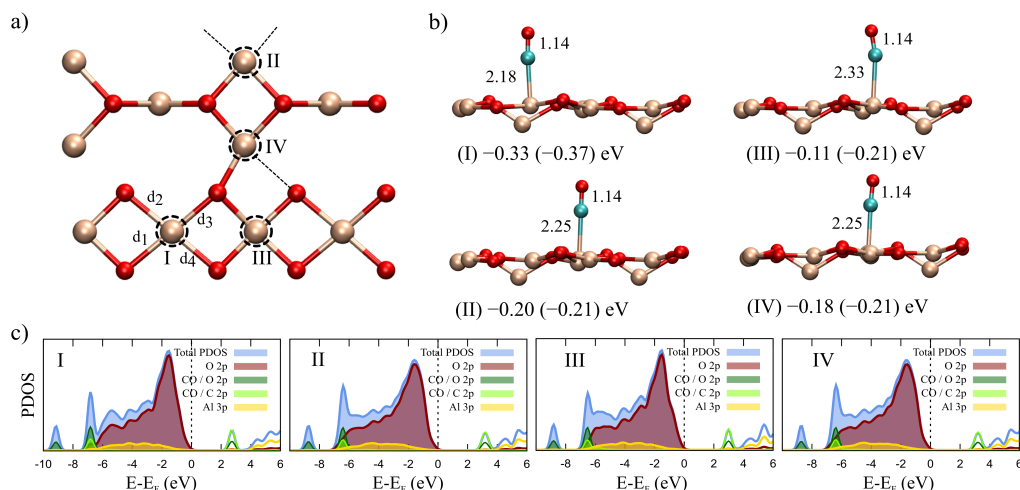


Figure 3.2: Adsorption of CO on bare γ -Al₂O₃(100) surface. (a) The top view of bare γ -Al₂O₃(100) surface with the most stable adsorption sites for the CO molecule. (b) The side view of the most stable adsorption geometries with the adsorption energies. The adsorption energies in parenthesis refer to the previous works [229]. (c) Projected density of states (PDOS) of CO molecule on the surface. White, red, and cyan balls stand for Al, O, and C atoms, respectively.

H₂O. Projected density of states (PDOS) plots are given in the related figures for the molecules.

The adsorption geometries with the adsorption energies and projected density of states (PDOS) of the CO molecule on the bare surface are given in Figure 3.2. CO molecules preferentially adsorb C-down on-top Al site (5-folds) forming C-Al bond in the range of 2.18-2.33 Å as seen Figure 3.2 (a). All four different adsorption geometries for CO molecule have adsorption energies in the range of -0.33 - -0.11 eV. The most stable configuration found on site I with the energy of -0.33 eV as may be expected from the shorter Al-C distance (2.18 Å). O-down adsorption configuration was also studied however, due to their smaller adsorption energy results are not reported. When the CO molecule adsorbs on the bare surface, there is a small degree of interaction between the surface states and CO, as shown in Figure 3.2 (c). For all configurations, surface Al states and C atom of the molecule show small hybridization at around 3 eV. This small hybridization can be supported with the small adsorption energies and longer Al-C distances.

Table 3.1: C-O and C-Al bond distances (d), partial Bader charge (ρ) of CO and shift of the vibrational mode frequencies of adsorbed CO molecule on bare γ -Al₂O₃. Distances are in Å and partial Bader charges in $|e|$. Vibrational frequencies are given in cm⁻¹. Vibrational frequencies are shifted by the value of 2142.4 cm⁻¹ for the CO in gas phase.

confg.	$d^{[C-O]}$	$d^{[C-Al]}$	d_1	d_2	d_3	d_4	ρ	$\Delta\nu$ [229]	$\Delta\nu$
I	1.14	2.18	2.01	2.01	1.98	1.98	0.11	20	25.2
II	1.14	2.25	1.90	1.98	1.97	1.95	0.09	4	10
III	1.14	2.33	1.85	1.85	1.84	1.84	0.08	8	7.7
IV	1.14	2.25	1.90	1.96	1.98	1.95	0.09	5	9.2

The differences in the adsorption energies are related with the different coordination number and bond distances between the adsorption site and neighboring surface atoms. As a measure of the distortion caused by the adsorbate on the surface, we also report the four Al-O distance (d_1 , d_2 , d_3 and d_4 in Figure 3.2) in the intermediate neighborhood of the adsorption site. These bond lengths, Bader charges of the molecule and shift of vibrational frequencies are summarized in Table 3.1. Our calculated vibrational frequencies are in very good agreement with the results by Wischert *et al.* [229]. The recent experimental study on the adsorption CO on the γ - and δ -Al₂O₃ surfaces shows three major bands at 2200-2190, 2184-2173 and 2153-2148 cm⁻¹ [224]. These reported bands were assigned to CO adsorbed on active surface Al sites on Al₂O₃ surfaces. The last band associated with the frequency shift on γ -Al₂O₃ surface is in good agreement with our results reported in Table 3.1. The surface Al-O bond lengths on the adsorption sites are given in Table 3.1. Results show that the calculated vibrational mode frequencies are nearly same as the vibrational mode frequencies of CO in gas phase due to weak interaction between the CO and the surface atoms.

On bare γ -Al₂O₃(100), CO₂ on an Al-O bridge site (config. I in Figure 3.3) forming a bidentate structure with an adsorption energy of -0.63 eV in agreement with previous work [238]. The total charge on the CO₃ entity formed as a result of adsorption is -2 $|e|$. This value, together with the O-C distances and O-C-O angles (See Table 3.2) indicate that CO₂ is adsorbed as a surface carbonate. In config. II, the adsorbed CO₂ was considered to form a monodentate carbonate species. Upon adsorption of CO₂, a limited amount of overlap was observed between the orbitals of the C and O atoms

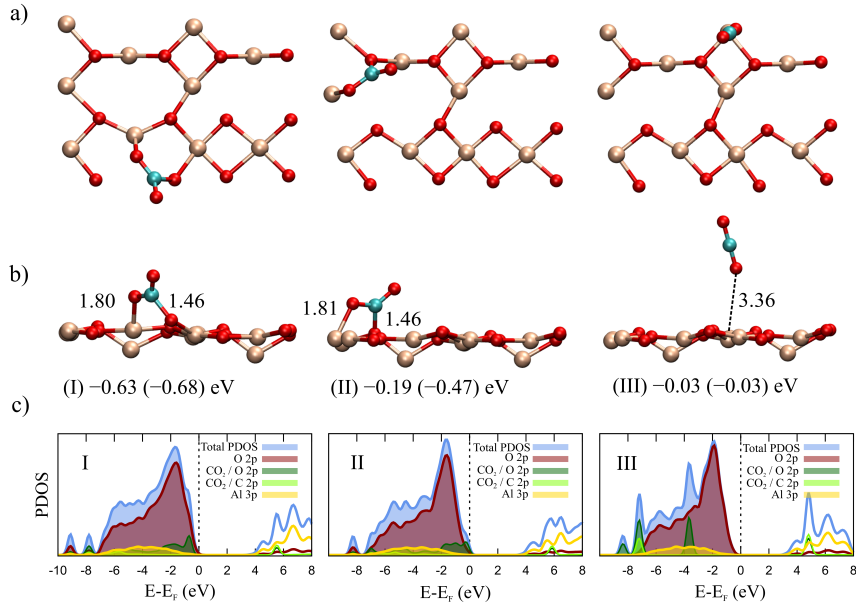


Figure 3.3: Adsorption of CO_2 on bare γ - $\text{Al}_2\text{O}_3(100)$ surface. (a)-(b) The top and side views of the most stable adsorption geometries with the adsorption energies. The adsorption energies in parenthesis refer to the previous works [238]. (c) PDOS of CO_2 molecule on the surface. White, red, and cyan balls stand for Al, O, and C atoms, respectively.

of the molecule and neighboring surface atoms as seen in PDOS plots (Figure 3.3 (c)). In the configurations I and II, the hybridizations between the molecule and surface atoms were observed at around -9 and -8 eV upon adsorption of the molecule. The extent of the overlapping states of CO_2 and surface atoms in config. I is smaller than the states in config. II. This is consistent with the fact that config. I is more stable than config. II. The less favourable adsorption geometry with $E_{ads} = -0.03$ eV is linear geometry in which CO_2 on top Al site (config. III) as O-C-O atomic arrangement. For this configuration, the molecule shows no hybridization due to the weak interaction with the surface states, see Figure 3.3 (c).

The bond angles, bond lengths in the molecule and neighboring surface atoms, partial Bader charges of the molecule and shift of vibrational frequencies with respect to the molecule in gas phase are given in Table 3.2 for adsorbed CO_2 . Our calculated vibrational frequencies ν_s , ν_a and ν_b for the linearly adsorbed CO_2 experience only a very small shift with respect to the CO_2 in gas phase, in line with the weak molecule-surface interaction [239, 240]. In the work of Gregg *et al.* [239] it is reported that

Table 3.2: Bond angle, C-O and C-Al bond distances, partial Bader charge of CO₂ and shift of vibrational mode frequencies of adsorbed CO₂ molecule on bare γ -Al₂O₃(100) surface. Distances are in Å and partial Bader charges in |e|. Vibrational frequencies are given in cm⁻¹. Vibrational frequencies are shifted by the value of $\nu_b=634.0$ cm⁻¹, $\nu_s=1312.9$ cm⁻¹ and $\nu_a=2367.4$ cm⁻¹ for the CO₂ in gas phase. $\Delta\nu_b^{[ip]}$ and $\Delta\nu_b^{[oop]}$ are shift of in-plane and out of-plane bending mode frequencies. ν_s : symmetric stretching, ν_a : asymmetric stretching and ν_b : bending modes.

config.	$\angle(\text{C-O-C})$	$d^{[\text{C-O}]}$	$d^{[\text{C-Al}]}$	ρ	$\Delta\nu_s$	$\Delta\nu_a$	$\Delta\nu_b^{[ip]}$	$\Delta\nu_b^{[oop]}$
I	130.9	1.29,1.21	1.80	0.21	-96.1	-516.5	218.9	111.4
II	131.1	1.29,1.21	1.81	0.39	-105.6	-630.8	152.6	127.8
III	179.9	1.16,1.18	3.36	0.01	3.6	2.2	-10.1	-11.3

the surface carbonate and bicarbonate can be easily distinguished with the vibrational bands. In our calculations, the CO₂ was not observed as bidentate carbonate form on the surface (symmetric and asymmetric stretching frequencies switch order in bidentate and monodentate form) according to the characteristic vibrational frequencies of the molecule reported by Pan *et al.* [241]. Our calculated vibrational mode frequencies are also in good agreement with the experimental and theoretical results [241] and fall in the range of the experimental reported results. It is important to note that the degenerate bending modes of CO₂ in gas phase due to the linear geometry of the molecule disappears upon adsorption of the molecule on the surface, and the bending modes are lifted to two different bending modes as in-plane ($\nu_b^{[ip]}$) and out of-plane ($\nu_b^{[oop]}$), see Table 3.2. In order to understand the charge distribution after adsorption of the molecule on the surface, the Bader charge analysis was performed for the all configurations. Config. II is accompanied by a larger charge transfer in comparison to config. I in spite of the lower adsorption energy. For config. III, the small charge transfer to the molecule is once again consistent with the weak interaction.

For H₂O adsorption on bare γ -Al₂O₃(100) surface, the adsorption energies are significantly larger than CO and CO₂ as reported in Figure 3.4. This is consistent with the commonly known affinity of the γ -Al₂O₃ surface to H₂O molecules. The most stable adsorption configuration is the config. I which is an on-top Al site with the adsorption energy of -1.48 eV. The magnitude of the adsorption energy of this configuration is justified by the weakened C-O bond that increases in length to 1.48 Å. In the most recent DFT study by Cao *et al.* [238] the most stable configuration was reported to

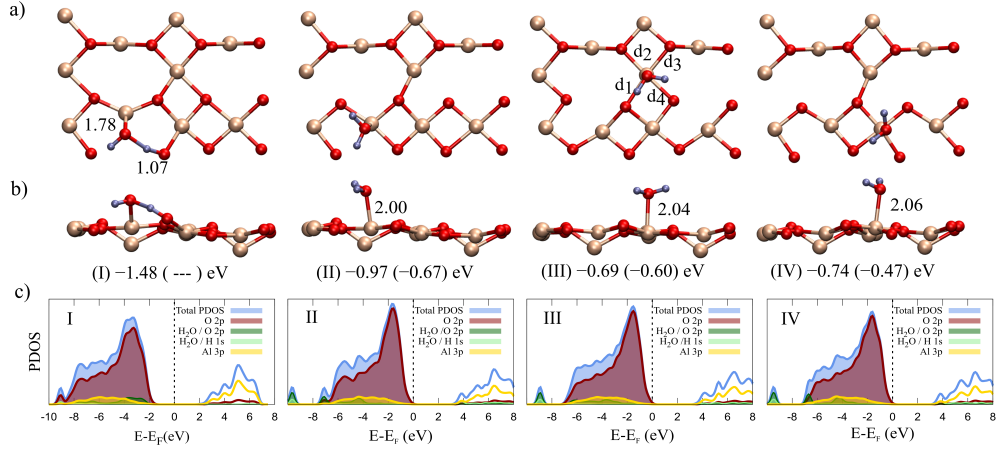


Figure 3.4: Adsorption of H_2O on bare $\gamma\text{-Al}_2\text{O}_3(100)$ surface. (a)-(b) The top and side views of the most stable adsorption geometries with the adsorption energies. The adsorption energies in parenthesis refer to the previous works [238]. (c) PDOS of H_2O molecule on the surface. White, red, and blue balls stand for Al, O, and H atoms, respectively.

be on-top Al site as same as config. II. According to the PDOS plots, the states of the H_2O molecule in config. II, III and IV shows small hybridizations between the surface Al p-orbital states and H s-orbital states at around +4 eV above the Fermi level. However, a hybridization for the molecule on site I was observed at around -8 eV, see Figure 3.4 (c). Depending on the bond distance, longer than 2 Å, between the surface Al and O atom of the molecule, the overlapping of the states are decreasing as seen in Figure 3.4 (c), config. III and IV.

Table 3.3: Bond angle, O-H and O-Al bond distances, partial Bader charge of H_2O and shift of vibrational mode frequencies of adsorbed H_2O molecule on bare $\gamma\text{-Al}_2\text{O}_3(100)$ surface. Distances are in Å and partial Bader charges in $|e|$. Vibrational frequencies are given in cm^{-1} . Vibrational frequencies are shifted by the value of $\nu_s=3768.7 \text{ cm}^{-1}$, $\nu_a=3892.4 \text{ cm}^{-1}$ and $\nu_b=1566.8 \text{ cm}^{-1}$ for the H_2O in gas phase.

config.	$\angle(\text{H-O-H})$	$d^{[\text{O-H}]}$	$d^{[\text{O-Al}]}$	ρ	$\Delta\nu_s$	$\Delta\nu_a$	$\Delta\nu_b$
I	-	0.99,1.40	1.78	0.26	-	-	-
II	108.0	0.98,0.98	2.00	0.06	-90.3	-11.6	-96.1
III	108.8	0.98,0.98	2.04	0.06	-152.2	-40.3	-89.3
IV	107.1	0.98,0.98	2.06	0.04	-51.1	-4.5	-57.0

The bond angles, bond lengths of the molecule, Bader charges of the molecule and shift of vibrational frequencies with respect to the molecule in gas phase are given in Table 3.3 for the adsorbed H₂O molecule on the surface. The bond angles of adsorbed H₂O molecule are increased by around 4.5° with increasing of the H-O distance upon adsorption of H₂O. The calculated vibrational stretching frequency of H₂O by Digne *et al.* [242] is reported to be 3717 cm⁻¹ on Al site of the γ -Al₂O₃ surface. Our result on the same adsorption site of the surface yields a very similar vibrational stretching frequency value for H₂O. For the other adsorption sites, we have found that the symmetric stretching frequencies are in the range of 3616-3717 cm⁻¹. The differences in the symmetric stretch mode frequencies correlate with the decreasing O-H-O bond angle. The asymmetric stretch, on the other hand, is not affected to the same extent. The bending frequencies are once again rather sensitive to this angle. Interestingly, the charge transfer is negligible in spite of the large adsorption energies. This indicates a long-range Coulombic interaction between the negatively charged O atom of the H₂O molecule and the positively charged surface Al atom. Al-O bond distances in the intermediate neighborhood of the surface H₂O adsorption sites are reported in Table 3.4.

Table 3.4: Al-O bond distances (in Å) in the intermediate neighborhood of the surface H₂O adsorption sites.

config.	d ₁	d ₂	d ₃	d ₄
I	2.75	2.95	1.79	1.78
II	1.90	2.45	1.89	1.93
III	2.04	1.97	1.90	1.95
IV	1.88	1.88	1.82	1.81

3.3.3 CO, CO₂ and H₂O Adsorption on γ -Al₂O₃(100) Supported Pt and Pt₂ Clusters

3.3.3.1 Adsorption of CO

The adsorption energies and adsorption geometries of CO on the γ -Al₂O₃(100) surface with pre-adsorbed mono- and di-atomic Pt clusters are presented in Figure 3.5

and 3.6. Before going into the details of the adsorption process, we note the important and striking observation that the adsorption energies of the Pt_n -O-C ($n=1,2$)(C-down) adsorption configurations are larger than the corresponding geometries on the bare Pt(111) surface [243]. For the Pt+CO systems, the larger adsorption energies of the CO molecule may originate either from interaction between the surface Al atom and the molecule atoms (see Figure 3.5 (a)) or from the interaction between the C atom and Pt atom as seen in the other three configurations. After adsorption of the CO, an overlap between the CO molecule and the Pt and surface Al atoms was observed at the range of 2-4 eV above the Fermi level. Furthermore, a small hybridization between the molecule p states and Pt d states was observed around Fermi level, see Figure 3.5 (b).

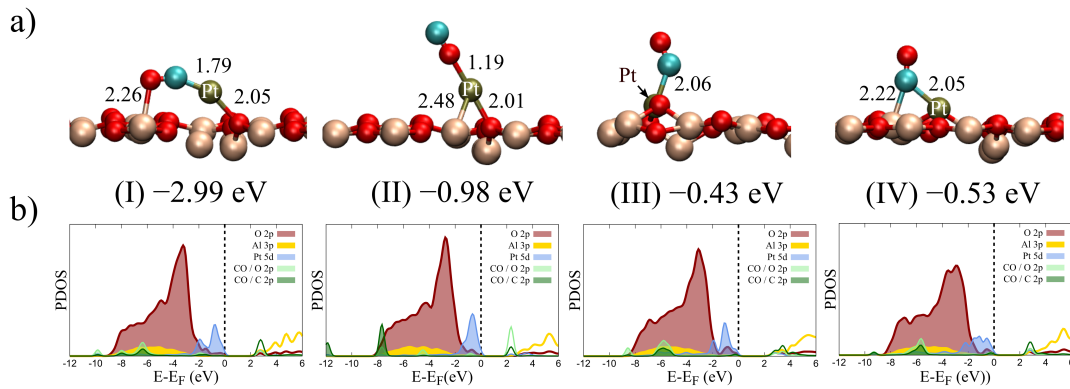


Figure 3.5: (a)-(c) The side view of the most stable adsorption geometries with the adsorption energies and (b)-(d) PDOS of CO molecule on γ - $Al_2O_3(100)$ surface supported mono-atomic Pt cluster. Bond distances are in Å. White, red, cyan and dark green balls stand for Al, O, C and Pt atoms, respectively.

The extra stability in config. I can be related to the stronger interaction between the molecular states as a combination the C and O p orbital states and the surface Al and Pt atoms in the region around -2.7 eV. The smaller adsorption energy of the config. IV as may be expected from the weak interaction of C p orbital states and surface Al p states with respect to the interaction of molecular states in config. I.

The Pt_2 +CO configurations (see Figure 3.5) fall into three categories bridge (config. I, II, III and VI), linear (config. IV, VII and VIII) and embedded (config. V). The

CO molecule tends to adsorb with higher adsorption energies between the two Pt atoms in the bridge geometries. The adsorption energy of the CO molecule with the embedded Pt atom in the bridge geometry (config. III) has lower adsorption energy because of the stronger interaction between the Pt and surface atoms. Another reason can be related with the interaction of the Pt d orbital states and surface Al p orbital states, see Figure 3.5 (b) and (d). The most favourable adsorption geometry is the linear geometry with the embedded Pt atom into the surface. However, the Pt_n -C-O ($n=1,2$)(O-down) adsorption geometries are less favourable because of the interaction between the oxygen and Pt atoms by increasing overlap between the molecular states and Pt atoms as seen Figure 3.5 (c) config. VII and VIII.

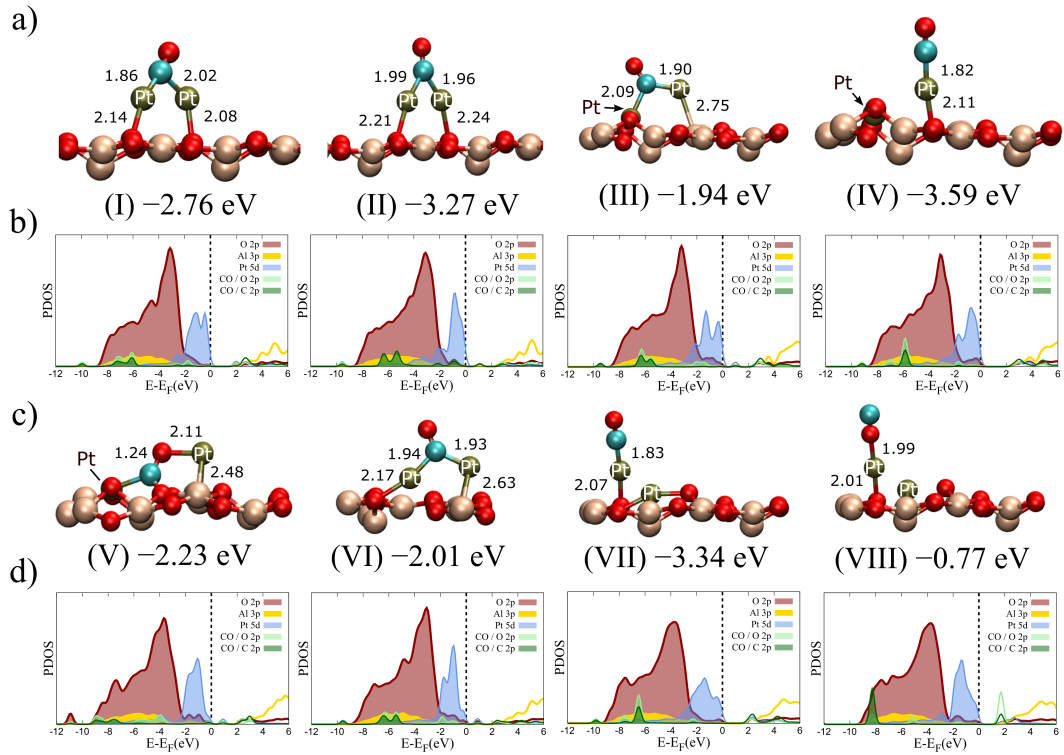


Figure 3.6: (a)-(c) The side view of the most stable adsorption geometries with the adsorption energies and (b)-(d) PDOS of CO molecule on γ - $Al_2O_3(100)$ surface supported di-atomic Pt_2 cluster. Bond distances are in \AA . White, red, cyan and dark green balls stand for Al, O, C and Pt atoms, respectively.

The higher adsorption energies of CO molecule on the surface can be assessed by taking into account the rather low adsorption energies of CO molecule on bare γ - $Al_2O_3(100)$ surface as represented in the previous section (Figure 3.2). While the

Table 3.5: C-O bond distance, partial Bader charges of CO and Pt and shift of vibrational mode frequencies of adsorbed CO molecule on γ -Al₂O₃(100) supported mono- and di-atomic Pt clusters. Distances are in Å and partial Bader charges in $|e|$. Vibrational frequencies are given in cm^{-1} . Vibrational frequencies are shifted by the value of $\nu=2142.4 \text{ cm}^{-1}$ for the CO in gas phase.

	config.	$d_{[C-O]}$	ρ_{CO}	ρ_{Pt}	$\Delta\nu$
CO + Pt	I	1.20	0.49	-0.28	-468.3
	II	1.16	0.16	0.15	-175.9
	III	1.16	0.19	0.25	-175.0
	IV	1.18	0.49	0.03	-276
CO + Pt ₂	I	1.22	0.42	-0.04	-409.2
	II	1.19	0.33	-0.05	-319.0
	III	1.19	0.26	0.32	338.7
	IV	1.16	0.20	0.39	-95.3
	V	1.24	-0.70	1.27	-593.1
	VI	1.21	0.37	0.10	-464.8
	VII	1.16	0.20	0.41	-84.5
	VIII	1.16	0.14	0.53	-167.5

C-O bond distance on the bare surface is 1.14 Å, for the supported Pt atoms the C-O bond lengths are in the range of 1.16-1.24 Å. The electrons are partially transferred from the d orbital of the metal to anti-bonding molecular orbitals of CO molecule. This electron transfer can strength the bond between the Pt and C atoms, and this can weaken the C-O bond of the molecule.

The CO molecule is a widely used probe molecule for the characterization of catalysts. The vibrational frequencies of adsorbed CO molecule on a surface can be sensitive to the active adsorption sites, coverage of the molecule and surface orientation. These are related with the changing the dipole moment of the molecule upon adsorption. Therefore, we have calculated vibrational frequencies (see Table 3.5) upon adsorption of the molecule on the surface to see a relation between the vibrational frequency and adsorption geometry of the adsorbed molecule. Our results show that the decrease in the vibrational frequency of the molecule (200-300 cm^{-1}) with respect to the free CO molecule (2142.4 cm^{-1}). The PDOS illustrates that the d orbitals of Pt atom overlaps with the molecular states and surface p orbital states. A large contribution to the tail of the valence band of the configurations after adsorption of the molecule on the surface. The molecule O p orbital states are mainly

localized around -6 eV in the case of larger adsorption energy configurations. The intensity of C p orbital states is lower than O-p states for all adsorption configurations of CO. The small magnetization, $\sim 0.20 \mu_B/\text{cell}$, observed after adsorption of the CO on Pt_n ($n=1,2$). Moreover, we have observed that spin polarize DFT calculation can effect the adsorption geometry of the molecule on the surface as seen in Figure 3.6 config. III and IV. While the molecule prefer to bind to the surface O atom in spin restricted DFT calculation in bridge geometry, config. III, we observed that the molecule bind to the surface Al atom in spin polarize DFT calculation in the linear geometry, config. IV.

3.3.3.2 Adsorption of CO_2

The selected adsorption geometries of CO_2 molecule are displayed as in Figure 3.7 with the adsorption energies. In this part of the study, we have identified three CO_2 geometries as bridge Al-Pt, bridge P-Pt and C-down monodentate, see Figure 3.7. From the comparison of CO_2 adsorption energies, the maximum adsorption energy configuration is the bridge Al-Pt geometry (config. II) deriving from the interaction between the surface Al and free O atom of the molecule.

For adsorption geometries supported both mono- and diatomic Pt clusters, the lower adsorption energies correspond to the molecules bounded to embedded Pt atom, which can be explained by the stronger interaction between the Pt and surface. In fact, this observation correlates with the large negative charge on the Pt atoms and the large positive charge induced on the adsorbed CO_2 species as seen in Table 3.6. After adsorption of the molecule, the C-O bond distance increase, and we found that the C-O bond distance (1.18 \AA in gas phase) in the range of 1.20 - 1.30 \AA , see 3.6. While the characteristic O-C-O bond angle is 180° in the gas phase, this value decreases upon adsorption of the molecule. The changes in the bond angle with the bond distances of the molecule affect the vibrational modes of the molecule after adsorption on the surface. The shift of the vibrational frequencies with respect to the CO_2 molecule in gas phase summarized in Table 3.6.

In the case of CO_2 adsorption, while the supported monoatomic Pt cluster configurations show a larger contribution from molecular O p states in the region of -4 to

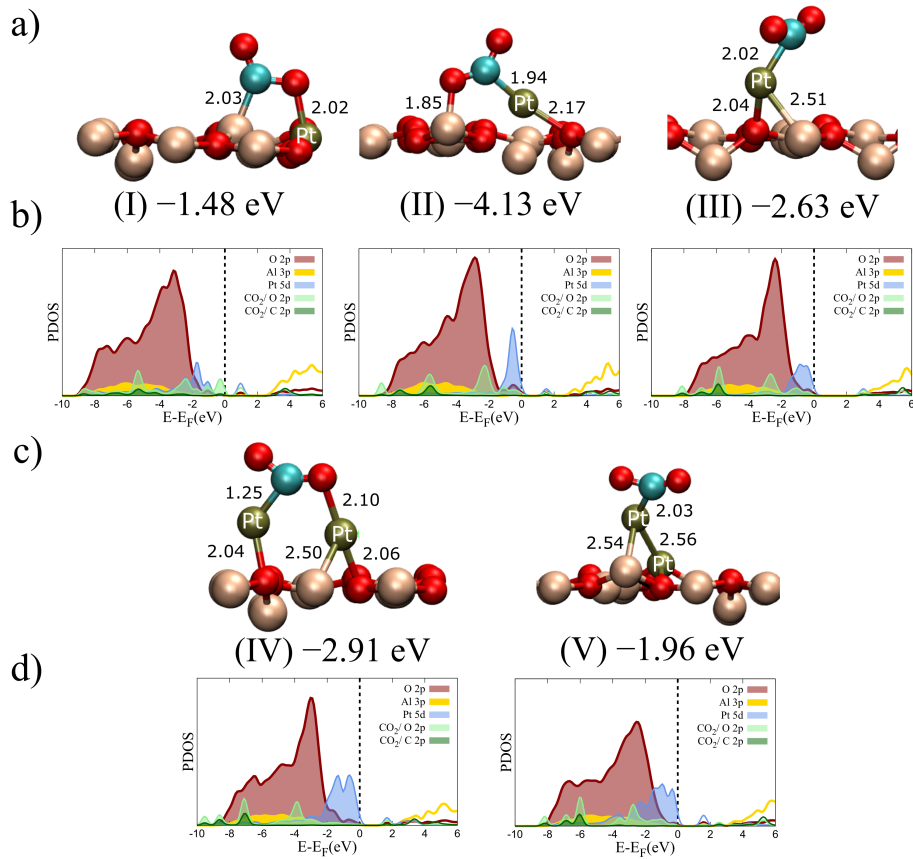


Figure 3.7: The side view of the most stable adsorption geometries with the adsorption energies and PDOS of CO₂ on γ -Al₂O₃(100) supported mono-atomic Pt (a)-(b) and di-atomic Pt₂ (c)-(d) clusters. Bond distances are in Å. White, red, cyan and dark green balls stand for Al, O, C and Pt atoms, respectively.

0 eV, for the supported diatomic Pt₂ cluster configurations this energy region was observed below the -4 eV, see Figure 3.7 (b) and (d). Overall, O p states and Pt d states hybridized between the energy range of -4 and the Fermi energy. In the case of adsorption CO₂, a small magnetization was observed in the range of 0.20-0.34 μ_B /cell.

3.3.3.3 Adsorption of H₂O

The optimized geometries of H₂O on supported mono-atomic Pt cluster are presented in Figure 3.8 with the adsorption energies. The molecular plane of H₂O molecule parallel to the γ -Al₂O₃(100) surface or having a certain tilted angle in the range of 9.6°-

Table 3.6: C-O bond distance, bond angle, partial Bader charges of CO₂ and Pt and shift of vibrational mode frequencies of adsorbed CO₂ molecule on γ -Al₂O₃(100) supported mono- and di-atomic Pt clusters. Distances are in Å and partial Bader charges in |e|. Vibrational frequencies are given in cm⁻¹. Vibrational mode frequencies are shifted by the value of $\nu_s=1312.9$, $\nu_a=2376.4$ and $\nu_b=634.0$ cm⁻¹ for the CO₂ in gas phase.

config.	d _[C-O]	ρ_{CO_2}	ρ_{Pt}	$\angle(C-O-C)$	$\Delta\nu_s$	$\Delta\nu_a$	$\Delta\nu_b$
I	1.22,1.38	1.29	-0.52	116.2	-144.3	-442.5	-21.6
II	1.30,1.24	0.97	-0.47	130.6	-102.5	-692.6	102.8
III	1.28,1.20	0.40	-0.04	145.1	-210.8	-438.8	-53.6
IV	1.25,1.25	0.50	0.02	140.2	-128.7	-648.5	-89.6
V	1.27,1.20	0.37	0.34	146.0	-198.8	-444.4	-65.4

20.3° with the surface. The most stable adsorption geometry is on top Pt although all three geometries identified in Figure 3.8 yield very close adsorption energies. We observed that the adsorption energies of the molecule compared to the adsorption energies on the bare surface increases around -0.8 eV with the metal atom. This enhancement is likely due to the increased charge transfer from the molecule to surface in the presence of the metal atom. For the all three configurations, the overlapping between the molecular states and Pt d orbital states was observed at around 2 eV above the Fermi level. This is also one reason why the adsorption energies are so close each other. The small differences in the adsorption energies can depend on the active sites of the surface with the position of the Pt atom on the surface. The H₂O adsorption geometries on the supported Pt₂ cluster tend to the H-dissociation as in the configurations III and V in Figure 3.9. The electron charge transfer from the H to Pt atom and lengthening of the O-H bond is particularly pronounced in config. III, which may also explain the higher adsorption energy. We have observed that the orientation of the H₂O molecule, in config. VII and VIII, shows a small effect on the adsorption energies of the molecule (around -0.07 eV difference) on the surface supported diatomic Pt cluster, see Figure 3.9 (c). An interesting phenomenon occurs in these configurations, however, where the adsorption of the H₂O molecule breaks the Pt₂ apart into its constituent Pt atoms. The molecule then sits on top of the elevated single Pt atom (see Figure 3.8) and acts much like H₂O molecules adsorbed on a single supported Pt atom. Before the relaxation of the molecule in the config. I, the molecule put on the surface nearby the Pt₂ cluster, and assumed a position straddling the cluster and

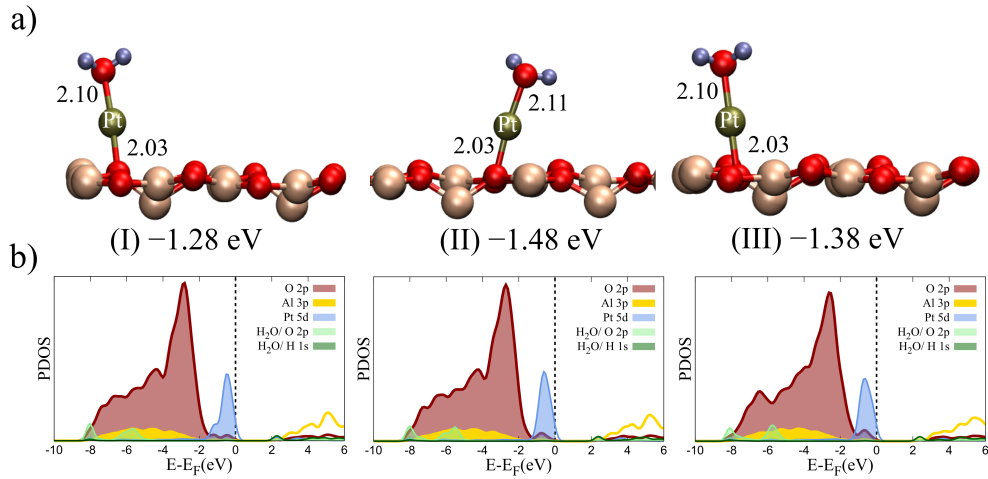


Figure 3.8: (a) The side view of the most stable adsorption geometries with the adsorption energies and (b) PDOS of H_2O molecule on $\gamma\text{-Al}_2\text{O}_3(100)$ surface supported mono-atomic Pt cluster. Bond distances are in Å. White, red, blue and dark green balls stand for Al, O, H and Pt atoms, respectively.

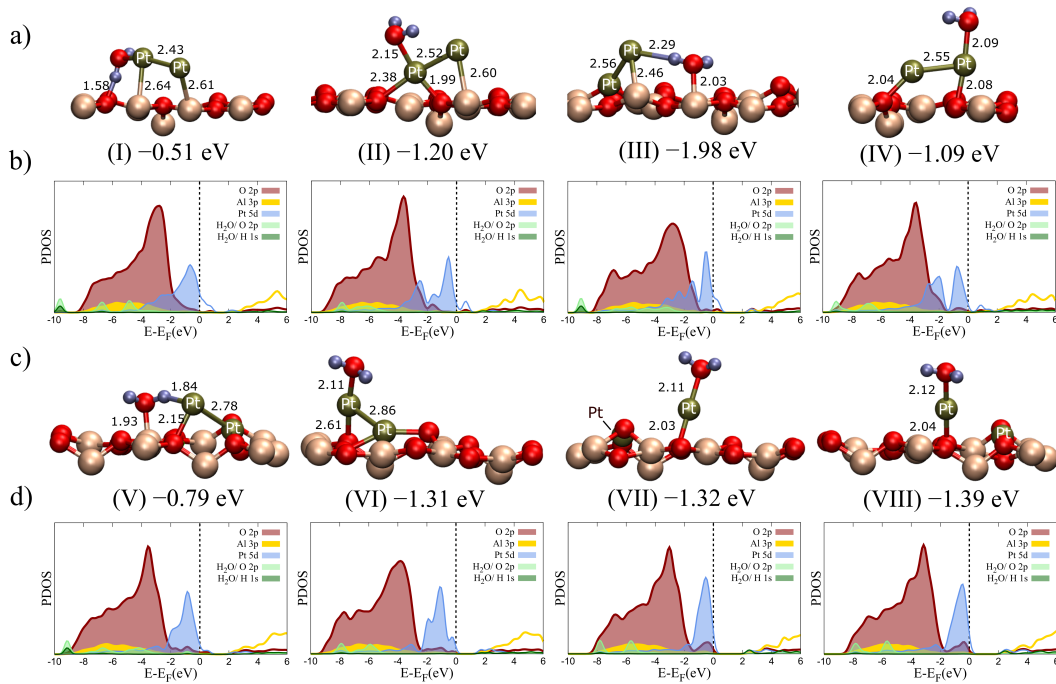


Figure 3.9: (a)-(c) The side view of the most stable adsorption geometries with the adsorption energies and (b)-(d) PDOS of CO molecule on $\gamma\text{-Al}_2\text{O}_3(100)$ surface supported di-atomic Pt_2 cluster. Bond distances are in Å. White, red, blue and dark green balls stand for Al, O, H and Pt atoms, respectively.

Table 3.7: O-H bond distance, bond angle, partial Bader charges of H₂O and Pt and shift of vibrational mode frequencies of adsorbed H₂O molecule on γ -Al₂O₃ supported mono- and di-atomic Pt clusters. Distances are in Å and partial Bader charges in |e|. Vibrational frequencies are given in cm⁻¹. Vibrational mode frequencies are shifted by the value of $\nu_s=3768.7$, $\nu_a=1566.8$ and $\nu_b=3892.4$ cm⁻¹ for the H₂O in gas phase.

	config.	$d_{[O-H]}$	ρ_{H_2O}	ρ_{Pt}	$\angle(H-O-H)$	$\Delta\nu_s$	$\Delta\nu_a$	$\Delta\nu_b$
H ₂ O + Pt	I	0.98,0.98	-0.11	0.34	107.0	-116.1	-48.3	-120.3
	II	0.98,0.98	-0.11	0.31	106.5	-99.1	-34.5	-108.4
	III	0.98,0.98	-0.11	0.29	106.0	-93.5	-34.5	-101.6
H ₂ O + Pt ₂	I	0.98,1.03	-0.09	0.40	108.7	-1008.6	-22.7	-106.1
	II	0.98,1.02	-0.06	0.62	104.9	-825.0	-22.7	-171.7
	III	0.98,1.02	0.14	0.71	106.8	-809.3	-36.7	-221.3
	IV	0.98,0.99	-0.09	0.65	106.4	-303.9	-43.0	-170.5
	V	0.98,1.12	0.28	0.50	105.6	-2127.0	-187.5	-169.3
	VI	0.98,1.00	-0.09	0.75	107.0	-393.0	-50.3	-133.8
	VII	0.98,0.98	-0.11	0.86	107.0	-95.3	-41.5	-103.4
	VIII	0.98,0.98	-0.11	0.85	106.7	-84.4	-26.6	-95.1

the surface with a Pt-O bond during the optimization of the system. This geometry is the least stable with the adsorption energy of -0.51 eV. In all on top Pt₂ adsorption geometries, config. II, IV and VI, we found similar adsorption energies and almost identical molecule-Pt₂ bond distances. In the adsorption of the molecule on Pt and Pt₂ clusters, the hybridization between the O p states and Pt d states (see Figure 3.9 (b) and (d)) are very low around the Fermi level, and the overlapping of molecular states and surface states with metal atom occurs above the Fermi level.

The Bader charge analysis shows a small charge transfer from the Pt atom to the molecule in all adsorption configurations, see Table 3.7. Depending on the adsorption geometries, the charge transfer may occur from the surface metal atom to the molecule on top Pt cluster geometries or from the molecule to the metal atom in the configuration of the molecule on top surface (config. III and V in Figure 3.9). This is totally related with the effect of the activation of Pt atom on the adsorption of the molecule. The vibrational frequencies for all geometries are calculated and shift of the vibrational frequencies with respect to the H₂O molecule in gas phase summarized in Table 3.7. The increases of the molecule angle and O-H bond distance can explain the changes in the characteristic vibrational frequencies of the molecule on top Pt geometries. Moreover, the interaction between the Pt₂ and H₂O in config. III

and V changes the vibrational mode frequencies of H_2O since the H-O bond distance are increase.

CHAPTER 4

STRUCTURAL AND ELECTRONIC PROPERTIES OF BULK AND LOW-INDEX SURFACES OF ZINCBLLENDE PLATINUM-CARBIDE

In this chapter we investigate structural, electronic and oxidation properties of the (100), (110) and (111) surfaces of zincblende (ZB) PtC. After reporting on the bulk properties of PtC where results obtained using our computational protocol are compared with published data, we proceed to discuss several aspects of the clean surfaces including relaxation patterns and the energetic cost of Pt and C vacancy formation. We found that the calculated vacancy formation energies indicate facile C removal on the PtC(111) surface which is an exothermic process while Pt-vacancy formation is endothermic. Finally, the energetics and thermodynamics of atomic oxygen adsorption on all surfaces were investigated, due to its relevance in many catalytic processes involving transition metal carbides (TMCs). We found that the atomic O adsorption energies on all surfaces reveal a high affinity of the C-terminated surfaces towards this species. Moreover, we perform a trend study to understand the nature of chemisorption on the surfaces considering the first- (H), second- (B, N and F) and third-period (Al and S) elements. This work was published as Sensoy M.G., Ustunel H., Toffoli D., "Structural and electronic properties of bulk and low-index surfaces of zincblende PtC", *J. Phys.: Condens. Matter*, 29, (2017), 125002 (11p).

4.1 Introduction

TMCs have attracted considerable interest from the scientific community in the recent years due to their desirable properties. In addition to uncovering their superior physical properties such as strength, remarkable machinable properties, high damage tolerance, metallic conductance [244, 245], a considerable amount of recent work

has concentrated on their catalytic properties [246–251]. TMCs are characterized by their hardness and strength along with high melting points [252, 253] due to the excess of electrons contributed to the chemical bonds by the metal. Bonding in TMC's is ordinarily of mixed character, simultaneously carrying signatures of covalent, ionic and metallic [254, 255]. For example, the covalent character manifests itself in the the directional bonds formed by the overlap of the C $2p$ orbital electrons and the metal (such as Ti, Pt) d electrons. The metallic character can also be observed because of the large electron density close to Fermi energy level [63]. In addition to applications requiring superhard materials, TMCs have potential as substitutes for precious metal catalysts because of similar catalytic behaviour compared with noble metals (Ru, Au, Pd, Ag, Ir, Pt, and Rh). However, kinetics and product selectivity of TMCs can be different depending on catalytic reaction pathway [249–251]. Recent experimental studies show that TMCs have efficient activity and stability in WGS reactions. Reactions catalysed by TMCs include CO-B-C-N-F-Cl-S-P-Si-O/TiC, CO-C₂H₆-benzene-methanol/Mo₂C, C₂H₄-C₆H₆-benzene-H-HF/SiC and H-Pd,Pt-CO₂/WC reactions [246, 247, 256–264]. Furthermore, some TMC clusters such as Metcars (M₈C₁₂) [250, 265–267] can show different reaction activity compared with TMCs surfaces [70, 246, 256–260, 268, 269]. However, using TMCs in catalytic reaction has some problems such as oxygen poisoning in reaction conditions. Overcoming these problems and understanding the WGS reaction mechanism are pivotal in the use TMCs in catalytic reactions efficiently.

In contrast to most of TMCs, the synthesis of PtC has proven rather challenging due to the high temperatures and pressures involved [270, 271]. PtC was successfully synthesized for the first time by Ono *et al.* [271] at high temperatures and pressures. It was initially identified as having a rocksalt (RS) structure. Later experimental studies pointed out that identifying the phase of RS is difficult based on the X-ray diffraction data due to the large discrepancy in mass between Pt and C atoms [255, 272]. The work by Li *et al.* [273] reported that the PtC in zincblende (ZB) phase is the stable phase of PtC at low temperature. As a result, the current consensus remains pinned to the ZB phase, which we use in this chapter. Many theoretical studies [274–279] based on DFT have been focused on the structural, elastic, electronic and vibrational properties of bulk PtC. However. the surface properties of PtC remain unexplored.

TMCs usually contain a mixture of different stoichiometries and are therefore likely to include Metal-C phases as well. The existence of a surface in the form of Pt_xC_y phase was showed in an early experimental study by Lambert *et al.* [280]. Additionally, a study by Harding *et al.* [281] reported the possibility of the small Pt_nC^+ ($n = 3 - 5$) clusters which can be a motivation to study the PtC surfaces.

4.2 Computational Details

All calculations are based on plane-wave, pseudopotential density functional theory (DFT) as implemented in the QUANTUM ESPRESSO code [163]. The generalized-gradient approximation (GGA) functional is used for the exchange-correlation functional developed by Perdew, Burke and Ernzerhof (PBE) [141, 230]. Local density approximation (LDA) [142, 282] was also used in the calculation of the bulk properties. Atomic pseudopotentials have been generated for Pt and C atoms by using the $6s^15d^9$ and $2s^22p^2$ atomic configurations, respectively. For the bulk calculations, Brillouin zone integrations were performed with a Monkhorst-Pack [233] mesh of $12 \times 12 \times 12$ while a cut-off energy of 40 Ry was used to truncate the basis-set expansion. Even though we focus on the ZB structure in our production calculations, in the initial, exploratory part of this chapter, we present the bulk properties of both the ZB and RS phases. The calculated bulk PtC lattice constants are 4.50 and 4.76 Å for the RS and ZB phases, respectively, in good agreement with the previous experimental and theoretical studies [272, 277, 278, 283]. The static bulk modulus B and the first-order pressure derivative of the bulk modulus B' have been obtained by means of a fit to the using Birch-Murnaghan equation of state [284]. Bulk cohesive energies were calculated in reference to isolated Pt and C atoms in a simulation cell box. Surface facets are generated by periodically repeated slabs with atomic positions that are obtained from the bulk, with the addition of some vacuum after each slab (12-13 Å). At least six atomic layers were used in all calculations depending on the surface facets. During geometry optimization, the bottom two layers are kept frozen completely in all surface facets. The smallest, 1×1 surface unit cell is constructed with 2 C and 2 Pt atoms on each layer. The larger super-cell is modeled 2×2 using a slab for the molecule adsorption study. A 30 Å cubic super-cell was used to calculate

the isolated energies of the species Pt, O, CO, CO₂ and H₂O. All atoms are located on the same plane for the PtC(100) and PtC(110) surfaces, while for the PtC(111) surface Pt and C atoms are spaced closely together, and are therefore considered to be the same layer. All calculations were spin-polarized.

The surface free energies of each surface were calculated as

$$\begin{aligned} E_{surf} &= \frac{1}{2A} [E_{slab} - n_C \mu_C - n_{Pt} \mu_{Pt}] \\ &= \frac{1}{2A} [E_{slab} - (n_{Pt} - n_C) \mu_C - n_{PtC} \mu_{PtC}] \end{aligned} \quad (4.1)$$

where E_{slab} is the total energy of a symmetric slab, n_{Pt} and n_C are the numbers of Pt and C atoms in the slab, respectively. μ_C , μ_{Pt} and μ_{PtC} are the chemical potentials calculated for the most stable phase of each species. A is the surface area of each slab.

The interlayer distances of the surface facets are calculated, and the percent difference of interlayer distances from the bulk value defined as

$$\Delta d = 100 \times \frac{d_n - d_{bulk}}{d_{bulk}} \quad (4.2)$$

in the direction of perpendicular to the surface plane. In Equation 4.2, $n = 1, 2, 3$ and d_{bulk} is the layer separation along the direction of interest. The interlayer distances are calculated for our largest slab, namely the slab with 12 layers.

Adsorption energies were obtained by subtracting the energies of the gas phase and surface species from the energy of adsorbed system by using the formula as given by Equation 3.2 in Chapter 3. The negative adsorption energies correspond to exothermic adsorption processes, and larger magnitudes correspond to more stable structures.

Adsorption energies for atomic O adsorption on the surfaces are referenced to an isolated O₂ molecule using the formula:

$$E_{ads}^n = E_{surf+O} - E_{surf} - \frac{n}{2} E_{O_2} \quad (4.3)$$

where E_{surf+O} is the total optimized energy of the surface slab with an adsorbed O

atom, E_{surf} is the energy of the bare surface, E_{O_2} is the energy of an isolated O_2 molecule, and n is the number of atomic oxygen on the surface.

In the calculation of the vacancy formation energies on the PtC(111) surfaces

$$E_{f,vac} = E_{surf+vac} + \mu_X^0 - E_{surf} \quad (4.4)$$

where X can be either Pt or C, $E_{surf+vac}$ is the total energy of the optimized slab with the Pt or C vacancy, E_{surf} is the total energy of the equivalent defect-free surface and μ_X^0 is the bulk chemical potential Pt or C atoms.

In order to understand the thermodynamic stability of oxide surfaces at different coverages, the surface free energies were calculated using the standard formula [285]:

$$\begin{aligned} \gamma(T, P) &= \frac{\Delta G(T, P)}{A} \\ &= \frac{1}{A} (E_{ads}^n - n\Delta\mu(T, P)) \end{aligned} \quad (4.5)$$

where n is the number of adsorbed oxygen on the surface, $\Delta G(T, P)$ is the surface Gibbs free energy, A is the surface area, E_{ads}^n is the calculated adsorption energy as given in Equation 3.2 and $\Delta\mu(T, P)$ is the temperature- and pressure-dependent chemical potential of molecular oxygen. With the zero pressure chemical potential as reference, $\mu(T, P)$ is calculated given by the expression,

$$\mu_O(T, P) = \mu_O(T, P^0) + \frac{1}{2}kT \ln\left(\frac{P}{P^0}\right) \quad (4.6)$$

where $\mu_O(T, P^0)$ is the chemical potential of oxygen at $P^0=1$ atm. and is taken from thermochemical tables [286]. In the adsorption Gibbs free energy calculations, the zero point vibrational energies were ignored due to the small contribution to the Gibbs free energy.

4.3 Results and Discussion

4.3.1 Bulk Properties of RS and ZB PtC

Previous experimental [271] and theoretical [274–279] studies proposed two possible structures of PtC, RS and ZB phases. The RS and ZB phase of PtC are presented in Figure 4.1. In RS phase of PtC Pt and C atoms form a separate face-centered cubic (fcc) lattice with the two inter-penetrating lattices in NaCl basis with the ions related by a $(0, 1/2, 0)$ displacement. In the ZB phase of PtC Pt and C atoms form two inter-penetrating fcc lattices related by a displacement of $(1/4, 1/4, 1/4)$. As an indicator of relative phase stability, the bulk energies were calculated as a function of primitive unit cell volume at zero temperature for two phases, see Figure 4.1. It is clear that the ZB PtC has a lower energy minimum which occurs at a larger lattice constant (Table 4.1) compared to the RS PtC. From the E-V plot, it is evident that the RS PtC structure is stable only under high pressure with respect to the ZB PtC.

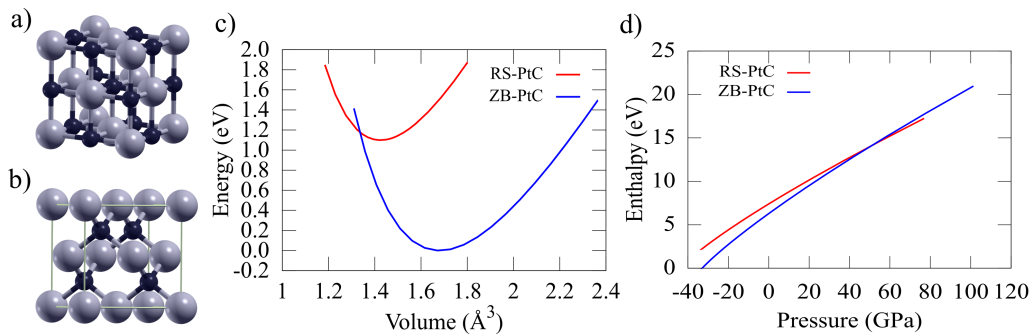


Figure 4.1: The unit cell of (a) RS and (b) ZB phase of PtC structures. (c) Calculated bulk energies as a function of primitive unit cell volume (d) Enthalpy as a function of pressure at zero temperature for RS and ZB phase of PtC. Gray and black balls stand for Pt and C atoms, respectively.

The energy band structures and PDOS are calculated for ZB and RS phase of PtC in Figure 4.2. For both phases, the bands cross the Fermi level that looks free electron like behavior along the high symmetry points. No energy gap has been observed in PDOS and energy band structures. This indicates the metallic characters of PtC structures. This metallic characters might make them good conductor under high pressure

and temperature conditions. The bands near the Fermi level and the valence band are formed mainly by Pt 5d orbitals in ZB PtC. The well-known mixed bonding character of TMCs is also seen in ZB PtC. The charge transfer of $0.6 |e|$ from Pt to C atom is an evidence for the ionic character of the structure. At the same time, it is clear that the ZB PtC is metallic as seen from the mixture of Pt d and C p states around the Fermi energy level (in the PDOS plot, Figure 4.3). Furthermore, this mixture of the Pt d and C p orbital states are indicate a strong covalent bonding between Pt and C atoms.

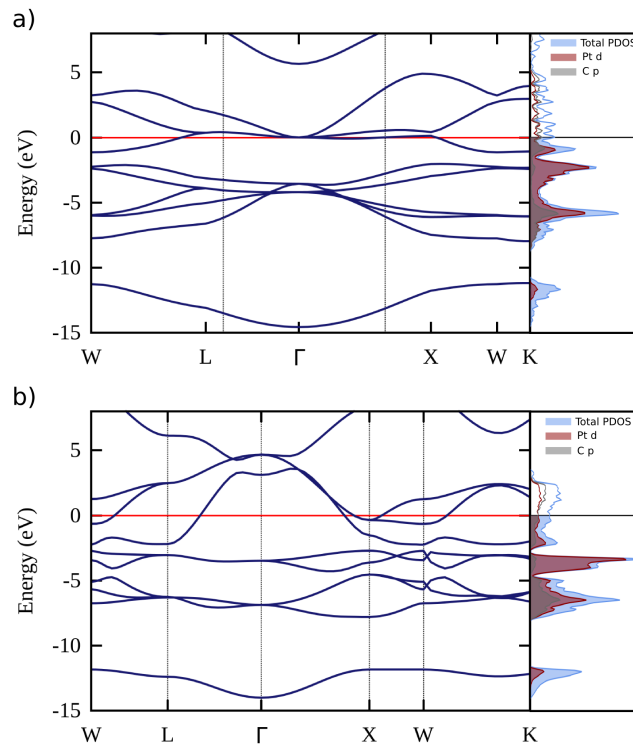


Figure 4.2: Band structures with PDOS profiles of bulk (a) RS and (b) ZB PtC.

We have also seen a pseudogap at around -2.5 eV presented in a previous study by Yang *et al.* [287] for many TMCs is also observed for ZB PtC PDOS. The metallicity of a metal carbide may be correlated to the number of occupied states between the pseudogap and the Fermi energy level as argued in the previous work by Yang and Gao [287]. Since the observed pseudogap is at a relatively lower energy, the structure likely displays higher metallicity. Because of these reasons and the nature of the hardness in a material related with the directional covalent bonds [287, 288], the ZB

PtC is softer than the majority of TMCs. However, the bulk modulus value of ZB PtC is still comparable to hard materials such as BN, for which $B=378$ GPa [289].

Table 4.1 reports the calculated LDA and GGA values for various structural and elastic parameters along with previous theoretical values from the literature. For the sake of completeness, PtC properties in the RS phase were also included with the corresponding values reported in the literature. Our calculated lattice constant values are in good agreement with the ones given in previous studies [272, 277, 278, 283].

Table 4.1: Lattice constants, bulk modulus, pressure derivatives of the bulk modulus, and cohesive energies of the RS and ZB phase of PtC.

	RS PtC				ZB PtC					
	GGA	Ref. [277]	LDA	Ref. [272]	GGA	Ref. [283]	LDA	Ref. [278]	HSE06	B3LYP
a_0 (Å)	4.501	4.490	4.413	4.425	4.755	4.760	4.664	4.687	4.680	4.750
B (GPa)	246.4	267.4	305.6	316	202.7	208.4	246.6	270	238.2	204.5
B'	5.25	5.25	5.21	4.89	5.06	-	4.91	3.92	4.83	4.86
E_c (eV/atom)	11.79	-	14.44	-	12.90	-	15.48	14.85	-	-

However, the bulk modulus with GGA is underestimated with respect to the experimental value of 301 GPa [271], while the LDA value is much closer. This is a well-known shortcoming of the GGA approximation reported previously in literature [290]. On the other hand, the computed GGA and LDA values of B' match with the experimental value [271]. Additionally, the structural parameters for both phases were calculated with hybrid B3LYP [144, 291] and HSE06 [146, 147, 292, 293] exchange-correlation functionals using the Vienna Ab Initio Simulation Package (VASP) [164, 165, 294, 295], and the results are presented in Table 4.1. The agreement between the GGA and hybrid exchange-correlation results point towards its reliability.

The phonon dispersion relation and the phonon density of states (PHDOS) of the ZB phase of PtC are presented in Figure 4.3. Previous theoretical studies [273, 283, 296] show that the RS phase of PtC has complex frequencies, which indicates structural instability. Moreover, in the current study, surface slabs for the RS PtC were found to cleave into layers in this phase during geometry optimization, and the calculated surface free energies are found to be negative. For these reasons, the unstable nature

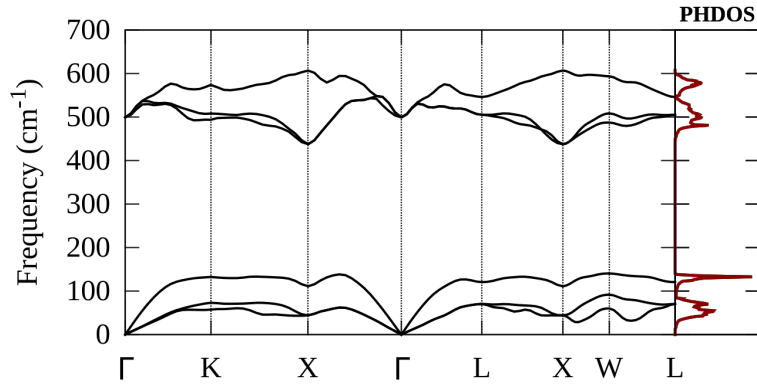


Figure 4.3: The phonon dispersion relation and phonon density of states (PHDOS) for bulk ZB PtC. Energies are shifted to the Fermi energy level.

of the RS structure was therefore verified and will no longer be considered in the following part of the study.

4.3.2 Surface Properties of ZB PtC

4.3.2.1 ZB PtC(100) Surface

The (100) surface of ZB-PtC in Figure 4.4 retains the primitive (1×1) periodicity and each atom is four-fold coordinated. The PtC(100) surface is polar and offers two possible terminations. Both surfaces show inward relaxation upon geometry optimization. The interlayer distances display an oscillatory behavior for C- and Pt-terminated surfaces, see Figure 4.4. For the C-terminated surface, the distance between the top layer and the layer below (d_1) is the largest which is smaller than the bulk separation of $d_0=1.2 \text{ \AA}$. The next interlayer distances are slightly smaller than d_0 by about 0.2% and 0.6% smaller for the d_2 and d_3 , respectively. For the Pt-terminated surface the distance d_1 is smaller than d_0 by about $\sim 14\%$ which reduces rapidly moving bottom layers into the crystal. While the bond length between the outermost Pt and C atoms is 1.95 \AA due to the inward relaxation, Pt-C bond length is 2.06 \AA in the sub layers. The resulting PDOS upon geometric optimization are presented in Figure 4.5 with the surface charge density. In the PDOS of bulk ZB PtC displays predominantly Pt

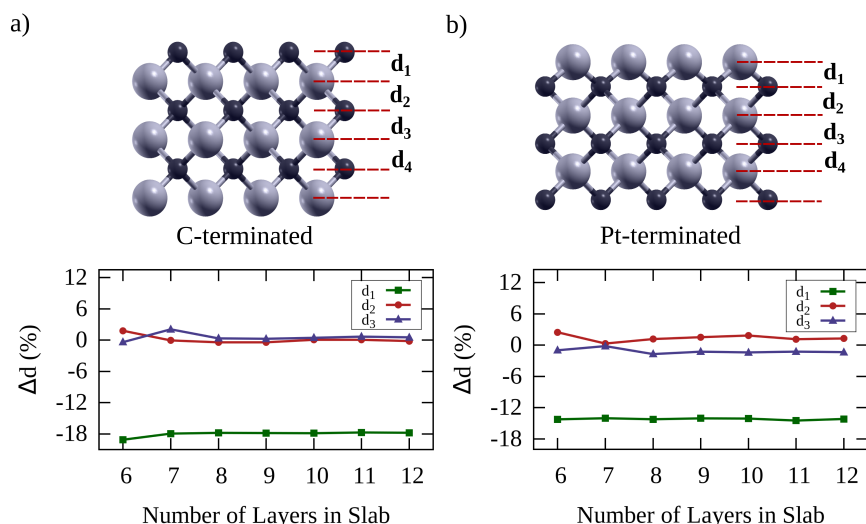


Figure 4.4: The side views and the relaxation patterns of (a) C-terminated and (b) Pt-terminated ZB PtC(100) surfaces. Small black and larger gray balls represent C and Pt atoms, respectively. For each surface, the per cent difference of interlayer separation from the bulk value (Δd) along the direction of interest is displayed as a function of increasing layer number in the slab model.

5d character with some hybridization with C 2p states. Retaining the high symmetry of the surface, the surface remains in bulk like geometry, and the absolute value of surface energy of the PtC(100) is relatively higher compared to the other surface facets. The Pt p and C p σ bonds can be seen easily in the surface charge distribution contour plot, see Figure 4.5 (b).

We also performed the Bader charge analysis to see the charge distribution after geometric optimization of both surfaces which are 1×1 simulation cells with 12 layers. We found the electron transfer from the top layer atoms to the second top layer atoms, see Figure 4.6. The inner layers do not vary appreciably in terms of partial charges. This is consistent with the aforementioned interlayer distance pattern.

4.3.2.2 ZB PtC(110) Surface

The stoichiometric ZB PtC(110) surface, see Figure 4.7, is nonpolar, and it has no different termination. Similarly to the PtC(100) surface, an inward relaxation has been observed upon geometric optimization. The top layer relaxes inwards where d_1

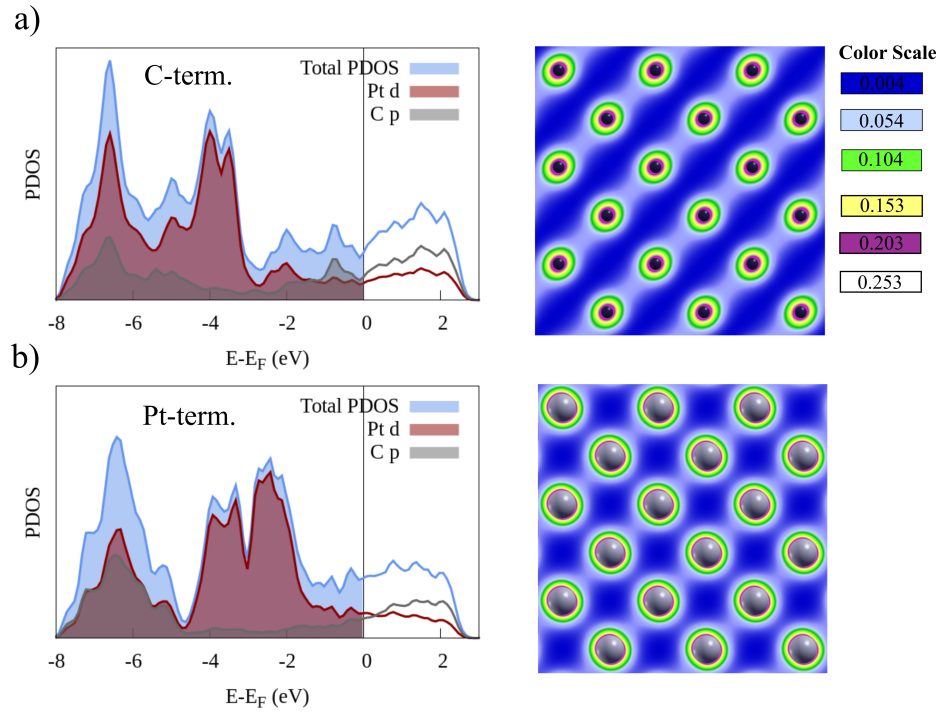


Figure 4.5: PDOS and surface charge density contour plots for (a) C- and (b) Pt-terminated ZB PtC(100) surfaces

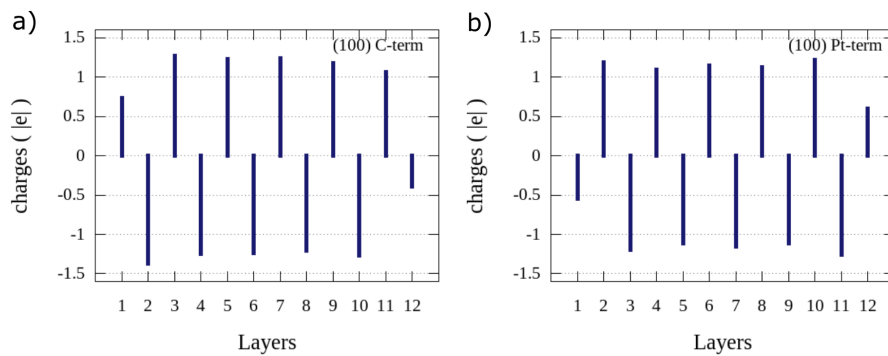


Figure 4.6: Bader charge analysis of each interlayer for C- (a) and Pt-terminated (b) ZB PtC(100) surfaces.

is $\sim 8\%$ smaller than the bulk interlayer distance of $d_0 = 1.7 \text{ \AA}$. The relaxation pattern of the subsequent layers is similar to the PtC(100) surfaces. The outermost Pt and C atoms are three fold coordinated, while the interlayer atoms are four fold coordinated. The surface Pt atoms show outward relaxation about 0.02 \AA , but four fold coordinated

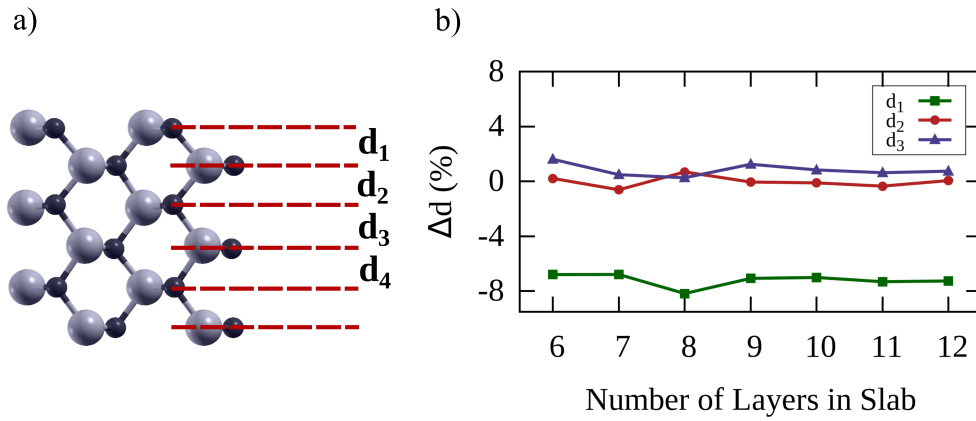


Figure 4.7: (a) The side view and (b) the relaxation patterns of the ZB PtC(110) surface. Small black and larger gray balls represent C and Pt atoms, respectively.

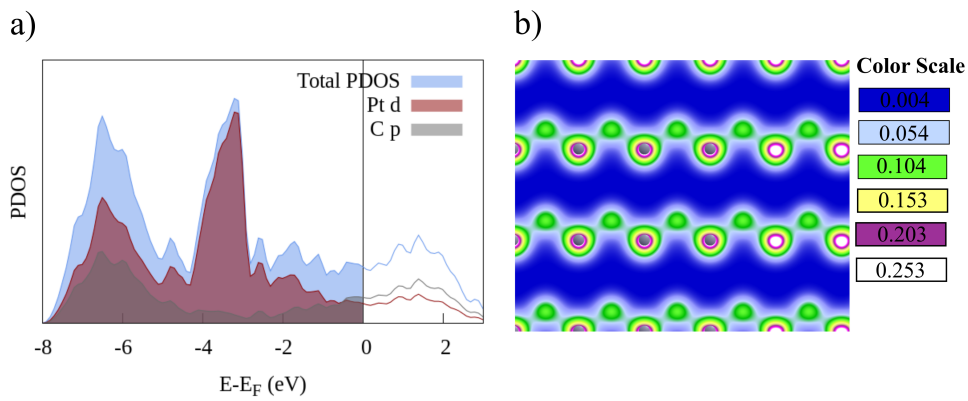


Figure 4.8: (a) PDOS and (b) surface charge density contour plots for ZB PtC(110) surface

Pt atoms relax inward about 0.13 Å. The Pt-C bond length of the bottom layer atoms is about 2.06 Å while the surface Pt-C bond is 1.98 Å due to the inward relaxation of the surface atoms. The inter-atomic layer distances do not change with respect to the different number of layers as well as seen in PtC(100) surface, see Figure 4.7.

The per cent difference of interlayer separation from the bulk value (Δd) along the direction of (110) is displayed as a function of increasing layer number in the slab model. The Δd values show nearly same trend (see Figure 4.7) with increasing the number of layer along the (110) direction. The PDOS and the surface charge density contour plots are displayed in Figure 4.8. As in the PtC(100) surface, the

PtC(110) surface shows predominantly Pt 5d character with some hybridization with C 2p states. Valence band shows dominantly d-orbital character, and there is no gap at the Fermi level, see Figure 4.8. The flat character as seen in bulk ZB PtC structure is not observed along the PtC(110) surface. The surface channels along the y-direction can be easily seen on the surface charge distribution plot.

The Bader charge analysis was also performed, and we found that a charge transfer, $\sim 0.2 |e|$, occurs from the surface Pt atom to the C atom. The interlayer Bader charge distribution plot shows that the large amount of charges transferred to the top surface layer atoms as may be a stabilization of the interlayers of the structure upon geometric optimization, see Figure 4.9.

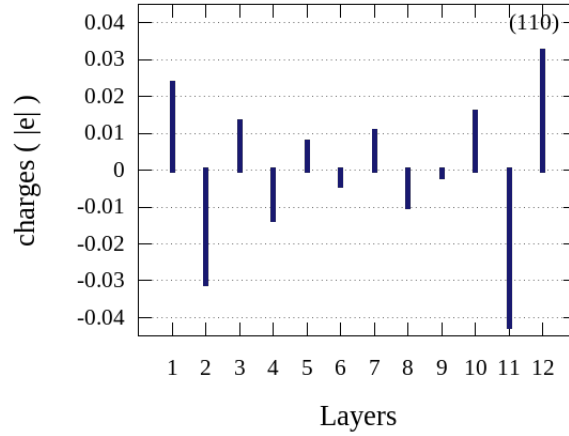


Figure 4.9: Bader charge analysis of each interlayer for ZB PtC(110) surface.

4.3.2.3 ZB PtC(111) Surface

Both terminations of the ZB PtC(111) surface reveal an inward relaxation, much milder than those of the PtC(100) and PtC(110) surfaces. d_1 is only $\sim 1.6\%$ and $\sim 1\%$ smaller than d_0 for the C- and Pt-terminated surfaces, respectively. In absolute distance terms, while the inward relaxation of the top layer is between 0.12 and 0.22 Å for the PtC(100) and PtC(110) surfaces, it is less than 0.05 Å for the PtC(111) surfaces. This behavior can be understood by recognizing that d_0 along the $\langle 111 \rangle$ direction is 2.7 Å, much larger than the interlayer bulk distance for the two other surfaces. The smaller interactions between the interlayers can be seen as a result of the

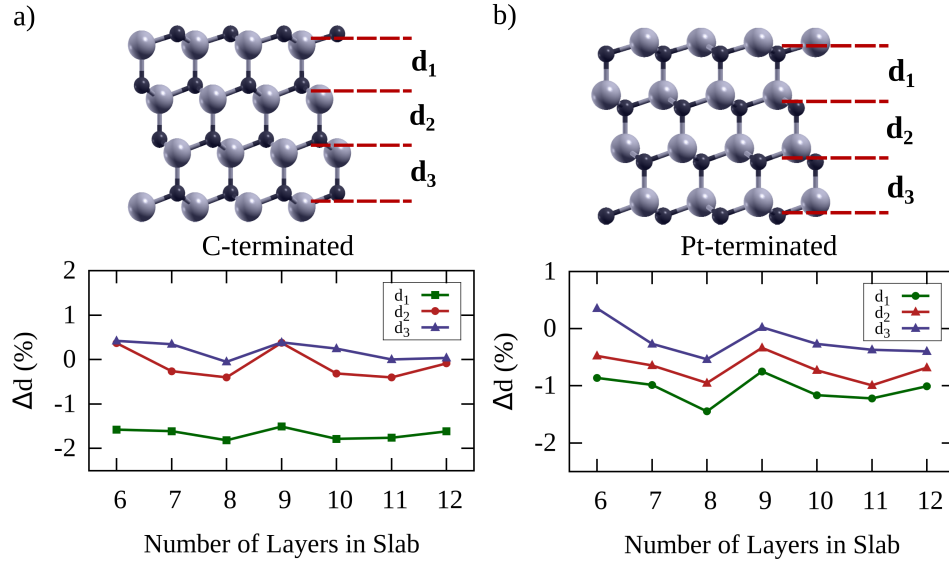


Figure 4.10: The side views and the relaxation patterns of the C- (a) and Pt-terminated (b) ZB PtC(111) surfaces. Small black and larger gray balls represent C and Pt atoms, respectively.

large interlayer distance.

The PDOS plots show almost identical character for both terminations. While the peaks below the Fermi level have a predominantly Pt 5d character, a hybridization of d and p orbital states of Pt and C atoms can be seen above the Fermi level, see Figure 4.11. The hexagonal atomic ordering can be easily seen from the surface charge density contour plots for C-terminated surfaces. However, the surface atoms shows a triangular atomic arrangement for the Pt-terminated surface due to the existing of the heavier atoms (Pt) at the top of the surface layer.

The interlayer Bader charge distribution is given in Figure 4.12 for both terminations. Same as PtC(110) surface, the charge distribution at the bottom layers are compensating each other upon geometric optimization of both surfaces.

The free surface energies of all surfaces are calculated using 12-layer, symmetric slabs with the middle two layers fixed. The surface energy calculations were carried out using the expression in Equation 4.1. The calculated surface free energies (see Figure 4.13) are given as a function of chemical potential of free C atom. In the case of the ZB PtC(111) surface, Equation 4.1 gives the sum of two different surfaces;

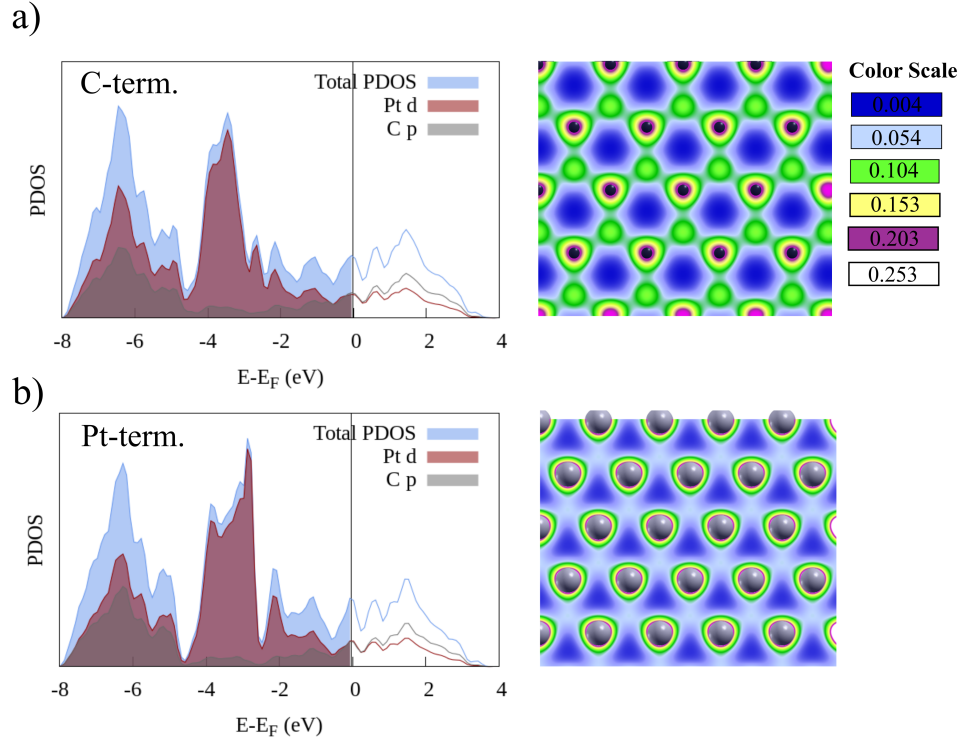


Figure 4.11: PDOS (left panel) and surface charge density contour (right panel) plots for (a) C- and (b) Pt-terminated ZB PtC(111) surfaces

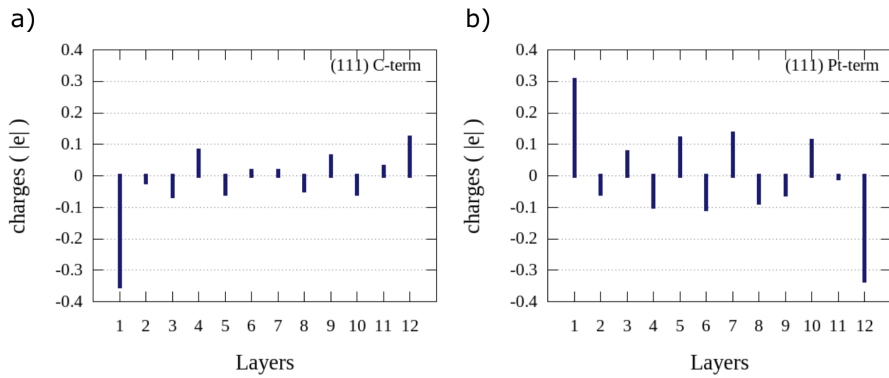


Figure 4.12: Bader charge analysis of each interlayer for (a) C- and (b) Pt-terminated PtC(111) surfaces.

however, we included it as a guide. While the stoichiometric ZB PtC(110) surface and the C-terminated surfaces yield reasonable results, the surface energies for the Pt-terminated surfaces are negative. Previously, one negative surface energy was reported for a ZB CuI surface, very similar to the structure studied in this part of the

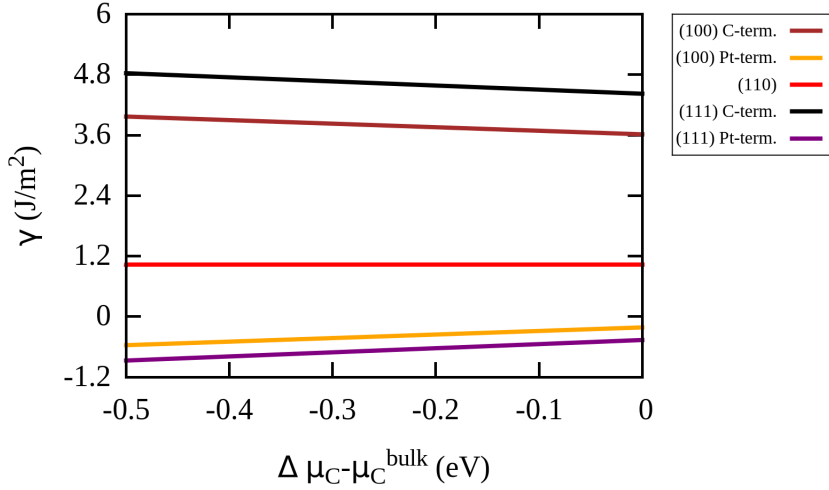


Figure 4.13: Surface free energies (γ) as a function of the chemical potential of C atom (μ_C) for ZB PtC(100), PtC(110) and PtC(111) surfaces.

study [297], however, not many similar examples were found elsewhere in the literature. As a result of our findings, the C-terminated surfaces are more stable than the Pt-terminated surfaces.

In order to stabilize the ionic crystals against structural instability [298, 299], the polar surfaces undergo charge transfers. In the case of the ZB PtC(100), PtC(110) and PtC(111) surfaces, the Bader charges of the top layers are reported in Table 4.2. The charge transfer occurs to reduce the dipole moment of the surfaces upon geometric optimization. In spite of this transfer, we have found a nonzero electric field in the vacuum region between the two periodic images along the perpendicular to the surface. In order to calculate the work functions of the surfaces, an opposing electric field was applied to the vacuum region as a correction on the vacuum potential [300]. This corrected vacuum potential was used to calculate the work function, Φ , which is the minimum energy needed to remove an electron from the bulk of a material through a surface to a point outside the material. From the point of view of both magnitude and variation between crystallographic directions, the ZB PtC work functions are similar to noble metals (Au, Pd, Pt), which are on the higher end of the spectrum of all the metallic work functions, see Table 4.2. A previous DFT study by Hugosson *et al.* [301] reported that the calculated work functions of the PtC(100) surfaces of metal carbides in the RS phase extend from 3.95 eV (NbC) to 5.57 eV (PdC). In the

Table 4.2: Bader charges of Pt and C atoms on the top layer for the ZB PtC(110) surface and the top two layers for the ZB PtC(100) and ZB PtC(111) surfaces. The work function, Φ , is also reported.

Surface	ρ_{Pt} ($ e $)	ρ_C ($ e $)	Φ (eV)
(100) Pt-term.	0.27	-0.59	5.49
(100) C-term.	0.68	-0.37	5.41
(110)	0.48	-0.51	5.18
(111) Pt-term.	0.43	-0.58	5.33
(111) C-term.	0.66	-0.48	5.26

study of surfaces, non of them were found to be magnetic.

The possibility of surface reconstruction patterns have been explored for all studied surfaces such as dimerization [261], however, all initially reconstructed surfaces were observed to revert to the bulk structure upon geometry optimization. As a result, we conclude that no small-scale reconstructions are seen on the PtC surfaces under investigation.

4.3.3 Vacancies on C- and Pt-terminated ZB PtC(111) Surfaces

In any realistic experimental scenario, surface vacancies are a commonly observed phenomenon [78–80]. In catalytic processes in particular, they are vital to the enhancement of the activity of the surface. to increase the surface activation during the catalytic processes. For this reason, the calculation of vacancy formation energies can be important in assessing the potential of a surface as a catalyst. In order to assess the likelihood of vacancy formation on the PtC surfaces, the surface vacancies are created by removing a C atom from the C-terminated ZB PtC(111) surface, while a Pt atom removed from the Pt-terminated surface. The vacancy formation energies were calculated in a 2×2 asymmetric surface slab of the ZB PtC(111) surface with 6 layers. The calculated vacancy formation energies are -2.42 and 1.82 eV, for the C and Pt vacancies, respectively. The surface charge density map and PDOS plots are shown in Figure 4.14.

After geometric optimization of the C-terminated surface upon the removal of surface C atom, the surface neighbouring atoms are slightly rearranged, and the Pt-Pt distance

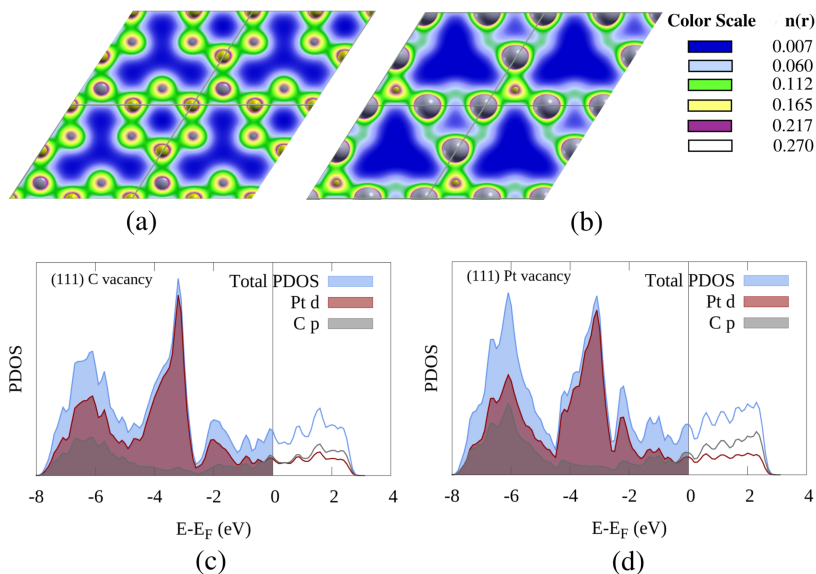


Figure 4.14: Charge density profiles and PDOS plots of (a)-(c) the C vacancy on C-terminated ZB PtC(111) surface and (b)-(d) the Pt vacancy on the Pt-terminated ZB PtC(111) surface.

are shortened about 1.8% with respect to the defect free surface. In contrast to this mild reconstruction, in the case of the Pt vacancy, the surface neighboring atoms are significantly displaced by about 14%.

As concerns the PDOS plots, Pt and C vacancies both have very similar profiles (Figure 4.14 (c) and (d)). The peaks in valence band are still significantly shown Pt d orbital character. The peaks at the Fermi level have a stronger C p orbital character than Pt d orbital for the Pt vacancy. However, the unoccupied states are an equal mixture of the C p and Pt d orbital states for the C vacancy.

4.3.4 Adsorption Properties on ZB PtC(100), PtC(110) and PtC(111) Surfaces

In this part of the study, we present the surface adsorption characteristics of atomic O, which is ubiquitous in industrially important reactions, either directly among the reactants or as a part of the environment [36, 302, 303]. Furthermore, to understand the nature of chemisorption a broader range of species that could be relevant for catalysis, a large survey was conducted where adsorption of Al, B, F, H, N and S atoms is considered in Section 4.3.4.2.

4.3.4.1 Oxidation Behavior of ZB PtC(100), PtC(110) and PtC(111) Surfaces

For the studied surfaces, several high-symmetry adsorption sites are considered, and the most stable geometries of atomic O are presented in Figure 4.16-4.18. In this part of the study, rectangular surface slabs were used in the oxygen adsorption calculations. The size of unit cells were chosen to be large enough to minimize the lateral interaction between the adsorbed O with closest lateral O-O distances of 9.52 Å, 6.73 Å and 6.73 Å for the ZB PtC(100), PtC(110) and PtC(111) surfaces, respectively. In the present work, the stable adsorption configurations in our calculations are identified as *on-top*, *bridge* and *hollow* as seen in Figure 4.15.

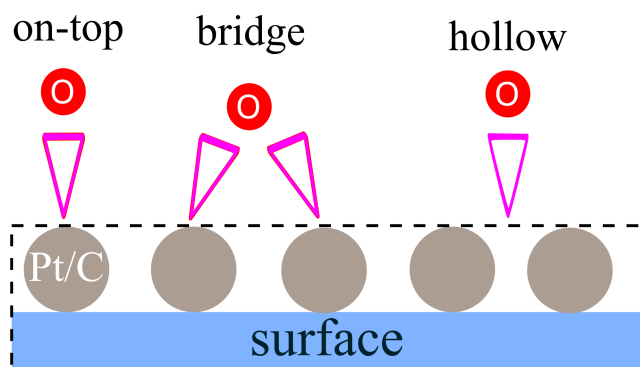


Figure 4.15: A schematic representation of the stable adsorption configurations which are identified as *on-top*, *bridge* and *hollow* on PtC(100), PtC(110) and PtC(111) surfaces.

Some of the O adsorption energies calculated by using the molecular oxygen (O_2) turn out to be positive, which appears to indicate an endothermic adsorption process. However, the actual reaction energy can only be determined with an appropriate minimum energy path calculation. All adsorption energies would appear to have an extra stability of -3.28 eV, if the atomic O were taken as a reference. In this part of the study, we report positive adsorption energies as well as negative ones. While the O atom is bonded to a single surface atom in the on-top configurations, it is suspended between two surface atoms in the bridge geometry. In the case of the hollow adsorption geometry, the O atom is suspended above the surface voids, see Figure 4.15. The calculated adsorption energies, Bader charges of atomic O, and structural properties of initial and optimized final configurations are summarized in Table 4.3. All other

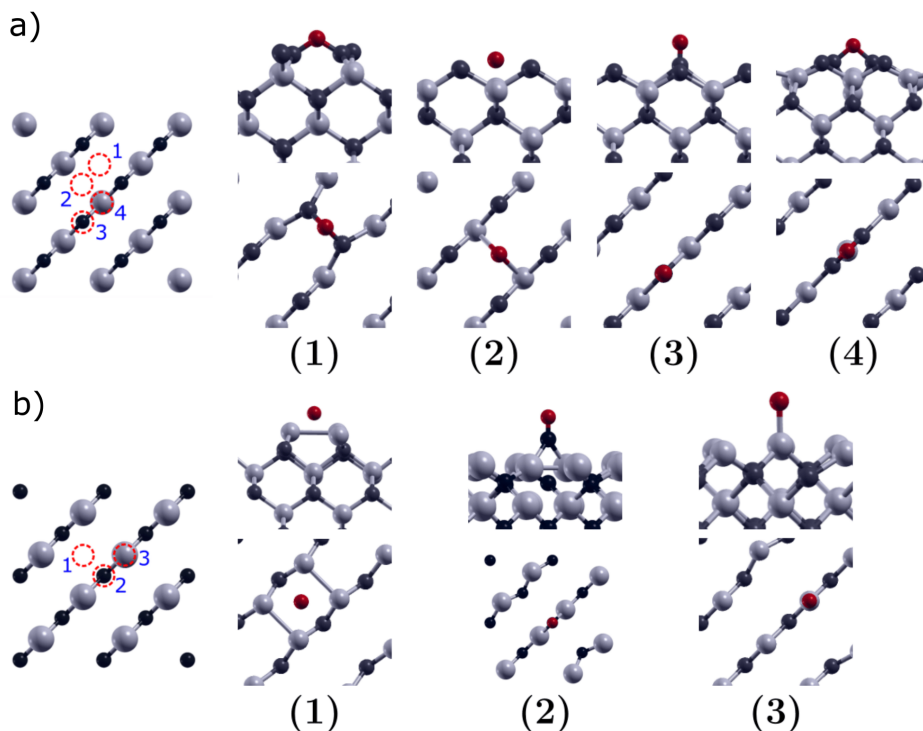


Figure 4.16: Atomic O adsorption on the (a) C- and (b) Pt-terminated ZB PtC(100) surfaces. For each termination, initial adsorption configurations (red circles) are indicated in the leftmost scheme with numbers. Red, black and gray spheres represent O, C and Pt atoms, respectively.

initial configurations explored were found to converge to one of the final configurations presented here. Our results show that the formation of C–O bonds are clearly preferred over Pt–O bonds in the adsorption of the O on studied surfaces resulting in the higher adsorption energies. As an example to this, the calculated adsorption energy of atomic O on C-terminated ZB PtC(100) surface is found -4.59 eV which is the most favorable adsorption configuration (confg. 3). However, the adsorption energy is calculated as -0.09 eV in the *on-top* configuration (confg. 3) on Pt-terminated PtC(100) surface, see Figure 4.16 (b). The on-C configuration is followed by C-C bridge configurations (confg. 1 and 4) in stability, shown in Figure 4.16. In the adsorption of O on C-terminated PtC(100) surface, we also observed a large O-induced reconstruction in surface C atoms (confg. 1 and 4).

A similar trend is seen on the non-polar ZB PtC(110) surface, and the calculated adsorption energy of the most favorable geometry is calculated as -4.13 eV. The dif-

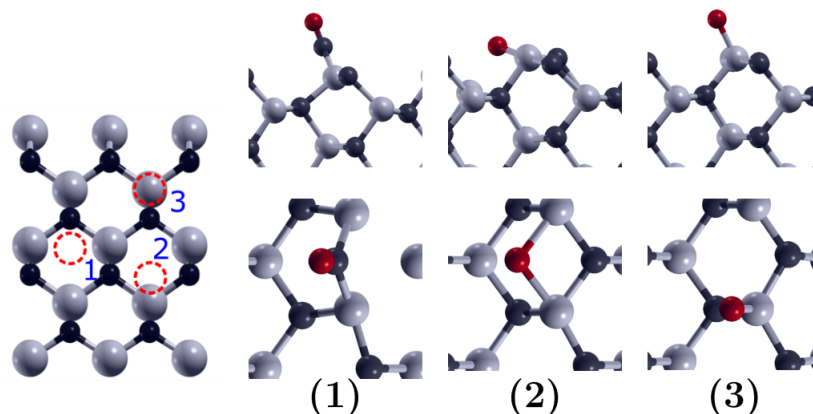


Figure 4.17: Atomic O adsorption on the ZB PtC(110) surface. For each termination, initial adsorption configurations (red circles) are indicated in the leftmost scheme with numbers. Red, black and gray spheres represent O, C and Pt atoms, respectively.

ference is found to be about 4.8 eV between the adsorption energies (see Table 4.3) of the config. 2 and 3 in Figure 4.17 where the O atom is attached to the Pt and the C atoms. For config. 1 the adsorption is accompanied by the rupture of a Pt-C bond, and this is reflected in the magnitude of the adsorption energy.

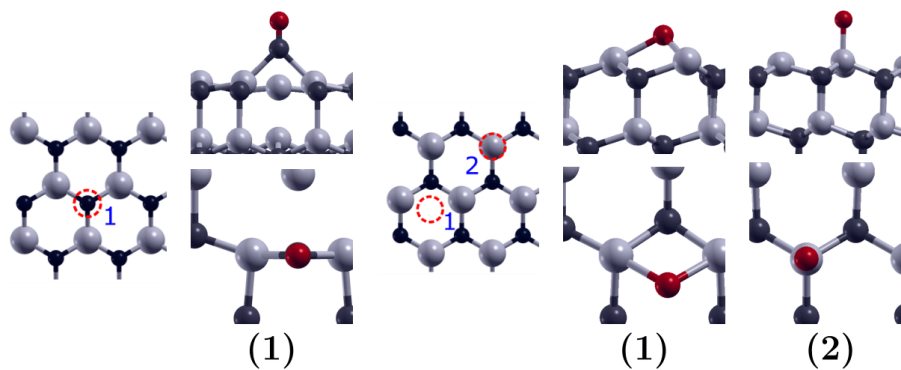


Figure 4.18: Atomic O adsorption on (a) C- and (b) Pt-terminated ZB PtC(111) surfaces. For each termination, initial adsorption configurations (red circles) are indicated in the leftmost scheme with numbers. Red, black and gray spheres represent O, C and Pt atoms, respectively.

In the case of atomic O adsorption on ZB PtC(111) surface, the strong interaction was seen between the adsorbate and surface C atom in C-terminated ZB PtC(111) surface, see Figure 4.18. In this configuration, the oxygen atom causes the C atom on the top

Table 4.3: Adsorption energies (E_{ads}), oxygen partial charges (ρ_O) and descriptions of the initial and optimized geometries of the adsorption configurations presented in Figures 4.16, 4.17 and 4.18. The numerical codes in the initial configurations column correspond to the locations shown in the corresponding figures.

Surface	E_{ads} (eV)	ρ_O ($ e $)	Initial	Optimized
PtC(100) C-term.	-2.18	-2.0	(1) C-C bridge	C-C bridge
	1.21	-0.7	(2) Pt-Pt bridge	Pt-Pt bridge
	-4.59	-1.9	(3) On C	On C
	-3.47	-1.9	(4) C-C bridge	C-C bridge
PtC(100) Pt-term.	-0.67	-0.9	(1) C-C bridge	Hollow
	-4.53	-1.9	(2) Pt-Pt bridge	On C (from lower layer)
	-0.09	-0.7	(3) On Pt	On Pt
PtC(110)	-0.10	-0.8	(1) Pt-Pt bridge	On detached C
	-4.13	-1.9	(2) C-C bridge	Pt-Pt bridge
	0.71	-0.7	(3) Hollow	Hollow
PtC(111) C-term.	-3.75	-1.9	(1) On C	On detached C
PtC(100) Pt-term.	-0.47	-0.8	(2) Pt-Pt bridge	Pt-Pt bridge
Pt-term.	0.74	-0.7	(3) On Pt	On Pt

layer to detach upon adsorption of the atomic O. This is also seen in the adsorption of O on Pt-terminated ZB PtC(100) surface (config. 2). All adsorption energies and Bader charges are summarized in Table 4.3.

All of these observations support the finding regarding the relative facility of the formation of the C vacancy on ZB PtC(111) surface. A reasonable conclusion is that, PtC surfaces would likely act as C donors. This immediately raises the question of the stability of these surfaces in ambient oxygen and under realistic thermodynamic conditions. The Bader charge analysis also supports the difference in the adsorption of O on Pt and C on all surfaces. The partial Bader charge in all adsorption configurations with a C-O bond is found in the range of -1.8 and $-2.0 |e|$. However, a Pt-O bond can be characterized by an excess of charge on O in the range of $-0.7 |e|$ to $-0.9 |e|$.

The stability of oxidized surfaces are therefore tested by using atomistic thermodynamic DFT method for the C-terminated ZB PtC(100) surface due to some uncertainty in the stability of the C-terminated surfaces. This calculation was performed by calculating the temperature- and pressure-dependent surface Gibbs free energy at

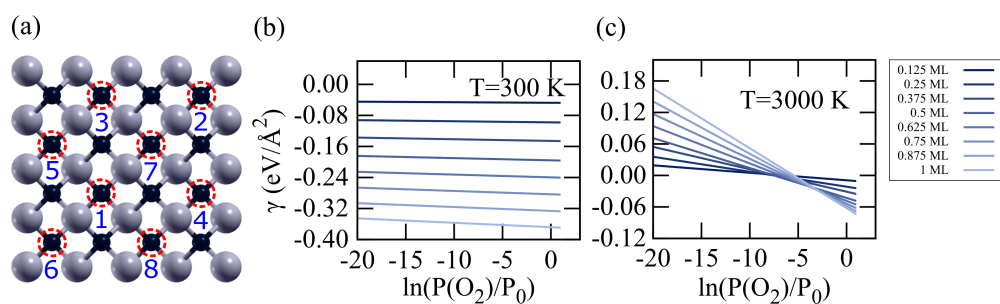


Figure 4.19: (a) The locations of the adsorption sites. The surface Gibbs free energy of adsorption per area of the C-terminated ZB PtC(100) surface at (b) T = 300 K and (c) T = 3000 K

different O coverages by taking 2×2 slab of C-terminated ZB PtC(100) surface. The corresponding O coverages are in the range of 0.125 monolayer (ML) to 1 ML depending on the number of adsorbed O on the surface. The O atoms were placed only on the on-top C sites since they were previously identified as the most stable adsorption configuration. The subsequent atoms following the first oxygen were placed on C sites so as to leave the maximum possible distance from the already adsorbed O atoms. The order of the adsorption sites of atomic O on the surface are presented in Figure 4.19. The calculated adsorption energy per O atom remains in the range between -4.7 and -4.5 eV. The Gibbs free energies are calculated for each O coverages at 300 K and 3000 K, and the surface Gibbs free energy of adsorption per area of the C-terminated ZB PtC(100) surface are plotted for various coverages, see Figure 4.19. The C-terminated ZB PtC(100) surface is stable at higher O coverages at 300 K and all pressure. At higher temperature, of around 3000 K, the surface is only stable at relatively high pressure values in the range of 10^{-5} - 10^0 atm. However, the surface at lower O coverage region become stable only at pressure values as low as 10^{-15} atm. In the stoichiometric ZB PtC(110) and C-terminated ZB PtC(111) surfaces, the C atom was found to detach from the surface upon adsorption of the O atom. Therefore, the stability calculation by using atomistic thermodynamic method for these surfaces was not performed. We also studied the adsorption of atomic O on the C-terminated ZB PtC(111) surface in the presence of the C vacancy. Three different adsorption configurations are considered as *on the vacancy* (see Figure 4.20 and 4.21), *on-Pt* and *on-C*.

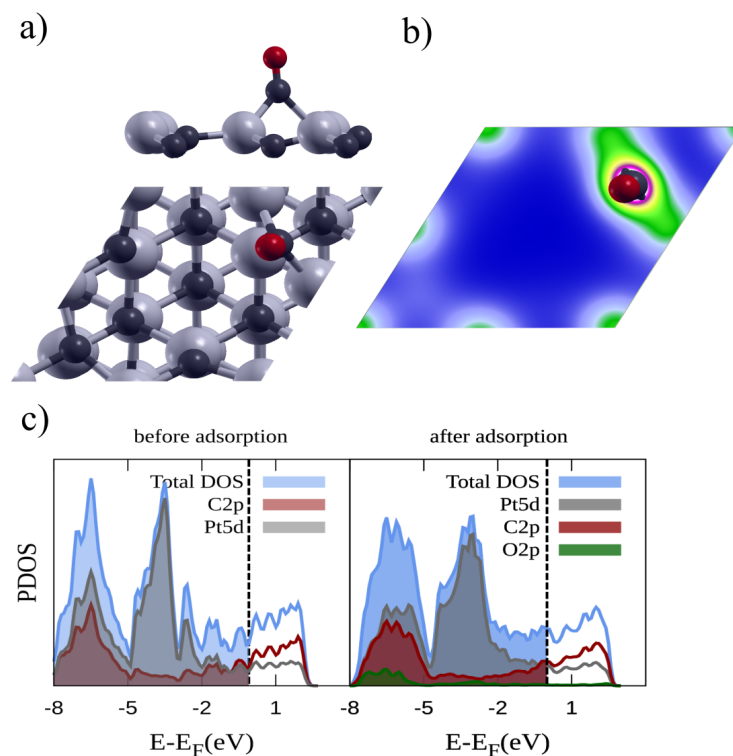


Figure 4.20: (a) Top and side view, (b) Charge density profiles and (c) PDOS plots of the adsorbed single O atom on the Pt vacancy defect on Pt-terminated ZB PtC(111) surface.

The adsorption energy for the *on-Pt* configuration is +1.9 eV which shows the same trend with the previous Pt-based adsorption configurations. The *on-C* geometry yields a adsorption energy of -3.29 eV, which is only about 0.45 eV weaker than the adsorption energy of C on the defect free C-terminated ZB PtC(111) surface. The surface C atoms display an upward displacement indicating a weakening bond with the surface neighboring atoms similar with the defect free surface. As a result, the calculated adsorption energies of O and oxidation characteristics of the surfaces with/without vacancy show similar properties. Therefore, the studied surface points towards a certain level of insensitivity of the surface reactivity to the formation of vacancies in the structure.

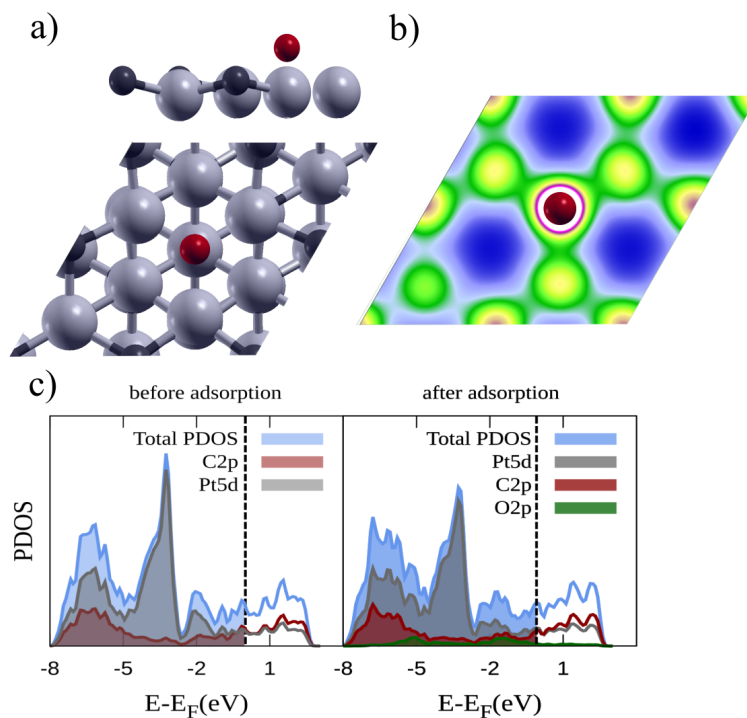


Figure 4.21: (a) Top and side view, (b) Charge density profiles and (c) PDOS plots of the adsorbed single O atom on the C vacancy defect on C-terminated ZB PtC(111) surface.

4.3.4.2 Atomic Adsorption on ZB PtC(100), PtC(110) and PtC(111) Surfaces

The adsorption properties of Al, B, F, H, N and S atoms on the C-terminated ZB PtC(100), PtC(110), and PtC(111) surfaces were investigated to understand the nature of the adsorption. All possible adsorption sites are considered on the surfaces, and the most stable ones are presented in Figure 4.22-4.26.

For C-terminated ZB PtC(100) four different stable adsorption geometries have been found as *C-on-top*, *Pt-on-top*, *bridge-Pt* and *bridge-C*. The most favorable adsorption site for each species is different. For example, the most favorable site is *bridge-Pt* for Al, while it is *C-on-top* for the F atom. We have observed the surface C reorganization after adsorption of the species in the *bridge-Pt* geometry, see Figure 4.22 and 4.23.

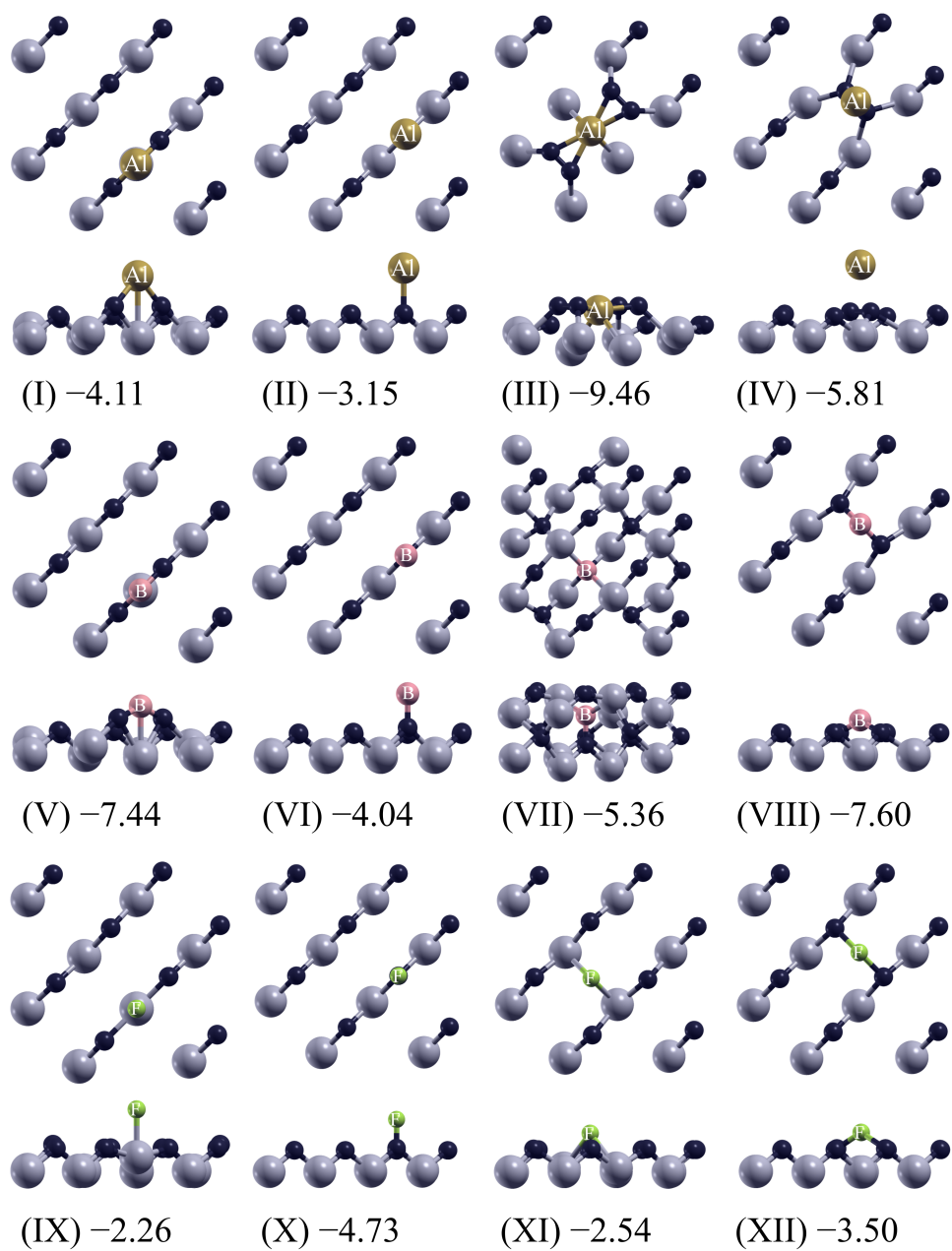


Figure 4.22: Top and side views of adsorption configurations with adsorption energies (eV) of atomic Al, B and F on the C-terminated ZB PtC(100). Gold, pink, green, black and gray spheres represent Al, B, F, C and Pt atoms, respectively.

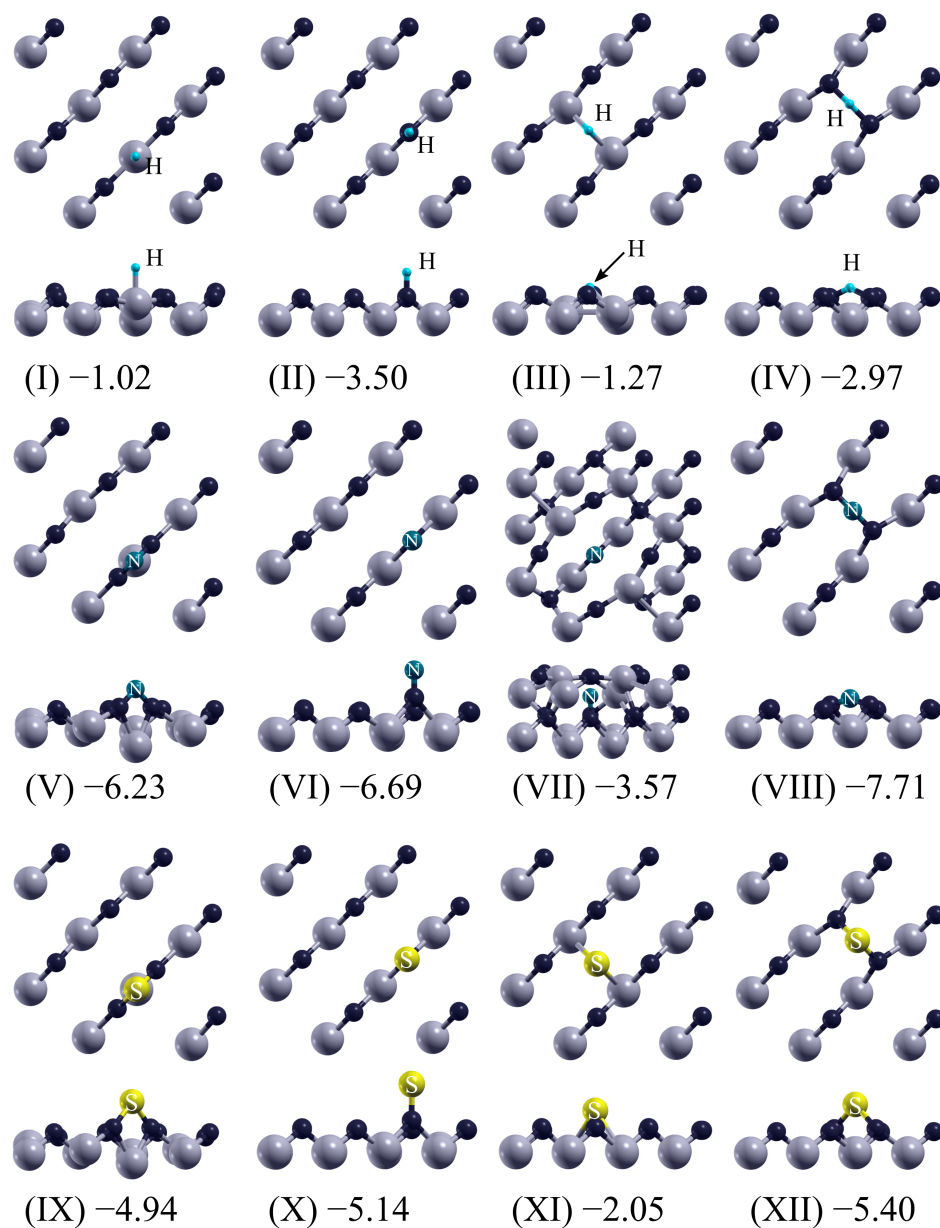


Figure 4.23: Top and side views of adsorption configurations with adsorption energies (eV) of atomic H, N and S on the C-terminated ZB PtC(100). Light blue, dark blue, yellow, black and gray spheres represent H, N, S, C and Pt atoms, respectively.

The B and N atoms bonded to the second layer C atom after geometric optimization as seen in Figure 4.22 (VII) and Figure 4.23 (VII). In the *Pt-on-top* adsorption geometry, the Pt atom moved through the bottom layer with the effect of the re-organization of the surface C atoms. The adsorption energies and Bader charges of the species are summarized in Table 4.4. For comparison with the adsorption of atomic O, we have only given the results for the C-terminated ZB PtC(100) surface. The partial Bader charge in all adsorption configurations can be characterized by an excess of charge on F and N. However, the charges transfer are from the adatom to the surface for the adsorption of Al, B, H and S atoms on the surface, see Table 4.4.

Table 4.4: Adsorption energies of Al, B, F, H, N and S atoms on the C-terminated ZB PtC(100) surface.

Atom	E_{ads} (eV)				ρ ($ e $)			
	<i>Pt-on-top</i>	<i>C-on-top</i>	<i>bridge-Pt</i>	<i>bridge-C</i>	<i>Pt-on-top</i>	<i>C-on-top</i>	<i>bridge-Pt</i>	<i>bridge-C</i>
Al	-4.11	-3.15	-9.46	-5.81	+2.33	+1.25	+3.00	+1.14
B	-7.44	-4.04	-5.36	-7.60	+3.00	+1.43	+1.58	+3.00
F	-2.26	-4.73	-2.54	-3.50	-0.59	-0.89	-0.61	-0.44
H	-1.20	-3.50	-1.27	-2.97	+0.20	+0.15	-0.04	+0.18
N	-6.23	-6.69	-3.57	-7.71	-3.40	-2.50	-2.44	-3.23
S	-4.94	-5.14	-2.05	-5.40	+0.48	+2.13	-0.09	+0.43

For ZB PtC(110) four different sites were considered, similarly to the C-terminated ZB PtC(100) surface, and the optimized structures are presented in Figure 4.24 and 4.25. We found a weak bond between the C (Pt) and two Pt (C) atoms in *bridge-Pt* (C) geometry as clearly seen for the Al in Figure 4.24 (I) and (II) causing a strong interaction between the adsorbate and the surface atom. In the case of atomic adsorption on ZB PtC(110) surface, the *on-top* sites are less favorable than the *bridge* sites. However, the *C-on-top* adsorption site is the most stable site for the H on the surface. We did not observe any surface atom re-organization upon adsorption of the species as was seen in the C-terminated ZB PtC(100) surface. Among all species, only the N atom causes the C atom on the top layer to detach upon adsorption of the atomic N same as with the atomic O on the ZB PtC(110) surface, see Figure 4.25 (IV). The calculated adsorption energies and Bader charges of the species are summarized in Table 4.5. Similarly to the C-terminated ZB PtC(100) surface, the species gained

Table 4.5: Adsorption energies of Al, B, F, H, N and S atoms on the ZB PtC(110) surface.

Atom	E_{ads} (eV)				ρ ($ e $)			
	<i>Pt-on-top</i>	<i>C-on-top</i>	<i>bridge-Pt</i>	<i>bridge-C</i>	<i>Pt-on-top</i>	<i>C-on-top</i>	<i>bridge-Pt</i>	<i>bridge-C</i>
Al	-	-	-4.06	-4.11	-	-	+3.00	+3.00
B	-3.36	-	-4.85, -6.03	-6.10	+1.48	+1.36	+1.57	+3.00
F	-3.23	-4.19	-3.35	-	-0.64	-0.81	-0.66	-
H	-2.10	-3.23	-1.84	-	-0.04	+0.13	-0.14	-
N	-1.23	-5.29	-6.15	-4.65	-0.52	-2.51	-2.43	-3.43
S	-	-2.24	-	-3.42	-	-0.33	-	-0.09

charges in the case of the adsorption of the F and N atoms. For the Al, B, H and S the charge transfer occurs from the adatoms to the surface atoms, see Table 4.5.

For the C-terminated ZB PtC(111) surface the most stable adsorption geometries of the species are presented in Figure 4.26. While the *bridge* geometry is the most favorable for the Al and B, the F, H and S prefer the *on-top* site on the surface. However, the N atom is not stable on the C-terminated ZB PtC(111) surface. In *bridge* geometry, the surface C re-organization was observed causing the highest adsorption energies of the species with the effect of the bond breaking of the surface atoms. Moreover, in the adsorption of N, the surface C atom detached from the surface forming a linear fragment, namely Pt-C-N. The partial Bader charges of these atomic species support the higher adsorption energies upon adsorption of the species on the surface.

Table 4.6: Adsorption energies of Al, B, F, H, N and S atoms on the C-terminated ZB PtC(111) surface.

Atom	E_{ads} (eV)				ρ ($ e $)			
	<i>Pt-on-top</i>	<i>C-on-top</i>	<i>bridge-Pt</i>	<i>bridge-C</i>	<i>Pt-on-top</i>	<i>C-on-top</i>	<i>bridge-Pt</i>	<i>bridge-C</i>
Al	-3.05	-2.88	-	-3.86	+2.61	+1.20	-	+3.00
B	-	-	-4.69	-6.62	-	-	+1.77	+3.00
F	-2.36	-4.33	-	-	-0.61	-0.85	-	-
H	-	-3.33	-0.92	-	-	+0.10	-0.07	-
N	-	-5.98	-	-	-	-0.47	-	-
S	-	-4.25	-	-3.61	-	+1.90	-	+0.24

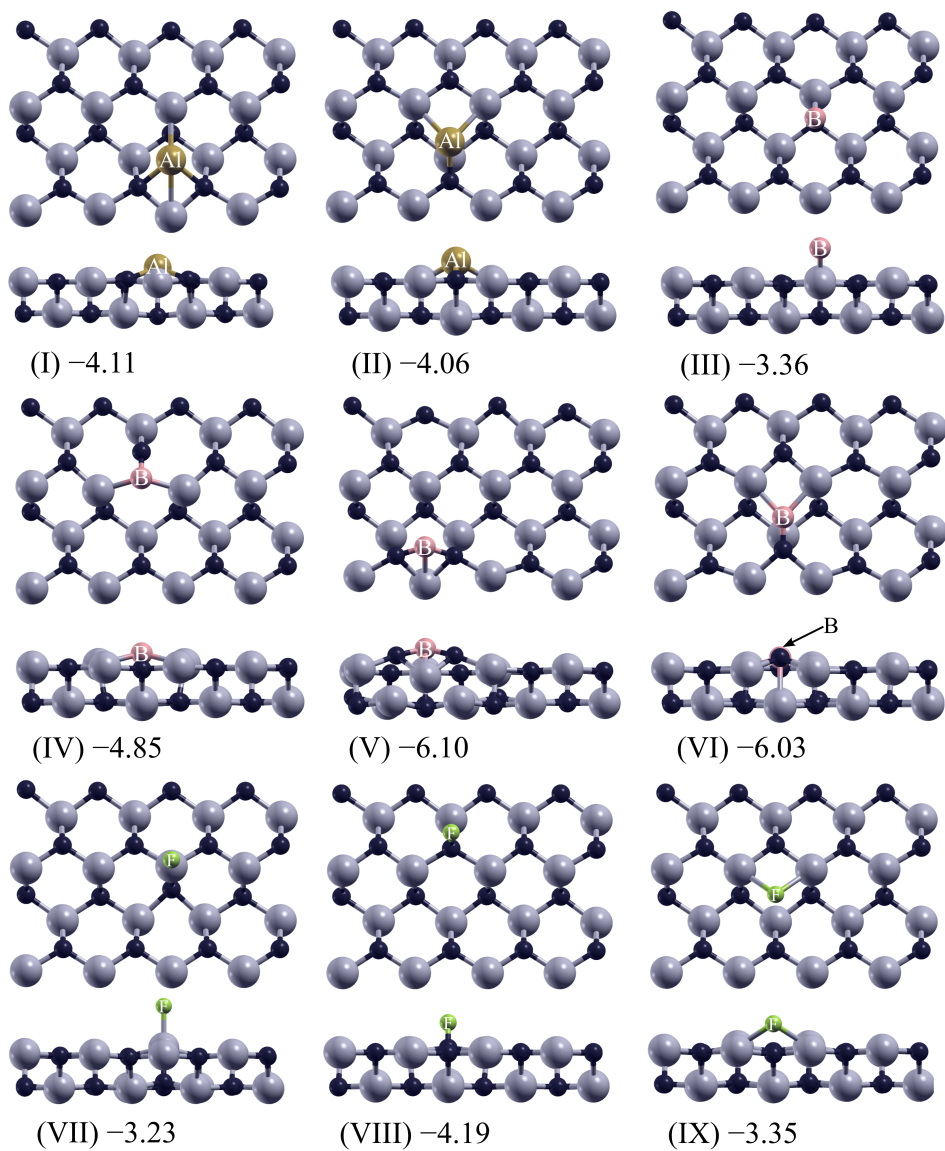


Figure 4.24: Top and side views of adsorption configurations with adsorption energies (eV) of atomic Al, B and F on the ZB PtC(110). Gold, pink, green, black and gray spheres represent Al, B, F, C and Pt atoms, respectively.

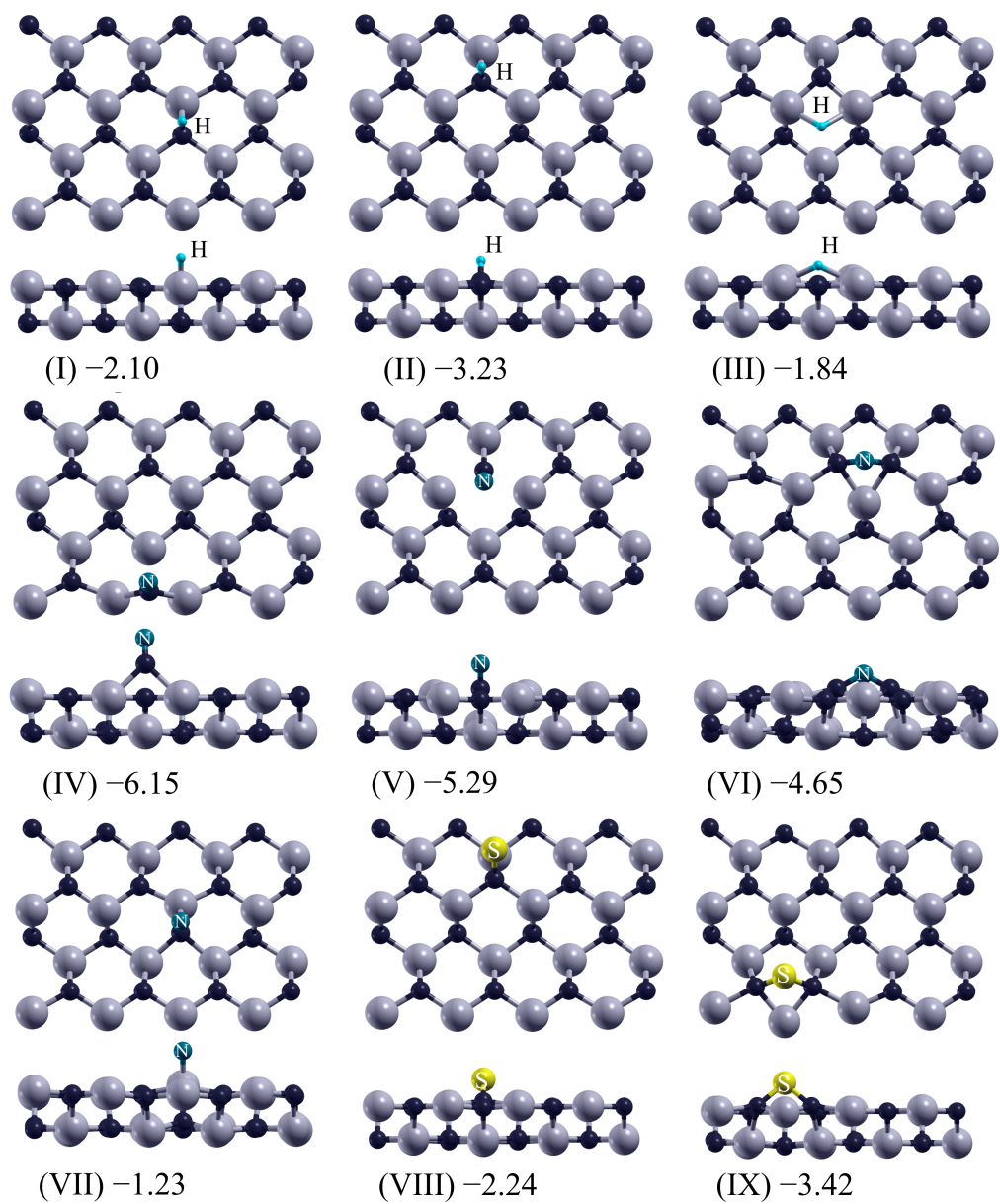


Figure 4.25: Top and side view of adsorption configurations with adsorption energies (eV) of atomic H, N and S on the ZB PtC(110). Light blue, dark blue, yellow, black and gray spheres represent H, N, S, C and Pt atoms, respectively.

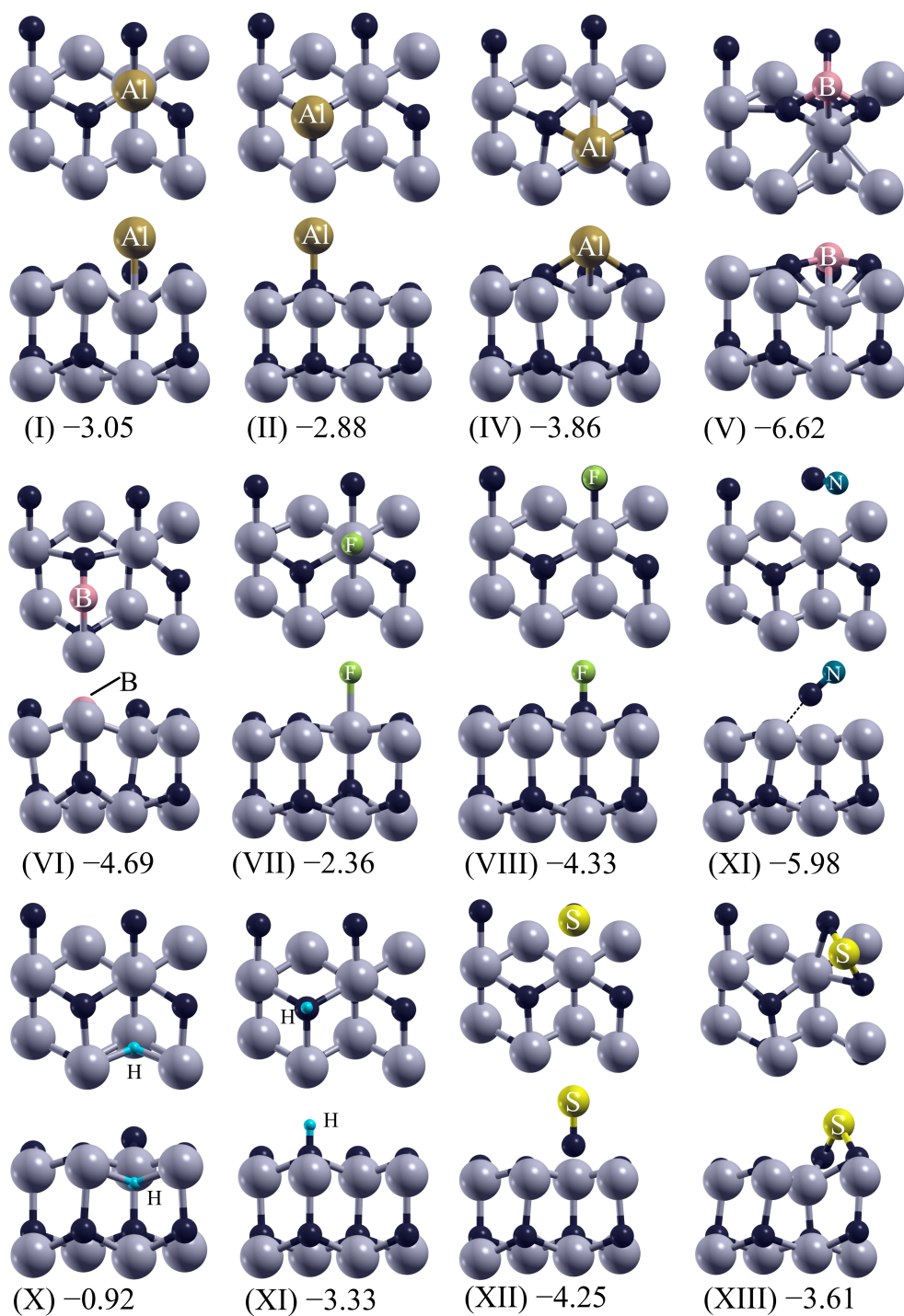


Figure 4.26: Top and side views of adsorption configurations with adsorption energies (eV) of atomic Al, B, F, H, N and S on the C-terminated ZB PtC(111). Gold, pink, green, light blue, dark blue, yellow, black and gray spheres represent Al, B, F, H, N, S, C and Pt atoms, respectively.

CHAPTER 5

CHLORINATED GRAPHENE AND GRAPHENE NANORIBBONS

In this chapter, the adsorption of mono- and di-atomic chlorine (Cl) on the graphene sheet, and zig-zag and armchair edge nanoribbons (ZGNR and AGNR) has been investigated using density functional theory with an empirical vdW correction. The bonding character of single Cl atom was found ionic due to the sizable charge transfer. In spite of the strong interaction, the migration of single Cl atom on the bare graphene sheet take places without energy barrier. In the case of di-atomic Cl₂, the in-plane single-sided geometry where the Cl-Cl bond is parallel to the graphene sheet, and the Cl atoms sit above the hollow sites. An external applied electric field was observed to stabilize the chlorinated defect free and defective graphene sheet as the intensity of the electric field increased. In addition, the electronic and structural properties have been studied upon adsorption of Cl atom on ZGNR and AGNR. Adsorption energies and electronic properties were investigated as a function of various parameters including ribbon width, length, adsorbate concentration and location.

5.1 Introduction

Graphene is a material with ample potential for electronic applications due to the its extraordinary electronic properties. One of the most important challenges of the electronic industry is to reduce the dimension of electronic devices to improve their performance. The unique properties of graphene makes it a very desirable material in the microelectronic industry in the fabrication of transistors since it allows for the easy tuning of the charge carriers.

Graphene-based electronic applications largely rely on the effective functionalization

of graphene, in particular, the manipulation of the Fermi points. Graphene is a so-called semimetal with a zero band gap and with the conduction and valence bands touching at six high-symmetry points of the Brillouin zone [121], referred to as the Fermi points. The unusual linear dispersion around these points makes graphene a desirable material with high mobility, while the lack of a band gap puts it at a disadvantage due to large on/off ratios. Fortunately, through various means such as doping with foreign species, introduction of strain and application of external fields, a band gap can be controllably introduced. Furthermore, the position of the Fermi level may also be adjusted, opening up the possibility of facile control of the doping level. Doping of graphene may be classified as electrical [100, 304] and chemical [305, 306]. Many studies focus on theoretical investigation of impurities which shows covalent, ionic and metal character [307–310]. Some of these studies are based on density functional theory treatments using standard exchange-correlation functional (LDA and GGA) without any vdW corrections. However, in the case of weakly bounded systems such as molecular adsorption, the vdW interaction plays an important role. In this chapter, we utilize a *DFT-D* [149] to investigate the structural and electronic properties of graphene systems.

Many experimental and theoretical studies [307, 311–316] have demonstrated the functionalization of graphene with halogen atoms such as fluorine and chlorine. For example, the structure of fully fluorinated and hydrogenated graphene shows similar properties. The halogen atoms covalently bound to the C atoms change the sp^2 hybridization to sp^3 , and introduce strong corrugation of the graphene layer upon adsorption [311–313]. Instead of using lighter halogens, fully halogenating graphene with heavier halogens (such as chlorine and iodine) has resulted in the formation of ionic bonds with no change in hybridization of C atoms. Therefore, the planar structure of the graphene can be preserved upon adsorption of the halogens. Theoretical studies on adsorption of heavier halogens [307, 314–316] on graphene show no covalent bonding between the halogens and graphene.

For graphene nanoribbons (GNRs) atomic chlorine adsorption, at the edges of zigzag GNR (ZGNR) and armchair GNR (AGNR) has been studied [314]. A recent experimental work by Li *et al.* [317] studied the interaction of molecular chlorine with graphene sheet, and showed the dissociation of the Cl_2 molecule to chlorine radi-

cals by using radiation. They reported that the band gap of the Cl/graphene system is around 45 meV. They also found that the average height of chlorinated graphene sheet is around 1.1-1.7 nm which is larger than the height of the pristine graphene, this result is consistent with the recent DFT results [318, 319].

In this part of thesis, the main motivation is to reveal the most stable Cl/graphene interfaces among the ones that can be designed and investigate their electronic structure. In order to understand the effect of Cl atom on graphene sheet, we start with the simple adsorption of atomic and molecular Cl on graphene sheet and graphene nanoribbons. We then study Cl adsorption on defected graphene sheets to understand the interplay of the modifications introduced by the defect and those introduced by Cl. In addition, the size effects on the electronic properties have been investigated for bare and chlorinated GNRs.

5.2 Computational Details

All calculations in this study were carried out using the QUANTUM ESPRESSO code package [163] with a London-type vdW correction (DFT-D) [149] and the PBE-GGA scheme [141, 230]. Valence electrons are treated explicitly and their interactions with ionic cores are described by the projected augmented wave (PAW) pseudopotential [294, 295]. Cold smearing [320] was used along with spin polarization for all calculations. Energy cut-offs of 60 Ry and 600 Ry were used for the wave function and the charge density, respectively. The sampling of the Brillouin zone was done using a $8 \times 8 \times 1$ k-point mesh for the 4×4 unit-cell with a vacuum spacing of 12 Å. For the nanoribbon part of this study, energy cut-offs of wave function and charge density were 50 Ry and 500 Ry, respectively, maximum force tolerance equal to 0.001 eV/Å, while total energies were converged to 10^{-8} eV. Due to the reduced dimensionality, a larger sample set of $24 \times 1 \times 1$ k-points in the Monkhorst-Pack scheme [233] could be afforded for the nanoribbon unit-cells with a vacuum spacing of 13 Å. The lattice constant for each size of nanoribbon was calculated, and the calculations were performed by using 1.422 and 1.437 Å for ZGNR and AGNR, respectively. The error caused by the mismatch in the lattice constants were found to be negligible.

The adsorption energies of atomic and molecular Cl atoms are calculated using the formula as given by Equation 3.2 in Chapter 3. The charge density difference analysis (Equation 3.3 in Chapter 3) is used in all configurations provides information on the charge partition of the systems.

To prepare for the calculations involving chlorine adsorption on defective graphene, the defect formation energy E_f is calculated by using the following formula

$$E_f = E_{def} - E_{pr} - n_C \mu_C \quad (5.1)$$

where E_{def} is the total energy of defective graphene, E_{pr} is the total energy of pristine graphene, μ_C is the chemical potential of C and n_C is the number of C vacancies in the DFT simulation cell. For the chemical potential of C we use the calculated energy of diamond per atom.

The climbing-image nudged elastic band method (CI-NEB) [158, 160, 161] was used to find energy barriers with five images in between the initial and final points. The energy barriers (E_B) are calculated as

$$E_B = E_{TS} - E_I \quad (5.2)$$

where E_{TS} is the transition state energy and E_I is the initial energy state.

5.3 Results and Discussion

5.3.1 Adsorption of Chlorine on Pristine Graphene

In this section adsorption characteristics of chlorine atom on graphene sheet were investigated. Moreover, we investigate the effect of the applied electric field on the electronic properties of defective and chlorinated graphene.

5.3.1.1 Adsorption of Single Cl Atom

In previous calculations [307, 316], it was reported that the adsorption of the Cl atom shows ionic character associated with charge transfer between the Cl and C

atoms [307]. In many theoretical studies, the lowest energy adsorption configuration are reported to be on top site or bridge site depending on the size of the simulation cell in DFT calculation [307, 316, 319]. The C-Cl bond distances were found to be approximately 2.9 Å which is clearly longer than the covalent bond distance of 1.72-1.85 Å in CCl₄ molecule [321], and the C-Cl distance on graphene sheet was found around 2.54 Å [318]. The calculated adsorption energies in the previous works [307, 316, 318, 319] were given in the range between -1.25 and -0.30 eV by taking the atomic Cl as a reference state.

To reproduce these results and benchmark out calculation parameters, we consider three different adsorption sites for the Cl atom: *on-top* (T), *bridge* (B) and *hollow* (H). The adsorption geometries and the associated adsorption energies are given in Figure 5.1 (a). The calculated adsorption energies, partial Bader charges on the chlorine atom and magnetization values are also summarized in Table 5.1.

The band structures of atomic Cl at different adsorption sites on 4×4 graphene with the PDOS for the C and Cl p orbitals are presented in Figure 5.1. While majority (Maj.) and minority (Min.) spin states are degenerate for bare graphene, this degeneracy below the Fermi energy level disappears and the additional Cl states appear upon adsorption of single Cl atom, see Figure 5.1. However, the bonding (π) and antibonding (π^*) bands are degenerated at the K point of the Brillouin zone, similar to bare graphene. The Fermi level moves to the valence band, 0.6 eV, below the energy of Dirac point. This changes the zero-gap semiconductor characteristic of the bare graphene to an n-doped metal. The Maj. and Min. spin state profiles are nearly the same and match each other for the carbon atoms. However, the p-Maj. and p-Min. orbital projected states for the Cl atom mismatch due to the spin magnetic moment imbalance that appears after adsorption of Cl atom on graphene. These observations shows a ionic bonding character between the Cl and C atoms involving a charge transfer at the adsorption sites B (-0.451 |e|), H (-0.356 |e|) and T (-0.452 |e|) from the graphene to the Cl atom. Upon adsorption of Cl atom on graphene, no corrugation was observed between Cl and C atoms which indicates that C-C bonds around adsorption sites still shows sp² characters. This further corroborates the claim concerning the ionic character of the interaction.

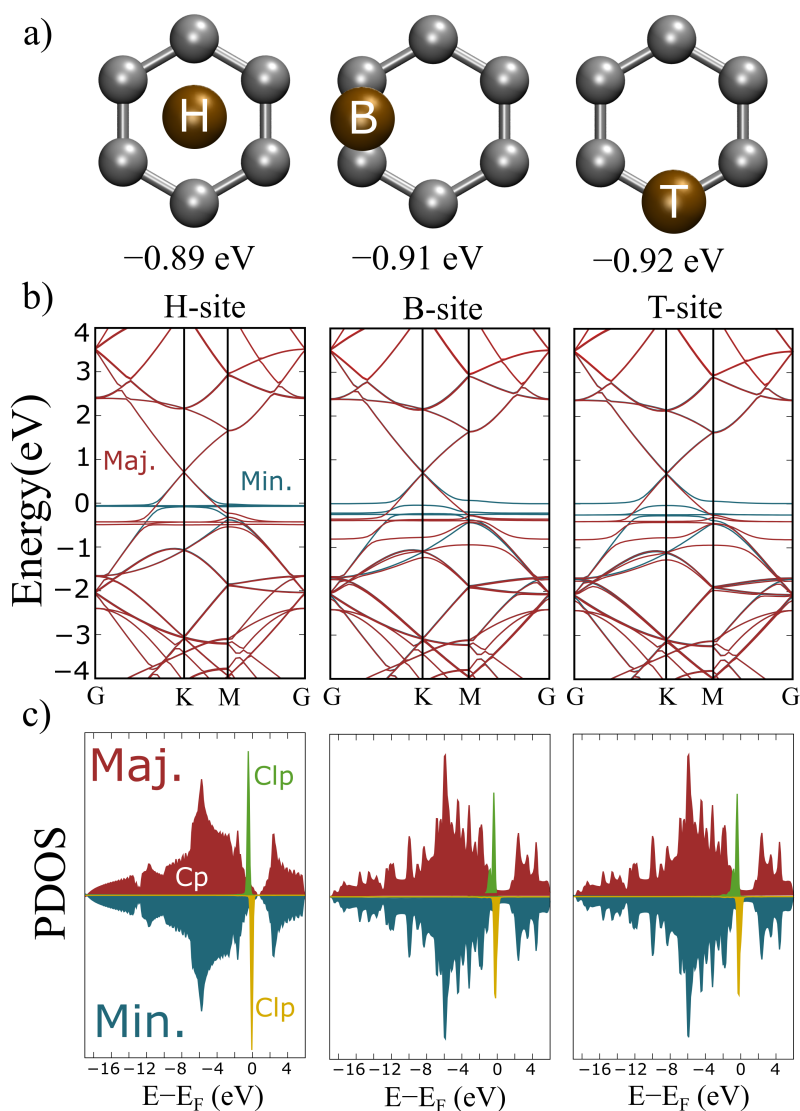


Figure 5.1: Adsorption sites and majority (red) and minority (blue) spin band structures with PDOS of chlorine atom at the adsorption sites on graphene. (a) Top view of adsorption sites of Cl atom with adsorption energies. (b) Energy band structures and (c) PDOS for three different adsorption geometries. Gray and brown balls represent C and Cl atoms, respectively. H: *hollow*, B: *bridge* and T: *on top* sites.

PDOS for the C atoms nearby the adsorbed Cl atom on top-site is given in Figure 5.2 to detailed understand the interaction of Cl atom with C atoms on graphene sheet. It is clear that the Fermi level of C atoms shifted to the left of the Dirac point indicates the charge transfer from C atoms to Cl. The Cl-C hybridization occurs near the Fermi level shortening the C-Cl distance causing strong interaction not only the on top C

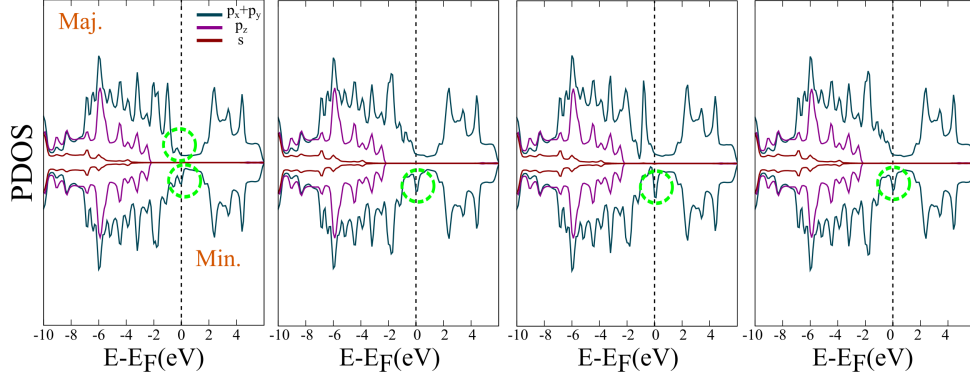


Figure 5.2: PDOS of neighboring C atom at around adsorbed Cl atom on top-site. Maj. and Min. means the majority and minority states, respectively. Green dashed circles show the C-Cl hybridization.

atom but also neighboring three C atoms. This observation says that the hybridization occurs between the Cl and π bond of graphene. It is interesting to note that the interaction between Cl and on top C atoms mainly changes the majority states, while the interaction with the neighboring three C atoms changes the minority states, see Figure 5.2.

The total magnetization around $0.5 \mu_B/\text{cell}$ was introduced for graphene with atomic Cl at three different sites, see Table 5.1. These structures can be interesting and important in some technological applications such as magnetic recording and spintronic [322, 323]. The computed Bader charges for adsorbed Cl atom on graphene sheet indicate an excess of charge on Cl atom, and it is consistent with the corresponding adsorption energies, see Table 5.1.

Table 5.1: Adsorption energies, total and absolute magnetization and partial Bader charge (ρ_{Cl}) of Cl atom on graphene sheet.

Ads.Sites	E_{ads} (eV)	m_{tot} (μ_B/cell)	m_{abs} (μ_B/cell)	ρ_{Cl} ($ e $)
B	-0.91	0.50	0.58	-0.451
H	-0.89	0.54	0.67	-0.356
T	-0.92	0.50	0.51	-0.452

The calculated energy barriers of adsorbed atomic Cl along the symmetry direction (T \rightarrow H \rightarrow B \rightarrow T) of graphene are given in Figure 5.3. We have found the energy

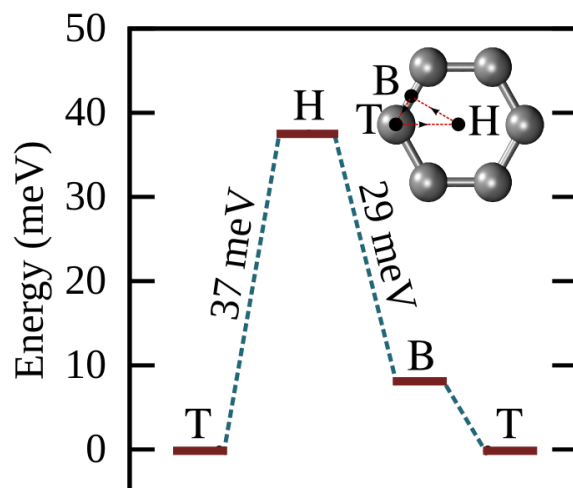


Figure 5.3: Diffusion path for atomic Cl atom along the symmetry direction of graphene structure. Gray and brown balls stand for C and Cl atoms, respectively.

barrier of 37 meV from the T site to the H site. This energy barrier plot suggests that the minimum energy path on graphene for the Cl atom occurs from T site to the B site. It is important to note that these energy values are very low and allow Cl atom to diffuse easily on graphene.

The migration energy and adsorption energies of single Cl atom with the changes of the bond lengths indicate that the C-Cl form ionic bond. However, the hybridization between the C and Cl atoms also suggests that a weaker covalent bond between the C and Cl atoms.

5.3.1.2 Adsorption of Di-atomic Cl₂ Molecule

For the adsorption of Cl₂ molecule on graphene sheet, nine different adsorption geometries were considered as shown in Figure 5.4 and 5.5. In Figure 5.4 the Cl₂ molecules are parallel to the graphene sheet in the form of molecular Cl₂, while the configurations in Figure 5.5 display adsorption geometries of Cl atom on opposite sides of the graphene sheet. In the most stable adsorption geometry (Figure 5.4 (a)), the Cl-Cl bond is parallel to the graphene sheet and the Cl atoms sit above the hollow sites. In the case of adsorption on double sided graphene, the Cl atoms sit above the

midpoint of C-C bond, and the neighboring C atoms undergo an upward relaxation upon adsorption of Cl atoms on both sides of graphene sheet with the shorter C-Cl bond distances, see Figure 5.5 (d). This may be the reason why the adsorption energy of Cl atoms is higher than the other adsorption configurations. The adsorption energies, Cl-C bond lengths, partial Bader charges of the Cl₂ molecules are summarized in Table 5.2.

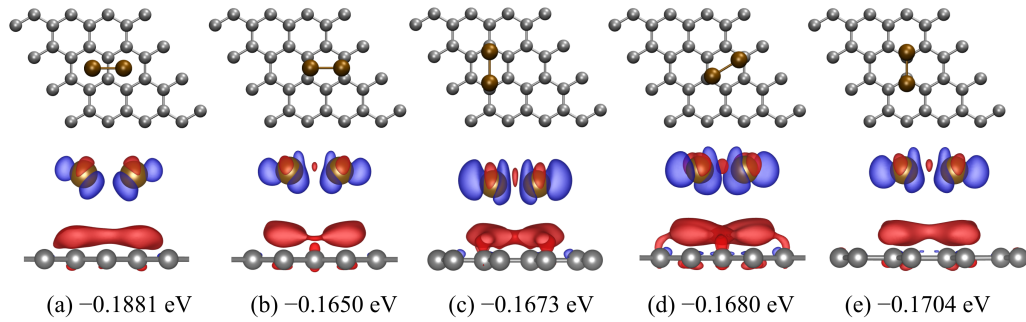


Figure 5.4: Adsorption geometries (upper panel) and charge density difference plots (lower panel) of di-atomic Cl₂ molecule on graphene sheet with the calculated adsorption energies. Cl₂ molecules are parallel to the graphene sheet. Gray and brown balls stand for C and Cl atoms, respectively.

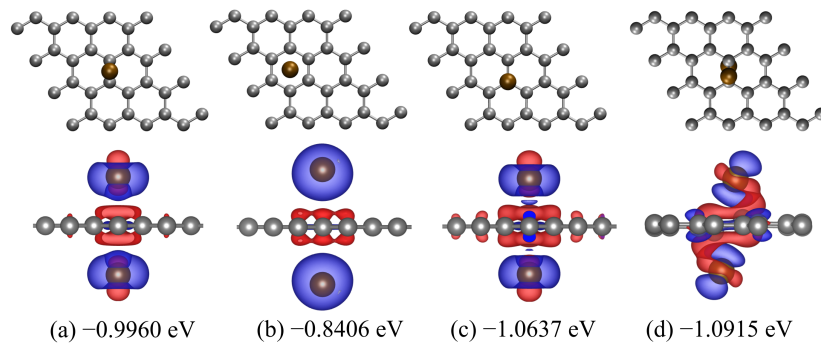


Figure 5.5: Adsorption geometries (upper panel) and charge density difference plots (lower panel) of di-atomic Cl₂ molecule on graphene sheet with the calculated adsorption energies. Cl₂ molecules are on opposite sides of the graphene sheet. Gray and brown balls stand for C and Cl atoms, respectively.

We found that the magnetization values are nearly 0.0 μ_B/cell except the optimized configuration (b) in Figure 5.5 with the total (absolute) magnetization value of 1.19 (1.23) μ_B/cell . For the parallel configurations the Cl-Cl and Cl-C bond distances are

around 2.0 Å and higher than 3.0 Å, respectively. However, the Cl-C distances for the Cl on opposite sides configurations are in the range of 2.16 to 2.91 Å. According to our Bader partial charge analysis, while the Cl atoms transfer all charges to the graphene in parallel geometries (Figure 5.4), the Cl atoms gained charges around 0.8 |e| from the C atoms of graphene in Cl on opposite sides geometries (Figure 5.5), see Table 5.2. From the charge density difference analysis (lower panels of Figure 5.4 and 5.5), it is clear that the adsorption of Cl₂ mainly shows ionic character. It is important to note that the configuration in Figure 5.5 (d) may show covalent character due to the higher adsorption energy and shorter C-Cl bond distance, and also a mixture of hybrid sp² and sp³ bonds in the charge distribution.

Table 5.2: Adsorption energies, Cl-C bond distance and partial Bader charges of diatomic Cl₂ molecule on graphane sheet.

Figure	config.	E _{ads} (eV)	d _{Cl-C} (Å)	ρ _{Cl} (e)
Figure 5.4	(a)	-0.1881	3.37	-0.01
	(b)	-0.1650	3.54	-0.01
	(c)	-0.1673	3.51	-0.02
	(d)	-0.1680	3.51	-0.01
	(e)	-0.1704	3.49	-0.01
Figure 5.5	(a)	+0.8890	2.58, 2.58	-0.82
	(b)	+1.1998	2.91, 2.91	-0.80
	(c)	+0.7538	2.39, 2.46	-0.84
	(d)	+0.6982	2.16, 2.27	-0.55

Obviously, the double sided adsorption configurations are more stable than the single sided molecular Cl adsorption. Consistent with the work of Yang *et al.*, the lower Cl coverage is much more stable than the other double sided configurations [324]. They reported that the 25% Cl (C₄Cl) and also lower coverage (C₁₆Cl) is the most stable with a adsorption energy of around -1.60 eV for covalent bonding.

5.3.2 Adsorption of Chlorine on Defective Graphene

In this part of the thesis, the defective graphene structures are investigated for the graphene sheet with single and double vacancies. Single vacancies (SV) with one removed C atom from pristine graphene can be experimentally observed by using

TEM and STM [325, 326]. A Jahn-Teller distortion has been showed in graphene with SV which leads to a saturation of two dangling bonds left behind by the missing C atom. The remaining C atom in the immediate vicinity has an unsaturated dangling bond [325]. The graphene with DV defects [327], on the other hand, have no dangling bond, and this kind of structures are known to be more stable than the structures which have dangling bonds [328] according to the formation energy of DV.

The first step toward understanding the effect of the C vacancies in the case of the adsorption of Cl atom on graphene is to create the defected graphene samples. For this reason, we have created single and double C vacancies in 4×4 graphene sheet, see Figure 5.6 (a) and (c). We then introduce the Cl atom to the defected graphene sheet, starting by placing the Cl atom at the possible sites around the vacancy, see Figure 5.6 (b) and (d). The calculated adsorption energies of the single Cl atom on defective graphene sheet with SV and DV are -3.13 and -1.46 eV per unit cell, respectively. We found the physisorption of the Cl atom on the defective graphene sheet occurs with a C-Cl bond length of ~ 1.8 Å. For comparison, the C-Cl bond distances on defect free graphene was found ~ 3.0 Å upon adsorption of Cl atom. The Bader charge analysis was performed for the SV+Cl and DV+Cl systems, and the partial charges on the Cl atom were found $-0.17 |e|$ and $-0.23 |e|$, respectively.

The single point vacancy is a source of local magnetic moment, $\sim 1.60 \mu_B/\text{cell}$, on graphene sheet. The existence of the defect at around the Fermi level in graphene changes the localization of the sp^2 orbitals becoming more sensitive to the structural changes. Therefore, a band splitting is observed in the presence of the single vacancy in graphene, see Figure 5.7 (a). The defect formation energy of SV, E_f^{SV} , was calculated to be 7.87 eV, and found to be in good agreement with the previous studies [329, 330]. Interestingly, this band splitting for σ bands totally disappears upon adsorption of the Cl atom on defective graphene. However, a weak band splitting can be seen for the π bands around the Fermi level, see Figure 5.7 (b). For the double vacancy the formation energy E_f^{DV} was found to be 8.39 eV which is consistent with the previous works [330]. The Dirac point moves up to the 1.21 eV and extra energy states appear in the presence of the defect in graphene sheet. A band gap opening (0.79 eV) was observed with the adsorption of Cl atom on graphene with DV, and the Cl states can be easily seen in the energy-band structure of the system, see Figure 5.7

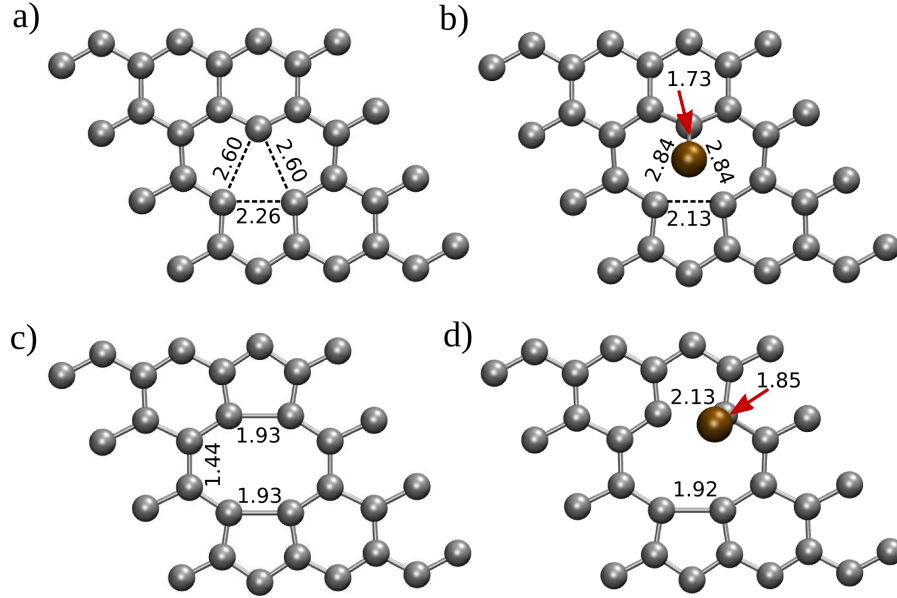


Figure 5.6: Optimized geometries of (a)-(c) bare and (b)-(d) chlorinated defective graphene sheet. Bond distances are in unit Å. Red arrows show the C-Cl bond distances. Gray and brown balls stand for C and Cl atoms, respectively.

(d). We found that the Cl adsorption does not have any substantial effect on the band gap opening in graphene with SV.

The electronic structure of defect states at the Gamma-point can be understood by considering the orbitals of σ and π bonds between the C and Cl atoms. The nodal planes are in the xz and yz planes, so the orbitals are labeled φ_x and φ_y , respectively as seen in Figure 5.8. As mentioned above, the local three-fold symmetry breaks down after removing the C atom from the graphene sheet. This single C vacancy undergoes a Jahn-Teller distortion which partially make bonds two of the dangling bonds, leaving one main defect state near the Dirac point. The third unsaturated dangling bond provides a contribution of $1.0 \mu_B/\text{cell}$ to the total magnetic moment [331]. The remaining magnetic moment, $0.54 \mu_B/\text{cell}$, unbalances the spin polarized π orbitals.

These features can explain the band splitting in defective graphene. With the adsorption of the Cl atom including a small amount of magnetic moment ($0.04 \mu_B/\text{cell}$) in defective graphene, the third unsaturated dangling bond is saturated. This the reason why a smaller band splitting occurs in the band at around Fermi energy level, and it

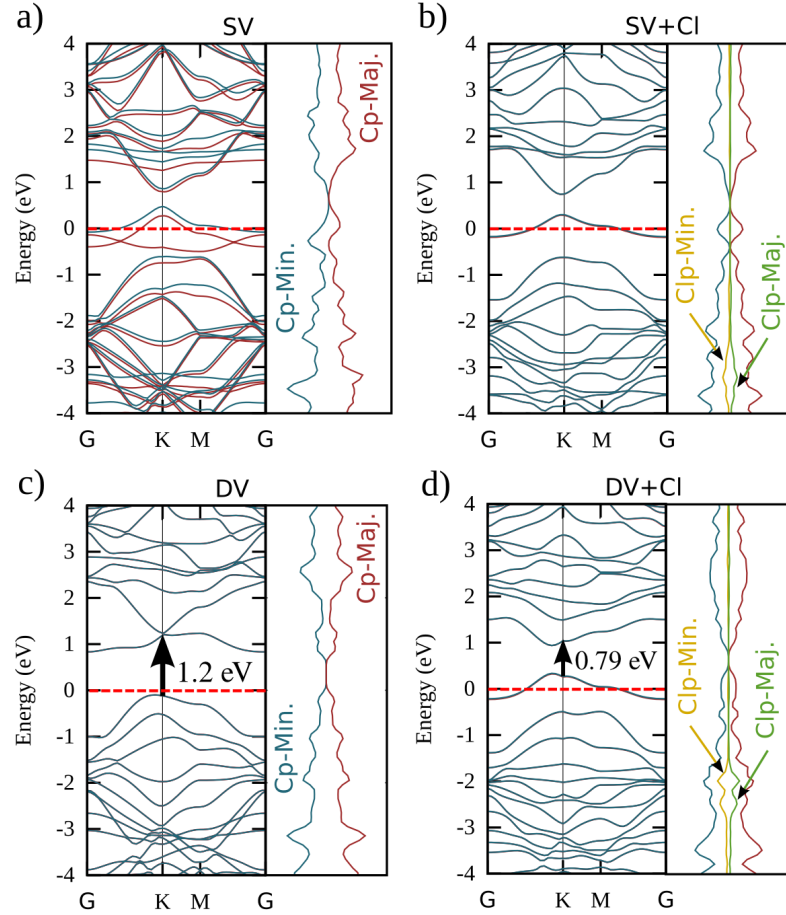


Figure 5.7: Energy band structures with PDOS plots of the Cl atom on defected graphene sheet with (a)-(b) SV and (c)-(d) DV. The Fermi energy is shifted to zero.

can be seen easily from the energy-band structure in Figure 5.7. In the case of double vacancy, no dangling bond is present so that two pentagons and one octagon appear instead of the hexagons in graphene sheet. Because of this reason, no magnetization induced to the defective graphene in the case of the DV in graphene sheet. Adsorption of the Cl atom on defective graphene provides a contribution of magnitude $0.04 \mu_B/\text{cell}$ to the total magnetic moment which gives rise to a smaller band splitting at around the Fermi energy level, see Figure 5.7.

5.3.3 Chlorinated Graphene Under Electric Field

In this part of the study, the pristine and chlorinated graphene were optimized in 4×4 unitcell using spin polarized DFT-D van der Waals correction. In the case of

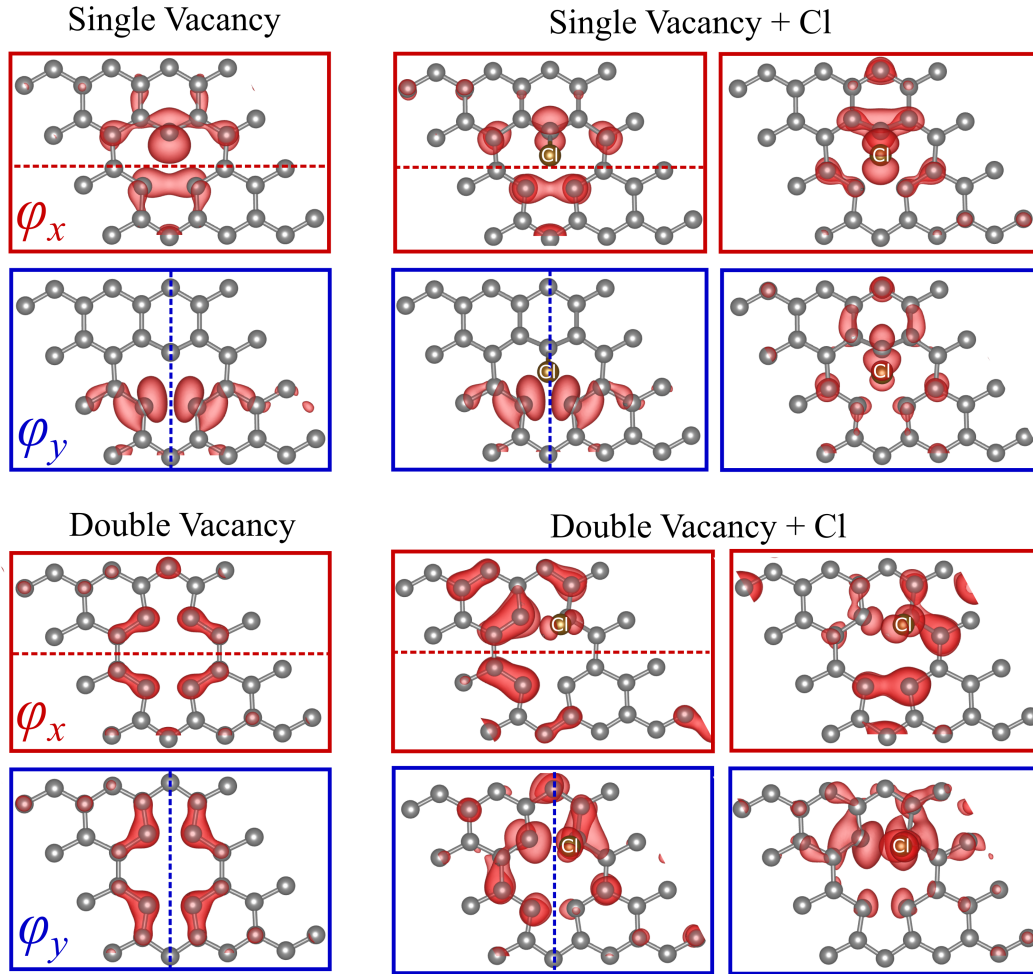


Figure 5.8: Isosurfaces of defect states $|\varphi_x(\vec{r})|^2$ and $|\varphi_y(\vec{r})|^2$ on bare and chlorinated defective graphene sheet; the nodal planes are shown as dashed lines in each cases. Gray and brown balls stand for C and Cl atoms, respectively.

chlorinated graphene, the Cl atom binds *on-top* site on graphene. The Fermi level shifts relative to the pristine graphene, partial Bader charges on Cl atom, adsorption energies of Cl atom and relative energies with respect to the graphene without external electric field are presented in Figure 5.9.

The C-Cl bond distances, total and absolute magnetization and partial charges on the Cl atom as a function of the applied electric field plots are given in Figure 5.10. We have seen a small amount of change in the adsorption energy of the Cl atom with the applied electric field. However, the C-Cl bond distance, magnetization values and the partial charge of Cl atom can change with the applied electric field depending on the

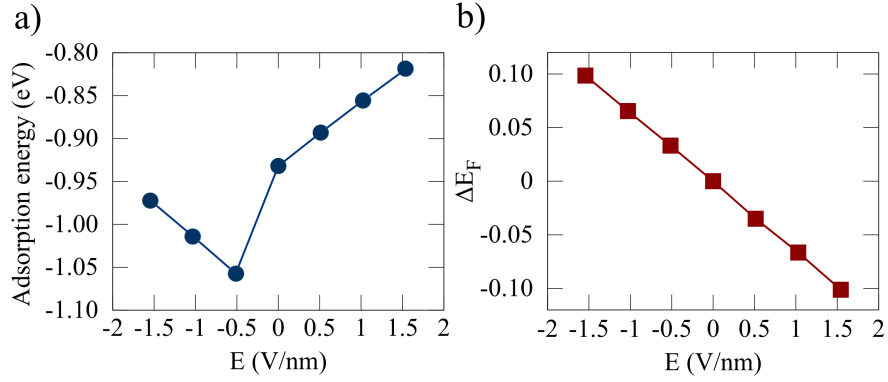


Figure 5.9: (a) Adsorption energies of Cl atom and (b) Fermi level shifts relative to the graphene without applied electric field as a function of applied electric field.

direction of the field. The C-Cl bond distances increase as the applied electric field intensity E is decreased from +1.54 to -1.54 V/nm. This trend was also observed on the behavior of the partial charge of Cl atom, see Figure 5.10 (a) and (c). The changes in both C-Cl bond distance and the partial charge of Cl atom exist as a result of induced dipole due to the effect of the applied electric field. In contrast, the total and absolute magnetization of chlorinated graphene under electric field increase as the electric field intensity is increased from -1.54 to $+1.54$ V/nm, see Figure 5.10 (b).

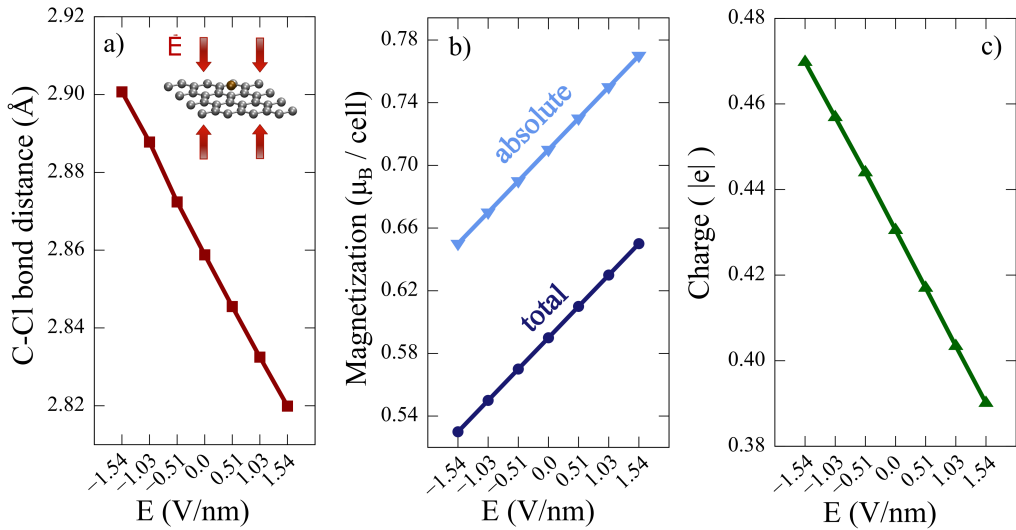


Figure 5.10: (a) The C-Cl bond distance, (b) the total and absolute magnetization values and (c) partial Bader charge of Cl atom for chlorinated graphene under electric field.

The relative energy was defined as the difference between the energy with and without external electric field along the z direction;

$$E_R = E_{E \neq 0} - E_{E=0} \quad (5.3)$$

where $E_{E \neq 0}$ is the total energy of the graphene with the applied electric field and $E_{E=0}$ is the total energy of the graphene without electric field. The relative energies are plotted as a function of the applied electric field in Figure 5.11. We can easily see that the relative energies for the pristine graphene become lower at stronger electric field. But, we can not increase the applied electric field due to damage the stable structure resulting broken chemical bonds. The intensity of applied electric field was kept in the range of structural limitations which is high enough for the Coulomb interaction between the atoms in the system. The relative energies for chlorinated graphene is dependent on the direction of the applied electric field, and the relative energy increases as the applied electric field intensity \mathbf{E} increases from -1.54 to $+1.54$ V/nm, see Figure 5.11. In the previous study by Mak *et al.* [332] a band gap of 200 meV was observed under the applied electric field around ~ 1.0 V/nm. However, our results show that the electric field does not have any substantial effect on the band gap. The reason for this discrepancy may be due to several differences in the experimental and theoretical treatments, and requires further analysis.

We have also investigated the electronic properties of the bare and chlorinated graphene with single and double vacancies under applied electric field. The relative energies, Fermi energy shifts, total and absolute magnetization values and partial charge of the Cl atom are summarized in Table 5.3. We found that the applied electric field increases the stability of stable and Fermi level higher for both pristine and chlorinated the defective graphene. The transferred charge to the Cl atom increases with the effect of the applied electric field, see Table 5.3.

The applied electric field in this study is enough to protect from broken bonds in graphene. In the previous studies [333–336], the perpendicular electric field were used in the same range (-1.54 - $+1.54$ V/nm) or higher. For example, it was shown that the applied electric field (100-200 V/nm) by femtosecond lasers can not damage the graphene-oxide layer [333, 334]. In a theoretical study [335], electric field of 10 V/nm is applied to the graphene layer for dissociative adsorption of hydrogen

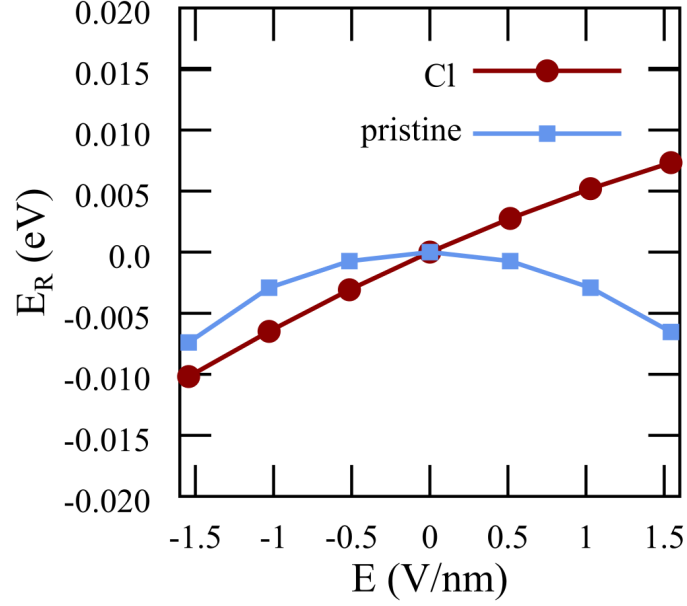


Figure 5.11: Relative energies induced by the external electric field for the pristine and chlorinated graphene.

molecules. Moreover, it is possible to applied higher electric field by using a tip of scanning probe microscope without any damage to the materials. This justifies the rather large electric field values used in this study.

Table 5.3: Relative energy (E_R), Fermi level shift (ΔE_F), total and absolute magnetization and partial Bader charge of Cl atom for the defective graphene under electric field ($|\mathbf{E}|=0.54$ V/nm)

System	E_R (eV)	ΔE_F (eV)	m_{tot} (μ_B/cell)	m_{abs} (μ_B/cell)	ρ_{Cl} ($ e $)
SV	-0.0102	-0.053	1.55	1.97	-
SV+Cl	-0.0021	0.062	0.04	0.07	-0.18
DV	-0.0013	0.040	0.0	0.0	-
DV+Cl	-0.0076	0.039	0.03	0.06	-0.24

5.3.4 Chlorinated Zig-zag and Armchair Graphene Nanoribbons

The electronic properties of graphene nano-ribbons (GNRs) depends on their structural properties [337], and the band gap of GNRs is sensitive to quantum confinement effects [112, 338, 339]. As an example, the ZGNRs show semiconductor behav-

ior [340], and their ferromagnetic behavior can be tuned with the edge functionalization [341]. AGNRs can have metallic and semiconducting characteristic depending on their sizes (i.e width of nanoribbons) [342].

As a model for zig-zag and armchair fully hydrogen terminated graphene nanoribbons, we consider a six zigzag and armchair row wide ZGNR (6ZGNR with the width of 13.5 \AA) and AGNR (6AGNR with the width of 14.8 \AA), respectively. We calculated the adsorption energies of the Cl atom on both graphene nanoribbons starting from the edge to the middle point of the ribbon, see Figure 5.12. We consider three different adsorption sites, namely *on top*, *bridge* and *hollow* sites. The most stable one is *on top* site for ZGNRs with an adsorption energy of -2.28 eV . For AGNRs we have also calculated adsorption energies which are found in the range of -1.14 to -1.11 eV . However, it is important to note that the most stable sites can be changed depending on the size of graphene nanoribbons. The adsorption energies show that the most stable site for the ZGNR is *site-1* in ZNGR edge, and the energies lowered at around the middle point of the ZGNR (*sites 4-6*), see Figure5.12 (a). In *site 1*, the Cl atom forms bonds both with Cl and H atoms, and the C and H atoms slightly relax upward and downward toward the planar ribbon structure, respectively. This interaction between the Cl and H atom may be the reason of the higher adsorption energy on *site 1*. However, the adsorption energies of single Cl atom are found in the range of -1.30 to -1.25 eV for AGNR. The negative energies indicate that the *site 1* for the Cl atom in AGNR edge is not stable, we therefore do not report further results for this site.

We have also considered different sized ZGNR and AGNR to examine the tendency for the adsorption of Cl atom on different size of graphene nanoribbons. For this reason, we prepared nanoribbons with different width and length to understand the effect of the size on magnetization of ribbons, C-Cl bond distance and adsorption energy of single Cl atom *on top* site on nanoribbons. Here, due to the periodic structure of our simulation cells, the length of the nanoribbons actually correspond to Cl concentration.

In Figure 5.13, we have investigated the adsorption energy of Cl, Bader charges on Cl and magnetization depending on the size of ZGNR. The total and absolute magneti-

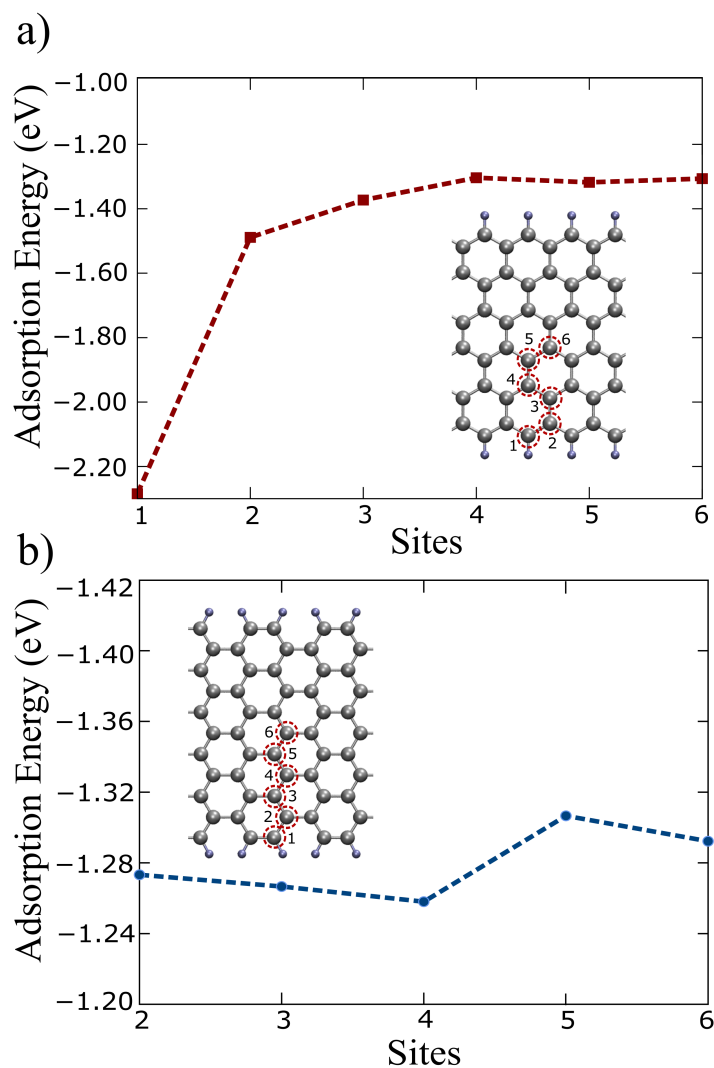


Figure 5.12: The adsorption energies of Cl atom on (a) ZGNR and (b) AGNR. The adsorption sites (red dashed circles) are given as inset figures. Gray and blue balls stand for the C and H atoms, respectively.

zation values increase with decreasing concentration and increasing width of ZGNR, see Figure 5.13 (a) and (b). Moreover, the adsorption energy of single Cl atom decreases while the width of ZGNR increases due to weaker interaction of Cl atom with H atom at the edge. For the wider ZGNR the interaction between the Cl and H atom is minimum, and the energetics begin to converge to bulk graphene. This trend shows that the adsorption energy of the Cl atom will be lower for the wider ZGNR. We have not observed any relation between the adsorption energy and length of ZGNR, and the adsorption energies vary between -1.27 and -1.17 eV for the structures presented in Figure 5.13 (b). While the partial Bader charges on Cl atom can vary in a small in-

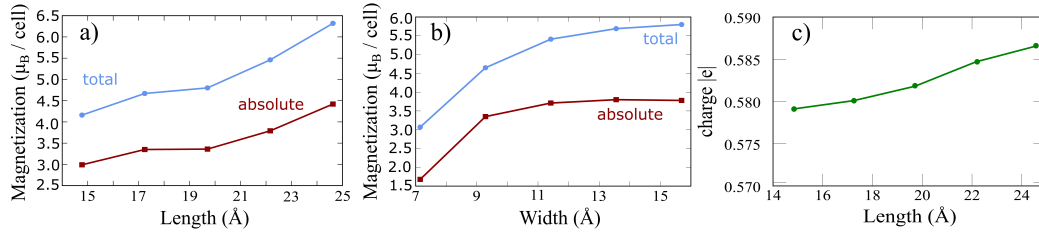


Figure 5.13: (a) Total and absolute magnetization as a function of length and (b) width of ZGNRs. (c) Transferred Bader charges to the single Cl atom on ZGNRs as a function of length.

interval with changing of the width, a clear increasing trend can be seen with increasing ZGNR length, see Figure 5.13 (c).

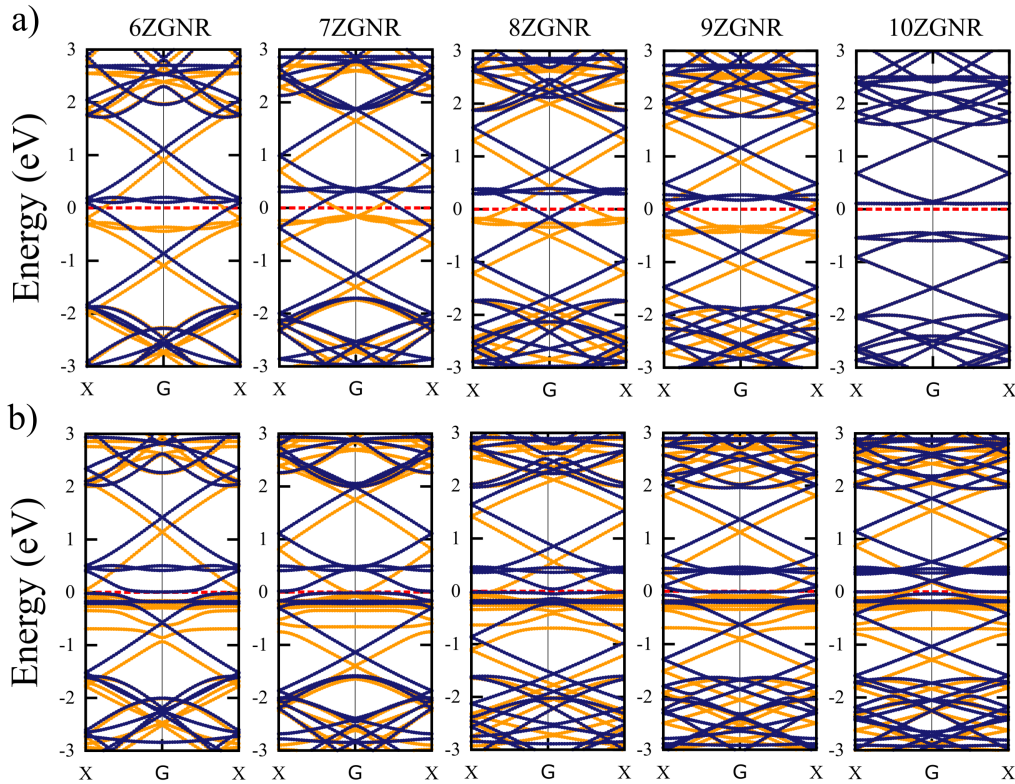


Figure 5.14: Energy band structure of (a) bare and (b) chlorinated ZGNRs as a function of length. Sizes of ZGNRs are given at the top of the figure for each. Blue and yellow lines represent the majority and minority spin states, respectively.

The calculated energy band structures of bare and chlorinated ZGNRs for different sizes are given in Figure 5.14. Comparing with the band structure of bare ZGNRs

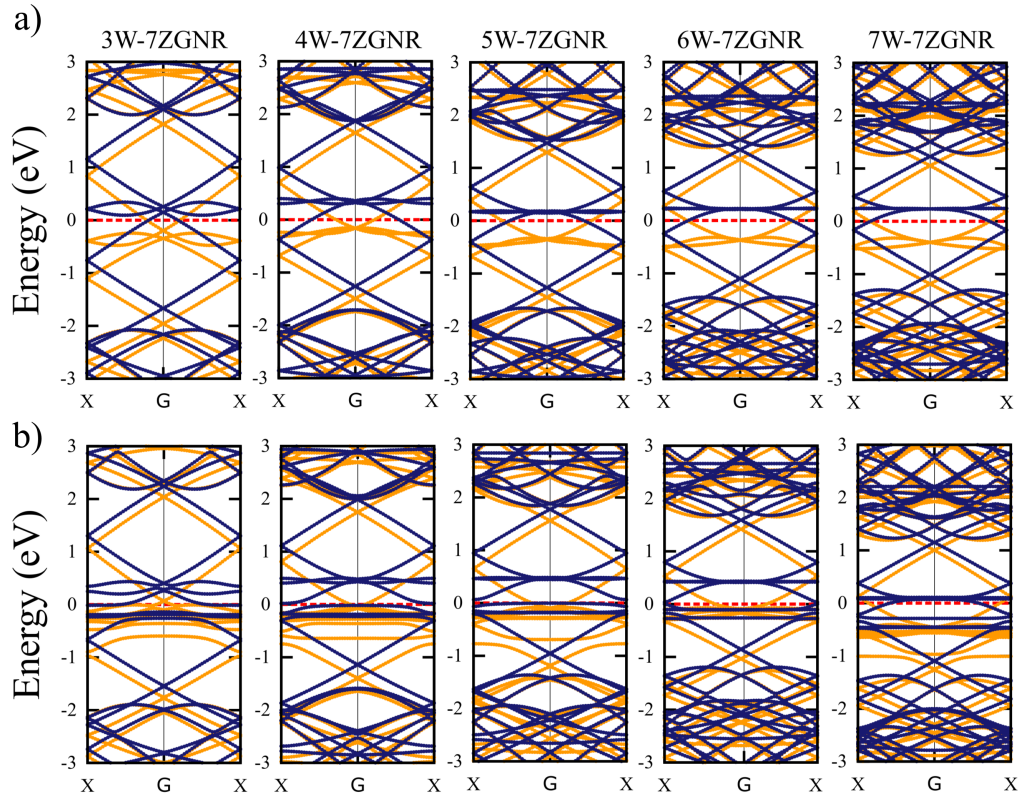


Figure 5.15: Energy band structure of bare (a) and chlorinated (b) ZGNRs as a function of width. Sizes of ZGNRs are given at the top of the figure for each. Blue and yellow lines represent the majority and minority spin states, respectively.

in Figure 5.14 (a), the electronic property of bare ZGNRs can be modulated upon the adsorption of the Cl atom. From Figure 5.14 (b), we can easily see that the Cl states are mostly localized around the top of valence band and hybridize with the states of bare ZGNRs the valence band. This is also suggest that the conductance of chlorinated ZGNRs can not be enhanced with the effect of the single Cl atom at the center of the ZGNRs.

In general, H-terminated ZGNRs are always metallic, and as expected, the energy bands become denser with increasing the width. Our results show that when the length and width of the structure increases, the state around the Fermi level becomes more flat, see Figure 5.14 and 5.15. As the Cl-Cl interaction decreases with decreasing concentration, this state loses its dispersive character and becomes more localized. It is interesting to note that the band splitting with the effect of the spin polarization for

the bare 10ZGNR disappears, and a band opening appears as seen in Figure 5.14 (a). However, this behavior changes with the adsorption of single Cl atom. We have also found that the states around the Fermi level move through the conduction band upon adsorption of single Cl atom.

The calculated adsorption energies of single Cl atom on different size of AGNRs as a function of length are given in Figure 5.16 (a). The results reveal that the adsorption energy of the Cl atom at the center of the AGNR decreases as the length of AGNR is increased. This indicates a substantial lateral repulsive interaction between the Cl atoms. The chlorinated AGNRs can be stabilized by decreasing the length, while the partial Bader charge of Cl atom increases, see Figure 5.16 (b). We observed that the C-Cl bond distances increase with increasing AGNR length. The changes of the C-Cl bond distance as a function of length and width are given in Figure 5.16 (c) and (d).

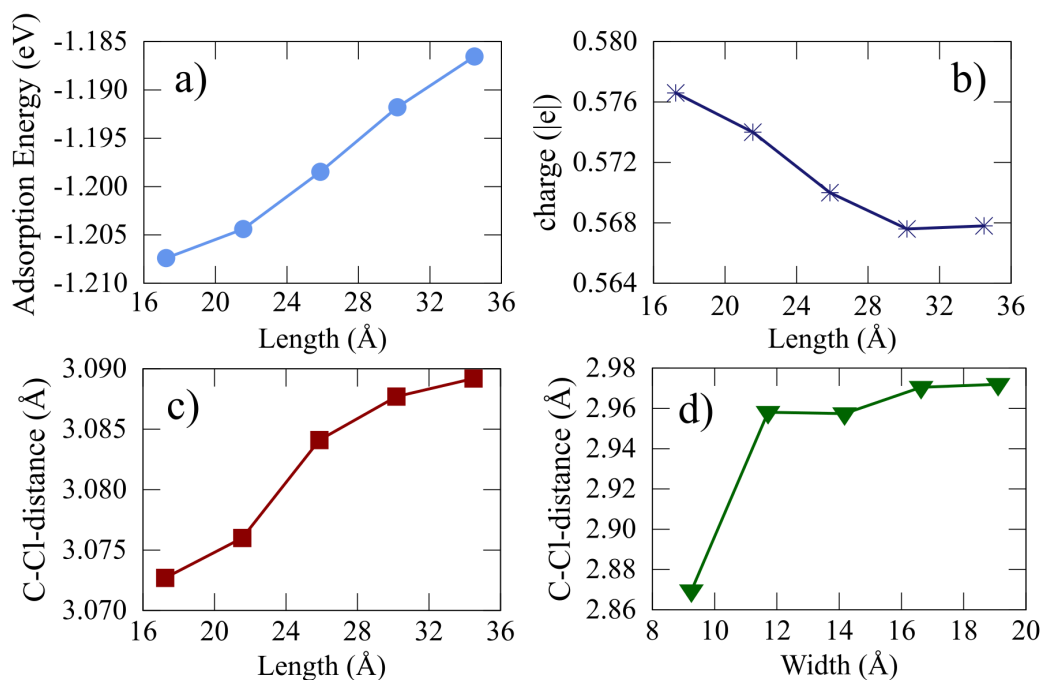


Figure 5.16: (a) Calculated adsorption energy of single Cl atom as a function of length of AGNRs. (b) Transferred Bader charges to the adsorbed Cl atom as a function of length of AGNRs. (c) and (d) C-Cl bond distance of adsorbed Cl atom as a function of length and width of AGNRs.

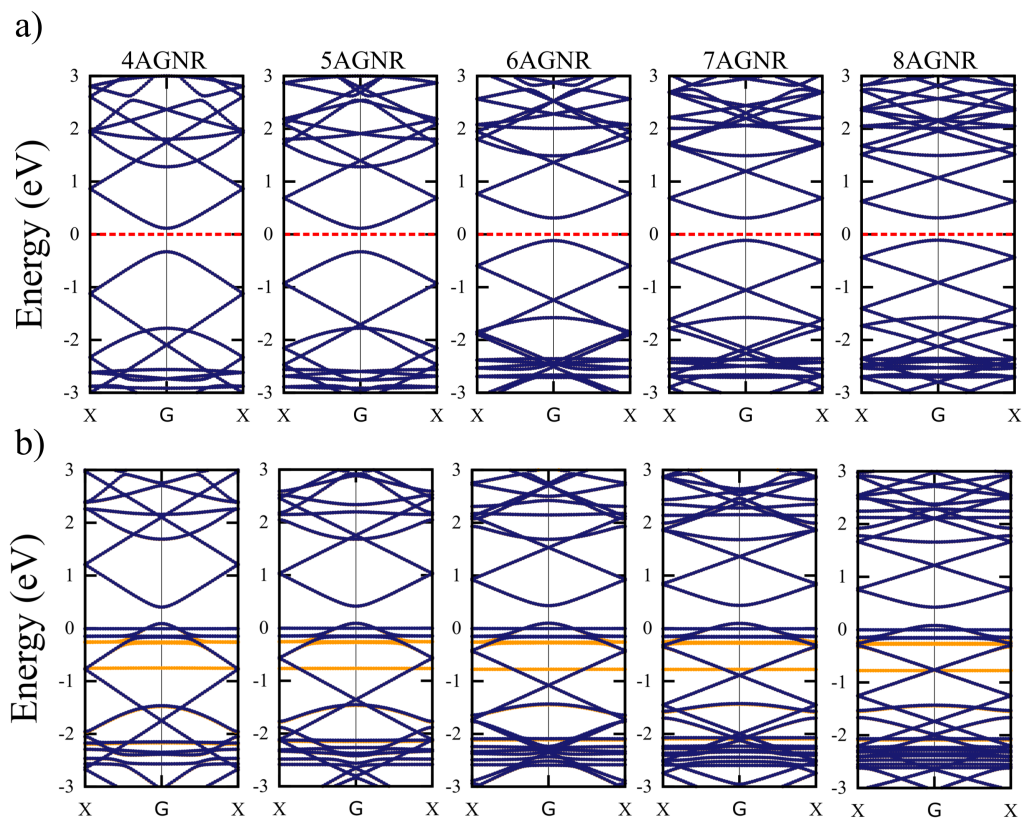


Figure 5.17: Energy band structure as a function of length of bare (a) and chlorinated (b) AGNRs. Sizes of AGNRs are given at the top of the figure for each. Blue and yellow lines represent the majority and minority spin states, respectively.

H-terminated AGNRs are nonmagnetic semiconductors and the band gap can vary depending on the size of structure. Our findings show that the opening band gap values are nearly same and the structures are nonmagnetic. The calculated energy band structures depending on the length and width of AGNRs are presented in Figure 5.17 and 5.18, respectively. Although the band gap values are not changed with increasing of the length, they can be tuned with the width of AGNRs. For example, the gap is decreasing until the width becomes 23.5 \AA (in 5W-4AGNR) then it is increasing as seen in Figure 5.18 (a). In theory, if the width of the structure increases well enough, the band gap goes to zero [343]. But, it is not possible to simulate the larger size of structure in DFT to see the zero band gap of AGNRs. Therefore, we have only tried to catch a trend between the size and some electronic properties in this part of study.

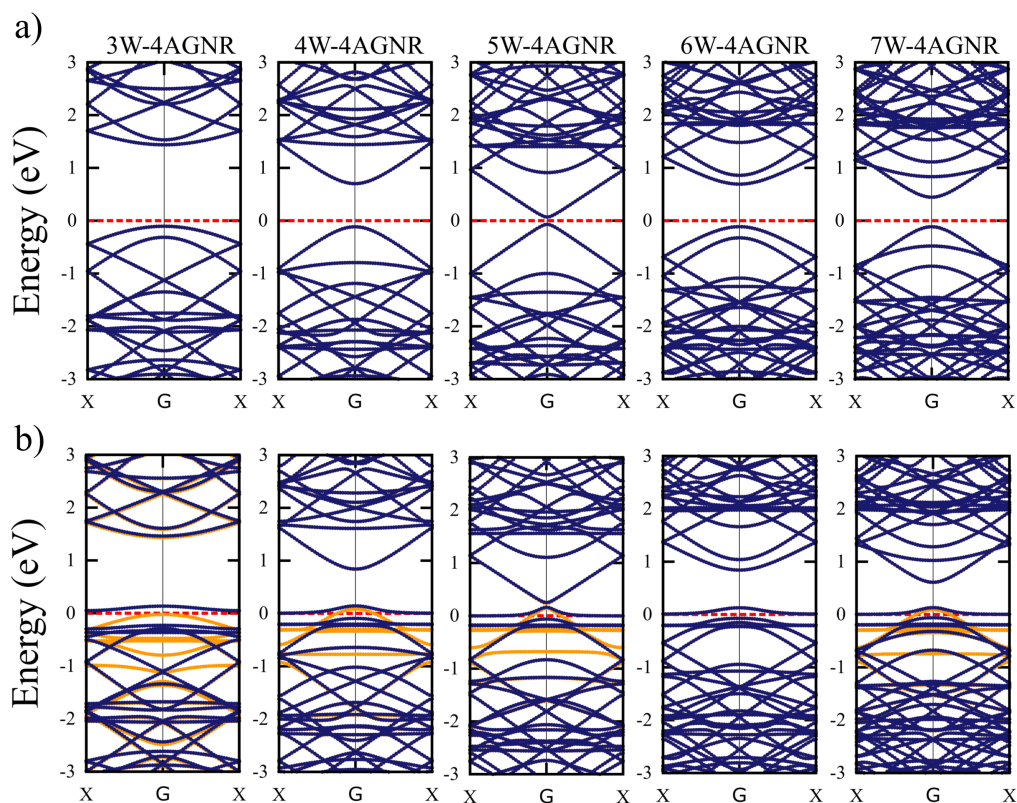


Figure 5.18: Energy band structure as a function of width of (a) bare and (b) chlorinated AGNRs. Sizes of AGNRs are given at the top of the figure for each. Blue and yellow lines represent the majority and minority spin states, respectively.

The adsorption of single Cl atom introduces new states in the band gap, and the Fermi levels cross these states, see Figure 5.17 (b) and 5.18 (b). The band gap values in chlorinated AGNRs decrease with respect to the ones in bare AGNRs. The majority/minority spin states of Cl atom can be easily seen at around the Fermi level. These states may enhance the conductance of the system because of the very localized new states. We also found that the adsorption of Cl atom does not change the band gap value when the size of AGNRs is changed.

CHAPTER 6

CONCLUSION

In the carbon based gas production, WGS reaction is one of the oldest key catalytic reactions and an intermediate step for H₂ enrichment and CO reduction in the synthesis gas. The rate of the WGS reaction is related with the active surface and structure of catalyst, the size of the catalyst and the thermodynamic conditions of the environment. In catalytic systems, the metal nano particles supported on oxides represent a promising new class of active catalysts. One of the mostly used oxides in heterogeneous catalysis is transition Al₂O₃, and its activity and reactivity can be tuned with an active metal such as Pt, Au or Rh. In the first part of the thesis, a DFT computations were carried out to investigate adsorption geometries of CO, CO₂ and H₂O molecules on bare and Pt supported γ - Al₂O₃(100) surface. The most stable adsorption configurations were identified in terms of the adsorption energies and the nature of bond. The vibrational analysis for the adsorbed molecules allows to find the most stable configurations. CO binds more strongly to di-atomic Pt clusters compared to a single Pt atom. However, the C-down geometries for CO molecule are not stable as much as O-down geometries with respect to the adsorption energies. In all cases, the CO bond weakens upon adsorption as evidenced by the larger bond lengths and decreased stretching frequencies. The vibrational energies of the adsorbate on the surface is very useful to appropriate the adsorption geometries of the CO molecule. The charge transfer occurs from the metal atom to the molecule in the case of CO adsorption. For the CO₂ adsorption on bare surface, we have identified three different geometries, and the most stable one with respect to the calculated adsorption energy is adsorbed on the surface as carbonate (CO₃). Moreover, the degenerate bending mode frequencies as a result of linear geometry of CO₂ in gas phase are lifted to two different bending modes as in-plane and out of-plane. We also observed that

the mono- and di-atomic Pt clusters play an important role on the interaction of the CO₂ depending on the adsorption geometries. H₂O adsorption energies on Pt clusters are enhanced with respect to the adsorption on the Al sites. However, the molecules do not contribute directly around the Fermi level upon adsorption of the H₂O on the surface and they change the Pt cluster structure causing its contribution to change. The calculated vibrational frequencies for H₂O on bare γ -Al₂O₃(100) surface are in good agreement with the literature. We found the differences in symmetric stretching mode frequencies correlate with the decreasing of H₂O bond angle. However, the asymmetric mode frequencies are not affected to the same extent.

TMCs have found growing application in materials science over the past decade, especially due to their desirable elastic properties. Their versatility is in part thanks to their unique bonding, which displays a mixture of ionic, metallic and covalent character. In addition to applications requiring superhard materials, TMCs have also been used more recently as catalysts in several industrially relevant reactions. Beside the importance of the active metal and adsorption configurations, one of the important factors in catalytic applications is the support material. It has a great influence on the efficiency and activity of a catalytic reaction. Kinetics and product selectivity of TMCs can be different depending on catalytic reaction path and the nature of metal center. The synthesizing and stabilizing of ZB phase of PtC are difficult due to the big mass difference between the Pt and C atoms. However, the bulk structure of PtC have been studied for several purpose such as exclusive elastic properties. In this part of thesis, structural and electronic properties of five different surface structure of ZB PtC were studied based on DFT. The work functions of the surfaces were found greater than 5.0 eV which is consistent with the other noble metals such as Au, Pt or Pd. Several adsorption geometries have been identified for atomic oxygen with the adsorption energies. In the case of catalytic applications, due to the importance of the support materials, the defected Pt/C-terminated PtC(111) surfaces have been studied, and vacancy formation energies and the energetics of O adsorption were also calculated. We found that the creating C-vacancy on C-terminated ZB PtC(111) surface is an exothermic while it is endothermic for the Pt-vacancy on Pt-terminated ZB PtC(111) surface. It is important to note that the existence of the vacancies on the PtC(111) surfaces does not change the activity of the surfaces in the case of the O

adsorption.

In the case of atomic O adsorption on ZB PtC(100), PtC(110) and PtC(111) surfaces, the C-terminated surfaces indicate high affinity of oxygen because of the higher charge transfer and adsorption energies. We have found that the most stable adsorption geometries are on-top C and C-C bridge configurations on C-terminated ZB PtC(100) surface which is significantly more stable than the Pt-terminated surfaces. Thermodynamic DFT analysis show that the C-terminated ZB PtC(100) surface is the most stable surface at higher temperature and lower partial O pressures. The higher stability of fully O covered C-terminated ZB PtC(100) surface at higher temperatures is consistent with the higher adsorption energies for the single O atom on the surface. Additionally, we have also investigated the adsorption geometries of IA, and IIIA-VIIA group of elements (B, Al, F, H, N and S) on the considered surfaces with the adsorption energies and partial charges of the species.

In many device applications, the graphene has a great potential due to their superior electronic properties. An important challenge in electronic industry is to reduce the size of devices to improve their electronic properties. Graphene is a very desirable material in the electronic industry because of its tunable properties such as charge carrier density or band gap. In the last part of the thesis, we have investigated the adsorption properties of atomic and molecular chlorine (Cl and Cl₂) on graphene sheet based on DFT. Possible adsorption geometries for Cl and Cl₂ have been identified performing the energetics of different configurations. The comparison of the adsorption energies has given that the most stable adsorption sites are on-top and hollow sites aligned parallel to the graphene plane for Cl and Cl₂, respectively. In the case of the adsorption of Cl on the opposite sides, the most stable configuration was Cl₂ on bridge site. We found that the Cl atom can be easily migrate on graphene sheet because of the lack of the energy barrier between the adsorption sites. For the adsorption of Cl atom on opposite sides on graphene sheet, the adsorption energies are found more negative with respect to the adsorbed single Cl atom because of the shorter bond length and it may be C-Cl covalent bonding character. Additionally, the electronic properties of adsorbed single Cl atom on defective graphene with SV and DV have been studied. The Dirac point moves up to the 1.21 eV with the effect of DV, and a band gap opening (0.79 eV) was observed upon adsorption of Cl atom on

defect site on graphene sheet. We observed that the adsorption of Cl on SV site in graphene does not have a substantial effect on the band gap. The applied electric field effect on the structural and electronic properties of chlorinated graphene sheet has also been studied, and the results are presented as a function of applied electric field. We found the applied electric field does not affect the Cl adsorption characteristics in graphene sheet and energy states around the Fermi energy level in the band structure. However, the created extra energy states in the conduction band implies that the conductivity of structure can be tuned with applied electric field. We have also studied the adsorption of single Cl atom on graphene nanoribbons with zig-zag and armchair edges. Although the size of nanoribbons affects the magnetization of the chlorinated ZGNRs, it does not significantly change the adsorption energies. For AGNRs the adsorption energies and also partial charges of Cl atom including the C-Cl bond distance are all affected by the size of AGNRs. We found that the single Cl atom adsorption does not influence the electronic and structural properties of ZGNRs and AGNRs so much. However, the existence of atomic Cl state at around the Fermi energy level can significantly change the transport properties of the structures, and this deserves further detailed consideration for the transport properties of the chlorinated graphene nanoribbons.

REFERENCES

- [1] Gerhard Ertl, Helmut Knozinger, Ferdi Schüth, and Jens Weitkamp. *Handbook of Heterogeneous Catalysis*. Wiley-VCH Verlag GmbH, Weinheim, Germany, 2nd edition, 2008.
- [2] David L. Trimm and Z. Ilsen Önsan. Onboard fuel conversion for hydrogen-fuel-cell-driven vehicles. *Catalysis Reviews*, 43(1-2):31–84, 2001.
- [3] Dresselhaus, M. S., and I. L. Thomas. Alternative energy technologies. *Nature*, 414(0):332 – 337, 2001.
- [4] Panagiotis Smirniotis and Krishna Gunugunuri. *Water Gas Shift Reaction, Research Developments and Applications*. Elsevier, 1st edition, 2015.
- [5] G. K. Boreskov, T. M. Yurieva, and A. S. Sergeeva. Role of phase mechanisms in oxidation reactions on solid catalysts. *Kinet. Katal.*, 11:374 – 381, 1970.
- [6] M.J. Tiernan and O.E. Finlayson. Effects of ceria on the combustion activity and surface properties of Pt/Al₂O₃ catalysts. *Applied Catalysis B: Environmental*, 19(1):23 – 35, 1998.
- [7] Alessandro Trovarelli. Catalytic properties of ceria and CeO₂-containing materials. *Catalysis Reviews*, 38(4):439–520, 1996.
- [8] Charles N. Satterfield. *Heterogeneous Catalysis in Industrial Practice*. McGraw-Hill, New York, 2nd edition, 1996.
- [9] K.G. Azzam, I.V. Babich, K. Seshan, and L. Lefferts. Bifunctional catalysts for single-stage water-gas shift reaction in fuel cell applications. *Journal of Catalysis*, 251(1):153 – 162, 2007.
- [10] K.G. Azzam, I.V. Babich, K. Seshan, and L. Lefferts. Role of Re in Pt-Re/TiO₂ catalyst for water gas shift reaction: A mechanistic and kinetic study. *Applied Catalysis B: Environmental*, 80(1):129 – 140, 2008.

- [11] P.O. Graf, D.J.M. de Vlieger, B.L. Mojet, and L. Lefferts. New insights in reactivity of hydroxyl groups in water gas shift reaction on Pt/ZrO₂. *Journal of Catalysis*, 262(2):181 – 187, 2009.
- [12] Linda Z. Liganiso, Gary Jacobs, Khalid G. Azzam, Uschi M. Graham, Burtron H. Davis, Donald C. Cronauer, A. Jeremy Kropf, and Christopher L. Marshall. Low-temperature water-gas shift: Strategy to lower Pt loading by doping ceria with Ca²⁺ improves formate mobility/wgs rate by increasing surface o-mobility. *Applied Catalysis A: General*, 394(1):105 – 116, 2011.
- [13] Neng Guo, Bradley R. Fingland, W. Damion Williams, Vincent F. Kispersky, Jelena Jelic, W. Nicholas Delgass, Fabio H. Ribeiro, Randall J. Meyer, and Jeffrey T. Miller. Determination of CO, H₂O and H₂ coverage by XANES and EXAFS on Pt and Au during water gas shift reaction. *Phys. Chem. Chem. Phys.*, 12:5678–5693, 2010.
- [14] Qiangqiang Yu, Wei Chen, Yang Li, Mingshan Jin, and Zhanghuai Suo. The action of Pt in bimetallic Au-Pt/CeO₂ catalyst for water-gas shift reaction. *Catalysis Today*, 158(3-4):324 – 328, 2010.
- [15] Weiling Deng and Maria Flytzani-Stephanopoulos. On the issue of the deactivation of Au-Ceria and Pt-Ceria water-gas shift catalysts in practical fuel-cell applications. *Angewandte Chemie International Edition*, 45(14):2285–2289, 2006.
- [16] George G. Olympiou, Christos M. Kalamaras, Constantinos D. Zeinalipour-Yazdi, and Angelos M. Efstathiou. Mechanistic aspects of the water-gas shift reaction on alumina-supported noble metal catalysts: In situ DRIFTS and SSITKA-mass spectrometry studies. *Catalysis Today*, 127(1-4):304 – 318, 2007.
- [17] D.C. Grenoble, M.M. Estadt, and D.F. Ollis. The chemistry and catalysis of the water gas shift reaction. *Journal of Catalysis*, 67(1):90 – 102, 1981.
- [18] Hyun You Kim, Hyuck Mo Lee, Raj Ganesh S. Pala, Vladimir Shapovalov, and Horia Metiu. CO oxidation by rutile TiO₂(110) doped with V, W, Cr, Mo, and Mn. *The Journal of Physical Chemistry C*, 112(32):12398–12408, 2008.

- [19] Joon B. Park, Jesus Graciani, Jaime Evans, Dario Stacchiola, Sanjaya D. Senanayake, Laura Barrio, Ping Liu, Javier Fdez. Sanz, Jan Hrbek, and José A. Rodriguez. Gold, copper, and platinum nanoparticles dispersed on $\text{CeO}_x/\text{TiO}_2(110)$ surfaces: High water-gas shift activity and the nature of the mixed-metal oxide at the nanometer level. *Journal of the American Chemical Society*, 132(1):356–363, 2010.
- [20] Vicente Rodríguez-González, Rodolfo Zanella, Lina A. Calzada, and Ricardo Gómez. Low-temperature CO oxidation and long-term stability of $\text{Au}/\text{In}_2\text{O}_3\text{-TiO}_2$ catalysts. *The Journal of Physical Chemistry C*, 113(20):8911–8917, 2009.
- [21] Antonio Gómez-Cortés, Gabriela Díaz, Rodolfo Zanella, Humberto Ramírez, Patricia Santiago, and José M. Saniger. $\text{Au-Ir}/\text{TiO}_2$ prepared by deposition precipitation with urea: Improved activity and stability in CO oxidation. *The Journal of Physical Chemistry C*, 113(22):9710–9720, 2009.
- [22] Xim Bokhimi, Rodolfo Zanella, and Carlos Angeles-Chavez. Rutile-supported Ir, Au, and Ir-Au catalysts for CO oxidation. *The Journal of Physical Chemistry C*, 114(33):14101–14109, 2010.
- [23] Paraskevi Panagiotopoulou and Dimitris I. Kondarides. Effects of alkali promotion of TiO_2 on the chemisorptive properties and water-gas shift activity of supported noble metal catalysts. *Journal of Catalysis*, 267(1):57 – 66, 2009.
- [24] Paraskevi Panagiotopoulou and Dimitris I. Kondarides. Effects of promotion of TiO_2 with alkaline earth metals on the chemisorptive properties and water-gas shift activity of supported platinum catalysts. *Applied Catalysis B: Environmental*, 101(3-4):738 – 746, 2011.
- [25] T. Shido and Y. Iwasawa. Reactant-promoted reaction mechanism for water-gas shift reaction on Rh-doped CeO_2 . *Journal of Catalysis*, 141(1):71 – 81, 1993.
- [26] Gary Jacobs, Leann Williams, Uschi Graham, Gerald A Thomas, Dennis E Sparks, and Burtron H Davis. Low temperature water-gas shift: in situ DRIFTS-reaction study of ceria surface area on the evolution of formates on

- Pt/CeO₂ fuel processing catalysts for fuel cell applications. *Applied Catalysis A: General*, 252(1):107 – 118, 2003.
- [27] Apanee Luengnaruemitchai, Somchai Osuwan, and Erdogan Gulari. Comparative studies of low-temperature water-gas shift reaction over Pt/CeO₂, Au/CeO₂, and Au/Fe₂O₃ catalysts. *Catalysis Communications*, 4(5):215 – 221, 2003.
- [28] H. Sakurai, T. Akita, S. Tsubota, M. Kiuchi, and M. Haruta. Low-temperature activity of Au/CeO₂ for water gas shift reaction, and characterization by ADF-STEM, temperature-programmed reaction, and pulse reaction. *Applied Catalysis A: General*, 291(1-2):179 – 187, 2005.
- [29] Weiling Deng, Anatoly I. Frenkel, Rui Si, and Maria Flytzani-Stephanopoulos. Reaction-relevant gold structures in the low temperature water-gas shift reaction on Au-CeO₂. *The Journal of Physical Chemistry C*, 112(33):12834–12840, 2008.
- [30] Ying Chen, Jun Cheng, P. Hu, and Haifeng Wang. Examining the redox and formate mechanisms for water-gas shift reaction on Au/CeO₂ using density functional theory. *Surface Science*, 602(17):2828 – 2834, 2008.
- [31] Kingkaew Chayakul, Tipaporn Srithanratana, and Sunantha Hengrasmee. Effect of re addition on the activities of Co/CeO₂ catalysts for water gas shift reaction. *Journal of Molecular Catalysis A: Chemical*, 340(1-2):39 – 47, 2011.
- [32] S. J. Tauster. Strong metal-support interactions. *Accounts of Chemical Research*, 20(11):389–394, 1987.
- [33] H. Cordatos, T. Bunluesin, J. Stubenrauch, J. M. Vohs, and R. J. Gorte. Effect of ceria structure on oxygen migration for Rh/Ceria catalysts. *The Journal of Physical Chemistry*, 100(2):785–789, 1996.
- [34] S Hilaire, X Wang, T Luo, R.J Gorte, and J Wagner. A comparative study of water-gas-shift reaction over ceria supported metallic catalysts. *Applied Catalysis A: General*, 215(1):271 – 278, 2001.
- [35] Lars C. Grabow, Amit A. Gokhale, Steven T. Evans, James A. Dumesic, and Manos Mavrikakis. Mechanism of the water gas shift reaction on Pt: First

principles, experiments, and microkinetic modeling. *The Journal of Physical Chemistry C*, 112(12):4608–4617, 2008.

- [36] Amit A. Gokhale, James A. Dumesic, and Manos Mavrikakis. On the mechanism of low-temperature water gas shift reaction on copper. *Journal of the American Chemical Society*, 130(4):1402–1414, 2008.
- [37] Gary Jacobs, Patricia M. Patterson, Uschi M. Graham, Adam C. Crawford, and Burtron H. Davis. Low temperature water gas shift: the link between the catalysis of WGS and formic acid decomposition over Pt/ceria. *International Journal of Hydrogen Energy*, 30(11):1265 – 1276, 2005.
- [38] Monica Trueba and Stefano P. Trasatti. γ -Alumina as a support for catalysts: A review of fundamental aspects. *European Journal of Inorganic Chemistry*, 2005(17):3393–3403, 2005.
- [39] S. A. Nepijko, M. Klimenkov, M. Adelt, H. Kuhlenbeck, R. Schlögl, and H.-J. Freund. Structural investigation of palladium clusters on γ -AlO₃(111)/NiAl(110) with transmission electron microscopy. *Langmuir*, 15(16):5309–5313, 1999.
- [40] H. Knözinger and P. Ratnasamy. Catalytic aluminas: Surface models and characterization of surface sites. *Catal.Rev.Sci.Eng.*, 17(1), 1978.
- [41] Henry P. Pinto, R. M. Nieminen, and Simon D. Elliott. Ab initio study of γ -AlO₃ surfaces. *Phys. Rev. B*, 70:125402, Sep 2004.
- [42] Xénophon Krokidis, Pascal Raybaud, Anne-Elisabeth Gobichon, Bernadette Rebours, Patrick Euzen, and Hervé Toulhoat. Theoretical study of the dehydration process of boehmite to γ -alumina. *The Journal of Physical Chemistry B*, 105(22):5121–5130, 2001.
- [43] M Digne, P Sautet, P Raybaud, P Euzen, and H Toulhoat. Use of DFT to achieve a rational understanding of acid-basic properties of γ -alumina surfaces. *Journal of Catalysis*, 226(1):54 – 68, 2004.
- [44] Igor Levin and David Brandon. Metastable alumina polymorphs: Crystal structures and transition sequences. *Journal of the American Ceramic Society*, 81(8):1995–2012, 1998.

- [45] Wei-Fu Chen, James T. Muckerman, and Etsuko Fujita. Recent developments in transition metal carbides and nitrides as hydrogen evolution electrocatalysts. *Chem. Commun.*, 49:8896–8909, 2013.
- [46] W. Kreuter and H. Hofmann. Electrolysis: The important energy transformer in a world of sustainable energy. *International Journal of Hydrogen Energy*, 23(8):661 – 666, 1998.
- [47] John A. Turner. Sustainable hydrogen production. *Science*, 305(5686):972–974, 2004.
- [48] Zhen Qiu, Hui Huang, Jun Du, Tong Feng, Wenkui Zhang, Yongping Gan, and Xinyong Tao. NbC nanowire-supported Pt nanoparticles as a high performance catalyst for methanol electrooxidation. *The Journal of Physical Chemistry C*, 117(27):13770–13775, 2013.
- [49] Qingzhong Xu, Jun Zhao, Xing Ai, Wenzhen Qin, Dawei Wang, and Weimin Huang. Effect of Mo₂C/(Mo₂C + WC) weight ratio on the microstructure and mechanical properties of Ti(C,N)-based cermet tool materials. *Journal of Alloys and Compounds*, 649:885 – 890, 2015.
- [50] Xuebing Zhao, Yuguo Zhuo, Sha Liu, Yefei Zhou, Changchun Zhao, Caixia Wang, and Qingxiang Yang. Investigation on WC/TiC interface relationship in wear-resistant coating by first-principles. *Surface and Coatings Technology*, 305:200 – 207, 2016.
- [51] Hee-Young Park, In-Su Park, Baek Choi, Kug-Seung Lee, Tae-Yeol Jeon, Yung-Eun Sung, and Sung Jong Yoo. Pd nanocrystals on WC as a synergistic electrocatalyst for hydrogen oxidation reactions. *Phys. Chem. Chem. Phys.*, 15:2125–2130, 2013.
- [52] Yuanyuan Liang, Litao Chen, and Chun'an Ma. Kinetics and thermodynamics of H₂O dissociation and CO oxidation on the Pt/WC (0001) surface: A density functional theory study. *Surface Science*, 656:7 – 16, 2017.
- [53] V. R. Kislov, V. V. Skudin, and A. Adamu. New bimetallic Mo₂C–WC/Al₂O₃ membrane catalysts in the dry reforming of methane. *Kinetics and Catalysis*, 58(1):73–80, 2017.

- [54] Yang Huang, Qiufang Gong, Xuening Song, Kun Feng, Kaiqi Nie, Feipeng Zhao, Yeyun Wang, Min Zeng, Jun Zhong, and Yanguang Li. Mo₂C nanoparticles dispersed on hierarchical carbon microflowers for efficient electrocatalytic hydrogen evolution. *ACS Nano*, 10(12):11337–11343, 2016.
- [55] Yongjun Tian, Bo Xu, and Zhisheng Zhao. Microscopic theory of hardness and design of novel superhard crystals. *International Journal of Refractory Metals and Hard Materials*, 33:93 – 106, 2012.
- [56] Louis Toth. *Transition Metal Carbides and Nitrides*. Elsevier, 1st edition, 1971.
- [57] Sergio Trasatti. Work function, electronegativity, and electrochemical behaviour of metals. *Journal of Electroanalytical Chemistry and Interfacial Electrochemistry*, 39(1):163 – 184, 1972.
- [58] Elizabeth Santos and Wolfgang Schmickler. d-band catalysis in electrochemistry. *ChemPhysChem*, 7(11):2282–2285, 2006.
- [59] Jeff Greeley, Thomas F. Jaramillo, Jacob Bonde, Ib Chorkendorff, and Jens K. Nørskov. Computational high-throughput screening of electrocatalytic materials for hydrogen evolution. *Nat Mater*, 5:909–913, 2006.
- [60] E. Santos and W. Schmickler. Fundamental aspects of electrocatalysis. *Chemical Physics*, 332(1):39 – 47, 2007.
- [61] W. Hume-Rothery. The engel-brewer theories of metals and alloys. *Progress in Materials Science*, 13:229 – 265, 1968.
- [62] Ram Subbaraman, Dusan Tripkovic, Dusan Strmcnik, Kee-Chul Chang, Masanobu Uchiumura, Arvydas P. Paulikas, Vojislav Stamenkovic, and Nenad M. Markovic. Enhancing hydrogen evolution activity in water splitting by tailoring Li⁺-Ni(OH)₂-Pt interfaces. *Science*, 334(6060):1256–1260, 2011.
- [63] F Viñes, C Sousa, P Liu, J a Rodriguez, and F Illas. A systematic density functional theory study of the electronic structure of bulk and (001) surface of transition-metals carbides. *The Journal of chemical physics*, 122(17):174709, 2005.

- [64] J. K. Norskov, T. Bligaard, J. Rossmeisl, and C. H. Christensen. Towards the computational design of solid catalysts. *Nat Chem*, 1:37–46, 2009.
- [65] Ram Subbaraman, Dusan Tripkovic, Kee-Chul Chang, Dusan Strmcnik, Arvydas P. Paulikas, Pussana Hirunsit, Maria Chan, Jeff Greeley, Vojislav Stamenkovic, and Nenad M. Markovic. Trends in activity for the water electrolyser reactions on 3d M(Ni, Co, Fe, Mn) hydr(oxy)oxide catalysts. *Nat Mater*, 11:550–557, 2012.
- [66] Tzu-Yin Chen, Yung-Huang Chang, Chang-Lung Hsu, Kung-Hwa Wei, Chia-Ying Chiang, and Lain-Jong Li. Comparative study on MoS₂ and WS₂ for electrocatalytic water splitting. *International Journal of Hydrogen Energy*, 38(28):12302 – 12309, 2013.
- [67] Thomas F. Jaramillo, Kristina P. Jørgensen, Jacob Bonde, Jane H. Nielsen, Sebastian Horch, and Ib Chorkendorff. Identification of active edge sites for electrochemical H₂ evolution from MoS₂ nanocatalysts. *Science*, 317(5834):100–102, 2007.
- [68] RB Levy and M Boudart. Platinum-like behavior of tungsten carbide in surface catalysis. *Science*, 181(4099):547–549, 1973.
- [69] Dong Ju Moon and Jong Woo Ryu. Molybdenum carbide water–gas shift catalyst for fuel cell-powered vehicles applications. *Catalysis letters*, 92(1-2):17–24, 2004.
- [70] C Pistonesi, A Juan, AP Farkas, and F Solymosi. Effects of potassium on the adsorption of methanol on β -Mo₂C (001) surface. *Surface Science*, 604(11):914–919, 2010.
- [71] Hui Ren, Danielle A. Hansgen, Alan L. Stottlemyer, Thomas G. Kelly, and Jingguang G. Chen. Replacing Platinum with Tungsten Carbide (WC) for Reforming Reactions: Similarities in Ethanol Decomposition on Ni/Pt and Ni/WC Surfaces. *ACS Catalysis*, 1(4):390–398, 2011.
- [72] Sanjubala Sahoo, Arthur C. Reber, and Shiv N. Khanna. Conceptual basis for understanding C-C bond activation in ethane by second row transition metal carbides. *The Journal of Physical Chemistry A*, 119(51):12855–12861, 2015.

- [73] Tian Yi Ma, Jian Liang Cao, Mietek Jaroniec, and Shi Zhang Qiao. Interacting carbon nitride and titanium carbide nanosheets for high-performance oxygen evolution. *Angewandte Chemie International Edition*, 55(3):1138–1142, 2016.
- [74] Christian Kunkel, Francesc Vines, and Francesc Illas. Transition metal carbides as novel materials for CO₂ capture, storage, and activation. *Energy Environ. Sci.*, 9:141–144, 2016.
- [75] Cristina Giordano, Christian Erpen, Weitang Yao, Bettina Milke, and Markus Antonietti. Metal nitride and metal carbide nanoparticles by a soft urea pathway. *Chemistry of Materials*, 21(21):5136–5144, 2009.
- [76] Cristina Giordano and Markus Antonietti. Synthesis of crystalline metal nitride and metal carbide nanostructures by sol-gel chemistry. *Nano Today*, 6(4):366–380, 2011.
- [77] Jingguang G. Chen. Carbide and nitride overlayers on early transition metal surfaces: Preparation, characterization, and reactivities. *Chemical Reviews*, 96(4):1477–1498, 1996.
- [78] M. D. Rasmussen, L. M. Molina, and B. Hammer. Adsorption, diffusion, and dissociation of molecular oxygen at defected TiO₂(110): A density functional theory study. *The Journal of Chemical Physics*, 120(2):988–997, 2004.
- [79] Gianfranco Pacchioni. Modeling doped and defective oxides in catalysis with density functional theory methods: Room for improvements. *The Journal of Chemical Physics*, 128(18):182505–182515, 2008.
- [80] Xin-Ping Wu and Xue-Qing Gong. Clustering of Oxygen Vacancies at CeO₂(111): Critical Role of Hydroxyls. *Physical Review Letters*, 116:086102, 2016.
- [81] Riichiro Saito, G. Dresselhaus, and M. S. Dresselhaus. *Physical Properties of Carbon Nanotubes*. Imperial College Press, 1st edition, 1998.
- [82] R. Keown. Energy bands in diamond. *Phys. Rev.*, 150:568–573, Oct 1966.
- [83] Heidi B. Martin, Alberto Argoitia, Uziel Landau, Alfred B. Anderson, and

- John C. Angus. Hydrogen and oxygen evolution on boron-doped diamond electrodes. *Journal of The Electrochemical Society*, 143(6):L133–L136, 1996.
- [84] Di Zhu, Linghong Zhang, Rose E. Ruther, and Robert J. Hamers. Photo-illuminated diamond as a solid-state source of solvated electrons in water for nitrogen reduction. *Nature Materials*, 12:836–841, 2013.
- [85] Brian Thomas Kelly. *Physics of graphite*. Applied Science, Englewood, N.J., London, 1st edition, 1981.
- [86] P. R. Wallace. The band theory of graphite. *Phys. Rev.*, 71:622–634, May 1947.
- [87] De en Jiang, Valentino R. Cooper, and Sheng Dai. Porous graphene as the ultimate membrane for gas separation. *Nano Letters*, 9(12):4019–4024, 2009.
- [88] Maher F. El-Kady, Yuanlong Shao, and Richard B. Kaner. Graphene for batteries, supercapacitors and beyond. *Nature Reviews Materials*, 1:16033, 2016.
- [89] Hyesung Park, Patrick R. Brown, Vladimir Bulović, and Jing Kong. Graphene as transparent conducting electrodes in organic photovoltaics: Studies in graphene morphology, hole transporting layers, and counter electrodes. *Nano Letters*, 12(1):133–140, 2012.
- [90] Marcus Freitag, Mathias Steiner, Yves Martin, Vasili Perebeinos, Zhihong Chen, James C. Tsang, and Phaedon Avouris. Energy dissipation in graphene field-effect transistors. *Nano Lett.*, 9:1883–1888, 2009.
- [91] Yu-Ming Lin, Keith A. Jenkins, Alberto Valdes-Garcia, Joshua P. Small, Damon B. Farmer, and Phaedon Avouris. Operation of graphene transistors at gigahertz frequencies. *Nano Lett.*, 9:422–426, 2009.
- [92] K. S. Novoselov, D. Jiang, F. Schedin, T. J. Booth, V. V. Khotkevich, S. V. Morozov, and A. K. Geim. Two-dimensional atomic crystals. *Proceedings of the National Academy of Sciences of the United States of America*, 102(30):10451–10453, 2005.
- [93] K.S. Novoselov, A.K. Geim, S.V. Morozov, M.I. Katsnelson D. Jiang, I.V.

- Grigorieva, S.V. Dubonos, and A.A. Firsov. Two-dimensional gas of massless dirac fermions in graphene. *Nature*, 438:197–200, 2005.
- [94] Yuanbo Zhang, Yan-Wen Tan, Horst L. Stormer, and Philip Kim. Experimental observation of the quantum hall effect and berry’s phase in graphene. *Nature*, 438:201–204, 2005.
- [95] Yoshiyuki Miyamoto, Kyoko Nakada, and Mitsutaka Fujita. First-principles study of edge states of h-terminated graphitic ribbons. *Phys. Rev. B*, 59:9858–9861, Apr 1999.
- [96] Katsunori Wakabayashi, Mitsutaka Fujita, Hiroshi Ajiki, and Manfred Sgrist. Electronic and magnetic properties of nanographite ribbons. *Phys. Rev. B*, 59:8271–8282, Mar 1999.
- [97] N. D. Mermin. Crystalline order in two dimensions. *Phys. Rev.*, 176:250–254, Dec 1968.
- [98] N. D. Mermin. Erratum: Crystalline order in two dimensions. *Phys. Rev. B*, 20:4762–4762, Dec 1979.
- [99] N. D. Mermin. Erratum: Erratum: Crystalline order in two dimensions [Phys. Rev. 176, 250 (1968)][Phys. Rev. B 20, 4762 (1979)]. *Phys. Rev. B*, 74:149902, Oct 2006.
- [100] K. S. Novoselov, A. K. Geim, S. V. Morozov, D. Jiang, Y. Zhang, S. V. Dubonos, I. V. Grigorieva, and A. A. Firsov. Electric field effect in atomically thin carbon films. *Science*, 306(5696):666–669, 2004.
- [101] Claire Berger, Zhimin Song, Xuebin Li, Xiaosong Wu, Nate Brown, Cécile Naud, Didier Mayou, Tianbo Li, Joanna Hass, Alexei N. Marchenkov, Edward H. Conrad, Phillip N. First, and Walt A. de Heer. Electronic confinement and coherence in patterned epitaxial graphene. *Science*, 312(5777):1191–1196, 2006.
- [102] S. Y. Zhou, G.-H. Gweon, J. Graf, A. V. Fedorov, C. D. Spataru, R. D. Diehl, Y. Kopelevich, D.-H. Lee, Steven G. Louie, , and A. Lanzara. First direct observation of dirac fermions in graphite. *Nat Phys*, 2:595–599, 2006.

- [103] Vadim V. Cheianov and Vladimir I. Fal'ko. Friedel oscillations, impurity scattering, and temperature dependence of resistivity in graphene. *Phys. Rev. Lett.*, 97:226801, Nov 2006.
- [104] K.I. Bolotin, K.J. Sikes, Z. Jiang, M. Klima, G. Fudenberg, J. Hone, P. Kim, and H.L. Stormer. Ultrahigh electron mobility in suspended graphene. *Solid State Communications*, 146(9):351 – 355, 2008.
- [105] A. A. Balandin, S. Ghosh, W. Bao, I. Calizo, D. Teweldebrhan, F. Miao, and C. N. Lau. Superior thermal conductivity of single-layer graphene. *Nano Lett.*, 8(3):902–907, 2008.
- [106] Daniel Huertas-Hernando, F. Guinea, and Arne Brataas. Spin-orbit coupling in curved graphene, fullerenes, nanotubes, and nanotube caps. *Phys. Rev. B*, 74:155426, Oct 2006.
- [107] Tim J. Booth, Peter Blake, Rahul R. Nair, Da Jiang and Ernie W. Hill, Ursel Bangert, Andrew Bleloch, Mhairi Gass, Kostya Novoselov, M. I. Katsnelson, , and A. K. Geim. Macroscopic graphene membranes and their extraordinary stiffness. *Nano Lett.*, 8(8):2442–2446, 2008.
- [108] Changyao Chen, Sami Rosenblatt, Kirill I. Bolotin, William Kalb, Philip Kim, Ioannis Kymissis, Horst L. Stormer, Tony F. Heinz, , and James Hone. Performance of monolayer graphene nanomechanical resonators with electrical readout. *Nature Nanotechnology*, 4:861–867, 2009.
- [109] E. W. Hill, A. K. Geim, K. Novoselov, F. Schedin, and P. Blake. Graphene spin valve devices. *IEEE Transactions on Magnetism*, 42(10):2694–2696, Oct 2006.
- [110] Nikolaos Tombros, Csaba Jozsa, Mihaita Popinciuc, Harry T. Jonkman, and Bart J. van Wees. Electronic spin transport and spin precession in single graphene layers at room temperature. *Nature*, 448:571–574, 2007.
- [111] Sungjae Cho, Yung-Fu Chen, and Michael S. Fuhrer. Gate-tunable graphene spin valve. *Applied Physics Letters*, 91(12):123105, 2007.

- [112] Melinda Y. Han, Barbaros Özyilmaz, Yuanbo Zhang, and Philip Kim. Energy band-gap engineering of graphene nanoribbons. *Phys. Rev. Lett.*, 98:206805, May 2007.
- [113] Xiaoting Jia, Mario Hofmann, Vincent Meunier, Bobby G. Sumpter, Jessica Campos-Delgado, José Manuel Romo-Herrera, Hyungbin Son, Ya-Ping Hsieh, Alfonso Reina, Jing Kong, Mauricio Terrones, and Mildred S. Dresselhaus. Controlled formation of sharp zigzag and armchair edges in graphitic nanoribbons. *Science*, 323(5922):1701–1705, 2009.
- [114] Jinming Cai, Pascal Ruffieux, Rached Jaafar, Marco Bieri, Thomas Braun, Stephan Blankenburg, Matthias Muoth, Ari P. Seitsonen, Moussa Saleh, Xinliang Feng, Klaus Müllen, and Roman Fasel. Atomically precise bottom-up fabrication of graphene nanoribbons. *Nature*, 466:470–473, 2010.
- [115] Dmitry V. Kosynkin, Amanda L. Higginbotham, Alexander Sinitskii, Jay R. Lomeda, Ayrat Dimiev, B. Katherine Price, and James M. Tour. Longitudinal unzipping of carbon nanotubes to form graphene nanoribbons. *Nature*, 458:872–876, 2009.
- [116] Chenggang Tao, Liying Jiao, Oleg V. Yazyev, Yen-Chia Chen, Juanjuan Feng, Xiaowei Zhang, Rodrigo B. Capaz, James M. Tour, Alex Zettl, Steven G. Louie, Hongjie Dai, and Michael F. Crommie. Spatially resolving edge states of chiral graphene nanoribbons. *Nature Physics*, 7:616–620, 2011.
- [117] W. Jaskólski, A. Ayuela, M. Pelc, H. Santos, and L. Chico. Edge states and flat bands in graphene nanoribbons with arbitrary geometries. *Phys. Rev. B*, 83:235424, Jun 2011.
- [118] K Tanaka, S Yamashita, H Yamabe, and T Yamabe. Electronic properties of one-dimensional graphite family. *Synthetic Metals*, 17(1):143 – 148, 1987.
- [119] Stephen E. Stein and R. L. Brown. π -electron properties of large condensed polyaromatic hydrocarbons. *Journal of the American Chemical Society*, 109(12):3721–3729, 1987.
- [120] Kyoko Nakada, Mitsutaka Fujita, Gene Dresselhaus, and Mildred S. Dressel-

- haus. Edge state in graphene ribbons: Nanometer size effect and edge shape dependence. *Phys. Rev. B*, 54:17954–17961, Dec 1996.
- [121] E. Bright Wilson and Paul C. Cross J.C. Decius. *Physics of Condensed Matter*. Academic Press, Inc, New York, 1st edition, 2010.
- [122] D.R. Hartree. The wave mechanics of an atom with a non-coulomb central field. part iii. term values and intensities in series in optical spectra. *Mathematical Proceedings of the Cambridge Philosophical Society*, 24(3):426–437, 1928.
- [123] D.R. Hartree. Näherungsmethode zur lösung des quantenmechanischen mehrkörperproblems. *Z.Phys.*, 61(-):126–148, 1930.
- [124] L. H. Thomas. The calculation of atomic fields. *Mathematical Proceedings of the Cambridge Philosophical Society*, 23(5):542–548, 1927.
- [125] E. Fermi. Eine statistische methode zur bestimmung einiger eigenschaften des atoms und ihre anwendung auf die theorie des periodischen systems der elemente. *Zeitschrift für Physik*, 48(1):73–79, 1928.
- [126] P. A. M. Dirac. Quantum mechanics of many-electron systems. *Proceedings of the Royal Society of London A: Mathematical, Physical and Engineering Sciences*, 123(792):714–733, 1929.
- [127] P. A. M. Dirac. Note on exchange phenomena in the thomas atom. *Mathematical Proceedings of the Cambridge Philosophical Society*, 26(3):376–385, 1930.
- [128] R. O. Jones and O. Gunnarsson. The density functional formalism, its applications and prospects. *Rev. Mod. Phys.*, 61:689–746, Jul 1989.
- [129] P. Hohenberg and W. Kohn. Inhomogeneous electron gas. *Phys. Rev.*, 136:B864–B871, Nov 1964.
- [130] W. Kohn and L. J. Sham. Self-consistent equations including exchange and correlation effects. *Phys. Rev.*, 140:A1133–A1138, Nov 1965.
- [131] P. Pulay. Improved SCF convergence acceleration. *Journal of Computational Chemistry*, 3(4):556–560, 1982.

- [132] Péter Pulay. Convergence acceleration of iterative sequences. the case of scf iteration. *Chemical Physics Letters*, 73(2):393 – 398, 1980.
- [133] Ernest R. Davidson. Super-matrix methods. *Computer Physics Communications*, 53(1):49 – 60, 1989.
- [134] Ernest R. Davidson. The iterative calculation of a few of the lowest eigenvalues and corresponding eigenvectors of large real-symmetric matrices. *Journal of Computational Physics*, 17(1):87 – 94, 1975.
- [135] D M Wood and A Zunger. A new method for diagonalising large matrices. *Journal of Physics A: Mathematical and General*, 18(9):1343, 1985.
- [136] E. Wigner. On the interaction of electrons in metals. *Phys. Rev.*, 46:1002–1011, Dec 1934.
- [137] Murray Gell-Mann and Keith A. Brueckner. Correlation energy of an electron gas at high density. *Phys. Rev.*, 106:364–368, Apr 1957.
- [138] J. P. Perdew and Alex Zunger. Self-interaction correction to density-functional approximations for many-electron systems. *Phys. Rev. B*, 23:5048–5079, May 1981.
- [139] S. H. Vosko, L. Wilk, and M. Nusair. Accurate spin-dependent electron liquid correlation energies for local spin density calculations: a critical analysis. *Canadian Journal of Physics*, 58(8):1200–1211, 1980.
- [140] John P. Perdew. Density-functional approximation for the correlation energy of the inhomogeneous electron gas. *Phys. Rev. B*, 33:8822–8824, Jun 1986.
- [141] John P. Perdew, Kieron Burke, and Matthias Ernzerhof. Generalized Gradient Approximation Made Simple. *Phys. Rev. Lett.*, 77:3865–3868, Oct 1996.
- [142] John P. Perdew and Yue Wang. Accurate and simple analytic representation of the electron-gas correlation energy. *Physical Review B*, 45:13244–13249, Jun 1992.
- [143] Stephan Kümmel and Leor Kronik. Orbital-dependent density functionals: Theory and applications. *Rev. Mod. Phys.*, 80:3–60, Jan 2008.

- [144] Axel D. Becke. Density-functional thermochemistry. iii. the role of exact exchange. *The Journal of Chemical Physics*, 98(7):5648–5652, 1993.
- [145] Andreas Görling and Mel Levy. Hybrid schemes combining the hartree-fock method and density-functional theory: Underlying formalism and properties of correlation functionals. *The Journal of Chemical Physics*, 106(7):2675–2680, 1997.
- [146] Jochen Heyd and Gustavo E. Scuseria. Efficient hybrid density functional calculations in solids: Assessment of the heyd-scuseria-ernzerhof screened coulomb hybrid functional. *The Journal of Chemical Physics*, 121(3):1187–1192, 2004.
- [147] Jochen Heyd, Gustavo E. Scuseria, and Matthias Ernzerhof. Hybrid functionals based on a screened coulomb potential. *The Journal of Chemical Physics*, 118(18):8207–8215, 2003.
- [148] D. R. Hamann, M. Schlüter, and C. Chiang. Norm-conserving pseudopotentials. *Phys. Rev. Lett.*, 43:1494–1497, Nov 1979.
- [149] Stefan Grimme. Accurate description of van der waals complexes by density functional theory including empirical corrections. *Journal of Computational Chemistry*, 25(12):1463–1473, 2004.
- [150] Stefan Grimme. Semiempirical GGA-type density functional constructed with a long-range dispersion correction. *Journal of Computational Chemistry*, 27(15):1787–1799, 2006.
- [151] Stefan Grimme, Jens Antony, Stephan Ehrlich, and Helge Krieg. A consistent and accurate ab initio parametrization of density functional dispersion correction (DFT-D) for the 94 elements H-Pu. *The Journal of Chemical Physics*, 132(15):154104, 2010.
- [152] Alexandre Tkatchenko and Matthias Scheffler. Accurate molecular van der waals interactions from ground-state electron density and free-atom reference data. *Phys. Rev. Lett.*, 102:073005, Feb 2009.

- [153] Axel D. Becke and Erin R. Johnson. Exchange-hole dipole moment and the dispersion interaction revisited. *The Journal of Chemical Physics*, 127(15):154108, 2007.
- [154] Axel D. Becke and Erin R. Johnson. A density-functional model of the dispersion interaction. *The Journal of Chemical Physics*, 123(15):154101, 2005.
- [155] M. T. Yin and Marvin L. Cohen. Theory of ab initio pseudopotential calculations. *Phys. Rev. B*, 25:7403–7412, Jun 1982.
- [156] James C. Phillips and Leonard Kleinman. New method for calculating wave functions in crystals and molecules. *Phys. Rev.*, 116:287–294, Oct 1959.
- [157] David Vanderbilt. Soft self-consistent pseudopotentials in a generalized eigenvalue formalism. *Phys. Rev. B*, 41:7892–7895, Apr 1990.
- [158] Graeme Henkelman, Gísli Jóhannesson, and Hannes Jónsson. *Methods for Finding Saddle Points and Minimum Energy Paths*, pages 269–302. Springer Netherlands, Dordrecht, 2002.
- [159] Hannes Jossion, Greg Mills, and Karsten W. Jacobsen. *Nudged elastic band method for finding minimum energy paths of transitions*, pages 385–404. World Scientific, 2011.
- [160] Graeme Henkelman, Blas P. Uberuaga, and Hannes Jónsson. A climbing image nudged elastic band method for finding saddle points and minimum energy paths. *The Journal of Chemical Physics*, 113(22):9901–9904, 2000.
- [161] Daniel Sheppard, Rye Terrell, and Graeme Henkelman. Optimization methods for finding minimum energy paths. *The Journal of Chemical Physics*, 128(13):134106, 2008.
- [162] Graeme Henkelman and Hannes Jónsson. A dimer method for finding saddle points on high dimensional potential surfaces using only first derivatives. *The Journal of Chemical Physics*, 111(15):7010–7022, 1999.
- [163] Paolo Giannozzi, Stefano Baroni, Nicola Bonini, Matteo Calandra, Roberto Car, Carlo Cavazzoni, Davide Ceresoli, Guido L Chiarotti, Matteo Cococcioni, Ismaila Dabo, Andrea Dal Corso, Stefano de Gironcoli, Stefano Fab-

- ris, Guido Fratesi, Ralph Gebauer, Uwe Gerstmann, Christos Gougoussis, Anton Kokalj, Michele Lazzeri, Layla Martin-Samos, Nicola Marzari, Francesco Mauri, Riccardo Mazzarello, Stefano Paolini, Alfredo Pasquarello, Lorenzo Paulatto, Carlo Sbraccia, Sandro Scandolo, Gabriele Sclauzero, Ari P Seitsonen, Alexander Smogunov, Paolo Umari, and Renata M Wentzcovitch. QUANTUM ESPRESSO: a modular and open-source software project for quantum simulations of materials. *Journal of Physics: Condensed Matter*, 21(39):395502, 2009.
- [164] G. Kresse and J. Furthmüller. Efficiency of ab-initio total energy calculations for metals and semiconductors using a plane-wave basis set. *Computational Materials Science*, 6(1):15 – 50, 1996.
- [165] G. Kresse and J. Hafner. *Ab initio* molecular dynamics for liquid metals. *Phys. Rev. B*, 47:558–561, Jan 1993.
- [166] Greg Mills and Hannes Jónsson. Quantum and thermal effects in h₂ dissociative adsorption: Evaluation of free energy barriers in multidimensional quantum systems. *Phys. Rev. Lett.*, 72:1124–1127, Feb 1994.
- [167] George H. Vineyard. Frequency factors and isotope effects in solid state rate processes. *Journal of Physics and Chemistry of Solids*, 3(1):121 – 127, 1957.
- [168] E. Kaxiras, Y. Bar-Yam, J. D. Joannopoulos, and K. C. Pandey. Ab initio. *Phys. Rev. B*, 35:9625–9635, Jun 1987.
- [169] Matthias Scheffler and Jaroslaw Dabrowski. Parameter-free calculations of total energies, interatomic forces and vibrational entropies of defects in semiconductors. *Philosophical Magazine A*, 58(1):107–121, 1988.
- [170] Guo-Xin Qian, Richard M. Martin, and D. J. Chadi. First-principles study of the atomic reconstructions and energies of Ga- and As-stabilized GaAs(100) surfaces. *Phys. Rev. B*, 38:7649–7663, Oct 1988.
- [171] Terrell L. Hill. *An Introduction to Statistical Thermodynamics (Dover Books on Physics)*. Dover Publications, jan 1987.
- [172] L. Couture and R. Zitoun. *Statistical Thermodynamics and Properties of Matter*. Taylor & Francis, 2000.

- [173] Mauricio Cafiero, Sergiy Bubin, and Ludwik Adamowicz. Non-born-
oppenheimer calculations of atoms and molecules. *Phys. Chem. Chem. Phys.*,
5:1491–1501, 2003.
- [174] J. E. Jones. On the determination of molecular fields. i. from the variation of
the viscosity of a gas with temperature. *Proceedings of the Royal Society of
London. Series A, Containing Papers of a Mathematical and Physical Charac-
ter*, 106(738):441–462, 1924.
- [175] J. E. Jones. On the determination of molecular fields. ii. from the equation of
state of a gas. *Proceedings of the Royal Society of London A: Mathematical,
Physical and Engineering Sciences*, 106(738):463–477, 1924.
- [176] John T. Yates and Theodore E. Madey. *Vibrational Spectroscopy of Molecules
on Surfaces*. Plenum Press, New York, 1st edition, 1987.
- [177] Charles Kittel. *Introduction to Solid State Physics*. John Wiley & Sons, Inc.,
New York, 6th edition, 1986.
- [178] S. Califano. *Vibrational States*. John Wiley & Sons, Inc., New York, 1st edition,
1976.
- [179] E. Bright Wilson and Paul C. Cross J.C. Decius. *Molecular Vibrations*.
McGraw-Hill Book Company, Inc., New York, 1st edition, 1955.
- [180] P. Pulay. Ab initio calculation of force constants and equilibrium geometries
in polyatomic molecules. *Molecular Physics*, 17(2):197–204, 1969.
- [181] Hans Horn, Horst Weiß, Marco Háser, Michael Ehrig, and Reinhart Ahlrichs.
Prescreening of two-electron integral derivatives in SCF gradient and hessian
calculations. *Journal of Computational Chemistry*, 12(9):1058–1064, 1991.
- [182] Peter Deglmann, Klaus May, Philipp Furche, and Reinhart Ahlrichs. Nuclear
second analytical derivative calculations using auxiliary basis set expansions.
Chemical Physics Letters, 384(1-3):103 – 107, 2004.
- [183] R. S. Mulliken. Electronic population analysis on LCAO-MO molecular wave
functions. i. *The Journal of Chemical Physics*, 23(10):1833–1840, 1955.

- [184] R. S. Mulliken. Electronic population analysis on LCAO-MO molecular wave functions. ii. overlap populations, bond orders, and covalent bond energies. *The Journal of Chemical Physics*, 23(10):1841–1846, 1955.
- [185] R. S. Mulliken. Electronic population analysis on LCAO-MO molecular wave functions. iii. effects of hybridization on overlap and gross AO populations. *The Journal of Chemical Physics*, 23(12):2338–2342, 1955.
- [186] R. S. Mulliken. Electronic population analysis on LCAO-MO molecular wave functions. iv. bonding and antibonding in LCAO and valence-bond theories. *The Journal of Chemical Physics*, 23(12):2343–2346, 1955.
- [187] Kenneth E. Edgecombe and Russell J. Boyd. Atomic orbital populations and atomic charges from self-consistent field molecular orbital wavefunctions. *J. Chem. Soc., Faraday Trans. 2*, 83:1307–1315, 1987.
- [188] R.E. Christoffersen and K.A. Baker. Electron population analysis. gross atomic charges in molecules. *Chemical Physics Letters*, 8(1):4 – 9, 1971.
- [189] S. Huzinaga, Y. Sakai, E. Miyoshi, and S. Narita. Extended mulliken electron population analysis. *The Journal of Chemical Physics*, 93(5):3319–3325, 1990.
- [190] Alan E. Reed, Robert B. Weinstock, and Frank Weinhold. Natural population analysis. *The Journal of Chemical Physics*, 83(2):735–746, 1985.
- [191] Alan E. Reed, Larry A. Curtiss, and Frank Weinhold. Intermolecular interactions from a natural bond orbital, donor-acceptor viewpoint. *Chemical Reviews*, 88(6):899–926, 1988.
- [192] F. L. Hirshfeld. Bonded-atom fragments for describing molecular charge densities. *Theoretica chimica acta*, 44(2):129–138, 1977.
- [193] Richard F. W. Bader. *Atoms in Molecules; A Quantum Theory*. ClarendonPress, Oxford, UK, - edition, 1990.
- [194] Célia Fonseca Guerra, Jan-Willem Handgraaf, Evert Jan Baerends, and F. Matthias Bickelhaupt. Voronoi deformation density (VDD) charges: As-

- assessment of the mulliken, bader, hirshfeld, weinhold, and VDD methods for charge analysis. *Journal of Computational Chemistry*, 25(2):189–210, 2004.
- [195] Kris P. F. Janssen, Gert De Cremer, Robert K. Neely, Alexey V. Kubarev, Jordi Van Loon, Johan A. Martens, Dirk E. De Vos, Maarten B. J. Roeffaers, and Johan Hofkens. Single molecule methods for the study of catalysis: from enzymes to heterogeneous catalysts. *Chem. Soc. Rev.*, 43:990–1006, 2014.
- [196] G. Martino. Catalysis for oil refining and petrochemistry, recent developments and future trends. In Sagrario Mendiorez Avelino Corma, Francisco V. Melo and José Luis G. Fierro, editors, *12th International Congress on Catalysis Proceedings of the 12th ICC*, volume 130 of *Studies in Surface Science and Catalysis*, pages 83 – 103. Elsevier, 2000.
- [197] Surbhi Semwal, Ajay K. Arora, Rajendra P. Badoni, and Deepak K. Tuli. Biodiesel production using heterogeneous catalysts. *Bioresource Technology*, 102(3):2151 – 2161, 2011.
- [198] Vincent Artero and Marc Fontecave. Solar fuels generation and molecular systems: is it homogeneous or heterogeneous catalysis? *Chem. Soc. Rev.*, 42:2338–2356, 2013.
- [199] Rern Jern Lim, Mingshi Xie, Mahasin Alam Sk, Jong-Min Lee, Adrian Fisher, Xin Wang, and Kok Hwa Lim. A review on the electrochemical reduction of CO₂ in fuel cells, metal electrodes and molecular catalysts. *Catalysis Today*, 233(0):169 – 180, 2014.
- [200] Chandra Ratnasamy and Jon P. Wagner. Water gas shift catalysis. *Catalysis Reviews*, 51(3):325–440, 2009.
- [201] Salai Cheettu Ammal and Andreas Heyden. Origin of the unique activity of Pt / TiO₂ catalysts for the water-gas shift reaction . *Journal of Catalysis*, 306(0):78 – 90, 2013.
- [202] Chapman. The hydrogen economy blasts off. *Physics World*, 2002.
- [203] A. Hodgson and S. Haq. Water adsorption and the wetting of metal surfaces. *Surface Science Reports*, 64(9):381 – 451, 2009.

- [204] Uwe Burghaus. Surface chemistry of CO₂ - adsorption of carbon dioxide on clean surfaces at ultrahigh vacuum. *Progress in Surface Science*, 89(2):161 – 217, 2014.
- [205] David W. Flaherty, Wen-Yueh Yu, Zachary D. Pozun, Graeme Henkelman, and C. Buddie Mullins. Mechanism for the water-gas shift reaction on mono-functional platinum and cause of catalyst deactivation. *Journal of Catalysis*, 282(2):278 – 288, 2011.
- [206] Weiting Yu, Marc D. Porosoff, and Jingguang G. Chen. Review of pt-based bimetallic catalysis: From model surfaces to supported catalysts. *Chemical Reviews*, 112(11):5780–5817, 2012.
- [207] José A. Rodriguez. Gold-based catalysts for the water-gas shift reaction: Active sites and reaction mechanism. *Catalysis Today*, 160(1):3 – 10, 2011.
- [208] Rostam J. Madon, Drew Braden, Shampa Kandoi, Peter Nagel, Manos Mavrikakis, and James A. Dumesic. Microkinetic analysis and mechanism of the water gas shift reaction over copper catalysts. *Journal of Catalysis*, 281(1):1 – 11, 2011.
- [209] Shih-Chang Huang, Chia-Hao Lin, and J.-H. Wang. Trends of water gas shift reaction on close-packed transition metal surfaces. *The Journal of Physical Chemistry C*, 114(21):9826–9834, 2010.
- [210] Sara Aranifard, Salai Cheettu Ammal, and Andreas Heyden. On the importance of metal-oxide interface sites for the water-gas shift reaction over Pt/CeO₂ catalysts. *Journal of Catalysis*, 309(0):314 – 324, 2014.
- [211] C.I. Vignatti, M.S. Avila, C.R. Apesteguía, and T.F. Garetto. Study of the water-gas shift reaction over Pt supported on CeO₂-ZrO₂ mixed oxides. *Catalysis Today*, 171(1):297 – 303, 2011.
- [212] Sung Su Kim, Kwang Hee Park, and Sung Chang Hong. A study of the selectivity of the reverse water-gas-shift reaction over Pt/TiO₂ catalysts. *Fuel Processing Technology*, 108(0):47 – 54, 2013.
- [213] Jorge H. Pazmiño, Mayank Shekhar, W. Damion Williams, M. Cem Akatay, Jeffrey T. Miller, W. Nicholas Delgass, and Fabio H. Ribeiro. Metallic pt

- as active sites for the water-gas shift reaction on alkali-promoted supported catalysts. *Journal of Catalysis*, 286(0):279 – 286, 2012.
- [214] Kee Young Koo, Un Ho Jung, and Wang Lai Yoon. A highly dispersed Pt/ γ -Al₂O₃ catalyst prepared via deposition-precipitation method for preferential CO oxidation. *International Journal of Hydrogen Energy*, 39(11):5696 – 5703, 2014.
- [215] A.S. Ivanova, E.M. Slavinskaya, R.V. Gulyaev, V.I. Zaikovskii, O.A. Stonkus, I.G. Danilova, L.M. Plyasova, I.A. Polukhina, and A.I. Boronin. Metal-support interactions in Pt/Al₂O₃ and Pd/Al₂O₃ catalysts for CO oxidation. *Applied Catalysis B: Environmental*, 97(1-2):57 – 71, 2010.
- [216] Denise Chan, Steffen Tischer, Jasmin Heck, Claudia Diehm, and Olaf Deutschmann. Correlation between catalytic activity and catalytic surface area of a Pt/Al₂O₃ doc: An experimental and microkinetic modeling study. *Applied Catalysis B: Environmental*, 156-157(0):153 – 165, 2014.
- [217] Hirofumi Kishi, Ferensa Oemry, Tien Quang Nguyen, Shinichi Kunikata, Hiroshi Nakanishi, Hideaki Kasai, Hiroyoshi Maekawa, and Kazuo Osumi. Study of NO oxidation reaction over the pt cluster supported on γ -Al₂O₃(111) surface. *Current Applied Physics*, 12(0):S110 – S114, 2012.
- [218] Ch. Vignatti, M.S. Avila, C.R. Apesteguía, and T.F. Garetto. Catalytic and DRIFTS study of the WGS reaction on Pt-based catalysts. *International Journal of Hydrogen Energy*, 35(14):7302 – 7312, 2010.
- [219] K.G. Azzam, I.V. Babich, K. Seshan, and L. Lefferts. Bifunctional catalysts for single-stage water-gas shift reaction in fuel cell applications.: Part 1. effect of the support on the reaction sequence. *Journal of Catalysis*, 251(1):153 – 162, 2007.
- [220] Louise Samain, Aleksander Jaworski, Mattias Edén, Danielle M. Ladd, Dong-Kyun Seo, F. Javier Garcia-Garcia, and Ulrich Häussermann. Structural analysis of highly porous γ -Al₂O₃. *Journal of Solid State Chemistry*, 217(0):1 – 8, 2014.

- [221] Xiaojiang Yao, Fei Gao, and Lin Dong. The application of incorporation model in γ -Al₂O₃ supported single and dual metal oxide catalysts: A review. *Chinese Journal of Catalysis*, 34(11):1975 – 1985, 2013.
- [222] Sung Su Kim, Hyun Hee Lee, and Sung Chang Hong. A study on the effect of support's reducibility on the reverse water-gas shift reaction over Pt catalysts. *Applied Catalysis A: General*, 423-424(0):100 – 107, 2012.
- [223] M. El Doukkali, A. Iriondo, J.F. Cambra, I. Gandarias, L. Jalowiecki-Duhamel, F. Dumeignil, and P.L. Arias. Deactivation study of the Pt and/or Ni-based γ -Al₂O₃ catalysts used in the aqueous phase reforming of glycerol for H₂ production. *Applied Catalysis A: General*, 472(0):80 – 91, 2014.
- [224] Evgeniy N. Gribov, Olena Zavorotynska, Giovanni Agostini, Jenny G. Vitillo, Gabriele Ricchiardi, Giuseppe Spoto, and Adriano Zecchina. Ftir spectroscopy and thermodynamics of CO and H₂ adsorbed on γ -, δ - and α -Al₂O₃. *Phys. Chem. Chem. Phys.*, 12:6474–6482, 2010.
- [225] Riguang Zhang, Hongyan Liu, Baojun Wang, and Lixia Ling. Insights into the effect of surface hydroxyls on CO₂ hydrogenation over Pd/ γ -Al₂O₃ catalyst: A computational study. *Applied Catalysis B: Environmental*, 126(0):108 – 120, 2012.
- [226] Hongtao Wang, Lijuan Chen, Yongkang Lv, and Ruipeng Ren. H₂ dissociation on γ -Al₂O₃ supported Cu/Pd atoms: A DFT investigation. *Applied Surface Science*, 290(0):154 – 160, 2014.
- [227] YunXiang Pan, ChangJun Liu, Tomasz S. Wiltowski, and Qingfeng Ge. CO₂ adsorption and activation over γ -Al₂O₃-supported transition metal dimers: A density functional study. *Catalysis Today*, 147(2):68 – 76, 2009.
- [228] Zhixue Liu, Yuhan Wang, Jingrui Li, and Riguang Zhang. The effect of γ -Al₂O₃ surface hydroxylation on the stability and nucleation of Ni in Ni/ γ -Al₂O₃ catalyst: a theoretical study. *RSC Adv.*, 4:13280–13292, 2014.
- [229] Raphael Wischert, Pierre Laurent, Christophe Copéret, Françoise Delbecq, and Philippe Sautet. γ -Alumina: The Essential and Unexpected Role of Water

- for the Structure, Stability, and Reactivity of “Defect” Sites. *Journal of the American Chemical Society*, 134(35):14430–14449, 2012.
- [230] John P. Perdew, Kieron Burke, and Matthias Ernzerhof. Errata:Generalized Gradient Approximation Made Simple. *Phys. Rev. Lett.*, 78:1396, Feb 1997.
- [231] Anton Kokalj. Xcrysden-a new program for displaying crystalline structures and electron densities. *Journal of Molecular Graphics and Modelling*, 17(3-4):176 – 179, 1999.
- [232] Anton Kokalj. Computer graphics and graphical user interfaces as tools in simulations of matter at the atomic scale. *Computational Materials Science*, 28(2):155 – 168, 2003. Proceedings of the Symposium on Software Development for Process and Materials Design.
- [233] Hendrik J. Monkhorst and James D. Pack. Special points for brillouin-zone integrations. *Physical Review B*, 13:5188–5192, 1976.
- [234] Nicola Marzari, David Vanderbilt, and M. C. Payne. Ensemble density-functional theory for ab initio molecular dynamics of metals and finite-temperature insulators. *Phys. Rev. Lett.*, 79:1337–1340, Aug 1997.
- [235] E. Sanville, S. D. Kenny, R. Smith, and Henkelman G. An improved grid-based algorithm for bader charge allocation. *Journal of Computational Chemistry*, 28:899–908, 2007.
- [236] G. Henkelman, A. Arnaldsson, and H. Jonsson. A fast and robust algorithm for bader decomposition of charge density. *Computational Materials Science*, 36:354–360, 2006.
- [237] N. Aaron Deskins, Donghai Mei, and Michel Dupuis. Adsorption and diffusion of a single Pt atom on γ -Al₂O₃ surfaces. *Surface Science*, 603(17):2793 – 2807, 2009.
- [238] Dong-Bo Cao, Yong-Wang Li, Jianguo Wang, and Haijun Jiao. Mechanism of γ -Al₂O₃ support in CO₂ reforming of CH₄ - a density functional theory study. *The Journal of Physical Chemistry C*, 115(1):225–233, 2011.

- [239] S. J. Gregg and J. D. F. Ramsay. Study of the adsorption of carbon dioxide by alumina using infrared and isotherm measurements. *The Journal of Physical Chemistry*, 73(5):1243–1247, 1969.
- [240] M. Cabrejas Manchado, J. M. Guil, A. Perez Masia, A. Ruiz Paniego, and J. M. Trejo Menayo. Adsorption of H₂, O₂, CO, and CO₂ on a γ -alumina: Volumetric and calorimetric studies. *Langmuir*, 10(3):685–691, 1994.
- [241] Yunxiang Pan, Chang-jun Liu, and Qingfeng Ge. Adsorption and protonation of CO₂ on partially hydroxylated γ -Al₂O₃ surfaces: A density functional theory study. *Langmuir*, 24(21):12410–12419, 2008.
- [242] M. Digne, P. Sautet, P. Raybaud, P. Euzen, and H. Toulhoat. Hydroxyl groups on γ -alumina surfaces: A DFT study. *Journal of Catalysis*, 211(1):1 – 5, 2002.
- [243] Patanachai Janthon, Francesc Viñes, Jakkapan Sirijaraensre, Jumras Limtrakul, and Francesc Illas. Adding pieces to the CO/Pt(111) puzzle: The role of dispersion. *The Journal of Physical Chemistry C*, 121(7):3970–3977, 2017.
- [244] Vadim V. Brazhkin, Alexander G. Lyapin, and Russell J. Hemley. Harder than diamond: Dreams and reality. *Philosophical Magazine A*, 82(2):231–253, 2002.
- [245] Seung-Hoon Jhi, Jisoon Ihm, Steven G. Louie, and Marvin L. Cohen. Electronic mechanism of hardness enhancement in transition-metal carbonitrides. *Nature*, 399(46):132–134, 1999.
- [246] Nicola Gaston and Shaun Hendy. Hydrogen adsorption on model tungsten carbide surfaces. *Catalysis Today*, 146(1-2):223 – 229, 2009.
- [247] Vladimir M. Nikolic, Dragana L. Zugic, Ivana M. Perovic, Aleksandra B. Saponjic, Biljana M. Babic, Igor A. Pasti, and Milica P. Marceta Kaninski. Investigation of tungsten carbide supported Pd or Pt as anode catalysts for PEM fuel cells. *International Journal of Hydrogen Energy*, 38(26):11340 – 11345, 2013.
- [248] Alexander N. Simonov, Pavel A. Pyrjaev, Pavel A. Simonov, Boris L. Moroz, Svetlana V. Cherepanova, Dmitry A. Zyuzin, Valery I. Bukhtiyarov, and

- Valentin N. Parmon. Enhanced catalytic activity for hydrogen electrooxidation and CO tolerance of carbon-supported non-stoichiometric palladium carbides. *Journal of Molecular Catalysis A: Chemical*, 353-354(0):204 – 214, 2012.
- [249] Dragana D. Vasic Anicijevic, Vladimir M. Nikolic, Milica P. Marceta-Kaninski, and Igor A. Pasti. Is platinum necessary for efficient hydrogen evolution? - DFT study of metal monolayers on tungsten carbide. *International Journal of Hydrogen Energy*, 38(36):16071 – 16079, 2013.
- [250] Francesc Vines, Jose A. Rodriguez, Ping Liu, and Francesc Illas. Catalyst size matters: Tuning the molecular mechanism of the water-gas shift reaction on titanium carbide based compounds. *Journal of Catalysis*, 260(1):103 – 112, 2008.
- [251] Qiquan Luo, Tao Wang, Guido Walther, Matthias Beller, and Haijun Jiao. Molybdenum carbide catalysed hydrogen production from formic acid - a density functional theory study. *Journal of Power Sources*, 246(0):548 – 555, 2014.
- [252] Jun Yang and Faming Gao. Hardness calculations of 5d transition metal monocarbides with tungsten carbide structure. *Physica Status Solidi (b)*, 247(9):2161–2167, September 2010.
- [253] S.T. Oyama. Preparation and catalytic properties of transition metal carbides and nitrides. *Catalysis Today*, 15:179–200, 1992.
- [254] J. Häglund, A. Fernández Guillermet, G. Grimvall, and M. Körling. Theory of bonding in transition-metal carbides and nitrides. *Physical Review B*, 48(16):11685–11691, October 1993.
- [255] A. Zaoui, S. Kacimi, B. Bouhafs, and A. Roula. First-principles study of bonding mechanisms in the series of Ti, V, Cr, Mo, and their carbides and nitrides. *Physica B: Condensed Matter*, 358(1-4):63–71, April 2005.
- [256] Barry P. Mant, Gian Giacomo Asara, James A. Anderson, Narcis Homs, Pilar Ramírez de la Piscina, Sònia Rodríguez, Josep M. Ricart, and Francesc Illas. Theoretical and experimental study of the interaction of CO on TiC sur-

- faces: Regular versus low coordinated sites. *Surface Science*, 613(0):63 – 73, 2013.
- [257] Carlo Ruberto and Bengt I. Lundqvist. Nature of adsorption on TiC(111) investigated with density-functional calculations. *Phys. Rev. B*, 75:235438, Jun 2007.
- [258] Ke-Zhen Qi, Gui-Chang Wang, and Wen-Jun Zheng. A first-principles study of CO hydrogenation into methane on molybdenum carbides catalysts. *Surface Science*, 614(0):53 – 63, 2013.
- [259] A.S. Rocha, A.B. Rocha, and V. Teixeira da Silva. Benzene adsorption on Mo₂C: A theoretical and experimental study. *Applied Catalysis A: General*, 379(1-2):54 – 60, 2010.
- [260] Carolina Pistonesi, María Estela Pronsato, László Bugyi, and A. Juan. The adsorption of CO on potassium doped molybdenum carbide surface: An ab-initio study. *Catalysis Today*, 181(1):102 – 107, 2012.
- [261] Johannes Pollmann, Xiangyang Peng, Jürgen Wieferink, and Peter Krüger. Adsorption of hydrogen and hydrocarbon molecules on SiC(001). *Surface Science Reports*, 69(2-3):55 – 104, 2014.
- [262] Pho Van Bui, Kouji Inagaki, Yasuhisa Sano, Kazuto Yamauchi, and Yoshitada Morikawa. Adsorption of hydrogen fluoride on sic surfaces: A density functional theory study. *Current Applied Physics*, 12, Supplement 3(0):S42 – S46, 2012.
- [263] F. Marinelli, A. Jelea, and A. Allouche. Interactions of h with tungsten carbide surfaces: An ab initio study. *Surface Science*, 601(2):578 – 587, 2007.
- [264] M.D. Ganji. Theoretical study of the adsorption of CO₂ on tungsten carbide nanotubes. *Physics Letters A*, 372(18):3277 – 3282, 2008.
- [265] Gang Chen, Qi Peng, and Yoshiyuki Kawazoe. Structural and electronic properties of neutral and charged Ca₈C₁₂ metal carbides. *Chemical Physics Letters*, 507(4-6):260 – 264, 2011.

- [266] Gang Chen, Qi Peng, and Yoshiyuki Kawazoe. First-principles study on Ca_8C_n () and Ca_mC_{12} () metal carbides. *Physics Letters A*, 375(6):994 – 999, 2011.
- [267] Marc Benard, Marie-Madeleine Rohmer, Josep-M. Poblet, and Carles Bo. Diversity in the electronic structures of metallocarbohedrenes: Ab initio study of M_8C_{12} (M = Ti, V, Zr, Nb) and $\text{Ti}_4\text{M}'_4\text{C}_{12}$ (M' = V, Zr). *The Journal of Physical Chemistry*, 99(46):16913–16924, 1995.
- [268] Ke-Zhen Qi, Gui-Chang Wang, and Wen-Jun Zheng. Structure-sensitivity of ethane hydrogenolysis over molybdenum carbides: A density functional theory study. *Applied Surface Science*, 276(0):369 – 376, 2013.
- [269] C. Pistonesi, A. Juan, A.P. Farkas, and F. Solymosi. DFT study of methanol adsorption and dissociation on $\beta\text{-Mo}_2\text{C}$. *Surface Science*, 602(13):2206 – 2211, 2008.
- [270] Linyan Li, Wen Yu, and Changqing Jin. First-principles calculations of a high-pressure synthesized compound PtC. *Journal of Physics: Condensed Matter*, 17:5965–5975, 2005.
- [271] Shigeaki Ono, Takumi Kikegawa, and Yasuo Ohishi. A high-pressure and high-temperature synthesis of platinum carbide. *Solid State Communications*, 133:55–59, 2005.
- [272] Xiao-Wei Sun, Qi-Feng Chen, Xiang-Rong Chen, Ling-Cang Cai, and Fu-Qian Jing. First-principles investigations of elastic stability and electronic structure of cubic platinum carbide under pressure. *Journal of Applied Physics*, 110(10):103507, 2011.
- [273] Qian Li, Xinxin Zhang, Hanyu Liu, Hui Wang, Miao Zhang, Quan Li, and Yanming Ma. Structural and mechanical properties of platinum carbide. *Inorganic chemistry*, 53(11):5797–802, June 2014.
- [274] X.W. Sun, Z.Y. Zeng, T. Song, Z.J. Fu, B. Kong, and Q.F. Chen. First-principles calculations of phase transition and bulk modulus of PtC. *Chemical Physics Letters*, 496(1-3):64 – 67, 2010.
- [275] Xiao-Wei Sun, Qi-Feng Chen, Ling-Cang Cai, Xiang-Rong Chen, and Fu-Qian Jing. High-temperature and high-pressure thermal expansivity of cubic PtC

- from quasi-harmonic Debye model. *Chemical Physics Letters*, 516(4-6):158 – 161, 2011.
- [276] V.V. Bannikov, I.R. Shein, and A.L. Ivanovskii. Trends in stability, elastic and electronic properties of cubic Rh, Ir, Pd and Pt carbides depending on carbon content: MC versus M₄C from first-principles calculations. *Journal of Physics and Chemistry of Solids*, 71(5):803 – 809, 2010.
- [277] Feng Peng, Hong-Zhi Fu, and Xiang-Dong Yang. Transition phase and thermodynamic properties of PtC from first-principles calculations. *Solid State Communications*, 145(3):91 – 94, 2008.
- [278] E. Deligoz, Y.O. Ciftci, P.T. Jochym, and K. Colakoglu. The first principles study on PtC compound. *Materials Chemistry and Physics*, 111(1):29 – 33, 2008.
- [279] C.Z. Fan, L.L. Sun, Y.X. Wang, R.P. Liu, S.Y. Zeng, and W.K. Wang. First-principles study on the structural, elastic and electronic properties of platinum carbide. *Physica B: Condensed Matter*, 381(1-2):174 – 178, 2006.
- [280] R.M. Lambert, W.H. Weinberg, C.M. Comrie, and J.W. Linnett. LEED-Auger investigation of a stable carbide overlayer on a platinum (111) surface. *Surface Science*, 27(3):653 – 658, 1971.
- [281] Dan J. Harding, Christian Kerpel, Gerard Meijer, and André Fielicke. Unusual bonding in platinum carbido clusters. *The Journal of Physical Chemistry Letters*, 4(6):892–896, 2013.
- [282] D. M. Ceperley and B. J. Alder. Ground state of the electron Gas by a stochastic method. *Physical Review Letters*, 45:566–569, Aug 1980.
- [283] Venu Mankad, Nikita Rathod, Sanjay D. Gupta, Sanjeev K. Gupta, and Prafulla K. Jha. Stable structure of platinum carbides: A first principles investigation on the structure, elastic, electronic and phonon properties. *Materials Chemistry and Physics*, 129(3):816–822, 2011.
- [284] Francis Birch. Finite elastic strain of cubic crystals. *Phys. Rev.*, 71:809–824, Jun 1947.

- [285] Eric Osei-Agyemang, Jean-François Paul, Romain Lucas, Sylvie Foucaud, and Sylvain Cristol. Oxidation and equilibrium morphology of zirconium carbide low index surfaces using DFT and atomistic thermodynamic modeling. *The Journal of Physical Chemistry C*, 120(16):8759–8771, 2016.
- [286] Malcolm W. J. Chase. *NIST-JANAF Thermochemical Tables, 4th Edition*. American Inst. of Physics, New York, 1998.
- [287] Jun Yang and Faming Gao. First principles calculations of mechanical properties of cubic 5d transition metal monocarbides. *Physica B: Condensed Matter*, 407(17):3527 – 3534, 2012.
- [288] Hsiu Ying Chung, Michelle B. Weinberger, Jenn Ming Yang, Sarah H. Tolbert, and Richard B. Kaner. Correlation between hardness and elastic moduli of the ultraincompressible transition metal diborides RuB₂, OsB₂, and ReB₂. *Applied Physics Letters*, 92:261904, 2008.
- [289] Xue Jiang, Jijun Zhao, and Rajeev Ahuja. A novel superhard bn allotrope under cold compression of h-BN. *Journal of Physics: Condensed Matter*, 25(12):122204, 2013.
- [290] Chang-Zeng Fan, Song-Yan Zeng, Zai-Ji Zhan, Ri-Ping Liu, Wen-Kui Wang, Ping Zhang, and Yu-Gui Yao. Low compressible noble metal carbides with rocksalt structure: Ab initio total energy calculations of the elastic stability. *Applied Physics Letters*, 89:071913, 2006.
- [291] A. D. Becke. Density-functional exchange-energy approximation with correct asymptotic behavior. *Phys. Rev. A*, 38:3098–3100, Sep 1988.
- [292] Aliaksandr V. Krukau, Oleg A. Vydrov, Artur F. Izmaylov, and Gustavo E. Scuseria. Influence of the exchange screening parameter on the performance of screened hybrid functionals. *The Journal of Chemical Physics*, 125(22):224106, 2006.
- [293] J. Paier, M. Marsman, K. Hummer, G. Kresse, I. C. Gerber, and J. G. Ángyán. Screened hybrid density functionals applied to solids. *The Journal of Chemical Physics*, 124(15):154709, 2006.

- [294] P. E. Blöchl. Projector augmented-wave method. *Phys. Rev. B*, 50:17953–17979, Dec 1994.
- [295] G. Kresse and D. Joubert. From ultrasoft pseudopotentials to the projector augmented-wave method. *Phys. Rev. B*, 59:1758–1775, Jan 1999.
- [296] A. Zaoui and Ferhat M. Dynamical stability and high pressure phases of platinum carbide. *Solid State Communications*, 151:867–869, 2011.
- [297] Jiajie Zhu, Mu Gu, and Ravindra Pandey. Stability and electronic properties of polar and non-polar surfaces of CuI. *Applied Surface Science*, 268:87 – 91, 2013.
- [298] P W Tasker. The stability of ionic crystal surfaces. *Journal of Physics C: Solid State Physics*, 12(22):4977–4984, 1979.
- [299] Maija M. Kuklja, Roman V. Tsyshevsky, and Onise Sharia. Effect of polar surfaces on decomposition of molecular materials. *Journal of the American Chemical Society*, 136(38):13289–13302, 2014.
- [300] Lennart Bengtsson. Dipole correction for surface supercell calculations. *Physical Review B*, 59:12301–12304, May 1999.
- [301] H.W. Hugosson, O. Eriksson, U. Jansson, A.V. Ruban, P. Souvatzis, and I.A. Abrikosov. Surface energies and work functions of the transition metal carbides. *Surface Science*, 557:243 – 254, 2004.
- [302] Kevin Kähler, Marie C. Holz, Markus Rohe, Andre C. van Veen, and Martin Muhler. Methanol oxidation as probe reaction for active sites in Au/ZnO and Au/TiO₂ catalysts. *Journal of Catalysis*, 299:162–170, 2013.
- [303] Gregory M Mullen, Liang Zhang, Edward J Evans, Ting Yan, Graeme Henkelman, and C Buddie Mullins. Oxygen and hydroxyl species induce multiple reaction pathways for the partial oxidation of allyl alcohol on gold. *Journal of the American Chemical Society*, 136(17):6489–6498, 2014.
- [304] Yuanbo Zhang, Joshua P. Small, Michael E. S. Amori, and Philip Kim. Electric field modulation of galvanomagnetic properties of mesoscopic graphite. *Phys. Rev. Lett.*, 94:176803, May 2005.

- [305] A. K. Geim and K. S. Novoselov. The rise of graphene. *Nature Materials*, 6:183–191, 2007.
- [306] E. H. Hwang, S. Adam, and S. Das Sarma. Transport in chemically doped graphene in the presence of adsorbed molecules. *Phys. Rev. B*, 76:195421, Nov 2007.
- [307] T. O. Wehling, M. I. Katsnelson, and A. I. Lichtenstein. Impurities on graphene: Midgap states and migration barriers. *Phys. Rev. B*, 80:085428, Aug 2009.
- [308] Tim O. Wehling, Alexander I. Lichtenstein, and Mikhail I. Katsnelson. First-principles studies of water adsorption on graphene: The role of the substrate. *Applied Physics Letters*, 93(20):202110, 2008.
- [309] P. A. Khomyakov, G. Giovannetti, P. C. Rusu, G. Brocks, J. van den Brink, and P. J. Kelly. First-principles study of the interaction and charge transfer between graphene and metals. *Phys. Rev. B*, 79:195425, May 2009.
- [310] Harman Johll, Hway Chuan Kang, and Eng Soon Tok. Density functional theory study of Fe, Co, and Ni adatoms and dimers adsorbed on graphene. *Phys. Rev. B*, 79:245416, Jun 2009.
- [311] Jorge O. Sofo, Ajay S. Chaudhari, and Greg D. Barber. Graphane: A two-dimensional hydrocarbon. *Phys. Rev. B*, 75:153401, Apr 2007.
- [312] D. C. Elias, R. R. Nair, T. M. G. Mohiuddin, S. V. Morozov, P. Blake, M. P. Halsall, A. C. Ferrari, D. W. Boukhvalov, M. I. Katsnelson, A. K. Geim, and K. S. Novoselov. Control of graphene's properties by reversible hydrogenation: Evidence for graphane. *Science*, 323(5914):610–613, 2009.
- [313] Sunmin Ryu, Melinda Y. Han, Janina Maultzsch, Tony F. Heinz, Philip Kim, Michael L. Steigerwald, and Louis E. Brus. Reversible basal plane hydrogenation of graphene. *Nano Letters*, 8(12):4597–4602, 2008.
- [314] Hoonkyung Lee, Marvin L. Cohen, and Steven G. Louie. Selective functionalization of halogens on zigzag graphene nanoribbons: A route to the separation of zigzag graphene nanoribbons. *Applied Physics Letters*, 97(23):233101, 2010.

- [315] A. N. Rudenko, F. J. Keil, M. I. Katsnelson, and A. I. Lichtenstein. Adsorption of diatomic halogen molecules on graphene: A van der waals density functional study. *Phys. Rev. B*, 82:035427, Jul 2010.
- [316] Y. G. Zhou, X. T. Zu, F. Gao, H. F. Lv, and H. Y. Xiao. Adsorption-induced magnetic properties and metallic behavior of graphene. *Applied Physics Letters*, 95(12):123119, 2009.
- [317] Bo Li, Lin Zhou, Di Wu, Hailin Peng, Kai Yan, Yu Zhou, and Zhongfan Liu. Photochemical chlorination of graphene. *ACS Nano*, 5(7):5957–5961, 2011.
- [318] H. Şahin and S. Ciraci. Chlorine adsorption on graphene: Chlorographene. *The Journal of Physical Chemistry C*, 116(45):24075–24083, 2012.
- [319] M. Ijäs, P. Havu, and A. Harju. Fracturing graphene by chlorination: A theoretical viewpoint. *Phys. Rev. B*, 85:035440, Jan 2012.
- [320] Nicola Marzari, David Vanderbilt, Alessandro De Vita, and M. C. Payne. Thermal contraction and disordering of the al(110) surface. *Phys. Rev. Lett.*, 82:3296–3299, Apr 1999.
- [321] Frank H. Allen, Olga Kennard, David G. Watson, Lee Brammer, A. Guy Orpen, and Robin Taylor. Tables of bond lengths determined by X-ray and neutron diffraction. part 1. bond lengths in organic compounds. *J. Chem. Soc., Perkin Trans. 2*, pages S1–S19, 1987.
- [322] Wei Han, Roland K. Kawakami, Martin Gmitra, and Jaroslav Fabian. Graphene spintronics. *Nature Nanotechnology*, 9:794–807, 2014.
- [323] Peng Yu, Shengkai Yu, and Weidong Zhou. Evaluation of thermal performance of graphene overcoat on multi-layered structure subject to laser heating. *International Communications in Heat and Mass Transfer*, 68:27 – 31, 2015.
- [324] Mingmei Yang, Lin Zhou, Jinying Wang, Zhongfan Liu, and Zhirong Liu. Evolutionary chlorination of graphene: From charge-transfer complex to covalent bonding and nonbonding. *The Journal of Physical Chemistry C*, 116(1):844–850, 2012.

- [325] Jannik C. Meyer, C. Kisielowski, R. Erni, Marta D. Rossell, M. F. Crommie, and A. Zettl. Direct imaging of lattice atoms and topological defects in graphene membranes. *Nano Letters*, 8(11):3582–3586, 2008.
- [326] M. M. Ugeda, I. Brihuega, F. Guinea, and J. M. Gómez-Rodríguez. Missing atom as a source of carbon magnetism. *Phys. Rev. Lett.*, 104:096804, Mar 2010.
- [327] Johan M. Carlsson and Matthias Scheffler. Structural, electronic, and chemical properties of nanoporous carbon. *Phys. Rev. Lett.*, 96:046806, Feb 2006.
- [328] G. Brunetto, P. A. S. Autreto, L. D. Machado, B. I. Santos, R. P. B. dos Santos, and D. S. Galvão. Nonzero gap two-dimensional carbon allotrope from porous graphene. *The Journal of Physical Chemistry C*, 116(23):12810–12813, 2012.
- [329] A. A. El-Barbary, R. H. Telling, C. P. Ewels, M. I. Heggie, and P. R. Briddon. Structure and energetics of the vacancy in graphite. *Phys. Rev. B*, 68:144107, Oct 2003.
- [330] Florian Banhart, Jani Kotakoski, and Arkady V. Krasheninnikov. Structural defects in graphene. *ACS Nano*, 5(1):26–41, 2011.
- [331] Oleg V. Yazyev and Lothar Helm. Defect-induced magnetism in graphene. *Phys. Rev. B*, 75:125408, Mar 2007.
- [332] Kin Fai Mak, Chun Hung Lui, Jie Shan, and Tony F. Heinz. Observation of an electric-field-induced band gap in bilayer graphene by infrared spectroscopy. *Phys. Rev. Lett.*, 102:256405, Jun 2009.
- [333] Hong Zhang and Yoshiyuki Miyamoto. Graphene production by laser shot on graphene oxide: An ab initio prediction. *Phys. Rev. B*, 85:033402, Jan 2012.
- [334] Hong Zhang and Yoshiyuki Miyamoto. Erratum: Graphene production by laser shot on graphene oxide: An ab initio prediction [phys. rev. b 85, 033402 (2012)]. *Phys. Rev. B*, 85:089901, Feb 2012.
- [335] Z. M. Ao and F. M. Peeters. Electric field: A catalyst for hydrogenation of graphene. *Applied Physics Letters*, 96(25):253106, 2010.

- [336] Pingping Yao, Penglei Chen, Lang Jiang, Huaping Zhao, Hongfei Zhu, Ding Zhou, Wenping Hu, Bao-Hang Han, and Minghua Liu. Electric current induced reduction of graphene oxide and its application as gap electrodes in organic photoswitching devices. *Advanced Materials*, 22(44):5008–5012, 2010.
- [337] L. Brey and H. A. Fertig. Electronic states of graphene nanoribbons studied with the dirac equation. *Phys. Rev. B*, 73:235411, Jun 2006.
- [338] Francisco J. Martín-Martínez, Stijn Fias, Gregory Van Lier, Frank De Proft, and Paul Geerlings. Electronic structure and aromaticity of graphene nanoribbons. *Chemistry - A European Journal*, 18(20):6183–6194, 2012.
- [339] Fuming Xu, Zhizhou Yu, Zhirui Gong, and Hao Jin. First-principles study on the electronic and transport properties of periodically nitrogen-doped graphene and carbon nanotube superlattices. *Frontiers of Physics*, 12(4):127306, 2017.
- [340] Xiaolin Li, Xinran Wang, Li Zhang, Sangwon Lee, and Hongjie Dai. Chemically derived, ultrasmooth graphene nanoribbon semiconductors. *Science*, 319(5867):1229–1232, 2008.
- [341] J. Baringhaus, M. Ruan, F. Edler, A. Tejada, M. Sicot, A. Taleb-Ibrahimi, A.-P. Li, Z. Jiang, E. H. Conrad, C. Berger, C. Tegenkamp, and W. A. de Heer. Exceptional ballistic transport in epitaxial graphene nanoribbons. *Nature*, 506:349–354, February 2014.
- [342] V. Torres, C. León, D. Faria, and A. Latgé. Gap engineering in strained fold-like armchair graphene nanoribbons. *Phys. Rev. B*, 95:045425, Jan 2017.
- [343] Young-Woo Son, Marvin L. Cohen, and Steven G. Louie. Energy gaps in graphene nanoribbons. *Phys. Rev. Lett.*, 97:216803, Nov 2006.

CURRICULUM VITAE

PERSONAL INFORMATION

Surname, Name: Şensoy, Mehmet Gökhan

Nationality: Turkish (TC)

Date and Place of Birth: 14 November 1985, Niğde/Turkey

Marital Status: Single

e-mail: mehmetgokhansensoy@gmail.com

Phone 1: +90 (312) 210 4329 (office)

Phone 2: +90 505 525 4605 (GSM)

EDUCATION

Degree	Institution	Year of Graduation
Ph.D.	Physics, Middle East Technical University	2017
M.S.	Physics, Balıkesir University	2010
B.S.	Physics (SSME), Balıkesir University	2008

PROFESSIONAL EXPERIENCE

Year	Place	Enrollment
2011-2015	METU	Teaching Assistant, Physics Laboratories
2015-2016	Harvard University	Visiting Researcher
2016-2017	METU	Teaching Assistant, Physics Laboratories

RESEARCH INTERESTS

- Condensed-Matter Physics, Computational Physics, Density functional theory methods, Nanotechnology, Material Science

PUBLICATIONS AND PREPRINTS

- *"Using the 18F programmable microchip series to transfer data via usb port"*. e-Journal of New World Sciences Academy, 1A0032, 4, (3), 332-339, (2009). Ege, Y. , Goktepe, M. , Sensoy, M.G. , Perin, D. ve Yillik, H.
- *"Converting analog signal to 12 bit resolution digital signal"*. e-Journal of New World Sciences Academy, 1A0060, 5, (1), 1-7, (2010). Ege, Y. , Sensoy, M.G.
- *"Wireless data transfer by using ASK type receiver-transceiver RF module"*. e-Journal of New World Sciences Academy, 1A0071, 5, (2), 172-179, (2010). Sensoy, M.G. , Ege, Y.
- *"Numerical Analysis for Remote Identification of Materials With Magnetic Characteristics"*. IEEE Transactions On Instrumentation And Measurement, Vol. 60, No. 9,(2011). Yavuz Ege, M.Gokhan Sensoy, Osman Kalender, and Sedat Nazlibilek
- *"Identification of materials with magnetic characteristics by neural Networks"*. Measurement, Volume 45, Issue 4, 734-744, (2012). Sedat Nazlibilek, Yavuz Ege, Osman Kalender, M.Gokhan Sensoy, Deniz Karacor, Murat Husnu Sazli
- *"A New Wireless Asynchronous Data Communications Module for Industrial Applications"*. Measurement, Volume 46, Issue 8, Pages 2672-2681, (2013). Yavuz Ege, M.Gokhan Sensoy, Osman Kalender, Sedat Nazlibilek, Hakan Citak
- *"New magnetic measurement system for determining metal covered mines by detecting magnetic anomaly using a sensor network"*. Indian Journal of Pure and Applied Physics, Vol.53, Pages 119-211, (2015). Yavuz Ege, Adnan Kakilli, Hakan Citak, Osman Kalender, Sedat Nazlibilek, Mehmet Gokhan Sensoy

- *"Structural and electronic properties of bulk and low-index surfaces of zincblende PtC"*. Journal of Physics: Condensed Matter, Volume 29, Number 12, (2017). M.Gokhan Sensoy, Hande Ustunel, Danielle Toffoli
- *"Strain effects on the behavior of isolated and paired sulfur vacancy defects in monolayer MoS₂"*. Phys. Rev. B 95, 014106, (2017). M.Gokhan Sensoy, Dmitry Vinichenko, Wei Chen, Cynthia M. Friend, and Efthimios Kaxiras
- *"Accurate formation energies of charged defects in solids: A systematic approach"*. Phys. Rev. B 95, 235310, (2017). Dmitry Vinichenko, M.Gokhan Sensoy, Cynthia M. Friend, and Efthimios Kaxiras

CONFERENCES, WORKSHOPS, SCHOOLS AND MEETINGS ATTENDED

- *"Density functional theory investigation of CO, CO₂ and H₂O activation on γ -Al₂O₃ Supported Pt Clusters"*, NanoTR-9, Erzurum, Turkey, June 2013.
- *"Density Functional Theory Investigation of Adsorption Properties of CO, CO₂ and H₂O on γ -Al₂O₃ Supported Pt Clusters"*, APS March Meeting, Denver, USA, March 2014.
- *"Density Functional Theory Investigation of the Structural, Electronic and Adsorption Properties of (100), (110) and (111) Surfaces of Zincblende PtC"*, NanoTR-11, Ankara, Turkey, June 2015.

COMPUTER SKILLS

- *Operating Systems ; UNIX/LINUX, MS WINDOWS*
- *Scientific Programs ; L^AT_EX, Mathematica, Octave, QUANTUM ESPRESSO (PWscf), VASP, SIESTA*